Laser Spectroscopy of the Boron Isotopic Chain

Laserspektroskopie in der Bor-Isotopenkette
Zur Erlangung des Grades eines Doktors der Naturwissenschaften (Dr. rer. nat.)
genehmigte Dissertation von Bernhard Maaß aus Hanau
Tag der Einreichung: 05.11.2019, Tag der Prüfung: 20.01.2020
Darmstadt — D 17

1. Gutachten: Prof. Dr. Wilfried Nörtershäuser
2. Gutachten: Prof. Dr. Thomas Aumann

TECHNISCHE
UNIVERSITÄT
DARMSTADT

Fachbereich Physik
Institut für Kernphysik
AG Nörtershäuser

LASER
SpHERe

Laser Spectroscopy of the Boron Isotopic Chain
Laserspektroskopie in der Bor-Isotopenkette

Genehmigte Dissertation von Bernhard Maaß aus Hanau

1. Gutachten: Prof. Dr. Wilfried Nörtershäuser
2. Gutachten: Prof. Dr. Thomas Aumann

Tag der Einreichung: 05.11.2019
Tag der Prüfung: 20.01.2020

Darmstadt — D 17

Erklärung gemäß §9 Promotionsordnung

Hiermit versichere ich, dass ich die vorliegende Dissertation selbstständig angefertigt und keine anderen als die angegebenen Quellen und Hilfsmittel verwendet habe. Alle wörtlichen und paraphrasierten Zitate wurden angemessen kenntlich gemacht. Die Arbeit hat bisher noch nicht zu Prüfungszwecken gedient.

Darmstadt, den 31. Oktober 2019

(B. Maaß)

Abstract

The charge radius of a nucleus is a fundamental physical property that corresponds to the binding strength and the structure of the bound nuclear system. This observable is particularly important for the investigation of so-called halo nuclei, which consist of a compact nuclear core with typical nuclear density and a dilute cloud of halo nucleons. Neutron halo nuclei have been subject to numerous investigations, but little is known about proton-halo systems.

The isotope ^{8}B is believed to be a prototype of a proton-halo, which was concluded indirectly from measurements of its quadrupole moment and analysis of the momentum distribution of breakup fragments. High-precision laser spectroscopy can provide direct proof of the halo structure by measuring the nuclear charge radius. Such measurements were performed previously for the most prominent (neutron) halo isotopes up to $Z = 4$ (beryllium). Extending these investigations to the boron isotopes ($Z = 5$) is the subject of this thesis. It covers the design and installation of the experimental setup for the on-line measurement of the short-lived ^{8}B $\left(t_{1/2} = 770\,\mathrm{ms}\right)$ as well as first off-line measurements of the charge radius difference between the two stable isotopes ^{10}B and ^{11}B.

The halo-candidate ^{8}B is produced in a ^{3}He$\left(^{6}\text{Li},^{8}\text{B}\right)$n reaction in inverse kinematics and the energetic ^{8}B ions are stopped in a gas cell and then transported to the collinear beamline by radiofrequency ion guides. The production of ^{8}B was optimized by improving the cryogenic gas target to avoid saturation effects. It was observed that the ^{8}B ions that leave the gas cell have water molecules attached. While this improves the transport process, it prohibits laser spectroscopy on the atomic system.

Therefore, a molecular breakup station based on the transmission of the molecules through nanometer-thin carbon foils was designed, built and tested. The apparatus to perform collinear laser spectroscopy was also installed at the experimental site during this work and the performance of its fluorescence detection region has been significantly improved. The progress achieved represents a significant step towards laser spectroscopy on the exotic proton-halo candidate ^{8}B in the near future.

The isotope shift between the stable isotopes of boron ^{10}B and ^{11}B was measured on a collimated atomic beam. Beams of two lasers crossed the atomic beam in perpendicular alignment to perform resonance ionization mass spectrometry. The first laser excited the $2p \rightarrow 3s$ ground state transition and the second laser was used for non-resonant ionization of the excited atoms. Exact control of the overlap angle of laser and the atomic beam is essential to eliminate the first-order Doppler effect, which otherwise introduces significant uncertainties for the spectroscopy of these light ions. Therefore, an elaborated double-pass scheme has been used where the uncertainty in the overlap angle was minimized together with other sources of systematic uncertainties that are typically prevalent in laser spectroscopy. The isotope shift between ^{10}B and ^{11}B was measured for the first time with sufficient accuracy to extract the difference in the mean-square nuclear charge radius. Results are compared with predictions from state-of-the-art ab-initio nuclear structure theories and show reasonable agreement with the no-core shell model as well as Green's function Monte Carlo calculations.

Zusammenfassung

Der Kernladungsradius ist eine fundamentale physikalische Observable, welche Aufschluss über die Größe und die Bindungsstärke eines Atomkerns gibt. Besondere Aussagekraft besitzt sie bei sogenannten Halokernen, welche aus einem kompakten Kern typischer Kerndichte bestehen, der von einer „diffusen Wolke" verdünnter Kernmaterie, bestehend aus einem oder mehreren Halo-Nukleonen, umgeben ist. Neutronen-Halokerne wurden in einer Vielzahl an Experimenten untersucht, Protonen-Halos aber sind noch wenig erforscht. Das Isotop ^{8}B wird als Prototyp eines Protonen-Halokerns gehandelt, dies aber nur auf Basis indirekter Messungen: sein großes Quadrupolmoment und die schmale Impulsverteilung der Komponenten in Aufbruchreaktionen sind Indizien für diese Zuordnung. Einen direkten Nachweis der Halo-Struktur kann eine laserspektroskopische Untersuchung liefern, wie sie bereits an Neutronen-Halokernen von Elementen mit Kernladungszahl $Z = 2$ (Helium) bis $Z = 4$ (Beryllium) durchgeführt wurde. Das Thema dieser Arbeit ist die Ausweitung dieser Messungen auf die Isotope von Bor ($Z = 5$). Dazu wurde der für die Messung des kurzlebigen Isotops ^{8}B (Halbwertszeit: $t_{1/2} = 770\,\mathrm{ms}$) notwendige Aufbau entworfen und installiert. Weiterhin gelang eine erste präzise Messung der Differenz der Ladungsradien der beiden stabilen Isotope ^{10}B und ^{11}B.

Das Isotop ^{8}B wird in der Reaktion $^{3}\mathrm{He}\left(^{6}\mathrm{Li},^{8}\mathrm{B}\right)\mathrm{n}$ in inverser Kinematik produziert, anschließend in einer Gaszelle gestoppt und mit Radiofrequenzquadrupolen zum Experimentieraufbau transportiert. Die Produktion von ^{8}B wurde optimiert, indem ein neues kryogenes Target entworfen wurde, welches Sättigungseffekte unterdrückt. Allerdings wurde festgestellt, dass ^{8}B die Gaszelle als Molekül im Verbund mit Wassermolekülen verlässt. Tatsächlich erhöht dies die Transporteffizienz aufgrund der höheren Masse, Laserspektroskopie aber kann nur am reinen Atom durchgeführt werden. Deshalb wurde eine Molekülaufbruchstation entwickelt, aufgebaut und getestet, in welcher die Molekülionen durch eine nur wenige Nanometer dünne Folie transmittiert werden. Zugleich wurde der Experimentaufbau für die kollineare Laserspektroskopie vor Ort in Betrieb genommen, und die Effizienz der Fluoreszenznachweisregion signifikant erhöht. Der erzielte Fortschritt ist wegweisend für die Messung des Protonen-Halo Kandidaten ^{8}B in der nahen Zukunft.

Die Isotopieverschiebung zwischen den beiden stabilen Bor-Isotopen ^{10}B und ^{11}B wurde an einem kollimierten Atomstrahl gemessen. Zwei Laserstrahlen wurden dafür mit einem Atomstrahl in lotrechter Geometrie überlagert um Resonanz-Ionisationsspektrometrie durchzuführen. Einer der beiden Laser regt den $2p \rightarrow 3s$ Grundzustandsübergang an, während der zweite Laser die resonant angeregten Atome ionisiert. Die Kontrolle des Winkels zwischen Atom- und Laserstrahl ist von Bedeutung, da ein Winkel, der von 90° abweicht, eine Dopplerverschiebung verursacht, welche gerade für leichte Ionen große Unsicherheiten verursacht. Um dies zu umgehen, wurde ein Rücküberlagerungsschema verwendet, in welchem die Unsicherheit der Winkelbestimmung sowie weitere typische systematische Unsicherheiten umgangen werden. Dadurch konnte die Isotopieverschiebung zwischen ^{10}B und ^{11}B zum ersten Mal mit einer Genauigkeit gemessen werden, welche die Extraktion der Differenz zwischen den beiden Kernladungsradien erlaubt. Dieses Ergebnis wird mit modernen theoretischen Kernstruktur-Modellen verglichen und zeigt eine gute Übereinstimmung mit Modellrechnungen des sogenannten „Green's function Monte Carlo" und des „no-core shell model".

Contents

List of Figures

List of Tables

List of Acronyms

Acronyms	
χEFT	chiral effective field theory
1P	first pass
2P	second passs
3N	three-nucleon (interaction)
AC	alternating current
AV18	Argonne v_{18} potential
c/ac	collinear/anticollinear
CF	Conflat$^{\circledR}$
CEC	charge-exchange-cell
CNM	carbon nano-membrane
CPC	compound parabolic concentrator
cw	continuous wave
DAC	digital-analog-converter
DAQ	data acquisition system
DC	direct current
DP	double-pass
EBIS	electron-beam ion source
FDR	fluorescence detection region
FS	field shift
g.s.	ground state
GFMC	Green's function Monte Carlo
HFS	hyperfine structure
HSA	hyperfine-structure anomaly
HV	high voltage
IL7	Illinois v7 potential
IP	ionization potential
IR	ionization region
LED	light-emitting diode
LN2	liquid nitrogen
LO	leading order
MB	Maxwell-Boltzmann
MBS	molecular breakup system
MS	mass shift
NCSM	no-core shell model
NMS	normal mass shift
NN	nucleon-nucleon (interaction)
OFC	optical frequency comb
PGC	primary gas catcher
PMT	photomultiplier tube
QCD	quantum chromodynamics
QED	quantum electrodynamics
QMS	quadrupole mass spectrometer
RFQ	radiofrequency quadrupole
SCS	superconducting solenoid
SGC	secondary gas catcher
SHG	second-harmonic generation
SMS	specific mass shift
SNR	signal-to-noise ratio
SP	single-pass
UHV	ultra-high vacuum
UV	ultraviolet

Facilities		*Located at*	
ANL	Argonne National Laboratory		Lemont, USA
ATLAS	Argonne Tandem Linac Accelerator System	ANL	Lemont, USA
BECOLA	Beam Cooler and Laser spectroscopy	NSCL	East Lansing, USA
CARIBU	Californium Rare Isotope Breeder Upgrade	ANL	Lemont, USA
CERN	European Organization for Nuclear Research		Geneva, Switzerland
COLLAPS	Collinear Laser Spectroscopy at ISOLDE-CERN	ISOLDE	Geneva, Switzerland
GANIL	Grand Accélérateur National d'Ions Lourds		Caen, France
ISOLDE	Isotope Separator On Line Device	CERN	Geneva, Switzerland
KOALA	Kollineare App. für Laserspek. u. angew. Wiss.	TU Darmstadt	Darmstadt, Germany
NSCL	National Superconducting Cyclotron Laboratory		East Lansing, USA
TRIGA	Training Research Isotopes General Atomics		Mainz, Germany
TRIUMF	Tri University Meson Facility		Vancouver, Canada

1 Motivation

1.1 Historical context

Since the dawn of humankind, the nature and structure of matter have been of interest to philosophers, scientists, and later physicists around the world. Already in ancient Greece, the idea that matter is made of small, undividable particles (Greek: átomos) is documented. While the general picture of small particles, nowadays called atoms, rendering the world around us is still valid, the perception of their indivisibility did not stand the test of time.

In 1911, after analyzing the scattering pattern of α-particles in gold foil, Ernest Rutherford proposed the existence of a nucleus, which combines the positive electric charge and almost the entire mass of the atom into a volume orders of magnitude smaller than the atom itself. Negatively charged electrons orbit the nucleus since they are attracted by the strong electric field and neutralize the total nuclear charge [1]. Another puzzle piece for understanding atoms was delivered by Max Planck, who proposed in 1900 that energy is quantized, which allowed the description of black-body radiation at the high-energy threshold [2]. Using the Planck constant to quantize the momenta of electrons orbiting the nuclear core, the Bohr model was already sufficient to describe phenomena like absorption and emission of photons in simple atomic systems [3].

Planck and Einstein can be referred to as the founders of quantum mechanics, which at that time allowed describing the electronic shell of the atom, but not the nature of the atomic nucleus. Experiments with ionic gases [4] showed the existence of a massive particle with charge $+1$, later named protons [5]. They were identified as the constituents of nuclear matter in the first induced nuclear reaction in a laboratory in 1919 [6].

Since particles with the same charge repel each other, it is inexplicable why nuclei heavier than hydrogen should be stable. The discovery of the neutron in 1932 [7] allowed the classification of different isotopes of one element but was also further evidence for a missing force that binds nuclear systems together. The phenomenological liquid drop model by Hans Bethe and Carl Friedrich von Weizsäcker was able to explain the gross nuclear structure and the energy balance in fission and fusion reactions [8]. These massive binding energies needed to contain the Coulomb repulsion inside the nuclei were made available –with its immense consequences for society– when nuclear fission was discovered in 1938 by Otto Hahn, Lise Meitner and Fritz Strassmann [9, 10].

The nuclear binding force was approached phenomenologically [11] by Yukawa long before interpretations of its origin. The structure of nuclei, investigated in experiments, delivered nuclear observables such as size and deformation, which allowed testing the newly formulated nuclear models. The discovery of “magic” numbers of nucleons, which form surpassingly stable nuclear compounds, lead to the description of the shell model by Maria Goeppert-Mayer and Hans Jensen in 1950 [12, 13, 14], which is still a groundwork for the understanding of complex nuclei up to the present day.

It took many years, until the seventies, when the outline of a strong, fundamental interaction named quantum chromodynamics (QCD) [15] was formulated to explain the new-born field of particle physics. Deduced from the new theories, the standard model predicted that hadrons consist of quarks, whose existence was confirmed in deep-inelastic scattering experiments. Residual forces from the strong interaction between these quarks result in an attractive potential between the nucleons.

The emergence of QCD [16] did not solve the problem of formalizing the inter-nucleon interaction, but rather added more pieces to the puzzle. The Hamiltonian of the strong interaction does not have an analytical expression that can be solved for all lengths and energy scales. Instead, realistic potentials were developed [17], which map the nuclear force in its respective energy regime, by introducing meson exchange as the underlying interaction principle [18, 19]. These potentials are refined by (chiral) effective field theories, which convey fundamen-

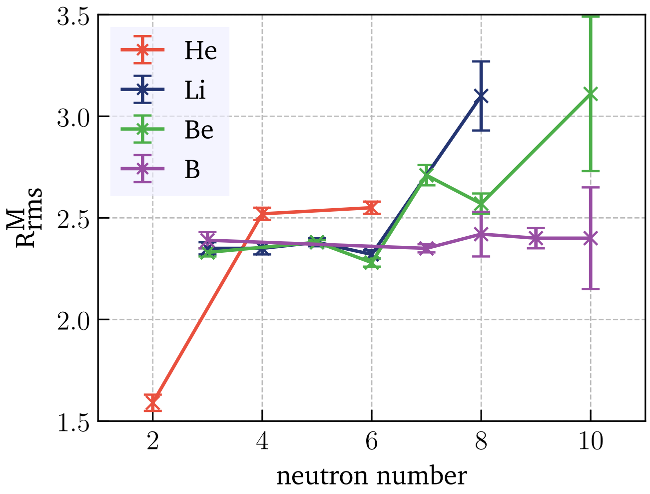

Figure 1.1.: Mass radii measured by I. Tanihata [23]. The large increase for neutron-rich nuclei was the first indication of the existence of neutron halo nuclei.

tal symmetries of the underlying QCD into the nuclear binding formalism [20]. Only recently, first attempts to derive an expression for the nuclear force solely from lattice QCD were performed [21, 22].

1.2 Light and exotic: halo nuclei

The residual force manifests in the structure and binding energy of nuclear systems. Ab-initio many-body methods such as Green's function Monte Carlo (GFMC) [24] or the no-core shell model (NCSM) [25] implement the theoretical formalism into realistic many-nucleon systems and can predict collective observables, such as radii and moments, which can be derived from the ground-state wave functions. Testing the same observables in experiments delivers the most dependable and stringent test of the understanding of the nuclear force and the predictive power of such advanced theories.

These observables become particularly interesting for nuclei with extreme neutron-to-proton ratios far from stability and in relatively simple systems, which are accessible to high-precision many-body nuclear theory. Such systems in the low mass (A<12) region of the nuclear chart exhibit rich phenomenology, of which the so-called halo nuclei are perhaps the most remarkable: nuclei that consist of a core plus a halo of dilute nuclear matter with an unusually large extent. These exotic nuclei were discovered first by I. Tanihata in 1985 in interaction cross-section measurements, which indicated an escalating increase in nuclear matter radius for neutron-rich, radioactive helium, lithium and beryllium isotopes [26].

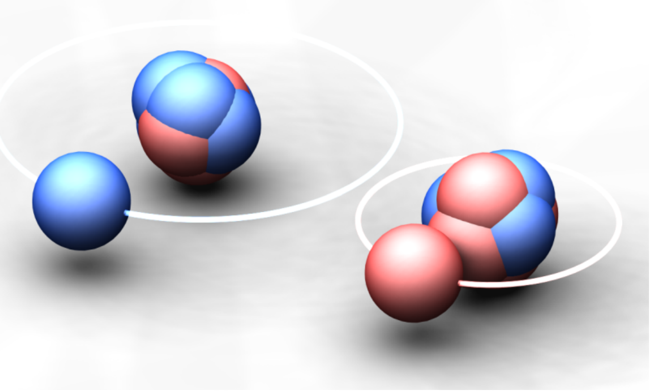

Figure 1.2.: An artist's perspective of the neutron halo nuclei ^{11}Be (left) and the suggested proton halo ^{8}B (right). The halo distance is smaller in boron than in the neutron halo due to the Coulomb barrier, but still of remarkable size.

^{8}B - A proton halo?

As opposed to the prominent cases of neutron-halo isotopes, studies on neutron-deficient isotopes with potentially extended proton wave function are scarce. The best candidate is the neutron-deficient nucleus ^{8}B, which drew attention in the context of the solar neutrino problem [27]. Since the β-decay of ^{8}B is the only source of high-energy neutrinos from the sun, the cross-section of the solar $^{7}\mathrm{Be}\,(p,\gamma)^{8}\,\mathrm{B}$ production mechanism was of large interest. Until the discovery of neutrino oscillations in 2002 [28, 29, 30], which analyzed the neutrino flux of the ^{8}B β-decay, many experimental studies thus tried to access the nuclear charge radius and proton binding parameters of ^{8}B. However, even now, after the immediate question connected with the solar neutrino problem has been resolved, no consistent conclusion on the ^{8}B halo character is made, and the nucleus is still subject to many investigations.

The quadrupole moment was measured employing nuclear quadrupole resonance (β-NQR) techniques. Its size indicated an unusually large deformation, which hints to an exotic structure [31, 32]. Another type of experiment measured the momentum distribution in the $^{8}\mathrm{B} \rightarrow {}^{7}\mathrm{Be} + \mathrm{p}$ breakup reaction in thin targets with an accelerated ^{8}B beam [33, 34, 35, 36]. Different models were used to extract the halo distance d_{halo} between

Table 1.1.: Laser spectroscopic investigations have confirmed the neutron halo character of several light isotopes. These investigations form the basis to expand the measurements to the boron isotopic chain and confirm the proton halo character of ^{8}B.

Isotope	Year	Institute	Ref.
^{6}He	2004	ATLAS/ANL	[38]
^{8}He	2007	GANIL	[39]
^{11}Li	2006	TRIUMF	[40]
^{11}Be	2009	ISOLDE/CERN	[41]

the ^{7}Be core and the valence (halo) proton from the kinematics that was observed in the reaction. This decisive parameter d_{halo} can also be deduced from precise mass radii measurements [37]. The results of several of these measurements are discussed in chapter 2. Most of them predict values around 4.5 fm, which suggest that the valence proton in ^{8}B orbits the ^{7}Be core well outside their respective charge and matter radii and thus support the existence of a proton halo, artistically presented in Fig. 1.2.

The model-dependency of the experiments allows a variety of interpretations, which include different statements about the proton halo character. Only laser spectroscopy can access the mean-square nuclear charge radius of light isotopes model-independently. From this value, the halo distance can be calculated, which will establish the first-ever definite testimony of the ^{8}B proton halo character.

1.3 The interplay between atomic and nuclear physics

Although nucleus and atomic shell are separated by orders of magnitude in size and energies, both systems are tightly interconnected. The nuclear spin splits electronic transition lines into the hyperfine structure. Also, since the nucleus is not infinitely small, there is a small probability that electrons will be immersed in the volume of the nuclear charge. This effect leads to a small shift in certain transition energies that is proportional to the charge radius of the respective nucleus. The resolution of laser spectroscopic experiments is large enough to measure atomic transitions with the necessary precision to resolve this contribution. With the help of state-of-the-art quantum-electrodynamic (QED) calculations, the impact of the nuclear charge radius on the optical spectrum can be disentangled and extracted. In the most simple case of the two-body system hydrogen, this can be done with a precision that allows the extraction of absolute nuclear charge radii directly from optical spectra that can be measured with sub-kHz precision. Interestingly, a significant discrepancy between the observed proton charge radius in muonic and electronic hydrogen was found, whose origin is still not resolved yet [42, 43, 44].

For more complex nuclear and atomic systems with more than one electron, the nuclear charge radius can only be extracted relative to the isotopic neighbors. This kind of precision spectroscopy on isotopic chains has been performed on elements all across the nuclear chart. Some of the most prominent measurements confirmed the neutron halo character of the neutron-rich halo nuclei of the lightest elements [38, 39, 40, 41]. The nuclear charge volume dilutes due to the center-of-mass motion in the halo system, which makes them sensitive to measurements of the nuclear charge radius. A survey of these investigations of light halo isotopes with laser spectroscopy can be found in Tab. 1.1.

1.4 Laser spectroscopy of the boron isotopic chain

To establish a model-independent value for the halo distance d_{halo} in the best-known proton halo candidate ^{8}B, this work addresses its laser-spectroscopic investigation. Significant progress has been made in the past years towards this ambitious goal. At ANL[1], ^{8}B is produced via the $^{3}\text{He}\left(^{6}\text{Li},^{8}\text{B}\right)\text{n}$ reaction in inverse kinematics using a 41 MeV primary beam of ^{6}Li, providing rates sufficient for online laser spectroscopy. The liquid-nitrogen cooled ^{3}He target was revised and improved to overcome saturation effects caused by local heating. The extraction of ^{8}B from the subsequent stopping and cooling gas catcher system turned out to be more difficult than expected. Most of the ejected radioactive ^{8}B is bound to water molecules, and those needs to be broken up into

---

[1] Argonne National Laboratory in Lemont, USA

a singly-charged state to perform laser spectroscopy. To accomplish the break-up, the boron molecules are sent through a few-nanometer-thin carbon nano-membrane into a second gas catcher system. An appended radiofrequency trapping and transport system will allow beam cooling and bunching, which is crucial for high-precision laser spectroscopy.

The measurements will be performed in a well-established laser spectroscopy beamline, which was transported from the TRIGA[2] nuclear reactor in Mainz, Germany, to ANL and was set up and re-commissioned there. The fluorescence detection system was swapped with a newly designed system, which is more versatile and sensitive to detect the expected low signal count rates in online experiments. The revised beamline has been tested successfully so far with calcium ions. It is now being prepared for measurements of palladium isotopes at the CARIBU[3] ^{252}Cf spontaneous fission source located at ANL. A detailed account of the status of the laser beamline and the ^{8}B production is given in this work.

At TU Darmstadt, a resonant ionization laser spectroscopy experiment was conducted on stable ^{10}B and ^{11}B. The isotope shift in the atomic ground state transition was determined with unprecedented accuracy, improving the old values in literature by almost two orders of magnitude. The values for the absolute transition frequencies are improved by a factor of ~ 60, while the hyperfine factors for the first excited $3s$ state were assessed for the first time. The isotope shift from this measurement was published in Physical Review Letters [45], combining the experimental results with the first-ever high-precision QED calculations for the five-electron system. These calculations were specifically performed to extract the field shift caused by the nuclear volume of the boron isotopes.

From this, the difference in mean-square nuclear charge radius between ^{10}B and ^{11}B was extracted, which is then used to benchmark new ab-initio nuclear structure calculations using the no-core shell model, and Green's function Monte Carlo approaches. The results present a striking convergence of these nuclear calculations, atomic theory, and experiment combined on a high-precision level. Furthermore, they are a showcase for further precision spectroscopy experiments to come at the limits of nuclear stability. The “offline” experiment, its results, and the subsequent derivation and comparison of nuclear charge radii are presented in this work in detail. The stable boron experiment produced the first high-precision laser spectroscopic results on the boron isotopic chain and provided a successful test of the theoretical frameworks. At the same time, vital components that will be utilized in the upcoming online ^{8}B experiment at ANL were introduced and tested.

---

[2] Training Research Isotopes General Atomics

[3] Californium Rare Isotope Breeder Upgrade

2 Nuclear Theory

Laser spectroscopic experiments allow extracting the mean-square nuclear charge radius from optical isotope shift measurements. This observable is interesting for theoretical nuclear physics since it reflects the binding strength and other properties of the investigated nuclear system. In low-mass systems such as the isotopes of boron, the charge radius can be calculated using a model of the nucleons and the force that is acting between them by solving the corresponding many-body problem. The predictive power of such calculations is a measure for the quality of the model, indicating the validity of the model assumptions.

This “benchmarking” of a nuclear theory is especially interesting in systems that exhibit exotic nuclear phenomena such as halo nuclei, in which one nucleon orbits a core in an extended orbit. The charge radii of halo nuclei are also increased, which makes laser spectroscopy an excellent tool to model-independently test such nuclei. The boron isotope ^{8}B is the best-known proton-halo candidate and is, along with the two stable isotopes ^{10}B and ^{11}B, subject of investigation in this work.

This chapter is split into two parts: First, the relevant nuclear properties of boron and specifically the proton halo candidate ^{8}B are discussed and explained. This part includes the calculation tools that are required to transfer laser spectroscopic results in a descriptive picture of the nucleus. The second part highlights two ab-initio theories, which are benchmarked in this work by determining the difference in mean-square nuclear charge radius between ^{10}B and ^{11}B.

2.1 The size and properties of boron

The relevant nuclear properties of the three isotopes of boron that are investigated in this work are summarized in Tab. 2.1. The nuclear spin I influences the hyperfine structure, the shape of the atomic spectrum that develops due to all interactions between nucleus and electronic shell apart from the Coulomb-interaction with a point-like nucleus with charge q. In the following, the focus lies on the nuclear halo structure of the short-lived isotope ^{8}B and the observables connected with its investigation.

2.1.1 Point-proton and nuclear charge radius

Many experimental and theoretical results quote the mean-square *point-proton* radii of nuclei given by

$$\langle r_{\mathrm{pp}}^2 \rangle = \frac{1}{Z} \int \rho_{\mathrm{p}}(r) r^2 d^3 r \tag{2.1}$$

where $\rho_{\mathrm{p}}(r)$ is the proton distribution. The point-proton radius only considers the center position of each proton, but does not take into account the finite size of the charge distribution of the proton itself. The mean-square nuclear charge radius

$$\langle r_{\mathrm{c}}^2 \rangle = \langle r_{\mathrm{pp}}^2 \rangle + \left(R_{\mathrm{p}}^2 + \frac{3\hbar^2}{4c^2 M_{\mathrm{p}}^2} \right) + \frac{N}{Z} R_{\mathrm{n}}^2 + r_{\mathrm{SO}}^2 + r_{\mathrm{MEC}}^2 \tag{2.2}$$

can be derived from $\langle r_{\mathrm{pp}}^2 \rangle$ by including several contributions [48]. R_{p} is the charge radius of the proton, as measured experimentally by laser spectroscopy, and the exact value accepted by CODATA[1] 2010 [49] and reported by the Particle Data Group (PDG) [50] is 0.8751(61) fm, which gives $R_{\mathrm{p}}^2 = 0.770(9)\,\mathrm{fm}^2$. The Darwin-Foldy term $3\hbar^2/4c^2M_{\mathrm{p}}^2 = 0.033\,\mathrm{fm}^2$ accounts for relativistic effects

---

[1] Committee on Data for Science and Technology

Table 2.1.: A summary of the relevant parameters of the three isotopes of boron that are investigated in this work. The values for the electrical quadrupole moment Q and the magnetic moment μ_I were taken from [46], citing the most precise value if more than one is given. The mean-square nuclear charge radii R_c taken from [47] were obtained by electron-scattering. The isotope ^{9}B is unbound $\left(t_{1/2} = 8.4 \times 10^{-19}\,\text{s}\right)$.

	nat. abund. (%)	$t_{1/2}$ (s)	I	μ_I (n.m.)	Q (b)	R_c (fm)
^{8}B		0.77	2+	1.035 79(5)	0.0643(14)	
^{10}B	19.9	∞	3+	1.800 644 78(6)	0.0845(2)	2.45(12)
^{11}B	80.1	∞	3/2−	2.688 648 9(10)	0.040 59(10)	2.42(12)

such as virtual particle-antiparticle pair production in the electric field and the so-called "Zitterbewegung" effect. The latter can be explained by a rapid oscillation resulting from quantum effects, which can formally be described by positive and negative frequency components in the proton wave function. The fact that the Darwin-Foldy term is not included in the phenomenological charge radius and thus needs to be subtracted for comparison even in proton radius measurements is mere convention [51]. Interestingly, the neutron mean square charge radius $R_\text{n}^2 = -0.1161(22)\,\text{fm}^2$ (PDG value [50]) contributes negatively. The neutron substructure can be seen as a positively charged core surrounded by a cloud of negative charge.

The last two contributions are the spin-orbit term r_SO^2, which represents the spin-orbit contribution of the nucleons with non-zero orbital angular momenta $l \neq 0$, and the contribution r_MEC^2 by meson-exchange currents binding to the nucleus. In most cases, the spin-orbit correction and r_MEC^2 are neglected for point-to-charge radii conversion.

2.1.2 The proton halo of ^{8}B

Halo nuclei were first experimentally discovered by Isao Tanihata, who measured a large increase in matter radius for neutron-rich light isotopes [26]. These neutron halos also exhibit a low one-neutron separation energy. In a simple square potential well, the neutron density distribution falls off outside the potential walls with

$$\rho(r) = |\Psi(r)|^2 \propto \frac{e^{-2kr}}{r^2} \text{ [52]} \tag{2.3}$$

where

$$(\hbar k)^2 = 2\mu E_s \,. \tag{2.4}$$

Here, μ is the reduced mass of the system and E_s the one-neutron separation energy. From this simple relation, it becomes clear that for s-wave valence neutrons, the separation energy directly corresponds to the extent of the halo nucleon density distribution, and is thus the most obvious indicator of a halo structure.

For valence nucleons that are not in an s-wave state, the centrifugal barrier limits the length of the matter tail [53]. The higher the angular momentum, the more confined the single-nucleon density distribution. For a proton halo, the Coulomb barrier plays an vital role since it limits the distance between core and valence proton due to their charge repulsion, which overcomes the strong binding in distances of a few femtometers.

For comparison and introduction, the most prominent example for a one-neutron halo, ^{11}Be, is briefly discussed. The ground state of ^{11}Be has a separation energy of $E_\text{s} = 503\,\text{keV}$ for the valence neutron in the s-wave. Using

$$\langle r_\text{M}^2\rangle_\text{tot} = \frac{m_\text{c}}{m_\text{c}+m_\text{h}}\left(\langle r_\text{M}^2\rangle_\text{core} + \frac{m_\text{h}}{m_\text{c}+m_\text{h}} d_\text{halo}^2\right) , \tag{2.5}$$

the distance d_halo between the core and the halo nucleon can be extracted from the respective measured mean-square matter radii $\langle r_\text{M}^2\rangle$ and the core and halo masses m_c and m_h [54]. In the case of beryllium, the core is ^{10}Be, and with the results from Tanihata [23], $d_\text{halo} = 5.7(8)\,\text{fm}$ can be calculated. This compares well to the distance $d_{\text{halo}} = 7.0\,\text{fm}$, which was measured with laser spectroscopy [41] in respect to the “crude” mechanical picture.

^{8}B has an even smaller one-proton separation energy of $E_s = 137\,\text{keV}$, but the valence proton occupies predominantly a $p_{3/2}$ shell. Furthermore, the Coulomb barrier is in effect for this system, which limits the size of d_{halo}. Many experiments tried to determine the mass radii of both ^{8}B and the “mother” nucleus ^{7}Be to extract this distinct parameter. A halo extent of $d_{\text{halo}} = 3.1\,(1.0)\,\text{fm}$ can already be extracted from Tanihatas data using Eq. 2.5, and suggests only a moderate halo character of ^{8}B.

Similar measurements of the matter radii of ^{7}Be and ^{8}B were repeated explicitly to determine the proton halo character of the latter. Most recently, Dobrovolsky and co-workers used a hydrogen-filled scattering target to measure absolute differential cross-sections in inverse kinematics [37]. The result depends on the model parameters of the projectile and target and is given with $d_{\text{halo}} = 4.24\,(25)\,\text{fm}$, which, in a simple frozen-particle picture, indicates that the valence proton in ^{8}B is entirely outside the volume of the nuclear core.

In another approach, ^{8}B produced in-flight is scattered at a secondary thin carbon target [36]. The longitudinal momenta of the residual ^{7}Be showed consistently narrow distributions, which correspond to weakly-bound systems with large halo distances. Using a cluster (α + ^{3}He + p) model of ^{8}B, Smedberg and co-workers deduce a halo distance of $d_{\text{halo}} = 4.6\,\text{fm}$ from the data.

The list of publications and experiments is vast, and giving a complete overview is beyond the scope of this thesis. Both publications that are referenced here, [37] and [36], give a broad survey of other experiments and theoretical models that use similar techniques to deduce the proton halo distance d_{halo} in ^{8}B. It is not undue to state that the mean value of all measurements so far agrees with $d_{\text{halo}} \sim 4.5\,\text{fm}$. This value will be used here to estimate the parameters for the laser spectroscopic experiment, which can provide a model-independent value for the mean-square nuclear charge radius.

2.1.3 The halo distance and charge radii

The nuclear charge radius of ^{8}B, which can be obtained from the laser spectroscopy experiments described in this work allows deriving d_{halo} in the ^{8}B proton halo system. Other than in the previous experiments that investigated this observable, no model assumptions need to be made, which makes the nuclear charge radius the ideal parameter to fix the proton halo distance.

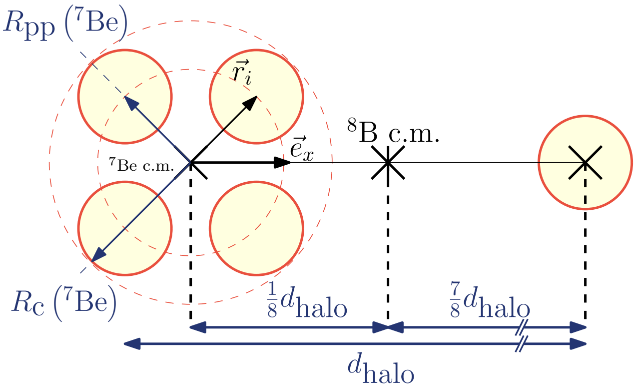

Figure 2.1.: A schematic visualization of the ^{8}B system, consisting of a ^{7}Be core and a halo valence proton. The dimensions are not to scale. Protons are depicted as red circles. Neutrons are left out for clarity.

As indicated in Fig. 2.1, the center of mass of the ^{7}Be + p system is located at

$$\vec{r}_{\text{cm}} = \frac{1}{8} d_{\text{halo}} \vec{e}_x \tag{2.6}$$

where the origin is the center of mass of ^{7}Be and the x-axis is defined as the direction towards the valence proton. Thus, $\vec{r}_{\text{cm}}$ only has a component in direction of x. The small differences in proton and neutron mass are negligible here.

The point-proton mean-square nuclear charge radius is defined as

$$\langle r_{\text{pp}}^2 \rangle = \frac{1}{N} \sum_{i=1}^{N} \vec{r}_i^{\,2} \tag{2.7}$$

where N is the number of elementary charges in the system and $\vec{r}_i$ denotes the positions of the i protons relative to the center of mass. In ^{8}B, there are five protons, four of which are located inside the ^{7}Be volume, and one in distance d_{halo}. Thus,

$$\langle r_{\text{pp}}^2 \rangle^{^8\text{B}} = \frac{1}{5} \left(\sum_{i=1}^{4} \left(\vec{r}_{i,\text{Be}} - \vec{r}_{\text{cm}} \right)^2 + \left(\frac{7}{8} d_{\text{halo}} \right)^2 \right) \tag{2.8}$$

where $\vec{r}_{i,\mathrm{Be}}$ are the positions of the protons that form the ^{7}Be core in coordinates relative to the ^{7}Be center of mass. This can be simplified since

$$\sum_{i=1}^{4}\left(\vec{r}_{i,\mathrm{Be}}-\vec{r}_{\mathrm{cm}}\right)^2 \tag{2.9}$$

$$=\sum_{i=1}^{4}\left(\vec{r}_{i,\mathrm{Be}}\right)^2-\sum_{i=1}^{4}2\vec{r}_{i,\mathrm{Be}}\vec{r}_{\mathrm{cm}}+\sum_{i=1}^{4}\vec{r}^{\,2}_{\mathrm{cm}}\,. \tag{2.10}$$

The first term is four times the mean-square nuclear charge radius of ^{7}Be by definition in Eq. 2.7. The product in the second term sums the x-component of the four protons in their center of charge system, which is zero if no polarization of the ^{7}Be core is assumed. The third term is the distance term, which follows the definition in Eq. 2.6. Apart from the necessary distinction between the center of charge and the center of mass in the ^{7}Be core, which defines a possible charge polarization, this derivation follows the parallel axis theorem.

As a result, the mean-square point-proton radius of ^{8}B can be written out as

$$\langle r^2_{\mathrm{pp}}\rangle^{^8\mathrm{B}}=\frac{4}{5}\langle r^2_{\mathrm{pp}}\rangle^{^7\mathrm{Be}}+\frac{53}{320}d^2_{\mathrm{halo}}\,, \tag{2.11}$$

which can easily be converted to a root mean-square nuclear charge radius with Eq. 2.2.

2.1.4 Value and uncertainty estimates

From the suggested value for $d_{\mathrm{halo}}=4.5\,\mathrm{fm}$ from [36] and using Eq. 2.11 the root mean-square charge radius of ^{8}B turns out to be

$$R_{\mathrm{c}}\left(^8\mathrm{B}\right)=\sqrt{\langle r^2_c\rangle^{^8\mathrm{B}}}=3.018\,(16)\,\mathrm{fm}\,, \tag{2.12}$$

where the uncertainty is based on the uncertainty of the nuclear charge radius of ^{7}Be

$$R_{\mathrm{c}}\left(^7\mathrm{Be}\right)=2.647\,(17)\,\mathrm{fm}\,, \tag{2.13}$$

which was measured with laser spectroscopy [41] and combined with results from electron scattering [55]. In [37], the ^{8}B nuclear charge radius is derived to be 2.89 (9) fm from an updated liquid-drop model [56], which is in reasonable agreement with the value calculated here and their slightly smaller $d_{\mathrm{halo}}=4.25\,\mathrm{fm}$.

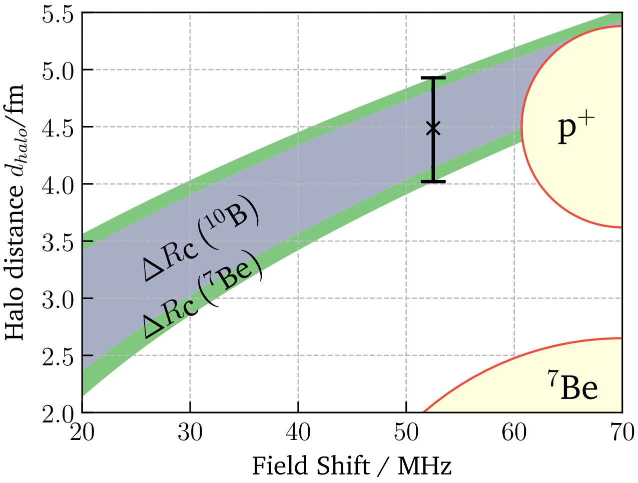

Figure 2.2.: The halo distance d_{halo} and its uncertainty for a measured field shift. The suggested value 4.5 fm is shown and projected onto a field shift of ∼ 52.5 MHz. The largest uncertainties come from the ^{10}B charge radius (blue) and the ^{7}Be charge radius (green). On the right-hand side of the plot, the relative size of the charge distribution and distance of the halo nucleus and the ^{7}Be core is shown to scale.

Field shift measurements

In a laser spectroscopy experiment that measures the isotope shift in a more-than-one electron system, it is not yet possible to extract the absolute nuclear charge radius. Instead, the size of the field shift $\delta\nu_{\mathrm{FS}}$ between two isotopes is measured, which is proportional to the change in mean-square nuclear charge radius

$$\delta\nu_{\mathrm{FS}}\propto\delta\langle rc^2\rangle^{AA'}=\langle rc^2\rangle^{A'}-\langle rc^2\rangle^{A}\,. \tag{2.14}$$

For the measurement of ^{8}B, it implies that the value for the absolute charge radius cannot be determined better than for its isotopic neighbor ^{10}B, conveying the considerable uncertainty from electronic scattering experiments into the result for the mean-square nuclear charge radius of ^{8}B.

Figure 2.2 visualizes the uncertainty contributions in a simulated isotope shift measurement of ^{8}B. The exemplary halo distance of $d_{\mathrm{halo}}=4.5\,\mathrm{fm}$ induces a field shift between ^{8}B and ^{10}B of 55 MHz. The uncertainty in the charge radius of ^{10}B

$$R_c\left(^{10}\mathrm{B}\right) = 2.45\,(12)\,\mathrm{fm}\ [47] \tag{2.15}$$

is responsible for $\Delta d_{\mathrm{halo}} = 0.39$ fm, while the charge radius of ^{7}Be (see Eq. 2.13) adds $\Delta d_{\mathrm{halo}} = 0.05$ fm. The uncertainty from the frequency measurement can be estimated to be comparatively small with values of $\Delta\nu \sim 1$ MHz, which does not add much to the total uncertainty budget and is uncritical due to the square-root dependence.

It is clear that especially the absolute nuclear charge radius of ^{10}B needs to be measured with higher accuracy than the current value that can be found in literature. Furthermore, to obtain a reliable measurement of the halo distance d_{halo}, also the absolute nuclear charge radius of ^{7}Be should be measured more precisely. One possible solution for both isotopes has come into reach recently, since atomic theory may soon be precise enough to calculate transition frequencies on a MHz-level also for two-electron systems [57]. The results would allow to measure absolute charge radii of light elements such as He, Li, Be, B and C in the helium-like electronic state offering suitable transitions for laser spectroscopy from the parallel-spin $2\,^3\mathrm{S}_1$ (ortho-)state, which can be accessed with the required precision as already demonstrated in collinear/anti-collinear laser spectroscopy [58, 59].

2.2 Advanced many-body models

Two multi-particle ab-initio methods have provided charge radii of boron isotopes, which are compared to experimental results acquired in this work. In the following, the no-core shell model (NCSM) and Green's function Monte Carlo (GFMC) will briefly be introduced. Such ab-initio methods are characterized as solutions for the non-relativistic quantum-mechanic many-body problem (the stationary Schrödinger equation) for a realistic Hamiltonian that do not contain uncontrolled approximations.

In both cases, the starting point for such calculations is the Hamiltonian

$$H_{\mathrm{A}} = T_{\mathrm{rel}} + V = \frac{1}{A}\sum_{i<j}\frac{\left(\vec{p}_i - \vec{p}_j\right)^2}{2m} + \sum_{i<j}^{A} V_{\mathrm{NN},ij} + \sum_{i<j<k}^{A} V_{\mathrm{3N},ijk}\,. \tag{2.16}$$

The first term is the kinetic energy in the center-of-mass system and the nuclear binding is mediated by the nuclear force, which is modeled through nucleon-nucleon V_{NN} and three-nucleon V_{3N} potentials. The calculation providing the nuclear wave function, which then allows to derive nuclear properties, is divided into two parts: Finding a suitable parametrization of the nuclear force, before computationally solving the resulting many-body equation.

Performing the nuclear structure calculations presented in the following was not part of this thesis, but were performed by Prof. Dr. Robert Roth and Thomas Hüther for the NCSM, and R.B. Wiringa and Alessandro Lovato for the GFMC.

2.2.1 Nucleon-nucleon potentials

Nucleons, such as the proton and the neutron, consist of three quarks, which are attributed with different color charges according to quantum chromodynamics. These quarks have never been observed individually, but are confined within their hadronic state. Still, they interact with each other across the nucleonic border, which leads to an inter-nucleon force that is repulsive for short distances below $\sim$ 0.7 fm but has an attractive well at $\sim$ 0.9 fm and a fast asymptotic decline towards larger distances. The attractive part binds protons and neutrons together inside nuclei, paralleling the Van-der-

Waals force, which binds atomic systems together, although the constituents are neutral. Since the interaction of their quark constituents mediates the force between nucleons, it is intuitive to look for resonances that these quarks can form, the simplest of which are light mesons such as the pion ($E \sim 140\,\mathrm{MeV}$). In fact, the so-called nuclear or residual force can be modeled by meson exchange, as suggested by Yukawa already in 1935, long before the underlying formalism of QCD was written out [11].

Looking at the abundant amount of sub-nuclear particles, which can be described in QCD and were experimentally verified, it becomes clear that it is impossible to derive a simple, self-contained formalism of the nuclear force. However, the first approaches to derive it directly from QCD are made [21]. In the following, the so-called realistic "Argonne" potential, which is used in the GFMC calculations, and the advanced chiral effective field theory (χEFT) potential used for the NCSM are briefly discussed.

Realistic potentials: Argonne

The Argonne v_{18} potential (AV18) [60, 18] is a realistic nucleon-nucleon two-body potential. Its operator sum can be written out as

$$v_{ij} = v_{ij}^{\gamma} + v_{ij}^{\pi} + v_{ij}^{I} + v_{ij}^{S} = \sum_{p} v_p\left(r_{ij}\right)\mathcal{O}_{ij}^{P} \qquad (2.17)$$

where the individual components express electromagnetic, one-pion-exchange, as well as phenomenological intermediate and short-range terms. The operators $\mathcal{O}_{ij}^{P}$ act on the properties of the nucleonic state, such as spin, momentum and isospin. They include a central term, tensor force, spin-orbit and quadratic spin-orbit coupling as well as quadratic orbit coupling. Four additional operators explicitly break the charge independence of the interaction. The binding strength of the individual terms, expressed by over 43 independent parameters, is fitted to experimental data from the deuteron and nucleon-nucleon scattering [18].

When applied to few-body nuclear systems, it becomes evident that at least 3-body forces are missed, since the triton binding energy is systematically underestimated [61]. This shortcoming can be addressed by introducing realistic 3N potentials such as the Illinois-7 (IL7) potential, which extends the operator structure with two-pion-exchange terms and a central, repulsive term [62]. The obvious downside of this approach is that the global fit on experimental data is much more model-dependent since no three-body scattering data is available. Instead, four parameters in the IL7 are fitted to reproduce best the properties of 20 ground or low-lying states of light nuclei with $3 \leq A \leq 8$, particularly binding energies.

Table 2.2.: The hierarchy of the Feynman diagrams in χEFT based on power counting. Solid lines represent nucleons, dashed lines pions. Each diagram denotes a possible interaction of these particles. The inclusion of higher orders gives a better rendering of the underlying nuclear potential. Reproduced from [66].

	2N force	3N force
LO	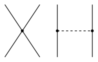	
NLO	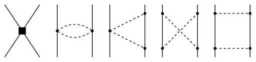	
N^{2}LO	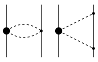	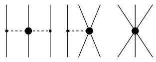

The AV18+IL7 potentials are local and formulated in coordinate space, which makes them predestined to be used in the Greens function Monte Carlo formalism, which will be explained below. They give an excellent reproduction of approximately 100 ground- and excited-state energies up to A=12. Apart from the AV18, several other realistic nuclear potentials use a similar approach to model the nature of the residual force, most prominently the Nijmegen [63] and the CD-Bonn [64] potential. The Illinois potentials themselves are based on the Urbana model [65], which is an alternative formulation of the 3N interaction.

χEFT potentials

Effective field theories (EFTs) describe phenomena that occur at a certain length or energy scale. An example is the multipole expansion of a charge distribution $\rho(r)$ as seen from a distance d. The multipole expansion is performed in orders of the "resolution scale", which is defined by d/R, where R resembles the extent of $\rho(r)$. For $d \gg R$, the first few orders (monopole, dipole, quadrupole) might be sufficient to give a good approximation of the field. Likewise, for $d \sim R$, more and more orders need to be included to construct a good representation of the physical field.

A similar approach can be used to describe the nuclear force in chiral effective field theory [67]. The chiral symmetry of QCD and its spontaneous breaking plays an vital role since a Lagrangian can be formulated that follows the chiral symmetry and all other fundamental symmetries that are obeyed in QCD. This Lagrangian can then be expanded as an infinite sum of Feynman diagrams denoting the interaction between nucleons and pions that are the primary degrees of freedom [68, 69].

At the same time, the chiral symmetry breaking by the π-meson due to the mass of the u and the d quark defines the resolution scale of the system. From a simple Fermi gas model, it can be derived that typical momenta for nucleons inside the core are in the order of the Fermi momentum $k_\mathrm{F} = 250\,\mathrm{MeV/c}$ [70]. Thus, it is expedient to expand the Lagrangian in the resolution scale of the pions, with E≈140 MeV. The upper limit, the breakdown scale, typically is $\Lambda_x \sim 1\,\mathrm{GeV}$ where the nucleons cannot be regarded as enclosed particles anymore. In the electromagnetic multipole expansion, Λ_x corresponds to the limit case were the sample charge is immersed inside the charge distribution so that $d \leq R$.

The advantage of χEFT is that just like in the case of a charge distribution, an order or "power" ν can be attributed to each possible Feynman diagram. The useful distinction and selection of those interactions in leading order (LO), next-to-leading order (NLO) and even higher orders, which are necessary to satisfy the precision demands, is called a "power counting" scheme.

The underlying symmetries and interactions, governed by the established rules of QCD, are conveyed into the description of the nuclear force. At the same time, just like in the electrical multipolar expansion, χEFT is only valid on a particular scale and within energy limits, but those are well-defined and can be expanded by the inclusion of higher-order terms. Furthermore, two-pion and higher-order meson exchange, as well as 3N forces, are introduced systematically and term-wise.

In Tab. 2.2, the Feynman diagrams are shown in the power counting scheme. The LO ($\nu = 0$) includes a simple contact term and one-pion-exchange. Higher orders introduce two-pion-exchange, 3N forces and more complicated interaction paths. Each of the contact terms appears in the denoted formalism as a low-energy coupling constant (LEC), which must be fitted to experimental data. Here, like in the realistic potentials, nucleonic scattering data and deuteron properties are used as input information. In its predictive power, full inclusion of the N^{3}LO provides results that compare to the AV18 and similar potentials [71], but the number of free parameters in the fit, 27, is significantly lower.

2.2.2 Green's function Monte Carlo

Green's function Monte Carlo (GFMC) was introduced in 1962 by Kalos [72] into the domain of nuclear physics, although the concept is present in many different fields of condensed matter physics and related topics. The starting point of the GFMC is a trial wave function Ψ_T, which is obtained by variational Monte-Carlo calculations and provides a first approximation with the energy $E_V = E_0$, which is still above the actual ground state energy E_0. Thus, it fulfills

$$E_V = \frac{\langle \Psi_T | \hat{H} | \Psi_T \rangle}{\langle \Psi_T | \Psi_T \rangle} \geq E_0 \text{ [73]}. \tag{2.18}$$

Excited-state contaminations are removed by applying an imaginary-time evolution operator

$$\Psi(\tau) = e^{-(\hat{H}-E_0)\tau} \Psi_T \,, \tag{2.19}$$

which in the infinite limit gives the ground-state wave function

$$\Psi_0 = \lim_{\tau \to \infty} \Psi(\tau) \,. \tag{2.20}$$

For sufficiently large τ, the ground-state energy eigenvalue can be approximated with high precision, but it is not possible to solve this integral directly. Instead, the imaginary time τ is segmented into small time steps $\Delta\tau$, $\tau = n\Delta\tau$, which yields

$$\Psi(\tau) = \left[e^{-(\hat{H}-E_0)\Delta\tau} \right]^n \Psi_T = G^n \Psi_T \,. \tag{2.21}$$

G is the short-time Green's function, which is a matrix function in spin-isospin space of the spatial coordinates $\vec{R}$ and $\vec{R}'$ [74].

Instead of a complete numerical solution of this equation, a Monte-Carlo approach is used: N points of the integration domain $\vec{R}$ are evaluated, and the mean value is calculated from the sampled points. The statistical error of this calculation decreases with $N^{-1/2}$. Several genuine algorithms help to sample and to solve the path integrals, keeping the fermion-sign problem under control [73].

GFMC calculations work best with parametrizations of the NN-potentials that are formulated in coordinate space, such as the Argonne v_{18} and the Illinois-7 3N-potentials briefly described above. It is, of course, no coincidence that these potentials and many refinements of GFMC have been developed by the same group of scientists around Steven Pieper and R.B. Wiringa at Argonne National Laboratory.

In principle, GFMC can predict ground-state energies and even excited states for low-mass nuclei with the-state-of-the art computing power. Remarkable agreements between experiment and calculation have been reached for $A < 8$ nuclei [75]. Higher masses tend to pose difficulties since higher-order contributions become significant, and they usually introduce non-local (momentum) operators, which are difficult to access in the Monte-Carlo methods. Nevertheless, much progress has been made to overcome these limitations, and calculations of up to ^{12}C are possible and reach spectroscopic accuracy [74]. GFMC calculations successfully predicted the charge radii of ^{6,8}He isotopes, while Li and Be isotope radii tend to be a little smaller than current experimental values [48].

Results

To predict values for the charge radii of stable boron isotopes ^{10,11}B with the help of GFMC, the AV18+IL7 Hamiltonian was employed, containing the Argonne v_{18} NN potential [18] and Illinois-7 3N potential [76, 62]. The calculated binding energy for ^{10}B agrees well with the experimental value, but it is slightly underbound for ^{11}B. To remedy this shortcoming of the AV18+IL7 interaction, when computing the radius of ^{11}B the phenomenological repulsive term of the 3N force was slightly quenched to reproduce the experimental binding energy. The results for charge radii can be found as item e) in Tab. 2.3.

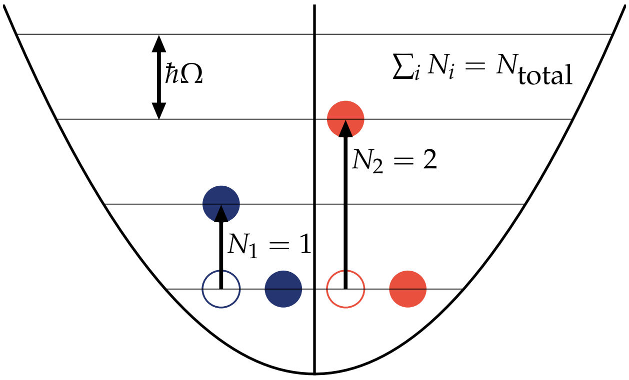

Figure 2.3.: The model space of the no-core shell model is truncated by the total number of allowed excitations $N_{\text{tot}} \leq N_{\text{max}}$, which is defined by the sum of the total excitation energy $N\hbar\omega$. This includes the possibility of multi-particle excitations.

2.2.3 The no-core shell model

The ab-initio no-core shell model is a theoretical framework for calculating nuclear many-body properties. In contrast to the classic shell model or Fermi gas models, all nucleons are considered to be active. Thus there is no external phenomenological mean-field potential applied (no-core). The Schrödinger equation is represented as a large-scale matrix eigenvalue problem

$$\sum_i \langle \Phi_j | H | \Phi_i \rangle \, c_j^{(n)} = E_n c_j^{(n)} \, . \tag{2.22}$$

using the Hamiltonian from Eq. 2.16, where all interactions between nucleons are explicitly included. The solution of the eigenwert problem, by diagonalization of the Schrödinger equation, directly yields the binding energy of the system, and nuclear properties can be extracted from the corresponding wave function eigenvectors [83].

Since the Hilbert space for this calculation has infinite dimensions, truncations need to be made, and a suitable basis must be chosen. In the NCSM, the harmonic oscillator basis with the oscillator energy $\hbar\Omega$ as a free parameter is employed. The advantage of this is that the center-of-mass term and interaction part can be separated exactly. The typical A-body product state

$$|\Phi_i\rangle = |p_1 p_2 ... p_A\rangle_i \tag{2.23}$$

Table 2.3.: Results from the no-core shell model and Green's function Monte Carlo calculations for the root mean-square nuclear charge radius R_c of ^{10,11}B. These results were obtained with different NN and 3N-potentials. These values were not calculated within this thesis. Please refer to the publication [45] and references here and therein for details.

	Model	NN-Potential	Properties	$R_c\left(^{10}\mathrm{B}\right)$ (fm)	$R_c\left(^{11}\mathrm{B}\right)$ (fm)
a)	NCSM	N2LO-SAT [77]	$\alpha = 0.08\,\mathrm{fm}^4$	2.343(30)	2.298(30)
b)	NCSM	EM+3N [78, 79, 80, 81]	$\Lambda_{3N} = 400\,\mathrm{MeV/c},\ \alpha = 0.08\,\mathrm{fm}^4$	2.439(30)	2.379(30)
c)	NCSM	EM+3N	$\Lambda_{3N} = 500\,\mathrm{MeV/c},\ \alpha = 0.12\,\mathrm{fm}^4$	2.505(30)	2.454(30)
d)	NCSM	EMN+3N [82]	$\Lambda_{3N} = 500\,\mathrm{MeV/c},\ \alpha = 0.16\,\mathrm{fm}^4$	2.491(30)	2.436(30)
e)	GFMC	AV18 + IL7 [18, 76, 62]		2.401(15)	2.368(40)

is built from single-particle states, which are parameterized by single-nucleon quantum numbers. In principle, infinitely many excitations can occur. Instead of limiting the number or level of excitation that each nucleon can experience, a total maximum number N_{max} of allowed excitations is introduced, as depicted in Fig. 2.3.

Typically for the NCSM calculations, the χEFT potentials, which were discussed above, are chosen. NCSM calculations are then limited by the available computing power, which can, up-to-date, diagonalize matrices with dimensions up to 10^{10}. This dimension of the model space grows factorially with an increasing number of nucleons and also N_{max} needs to be increased to reach convergence.

There are several methods to accelerate these expensive calculations, most of which rely on skillful transformations of the basis sets so that the initial matrix has less non-zero entries, which decouples low- and high-momentum states. An example of such a unitary transformation is the similarity renormalization group (SRG) [84], which is used in the NCSM calculations performed for the boron isotopes. The SRG is a continuous unitary transformation that depends on a flow parameter α. It is typically performed at the two- and three-body level. By variation of α, the effect of this truncation can be investigated. A more detailed discussion of such transformations is beyond the scope of this work. Progress is being made on the frontiers of these calculations, and results for $A \leq 12$ NCSM calculations are well feasible, and ground state and excitation energies fit well with experimental data [85, 86].

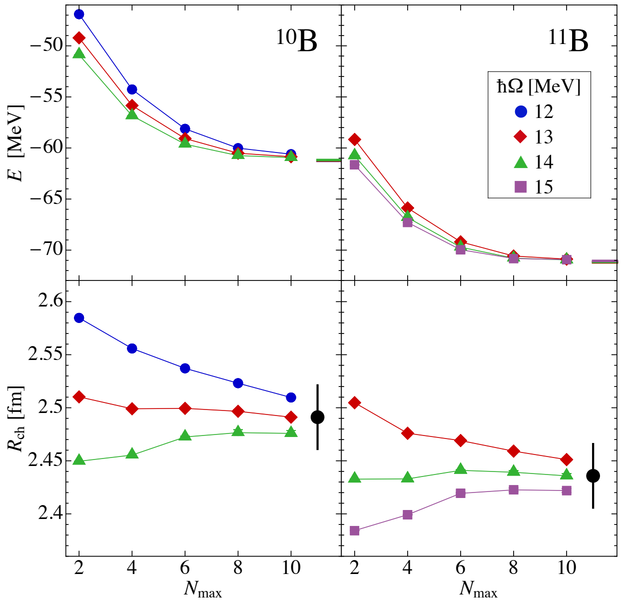

Figure 2.4.: The convergence of ground state energy and nuclear charge radii for ^{10,11}B with different oscillator frequencies at an increasing number of allowed excitation N_{max}. This example plot shows the calculations for model d) (see text). The uncertainties are derived from the convergence of the many-body calculation. Prof. Dr. Robert Roth courteously provided this plot.

Results

To provide values for the mean-square nuclear charge radius of stable boron, NCSM calculations were performed with different two-nucleon (NN) and three-nucleon (3N) interactions from chiral effective field theory:

a) the N2LO-SAT interaction with NN and 3N interaction at N2LO with flow parameter $\alpha = 0.08\,\mathrm{fm}^4$ [77];

b) the NN interaction at N3LO by Entem and Machleidt [71] supplemented with a 3N interaction at N2LO with local regulator and reduced cutoff ($\Lambda_{3N} = 400\,\mathrm{MeV/c}$, $\alpha = 0.08\,\mathrm{fm}^4$), which has been widely used in the past years [78, 79, 80, 81];

c) the Entem-Machleidt NN interaction at N3LO with a new 3N interaction at N2LO with nonlocal regulator ($\Lambda_{3N} = 500\,\mathrm{MeV/c}$, $\alpha = 0.12\,\mathrm{fm}^4$);

d) the recent NN interaction at N4LO by Entem, Machleidt, and Nosyk [82] plus a 3N interaction at N2LO with nonlocal regulator ($\Lambda_{3N} = 500\,\mathrm{MeV/c}$, $\alpha = 0.16\,\mathrm{fm}^4$) [87]

Only a) uses information beyond the few-body sector and explicit constraints on nuclear radii to determine the low-energy constants, in all other cases the NN interaction is fitted exclusively to two-nucleon scattering data and the 3N interaction to the triton binding energy, the triton β-decay half-life, or properties of the α particle.

For all interactions, a consistent SRG evolution up to the three-body level for the Hamiltonian and up to the two-body level for the radius operator is employed. The impact of variations of the flow parameter α on the radii is much smaller than the model-space convergence uncertainties. For each interaction large-scale NCSM calculations are performed for model spaces from $N_{\max} = 2$ to 10 using harmonic oscillator frequencies $\hbar\Omega$ from 12 to 18 MeV. To extract the nominal value and uncertainty for the point-proton radius, the $\hbar\Omega$-value that provides the most stable radius as a function of $N_{\max}$ is identified, and then the neighboring $\hbar\Omega$-values and the residual $N_{\max}$-dependence is used to estimate the many-body uncertainties. Fig. 2.4 shows the results for the calculation with NCSM EMN+3N (d).

The numerical results are summarized and labeled in Tab. 2.3. In chapter 7, the results of the measurements of the nuclear charge radii of ^{10,11}B are compared with the calculations performed here.

3 Atomic Theory

3.1 Atomic spectra

The Schrödinger equation

$$\left(-\frac{\hbar^2}{2m}\Delta + V\right)\Psi = E\Psi \tag{3.1}$$

allows a quantum mechanical formulation of atomic systems in the non-relativistic case. The Coulomb potential

$$V = \hbar c \alpha \frac{Z}{r} \tag{3.2}$$

acts between the electron and the atomic nucleus with Z protons in distance r. For one-electron hydrogen-like systems, the introduction of center-of-mass-motion coordinates enables a full analytical solution. For an i-electron system, the non-relativistic Hamiltonian for the electron motion in the central Coulomb field of a "frozen" nucleus (with infinite nuclear mass) is, in natural units,

$$H_0 = \sum_i \frac{p_i^2}{2m} - \sum_i \frac{Z\alpha}{r_i} - \sum_{i<j} \frac{\alpha}{r_{ij}} \tag{3.3}$$

where p_i are the single electron momenta and r_i their position, m the electron mass, Z the nuclear charge and r_{ij} the distance between two electrons i and j. With a trial wave function Ψ, the energy E_0 can be derived from a perturbative expansion in the fine structure constant α,

$$E_0 = E^{(2)} + E^{(4)} + E^{(5)} + \dots, \tag{3.4}$$

where

$$E^{(n)} \sim m\alpha^n\ . \tag{3.5}$$

Each of the terms in $m\alpha^{(n)}$ can be perturbatively expanded again in their dependence on the ratio $(\mu/M)^k$ between reduced mass μ and nuclear mass M. The non-relativistic energy $E^{(2)} = E_{\mathrm{NR}}$ is thus derived from

$$H_{\mathrm{NR}} = H_{\mathrm{NR}}^{(0)} + \left(\frac{\mu}{M}\right)^1 H_{\mathrm{NR}}^{(1)} + \left(\frac{\mu}{M}\right)^2 H_{\mathrm{NR}}^{(2)} + \dots\ . \tag{3.6}$$

The first-order term expresses the kinetic energy of the nucleus

$$H_{\mathrm{NR}}^{(1)} = \sum_i \frac{p_i^2}{2\mu} + \sum_{i>j} \frac{p_i p_j}{\mu} \tag{3.7}$$

where the second term is called mass polarization. This embeds the electron-electron correlation.

The energy E_{NR} of the non-relativistic Schrödinger equation with a corresponding wave function Ψ can be calculated with high precision. However, it lacks the relativistic effects of the electrons, including their spin and the interaction with the nuclear spin, summarized as a state-dependent $E^{(4)} = E_{\mathrm{rel}}$. Also, a quantum electrodynamic correction $E^{(5)} = E_{\mathrm{QED}}$ needs to be included since in the strong field of the nucleus effects such as virtual particle creation can occur. In analogy to Eq. 3.6, each of these energies can be derived from an expansion in μ/M since they include corrections to the mass-polarization and mass-independent terms, so that

$$H_{\mathrm{rel}} = H_{\mathrm{rel}}^{(0)} + \left(\frac{\mu}{M}\right)^1 H_{\mathrm{rel}}^{(1)} + \dots \tag{3.8}$$

$$H_{\mathrm{QED}} = H_{\mathrm{QED}}^{(0)} + \left(\frac{\mu}{M}\right)^1 H_{\mathrm{QED}}^{(1)} + \dots\ . \tag{3.9}$$

This systematic treatment of the different contributions to the atomic energy allows to access and calculate ground- and excited states in atoms. For hydrogen, higher-order mass terms disappear and the full energy can be calculated on a kilohertz level [88]. For two- and three-electron systems, this accuracy is not yet reached, but work is in progress to match spectroscopic precision [57] there as well. In all of these cases, it can be used to extract nuclear information from isotope shift measurements, which will be explained in the next sections.

3.1.1 Isotope shift

In the series expansion of the atomic energy levels, some terms include the nuclear properties mass M and mean-square nuclear charge radius $\langle r^2\rangle$. They introduce a shift in the energy difference between two atomic states i and f

$$E^A_{\mathrm{i}\to\mathrm{f}} = E^A_{\mathrm{tot,f}} - E^A_{\mathrm{tot,i}} \tag{3.10}$$

between two isotopes with mass numbers A and A'. The isotope shift (here defined in terms of energy)

$$\delta E^{AA'}_{\mathrm{IS}} = E^A_{\mathrm{i}\to\mathrm{f}} - E^{A'}_{\mathrm{i}\to\mathrm{f}} \tag{3.11}$$

can be measured with high accuracy, but also accessed theoretically with spectroscopic precision. To do so, the full expansion for two isotopes A and A' of Eq. 3.4 is subtracted for comparison with a measurement of the frequency in two isotopes of one element:

$$\begin{aligned}\Delta E =& E^A_{\mathrm{i}\to\mathrm{f}} - E^{A'}_{\mathrm{i}\to\mathrm{f}}\\ =&\left[\left(\frac{\mu}{M_A}\right)^1 - \left(\frac{\mu'}{M_{A'}}\right)^1\right]\left(E^{(1)}_{\mathrm{NR}} + E^{(1)}_{\mathrm{rel}} + E^{(1)}_{\mathrm{QED}}\right)\\ &+\left[\left(\frac{\mu}{M_A}\right)^2 - \left(\frac{\mu'}{M_{A'}}\right)^2\right]\left(E^{(2)}_{\mathrm{NR}} + \ldots\right)\\ &+\Delta E_{\mathrm{i}\to\mathrm{f}}\left(\langle r_c^2\rangle^{A'}, \langle r_c^2\rangle^{A}\right)\end{aligned} \tag{3.12}$$

Here, all zero-order terms of the expansion in μ/M cancel out, which leaves only higher order mass terms and contributions from the nuclear size in the equation.

Normal mass shift

In the first order non-relativistic expansion term presented in Eq. 3.7, the quadratic component

$$E^{(1)}_{\mathrm{NR,\,kE}} = \left(\frac{\mu}{M}\right)^1 \sum_i \frac{p_i^2}{2\mu}\,, \tag{3.13}$$

which represents the nuclear kinetic energy, depends on the nuclear mass. The corresponding shift in transition frequency when this mass changes is called “normal mass shift” (NMS) and is denoted as $\delta\nu^{AA'}_{\mathrm{NMS}}$.

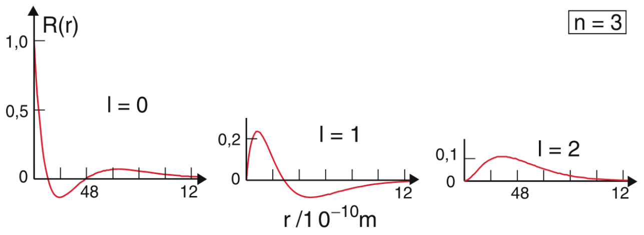

Figure 3.1.: The electron wave function Ψ forms orbitals that produce a significantly different electron probability density at $r = 0$ for different n and l. This difference $\Delta|\Psi(0)|^2$ is proportional to the field shift and nuclear size. Taken from [89].

Specific mass shift

The specific mass shift $\delta\nu^{AA'}_{\mathrm{SMS}}$ incorporates the mass polarization contributions

$$E^{(1)}_{\mathrm{MP}} = \left(\frac{\mu}{M}\right)^k \sum_{i<j} \frac{p_i p_j}{\mu} \tag{3.14}$$

introduced in Eq. 3.7 in all orders of $m\alpha^{(n)}$ and $(\mu/M)^k$. The higher order terms $k > 0$, which are left in the equation, can not be calculated with higher relative precision than those with $k = 0$, but their contribution to the total energy is much smaller. Usually, the non-relativistic terms are treated up to $k = 2$ while for the relativistic and QED effects $k = 1$ is sufficient. Especially the QED terms pose large difficulties for theory.

Field shift

The finite size of the nucleus appears in the relativistic $E^{(4)}$ expansion of the atomic energy in the form

$$\Delta E_{\mathrm{FS}} = \frac{2\pi}{3} Z\alpha\langle r_c^2\rangle\,|\Psi(0)|^2\,, \tag{3.15}$$

proportional to the probability density of a single electron being at the position of the nucleus. In a simple picture, the electron becomes immersed in the nuclear charge volume lowering the Coulomb potential, which would otherwise be infinitely deep for a point-like nucleus. This effect slightly alters the transition energy between two atomic states i and f and is thus proportional to the difference in electron probability density of the respective states

$$\Delta\,|\Psi(0)|^2_{\mathrm{i}\to\mathrm{f}} \propto \Delta E_{\mathrm{i}\to\mathrm{f}}\left(\langle r_c^2\rangle^{A'}, \langle r_c^2\rangle^{A}\right) . \tag{3.16}$$

To be sensitive for this effect, two states i and f with orbitals that have a pronounced difference in $|\Psi(0)|^2_{\mathrm{i,f}}$ should be measured. As depicted in Fig. 3.1, this is for example the case for an $s \to p$ transition.

In the isotope-shift calculation performed in Eq. 3.12, the difference between two isotopes in the same atomic transition is probed. This isotope shift is sensitive to the change in mean-square nuclear charge radius

$$\delta\langle r_c^2\rangle^{AA'} = \langle r_c^2\rangle^{A} - \langle r_c^2\rangle^{A'} \tag{3.17}$$

between the two isotopes with $A > A'$. This portion is the field shift

$$\delta\nu_{\mathrm{FS}}^{AA'} = \frac{2\pi}{3} Z\alpha\Delta\,|\Psi(0)|^2_{\mathrm{i}\to\mathrm{f}}\,\delta\langle r_c^2\rangle^{AA'} = K_{\mathrm{FS}}\delta\langle r_c^2\rangle^{AA'} , \tag{3.18}$$

which allows the extraction of the change in mean-square nuclear charge radius between two isotopes of the same element from an isotope shift measurement.

3.1.2 Hyperfine structure

Like the fine structure, also the hyperfine structure (HFS) traces back to the relativistic correction $E^{(4)}$ to the non-relativistic Schrödinger equation. It is introduced to describe the interaction between the total electron angular momentum **J** with the nuclear spin **I**. In isotopes with non-zero nuclear spin, it overrides the degeneracy of states with equal **J**. The amplitude of the splitting is defined by the electromagnetic moments of the nucleus, in first-order the magnetic dipole moment μ_I and the electric quadrupole moment Q. Thus, apart from mass and mean-square nuclear charge radius, spin and moments of the respective nucleus also influence the atomic level scheme [89].

Without the presence of an external field, spin **S** and orbital momentum **L** of the electrons couple to the total angular momentum $\mathbf{J} = \mathbf{L} + \mathbf{S}$, which generates a magnetic field

$$B_{\mathrm{e}} = B_0 \frac{\mathbf{J}}{\hbar} \tag{3.19}$$

at the nucleus position. This magnetic field interacts with the nuclear magnetic moment, which is oriented along **I**. The energy shift is given by

$$\Delta E_{\mathrm{HFS}} = -\mu_I B_0 \cos\left(\measuredangle(J, I)\right) , \tag{3.20}$$

where $\measuredangle(J, I)$ is the angle between nuclear spin and electron orbital momentum. Equation 3.20 can be evaluated by introducing a quantum number for the total angular momentum $\mathbf{F} = \mathbf{J} + \mathbf{I}$ whose absolute value F ranges in integral numbers between $|I - J|$ and $|J + I|$. The fine-structure level splits up into hyperfine structure levels with energy shifts

$$\Delta E_{\mathrm{HFS}} = \frac{A}{2}\left[F(F+1) - J(J+1) - I(I+1)\right] = \frac{A}{2}C \tag{3.21}$$

with C being the Casimir-factor, which is variable with all allowed values of F. The hyperfine factor

$$A = \frac{g_I \mu_{\mathrm{N}} B_0}{J} \tag{3.22}$$

incorporates the nuclear magneton

$$\mu_{\mathrm{N}} = \frac{e\hbar}{2m_p} , \tag{3.23}$$

the nuclear g-factor

$$g_I = \frac{\mu_I \hbar}{\mu_{\mathrm{N}} \mathbf{I}} \tag{3.24}$$

and B_0, which can be derived from the electronic wave function.

The electrical field gradient generated by the electrons in orbits with $J > 1/2$ orient the nuclear quadrupole moment Q and give rise to an additional energy shift E_{QP}. The amplitude of this shift is a measure for nuclear deformation, which usually is accompanied by a quadrupole moment. In the experiments described in this work, only $J = 1/2$ states are tested, and thus no E_{QP} or even higher-order moments are relevant.

3.1.3 Nuclear observables in atomic spectra

As mentioned previously, in a precise experiment on isotopes with nuclear spin $I \neq 0$, also the hyperfine structure is resolved, which manifests in the occurrence of several peaks that constitute the fine-structure transition. This section highlights how the center "undisturbed" fine-structure frequency ν_0 can be found, how the nuclear magnetic moment μ_I can be extracted from this resonance structure (also allowing to investigate the hyperfine structure anomaly), and how a comparison of ν_0 of different isotopes allows to extract their difference in mean-square nuclear charge radius.

Fine structure transition frequency

Since the amplitude of the hyperfine structure for light isotopes is usually in the same order of magnitude as the natural linewidth, it is recorded entirely when testing a fine structure transition in an experiment. Apart from cases where $J = 0$, both upper (denoted by u) and lower (l) fine structure level have a hyperfine structure on top. The i hyperfine structure transition frequencies ν_i are then shifted with respect to the fine structure transition frequency ν_0 according to

$$\nu_i = \nu_0 + \frac{C_u}{2} A_u - \frac{C_l}{2} A_l \tag{3.25}$$

when no higher-order moments are observed or $J = 1/2$ for all participating levels. The possible values for the Casimir-factor C can unambiguously be derived from the fine structure level quantum numbers, if the nuclear spin and details about the tested transition are known. This allows a fit of the recorded structure with the expected number of peaks, yielding the fine structure transition frequency ν_0, which is often denoted as "center of gravity" or centroid frequency.

Hyperfine-structure anomaly

The A-factors are fit parameters that respond to the distance between the HFS peaks. Once they are fitted to a spectrum, they allow extracting the nuclear magnetic dipole moment μ_I from the nuclear g-factor g_I and the atomic-state-dependent B_0. Their ratio

$$r_A(^A\mathrm{X}) = \frac{A_u}{A_l} \tag{3.26}$$

should be identical in two isotopes ^{A}X and $^{A'}$X. A discrepancy from

$$R_{\mathrm{HSA}} = \frac{r_A(^A\mathrm{X})}{r_A(^{A'}\mathrm{X})} = 1 \tag{3.27}$$

indicates a hyperfine-structure anomaly (HSA). Equation 3.27 is correct only for a nucleus with a point-like magnetic dipole moment. Practically, the magnetization distribution inside the nuclear volume has to be taken into account, which differs between isotopes. This so-called Bohr-Weisskopf effect becomes significant in larger nuclei or in high precision measurements, when comparing the A-factor ratio R_{HSA} of several isotopes with different magnetization and charge distribution.

Nuclear charge radius

Once the fine-structure transition frequency ν_0 of two isotopes with mass numbers $A > A'$ is obtained, the isotope shift

$$\delta\nu_{\mathrm{IS}}^{AA'} = \nu_0(A') - \nu_0(A) \tag{3.28}$$

can be calculated. As deduced in Sec. 3.1.1, the isotope shift is composed of the specific mass shift, the normal mass shift and the field shift, which incorporates the difference in nuclear size

$$\begin{aligned}\delta\nu_{\mathrm{IS}}^{AA'} &= \delta\nu_{\mathrm{SMS}}^{AA'} + \delta\nu_{\mathrm{NMS}}^{AA'} + \nu_{\mathrm{FS}}^{AA'} \\ &= \nu_{\mathrm{MS}}^{AA'} + K_{\mathrm{FS}}\delta\langle r_c^2\rangle^{AA'} .\end{aligned} \tag{3.29}$$

The mass shift $\delta\nu_{\mathrm{MS}}^{AA'}$ and the field shift factor K_{FS} are a result of an extensive calculation of the atomic wave function. With their help, the change in mean-square nuclear charge radius $\delta\langle r_c^2\rangle^{AA'}$ can thus be extracted from a measurement of $\delta\nu_{\mathrm{IS}}^{AA'}$ with

$$\delta\langle r_c^2\rangle^{AA'} = \frac{\delta\nu_{\mathrm{IS}}^{AA'} - \nu_{\mathrm{MS}}^{AA'}}{K_{\mathrm{FS}}} . \tag{3.30}$$

Following the sign convention, a negative

$$\delta\langle r_c^2\rangle^{AA'} = R_c(A) - R_c(A') \qquad (3.31)$$

indicates that the heavier isotope A has a smaller extent than A'.

3.2 Boron atoms

In the experiments described in this thesis, laser spectroscopy is performed on atomic boron in the ground state. Atomic boron offers an allowed $2p \rightarrow 3s$ transition, which is well suited for field shift measurements following the arguments presented before. Figure 3.2 shows the parameters that are important for a laser spectroscopic investigation. The wavelength, which is needed to excite this transition, is $\sim 250\,\mathrm{nm}$, which is well in reach for commercial laser systems. From the excited $2s$ state, photons with energy $E_\gamma > 3.3\,\mathrm{eV}$ ($\lambda < 371\,\mathrm{nm}$) are sufficient to ionize the atomic system, which allows a resonant ionization measurement scheme, which is used in the experiment described in chapter 7.

All levels that are displayed exhibit a hyperfine structure, since all isotopes of boron that are investigated here $\left({}^{8,10,11}\mathrm{B}\right)$ have a nuclear spin. Due to the small energy difference between the two $2p$ states, the ${}^2\mathrm{P}_{3/2}$ state is populated even in room temperature environments. This offers the possibility to test the electric quadrupole moment Q of the respective nucleus. On the downside, the fractional population of the two states needs to be considered in experiments, since only a portion of all atoms is available in each state. In the experiments described in this thesis, the $J = 3/2$ state was not measured, but its population was observed.

Boron is a five-electron system. For such light systems, the ratio between mass and field shift is enormous, making approaches like King-plots [90], which rely on known isotopic charge radii, impossible. Instead, a full calculation of the electronic shell needs to be conducted, which gives a reliable value for the mass shift and the field shift coefficient. This calculation is outlined in the following. It is based on the first theoretical assessment of the states in atomic boron [91] and delivers the first-ever precision calculation of the isotope shift in a five-electron-system [45].

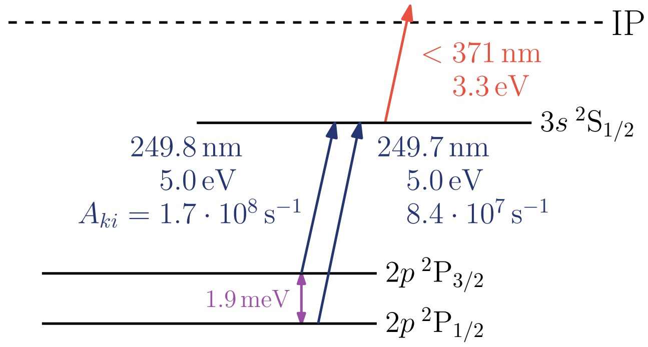

Figure 3.2.: Scheme of the atomic ground-state transition of boron, with parameters that are relevant for a laser spectroscopic experiment.

3.2.1 Exact calculations in the boron system

For the five-electron system of boron, numerical calculations of the electronic wave function in the $3s$ and the $2p$ state have been performed by Mariusz Puchalski and Krzysztof Pachucki. Although the absolute level and the derived transition energies carry large uncertainties of several GHz, the isotope shift can be calculated with the necessary precision to extract the field shift and the change in mean-square nuclear charge radius $\delta\langle r_c^2\rangle$ between the two isotopes ${}^{10,11}\mathrm{B}$.

The derivation of the wave function follows the approach that was discussed in the first section 3.1 of this chapter. The solution of the five-electron Schrödinger equation is perturbatively developed in α, including non-relativistic, relativistic and quantum-electrodynamical contributions.

The spin dependency of the target function is expressed as the n-electron spin eigenfunction $\Xi_{S,M_S}(\vec{\sigma})$ of the n-electron spin vector $\vec{\sigma}$. The spatial part is embodied by a K-term linear combination

$$\Psi_r(\vec{r}) = \sum_{l=1}^{K} c_l\, \psi_l(\vec{r}) \tag{3.32}$$

of explicitly correlated Gaussian wave functions (ECG), which either exhibit S or P symmetry

$$\psi_l(\vec{r}) = \exp\Big[-\sum_{a>b} c_{ab}\,(\vec{r}_a - \vec{r}_b)^2\Big]\,, \tag{3.33}$$

$$\vec{\psi}_l(\vec{r}) = \vec{r}_a\, \exp\Big[-\sum_{a>b} c_{ab}\,(\vec{r}_a - \vec{r}_b)^2\Big]\,. \tag{3.34}$$

Combined, the full five-electron wave function Ψ in spin-coordinate space is

$$\Psi(\mathbf{r}, \vec{\sigma}) = \hat{\mathscr{A}}\left(\Xi_{S,M_S}(\vec{\sigma}) \sum_{l=1}^{K} c_l\, \psi_l(\vec{r})\right). \tag{3.35}$$

Table 3.1.: The values of the absolute transition frequency of ^{11}B and the isotope shift in ^{10,11}B calculated in the different orders in $m\alpha^n$. All values presented were taken from [91] and [45]. The total isotope shift also includes the field shift. For more details and discussion, see text and the cited literature.

expansion order		transition freq. ν_0		isotope shift $\delta\nu_{\mathrm{IS}}$	
coeff.	*symbol*	*value* (MHz)	*rel unc.* $\log_{10}$	*value* (MHz)	*rel unc.* $\log_{10}$
$m\alpha^2$	E_{NR}	1 200 674 400(1500)	−6	−5027.27(3)	−5
$m\alpha^4$	E_{rel}	−372 460(90)	−4	4.78(7)	−2
$m\alpha^5$	E_{QED}	49 800(7200)	−1	−0.572(5)	−2
$m\alpha^6$	E_{QED}	3000(900)	−1	0.058(2)	−1
Total		1 200 354 700(7400)	−5	−5023.00(8)	−5

with $\hat{\mathscr{A}}$ being an antisymmetrization operator.

The linear and quadratic coefficients c_l and c_{ab} are determined with computational methods for each of the K basis functions to best match the non-relativistic Schrödinger equation. The basis size is increased from 1024 to 8192 terms to control the convergence before extrapolating to an infinite basis. The resulting non-relativistic wave function is then treated in perturbative calculations to include the relativistic $E^{(4)} = \langle\Psi|H^{(4)}|\Psi\rangle$ and QED contributions $E^{(5)} = \langle\Psi|H^{(5)}|\Psi\rangle$. The numerical calculation of $E^{(6)}$ is unfeasible, but its correction can be estimated from values obtained in the one- and two-electron systems [92].

Table 3.1 lists the contributions of the different expansion terms of $m\alpha^n$ for the ground-state $p \to s$ transition frequency ν_0 of ^{11}B as published in [91] and the corresponding contribution to the isotope shift $\delta\nu_{\mathrm{IS}}$, published in [45]. The underlying calculations, which were briefly explained here, were performed by Mariusz Puchalski, Krzysztof Pachucki and Jacek Komasa. The major component in each case, the non-relativistic energy $\sim m\alpha^2$, can be calculated with a precision of $\sim 10^{-6}$, which is much worse than (but agrees with) the experimental value for ν_0. Nevertheless, since the isotope shift is just a fraction of ν_0, the theoretical uncertainty is sufficiently good and exceeds the experimental precision of $\delta\nu_{\mathrm{IS}}$ by orders of magnitude. The mass-independent zero-order mass terms in $\sim m\alpha$ cancel out together with their large relative uncertainties, which allows calculating the mass shifts in the five-electron system with an uncertainty of only 80 kHz, while ν_0 has an uncertainty of 7.5 GHz. The experimental values for ground-state absolute transition frequency of ^{11}B and the isotope shift cited in the table were acquired in this work and will be discussed in Chap. 7. The discrepancy of the measured isotope shift from the mass shift is the field shift, which is proportional to the difference in nuclear size, as discussed along Eq. 3.18. For the boron system, not only the leading order contribution in the relativistic terms

$$E^{(4)}_{\mathrm{FS}} = C^{(4)}\langle r_c^2\rangle \tag{3.36}$$

is considered, but also the logarithmic QED contribution

$$E^{(6)}_{\mathrm{FS,log}} = (-Z\alpha)^2 \ln\left(Z\alpha m\langle r_c^2\rangle\right) E^{(4)}_{\mathrm{fs}} \approx C^{(6)}_{\mathrm{log}}\langle r_c^2\rangle\ , \tag{3.37}$$

which adds up to the isotope-dependent proportionally factor

$$C_A = C_A^{(4)} + C^{(6)}_{\mathrm{log},A}\ . \tag{3.38}$$

The resulting field shift factor

$$K_{\mathrm{FS}} = \frac{(C_{11} + C_{10})}{2} = 16.91\,(9)\,\mathrm{MHz/fm^2} \tag{3.39}$$

neglects the full $\langle r_c^2\rangle$ dependence but is a close approximation. The uncertainty can be estimated to be half of the logarithmic QED term. This is useful as an upper limit for neglected higher order $\langle r_c^2 \rangle$-dependent terms, which contribute even less.

4 Experimental Methods

This chapter introduces technical concepts and the underlying physical relations that are required in the experimental descriptions that follow. Radio-frequency quadrupole systems are used throughout the experiments as ion guides and as mass filters. They will be explained in the context of linear Paul traps in the first part. The second part focuses on the two laser spectroscopy schemes that are used to measure the isotope shift in the boron isotopic chain: collinear laser spectroscopy and laser spectroscopy on a collimated atomic beam.

4.1 Ion transport and manipulation

In the experiments described in this thesis, boron ions are transported in electrostatic beamlines, radio-frequency quadrupoles (RFQs) and gas catcher systems between different segments of the experiments. RFQs can be used as a mass filter or to forward ions under inert gas atmosphere while cooling them. Gas catchers allow to stop ions coming from large-emittance sources and to dissipate their kinetic energy. Both employ combinations of radio-frequency-driven AC as well as DC potentials.

4.1.1 Linear Paul traps and RFQs

Electromagnetic multipole fields can confine charged particles in small volumes. This principle can be used to trap and store ions, or to guide them along a defined path. Electromagnetic separators are composed of electric and magnetic fields to distinguish particles either by trapping of forwarding only selected charge-to-mass ratios q/m. The basis of a Paul trap and a Paul mass filter is an oscillating electrical quadrupole field, and their principle was first described and formulated by Paul [93, 94].

A purely electrical, static potential

$$\Phi(\vec{r}) = \Phi_0(ax^2 + by^2 + cz^2) , \tag{4.1}$$

which confines charged particles in all directions, is impossible, since it requires $a, b, c < 0$ (for $\Phi_0 > 0$). This contradicts the Laplace equation $\Delta\Phi = 0$, which restricts the three coefficients to follow

$$a + b + c = 0 . \tag{4.2}$$

The solution lies in the application of an additional AC field in such a way that for specific ratios of DC and AC voltages, stable orbits can be realized for selected q/m ratios. Two alternative solutions can be realized: $a = b$ and $c = -2a$ corresponds to the case of a classic Paul trap, which confines particles in all three dimensions. The case $a = -b$, $c = 0$ describes a mass filter or an ion guide. Such devices have been used here and will be further discussed.

In a mass filter, a perfect quadrupole potential would be realized by four hyperbolic electrodes that extend in z-direction. The distance between the electrode surfaces in the confinement region is $2r_0$, and the generated potential takes the form

$$\Phi(\vec{r}) = \Phi_0 \frac{x^2 - y^2}{r_0^2} \tag{4.3}$$

In most applications, the electrode shape is approximated by four cylindrical rods with diameter R in distance $2r_0$ that resemble the "perfect" field generated by hyperbolic electrodes well in the central region. Figure 4.1 shows a scheme of a rod-based linear Paul trap setup and outlines the electrical connections.

A positively charged ion that enters this geometry with static voltages applied will oscillate between the two electrodes in x-direction, but will immediately be pulled to one of the electrodes in y-direction and thus be lost. To confine the ions, a radio-frequency (RF) field is applied that switches the attractive and the repelling axis faster than an ion reaches either one of the electrode pairs. This switching is introduced by an additional time-dependent oscillating potential

$$\Phi_0(t) = U + V \cdot \cos\omega t \;, \tag{4.4}$$

which generates the time-dependent ideal quadrupole potential

$$\Phi(\vec{r}, t) = (U + V \cdot \cos\omega t)\, \frac{x^2 - y^2}{r_0^2} \tag{4.5}$$

with the DC amplitude U and the RF frequency ω with amplitude V.

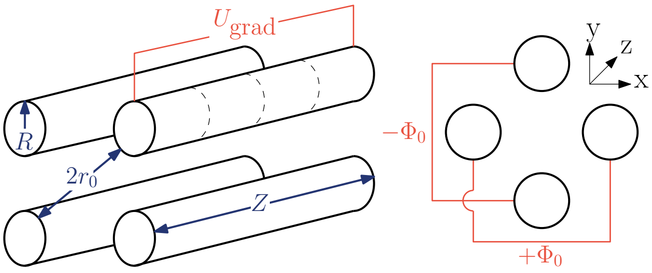

Figure 4.1.: A typical linear Paul trap is approximated by four cylindrical rods. The alternating potential is applied between the two pairs of opposing rods. In the top right rod, segmentation is indicated. A decreasing DC potential along the segments creates a longitudinal electric field, which drags ions while they collide with gas.

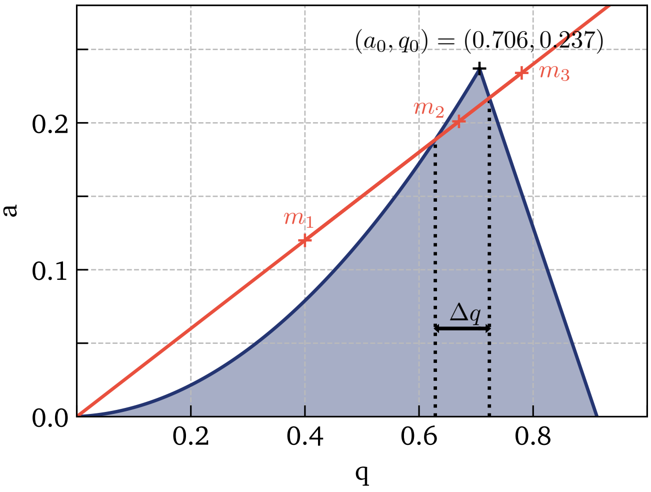

Figure 4.2.: The solutions of the Mathieu equation exhibit areas in the a/q plane that provide stable ion trajectories through a linear Paul trap. A given ratio of a and q, which is defined by the electrical field amplitudes, allows the selection of a certain mass range, defined by Δq, that is transported.

The corresponding differential equation of ion motion is the Mathieu equation, whose solutions give "stable" ion trajectories depending on the values of the dimensionless parameters

$$a_u = \frac{8eU}{mr_0^2\omega^2} \tag{4.6}$$

and

$$q_u = \frac{4eV}{mr_0^2\omega^2} \;. \tag{4.7}$$

Figure 4.2 shows the section of the a_u/q_u diagram in which an area of stable working conditions can be found. For a given set of U and V with a fixed ratio, only a certain mass range defined by Δq_u finds a stable trajectory through the RFQ, which is then acting as a mass filter. Ions with higher or lower mass are on "unsta-

Table 4.1.: **The properties of the quadrupole mass spectrometer used in the ^{10,11}B experiment.**

QMS property	Dimension
free field radius r_0	8.33 mm
rod radius R	9.39 mm
rod length Z	210.1 mm
RF frequency	2.9 MHz
mass range	0 u to 64 u

ble" trajectories and hit the electrode surfaces in x- or y-direction after a few oscillations. The ratio of U and V defines incline and, therefore, the mass resolution of the system, up to $U/V = a_0/(2q_0) \sim 0.17$ where the line includes only the cusp of the stability region in the diagram. The stability of the trajectory is in principle independent from the initial conditions of the ion, but in reality, constrained by the finite size of the geometry in x- and y-direction and the applied potential. In the theoretical discussion, the length Z of the trap in z-direction is infinite. Particles with high velocities $\dot{z}$ can pass a mass filter on an unstable trajectory in a realistic finite-Z system.

A more thorough discussion of the general properties and the fundamental physics of Paul traps is beyond the scope of this thesis and can be found in many textbooks, such as [95]. In the experiments described in this work, a mass filter and RFQ ion guides were employed, which will be introduced briefly in the following.

Quadrupole mass spectrometer

The quadrupole mass spectrometer (QMS) is an application of an RFQ and serves as a high-resolution mass filter. The DC and RF amplitudes are scanned with a fixed ratio $2U/V = a_u/q_u$ i.e. along the line in Fig. 4.1. The parameters a and q depend on the mass and therefore each mass has its own stability region that will be traversed successively along the line in a scan of the amplitudes. The incline can be changed to influence the mass resolution. In the experiment on stable boron isotopes, which is discussed in chapter 7, a commercial system from Extrel® is used. The parameters of this system can be found in Tab. 4.1. The combination of the high operation frequency of 2.9 MHz and the large diameter of 9.39 mm leads to a high transmission of almost 100 % and a high neighboring mass suppression as large as 10^9 [96, 97]. This system has previously been used to study short-lived lithium isotopes using resonance ionization mass spectrometry [98, 40].

Radio-frequency quadrupole guides

In the ^{8}B setup presented in chapter 5, RFQs guide ions in a helium buffer gas. After injection in such a gas-filled RFQ, ions thermalize to the gas temperature in collisions. This process also stops their forward motion in z-direction. To provoke movement in z-direction, the rods are segmented, and a DC gradient U_{grad} is applied stepwise along the segments. The field slope gradually pulls the ions along the rods to the exit of the RFQ, while collisions cool their x- and y-motion. The segmentation is indicated in one of the rods in Fig. 4.1. Such a DC gradient can be realized by combining the DC voltage drop along a chain of resistors with the applied RF. The segmentation also allows creating a linear Paul trap inside the RFQ guide by applying a decreasing potential along the axis with a steep rise at the last electrode. In this arrangement, a potential minimum is formed in which ions can be temporarily trapped and stored and then ejected in bunches by pulsing the "gate" electrode.

The RFQ guides are not primarily used for mass separation, but instead driven in RF-only mode for which the DC field amplitude is set to $U = 0$. This corresponds to operation on the q-axis of the stability diagram in Fig. 4.2, where all $0 < q_u < 0.92$ define stable trajectories. For a given parameter q_u, this corresponds to a high-pass filter that forwards all ions with mass

$$\frac{4eV}{q_u r_0^2 \omega^2} < m < \infty \; . \tag{4.8}$$

To change the low-mass threshold, the RF frequency ω or its amplitude V can be changed according to

$$\frac{V}{\omega^2} \sim m \; . \tag{4.9}$$

To transport light ions, high frequencies and low amplitudes are favorable. In principle, the RFQs can also be used in mass-selective mode by adding a DC potential U.

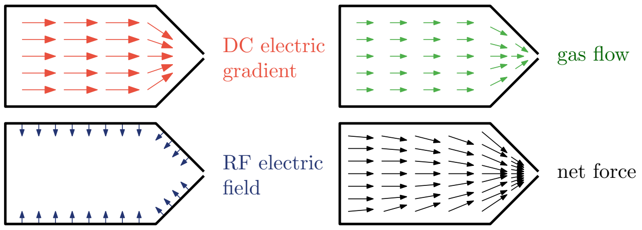

Figure 4.3.: The net force in a gas catcher system is composed of a DC field that supports the gas flow direction towards the nozzle, and an RF field that repels charged particles from the walls [99]. Ions enter from the left. The RF component becomes particularly relevant in the vicinity of the nozzle, where high DC gradients cannot be maintained.

4.1.2 Gas catcher

In the most simple form, a gas catcher is a volume filled with inert gas placed behind a source of fast ions. The ions entering the volume will collide with the gas and gradually lose their energy until they are thermalized. On the exit side of the gas catcher, a nozzle lets out a constant flow of gas, and since the stopped ions are in kinetic equilibrium with the flowing gas, they are transported to and ejected through the nozzle.

The recoils from the source need to stay ionized inside the gas volume since only then they can be forwarded and handled by the electric fields that are applied. To ensure the conservation of a charged state, the buffer gas needs a high first ionization potential, which makes helium the most suitable gas, since it has the highest ionization potential (24.6 eV) of all noble gases.

Substantial longitudinal momentum and angular straggling from the source require large gas volumes, which results in long extraction times for a gas-flow-only extraction. Thus, it is inefficient for radioactive particles, which often decay within shorter time scales. Also, the longer the time spent in the gas catcher, the more ion-gas collisions are induced, which can cause losses due to neutralization or the formation of molecular bonds with impurities in the catcher gas.

To overcome these limitations, an electric field gradient is applied along the extraction axis, which supports the transport of ions towards the nozzle. The electric field drags the radioactive ions into a small volume in front of the nozzle, where the force from the gas flow takes over and ensures the extraction. Typical extraction times are less than 10 ms for light ions such as boron.

The ions follow the field lines of the applied DC potential towards the nozzle. The field line density and thus the electric field strength becomes increasingly high when all ions are guided towards a small volume in front of the nozzle. Maintaining the required field strengths poses a technical problem since the voltage gradient is limited by the Paschen curve [100], which defines the break-through strength of fields in gases. The helium gas densities of several millibars, which are typically used, are distinctively bad for maintaining strong electric fields. Also, when a significant amount of charge is transported to the same spot, space charge effects spread the ion cloud and can lead to losses due to collisions with walls or to long extraction times.

To speed up the extraction and avoid losses, the nozzle is set up by tightly spaced electrodes. They are fed with an alternating electric field with an opposing phase. The resulting inhomogeneous RF field creates a net repulsive force

$$F = \frac{e^2}{2m\omega^2} V \frac{dV}{dx} \tag{4.10}$$

on the ions, with m being the mass of the ions and ω and V the frequency and amplitude of the electric field. This force repels the ions from the walls, allowing a higher charge density in the vicinity of the nozzle. Suitable electric RF field amplitudes are comparably weak and can be maintained even in the helium gas without breakdown. This design is called an RF carpet, which forms an RF cone in the nozzle.

To further increase the performance of the gas catcher, even the walls of the body are made of an RF structure, which generates a repelling force on the ions while pushing them towards the cone with the DC field. This allows a larger amount of charge to be preserved inside the gas catcher volume and thus increases the ion throughput. An overview of the acting forces in such a system is shown in Fig. 4.3.

4.2 Laser systems

The production and frequency measurement of laser light are essential in laser spectroscopy experiments. The resonant excitation of the investigated particles must be carried out with a low-power continuous-wave laser with a bandwidth much smaller than the natural linewidth of the transition. In some cases, the laser needs to be scanned or at least set to different frequencies during an experiment.

Measuring the optical frequencies $\sim 10^{15}$ Hz is also challenging, since the effects investigated in laser spectroscopy often are in the megahertz range, demanding 10^{-9} accuracy and better. While in some cases, relative shifts measured with simple interferometric wavelength meters (wavemeters) are sufficient, an optical frequency comb (OFC) fulfills the demand for accuracy.

4.2.1 Titanium-sapphire lasers

Titanium-sapphire (Ti:Sa) lasers have proven to be the optimal choice for many laser spectroscopic applications. They provide a wide scan range (680-1015 nm), which in combination with second- and fourth-harmonic generation covers almost the entire visible spectrum. In the typical ring-cavity lasers, a Ti:Sa crystal is optically pumped by a powerful continuous-wave (cw) laser with an adequately low wavelength, such as a frequency-doubled Nd:YAG laser (532 nm). The choice of cavity mirrors and several tunable optical elements in the ring path define the output frequency spectrum in the Matisse® 2 Ti:Sa laser systems that are used in the laser spectroscopy experiments described in this work. A photograph of this system is shown in Fig. 4.4. The optical elements in the Matisse® are side-of-fringe locked to a reference cavity with a stable-length resonator, which can be scanned with a piezo-driven mirror. This provides a narrow spectral width ($\sim$ 50 kHz) and high stability in frequency. However, the reference cavity does not provide an absolute calibration, which can be achieved by comparison with a wavemeter. In a simple stabilization scheme, the frequency offset measured by the wavemeter is converted to a voltage signal fed to the reference-cell piezo-actuated mirror. In this way, slow drifts in frequency, for example caused by thermal expansion, can be countered effectively.

This principle can be used to perform frequency scans in the megahertz to gigahertz range. The scanning pattern, namely the starting point, step size and duration, is defined by a software that also reads out the wavemeter. This readout is compared with the desired frequency in each step. The software then controls the reference piezo position to realize the scanning. Two techniques can be used: Either, the reference cell controller is addressed directly via a USB serial connection. Alternatively, the controller accepts a 0-5 V signal, which is translated into an absolute position of the piezo. This voltage can be generated by a standard digital-analog converter (DAC) card, which again is controlled by the software. Despite the detour, the latter approach proves to be more robust and stable in time. In both cases, a versatile scanning pattern can be run, including stabilization schemes on each frequency step or gigahertz-scale frequency jumps.

Two details are noteworthy: The maximum single frequency step is limited to a few megahertz. Larger steps in the scan pattern should be avoided, since they cause the Ti:Sa to lose its lock to the cavity, interrupting the scan. To facilitate a larger step (or the mentioned gigahertz-scale frequency jump), an appropriate amount of intermediate steps with a settling time of at least a few milliseconds should be implemented. Secondly, in the first few milliseconds after a new frequency is set, the reference cell piezo “relaxes”, which causes a small, but significant change in frequency, which is also visible on the wavemeter. The readout, stabilization and data taking should consider this effect.

4.2.2 Optical frequency comb

Wavemeters allow a quick interferometric measurement of a laser frequency with specified accuracies of 10^{-8}. More accurate optical frequency measurements below 10^{-10} relative uncertainty can be performed with an optical frequency comb (OFC). Figure 4.5 shows the principle of operation. The OFC generates optical modes in a precise, equidistant comb-like pattern across the visible and infrared regime with distance $f_{\mathrm{rep}} \sim 200$ MHz, facilitated by a mode-locked femtosecond laser. The absolute position of the comb modes can be evaluated by

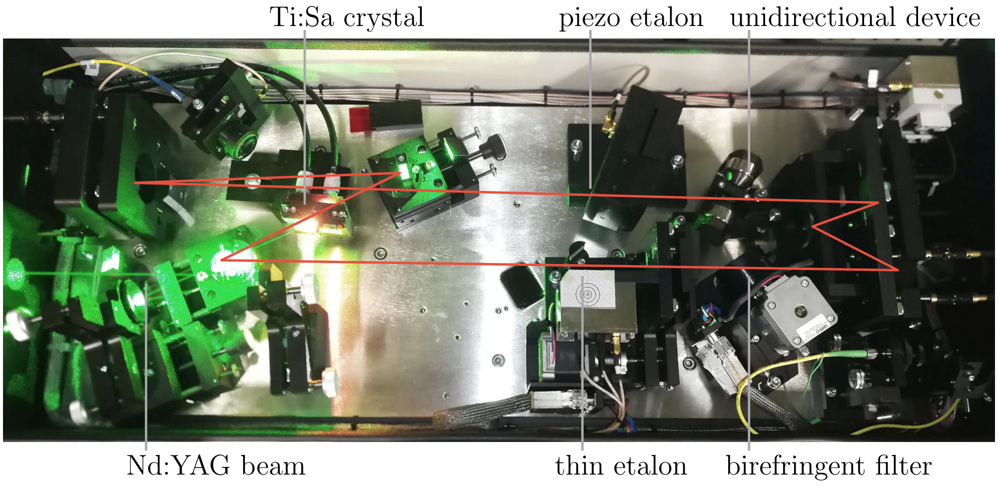

Figure 4.4.: The ring cavity of a Sirah[1] Matisse® 2 Ti:Sa laser. The crystal is pumped with light from a frequency-doubled Nd:YAG laser. Several optical elements allow adjusting, scanning and stabilizing the frequency output.

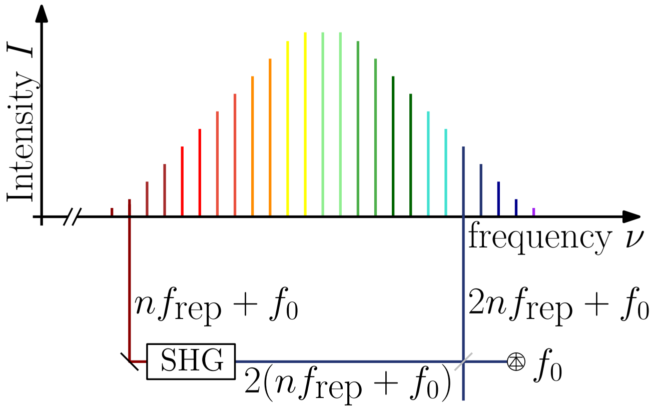

Figure 4.5.: In an optical frequency comb, a mode-locked femtosecond laser provides a comb-like pattern of optical modes with distance f_{rep}. The carrier envelope offset frequency f_0 can be determined and stabilized by comparing the frequency of the comb modes $2n$ and the second-harmonic of n, allowing an exact absolute frequency measurement [101]. Reproduced from [102].

comparing frequency-doubled light from a mode n on the "blue" side of the comb spectrum with a mode $2n$ on the "red" side. The beat between the two modes corresponds to the carrier offset amplitude f_0 and is stabilized to an RF reference, typically at $\approx 20\,\text{MHz}$. This provides a comb-pattern with optical modes with precisely known frequencies across the optical regime [101].

In a standard measurement, a small amount of light coming from a fixed-frequency laser is overlapped with the OFC spectrum. The beat frequency with the comb modes can either be measured or stabilized to an RF reference. The absolute frequency can be determined by identifying the nearest comb mode. This can be done by either systematically varying f_{rep} and f_0, or directly by comparison with a wavemeter, given that its absolute uncertainty is less than f_{rep}. The electronics that provides the stabilization and readout of the beat frequency are optimized for a frequency measurement in the distance $f_{\text{rep}}/4$ from an optical comb mode. Eventually, f_{rep} can be changed manually to guarantee this distance.

4.2.3 In-scan voltage measurement

A specific problem arises from the necessity to scan the laser frequency of the resonant system while measuring it. The titanium-sapphire ring-cavity lasers, which are used to generate the laser light with the probing frequency ν_{L}, can be scanned in a wide range that covers typical hyperfine structures. However, they need to be stabilized to an independent system such as an optical reference cavity to suppress short-term fluctuations and to a wavemeter to compensate for long-term drifts. These two elements can be combined to realize a scan of the Ti:Sa frequency across the resonance, as described above.

The wavemeters used in the experiments are relatively reliable in keeping the laser at a fixed frequency and report small deviations accurately. In an extended scan, however, the measured frequency can jump by several megahertz within an interval of a few hundred kilohertz leading to non-equidistant step sizes in a scan that is solely based on the wavemeter readout. This behavior

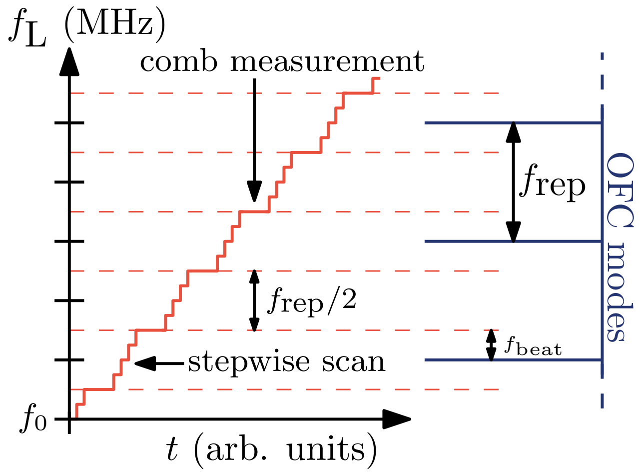

Figure 4.6.: A frequency f_L is scanned step-wise in an experiment. The scan is halted every $f_{rep}/2$ to perform a measurement of the beat frequency f_{beat} with a mode of a frequency comb with repetition rate f_{rep}. This allows an absolute frequency measurement with high precision at these points, which can be used to correct the relative frequency measurement from a wavemeter.

was extensively studied in [103], showing that an accurate calibration allows reproducing these jumps and using wavemeters above their specifications. If this calibration is not performed, the readout of absolute and relative frequencies with a wavemeter in a scan cannot be performed reliably.

An optical frequency comb, which is described above, offers a superior absolute frequency determination but intrinsically does not allow scanning. However, a simple scheme can circumvent this limitation. Figure 4.6 illustrates that without changing the repetition rate f_{rep}, it is possible to get an exact reading of ν_L every $f_{rep}/2$. At frequencies that are suited to be read out by the OFC the scanning stops and ν_L is stabilized with a proportional regulator via the reference cell and the wavemeter for an extended amount of time. This procedure allows recording a pattern of data points across the scan that have superior frequency uncertainty and also correcting the wavemeter frequency reading in adjacent steps.

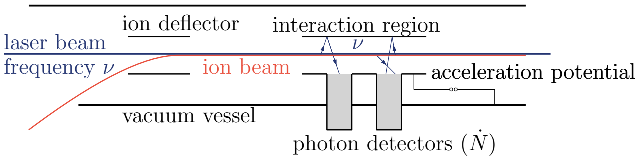

Figure 4.7.: In collinear laser spectroscopy, an ion beam is deflected and overlapped collinearly with a laser beam that runs at a well-controlled frequency ν. If ν matches the Doppler-shifted rest-frame transition frequency of an atomic transition of the moving particles, the transition is excited, and photons are emitted spontaneously. They are recorded with photon counters with respect to the applied acceleration voltage U_{acc} and ν_L

4.3 Collinear laser spectroscopy

In collinear laser spectroscopy, electronic transitions of ions and atoms are probed with laser light. A beam of potentially short-lived particles is superimposed with a laser beam in collinear alignment, which is schematically shown in Fig. 4.7. The acceleration potential of the ions defines their velocity, causing a Doppler-shift of the probed transition frequency. If the Doppler-shifted rest-frame transition frequency ν_0 matches the laser frequency in the laboratory frame, the transition is excited with a lifetime τ and photons are spontaneously emitted afterward. The photon scattering rate $\dot{N}$ can be recorded in single-photon detectors with respect to the applied voltage U_{acc} and the laser frequency ν. The rest-frame transition frequency ν_0 carries information about the nucleus that can be extracted directly, or in isotope shift measurements by comparison between different isotopes.

Collinear laser spectroscopy is a renowned tool to study nuclear ground-state properties of elements across the chart of nuclei. The collinear technique can be applied to nuclei with nuclear half-life $t_{1/2}$ down to a few milliseconds, limited by the time inherent from the production and the subsequent cooling and separation process.

The Doppler effect plays a central role in laser spectroscopic measurements since it defines the laser frequency ν_L, which has to be set in the laboratory frame to match the transition frequency ν_0 seen by the particle moving with velocity $\beta = v/c$. It is given by

$$\nu_L = \nu_0 \frac{1}{\gamma(1-\beta\cos\alpha)} \tag{4.11}$$

where $\gamma = \left(1-\beta^2\right)^{-1/2}$ is the relativistic time dilatation factor. For a collinear alignment of laser and particle beam, the Doppler formula is

$$\nu_L = \nu_0 \gamma(1 \pm \beta)\,, \tag{4.12}$$

where two cases can be distinguished: $\alpha = 0$ (positive sign) for co-propagating beams and $\alpha = \pi$ (negative sign) for counter-propagating beams.

4.3.1 Doppler compression

The resolution of a laser spectroscopic measurement is ultimately limited by the natural linewidth Γ_{nat}, which is correlated to the lifetime τ of the excited state (assuming that the lower state is the ground state). Following the Heisenberg principle, the frequency ν_0 of a transition has the uncertainty

$$\Delta\nu_0 = \frac{\Delta E}{h} = \frac{1}{2\pi\tau} = \frac{\Gamma_{\text{nat}}}{2\pi}\,, \tag{4.13}$$

yielding nanosecond lifetimes and the full-width at half-maximum $\Gamma_{\text{nat}} \approx 10\,\text{MHz}$ for dipole-allowed optical transitions. In realistic experiments, the observed linewidth is dominated by Doppler broadening, which results from the thermal motion of the investigated particles. Even with elaborate cooling techniques, it is not possible to generate ensembles of ions with adequate temperatures in short times.

However, the energy spread

$$\delta E = m v \delta v \tag{4.14}$$

originating from a source is maintained during electrostatic acceleration with a potential U_{acc} to

$$v = \sqrt{\frac{2qU_{\text{acc}}}{m}} \tag{4.15}$$

with q being the ion charge and m its mass. Combining these equation yields

$$\delta v = \frac{\delta E}{\sqrt{2qmU_{\text{acc}}}}\,, \tag{4.16}$$

which shows that the velocity spread δv decreases with larger U_{acc}. Since δv is responsible for the Doppler width of the spectroscopic line, this width is reduced accordingly. In the non-relativistic approximation ($\gamma = 1$) of the Doppler shift (Eq. 4.12)

$$\delta\nu_L = \nu_0 \frac{\delta v}{c} \tag{4.17}$$

the frequency shift grows proportionally with the velocity. Thus, the higher the total acceleration voltage, the smaller is the width from the original thermal distribution of the ions. This Doppler compression allows to resolve HFS spectra close to their natural linewidth using sufficiently high acceleration potentials of $\sim 30\,\text{kV}$.

4.3.2 Doppler tuning

Apart from the effects on the observed resonance width, the ions or atoms, which are accelerated, see a Doppler-shifted laser frequency according to Eq. 4.12 and in the non-relativistic approximation (Eq. 4.17)

$$\Delta\nu_{\text{Doppler}} \propto v \propto \sqrt{U_{\text{acc}}}\,. \tag{4.18}$$

In practice, this offers the possibility of Doppler tuning. Instead of scanning the laser frequency, the acceleration voltage is scanned, and the corresponding change in velocity represents a frequency scan in the ion rest frame. To realize such a scan, a small scan voltage U_{scan} is applied to the photon detection region or charge-exchange cell in addition to the acceleration voltage U_{acc}. Doppler-tuning allows keeping the laser systems running at fixed frequencies close to the Doppler-shifted transition frequency to be tested. This offers better stability and also more reliable locking and referencing schemes.

Measurement and the stability of U_{scan} and U_{acc} is essential, especially in experiments that try to measure absolute transition frequencies. Even for relative isotope shift measurements, this becomes relevant, which will be explained in Sec. 4.3.4.

4.3.3 Bunched beams

Bunching the ion beam is advantageous for collinear laser spectroscopy with fluorescence detection since it allows to suppress the laser-induced background of photons, which inevitably reach the photon counters. Instead of recording all events continuously, photons are only registered in a small time slot when the ion bunch passes the detection region. Since a typical spread of an ion bunch released from an RFQ trap is in the order of microseconds while the accumulation time is in the millisecond range, a factor $\sim 10^3 - 10^4$ background suppression can be reached. A more detailed survey of this can be found in chapter 6, which elaborates this concept in the context of the fluorescence detection region used in the experiment.

4.3.4 Collinear/Anticollinear laser spectroscopy

The differential Doppler shift

$$\begin{aligned}\delta\nu_{\text{diff}} &= \frac{\partial \nu_{\text{L}}}{\partial U} = \frac{\partial \nu_{\text{L}}}{\partial \beta} \cdot \frac{\partial \beta}{\partial U} \\ &= \nu_0 \frac{\gamma}{(1-\beta)} \cdot \sqrt{\frac{q}{2Umc^2}}\end{aligned} \tag{4.19}$$

represents the shift in observed frequency when the acceleration voltage, defined in Eq. 4.15, is changed by 1 V. Especially for light elements, $\delta\nu_{\text{diff}}$ changes significantly between different isotopes due to the mass dependency. This introduces an artificial isotope shift in the transition frequency, which can only be corrected for when the voltage U_{acc} is precisely known. Typical voltage uncertainties for ion sources and ions released from RFQ cooler and buncher systems are in the 10^{-4} range, limited by unknown potential distributions inside the source or the accuracy of the high voltage measurement. Thus, it is not possible to differentiate small field shifts for light isotopes from uncertainty in the voltage determination. In addition, light isotopes are especially prone to systematic errors since small forces have larger impact on the particle kinetics than in heavier particles.

Table 4.2.: Parameters for the measurement of ^{8}B in collinear alignment. The expected frequency is computed from mass an field shift, of which the latter is known only approximately.

Parameter	Value (MHz)
mass shift	10 046
field shift	50
expected ν_0	1 200 374 297
$\Delta\nu_{\text{Doppler}}$ at 30 kV	3 406 114
ν_{diff} (V^{-1})	56.9

This problem led to the implementation of collinear/anti-collinear laser spectroscopy, which was used for the measurements on beryllium [104, 41]. A second laser beam is superimposed with the particle beam but in counter-propagating direction. If the frequencies ν_{c} and ν_{ac} of the lasers are chosen in a way that the atomic transition is in resonance at the same acceleration potential U_{acc}, then by deploying Eq. 4.12 one obtains

$$\nu_{\text{c}} \cdot \nu_{\text{ac}} = \nu_0\gamma(1+\beta) \cdot \nu_0\gamma(1-\beta) = \nu_0^2 \tag{4.20}$$

with ν_0 being the “absolute” transition frequency in the ions rest frame. Hence, the voltage dependency is eliminated, allowing a precise absolute frequency to be determined for each isotope. To perform the calculation in 4.20, the absolute frequency of the laser system needs to be known. This can be realized with a laser system referenced to an optical frequency comb, or precisely known reference transitions.

4.3.5 Collinear laser spectroscopy on ^{8}B

In the experiment, which is introduced in chapter 5, the difference in mean-square nuclear charge radius in the boron isotopic chain will be measured. Using the atomic theory deduced in chapter 3, this value can be extracted from isotope shift measurements in the

$$2s^2\,2p\;^2\text{P}_{1/2} \xrightarrow{249.75\,\text{nm}} 2s^2\,3s\;^2\text{S}_{1/2}$$

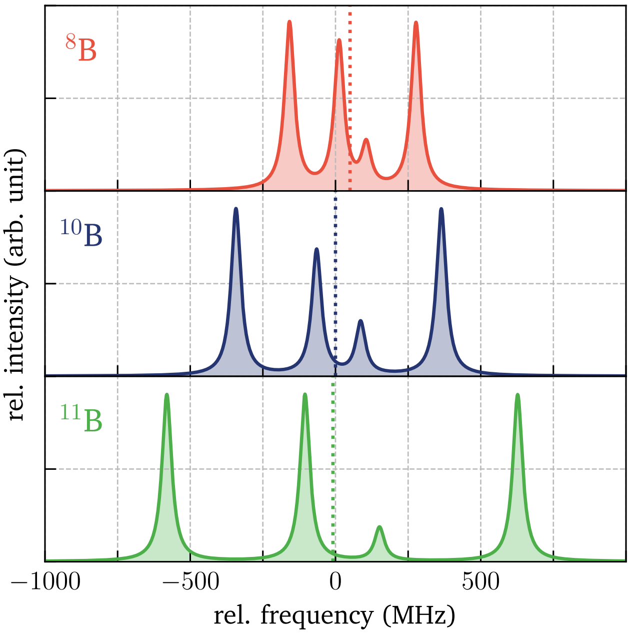

Figure 4.8.: Simulated hyperfine spectra of the three boron isotopes ^{8}B (red), ^{10}B (blue) and ^{11}B (green) with their natural linewidth. The hyperfine parameters of the stable isotopes are deduced in this work (see chapter 7) and extrapolated for ^{8}B using [46]. The centroid is shown as a dashed line. The mass shift has already been considered in the frequency axis. Hence, the shift represents the contribution of the field shift.

atomic transition of ^{8,10,11}B. For the light isotope boron, the collinear/anti-collinear approach is chosen since it combines the necessary sensitivity with the required precision. In Fig. 4.8, simulated spectra from the three boron isotopes are shown with their natural linewidth. Due to the nuclear spin and the magnetic moment, the hyperfine spectrum of ^{8}B spans $\sim$ 500 MHz, which is about half the width of the full ^{11}B spectrum. The differential Doppler factor derived in Eq. 4.19 is

$$\delta\nu_{\mathrm{diff}}^{^{8}\mathrm{B}} = 56.9\,\mathrm{MHz/V} \tag{4.21}$$

at 30 kV, which corresponds to approximately 18 V scan range to cover the entire resonance. Even with the natural linewidth of $\Gamma_{\mathrm{nat}} = 40.1$ MHz some lines are just barely resolved. This underlines the necessity of sufficient cooling to avoid residual Doppler broadening as far as possible.

The three spectra are separated by an isotope shift of $\sim$ 5 GHz/A, which mostly corresponds to the mass shift. The ^{8}B nuclear charge radius calculated in chapter 2, in combination with the isotope shift calculations from chapter 3, yield an expected field shift of $\sim$ 50 MHz between ^{8}B and its stable neighbors ^{10,11}B. In Fig. 4.8, the centroid of each spectrum is displayed as a dashed line, and the offset corresponds to this field shift. Table 4.2 lists the calculated parameters of the laser spectroscopy scheme for ^{8}B at $U_{\mathrm{acc}} = 30$ kV.

4.4 Laser spectroscopy on a collimated atomic beam

Laser spectroscopy can be performed on atomic beams that are prepared in thermal environments without further acceleration. The atoms of interest are vaporized and form a beam by collimation or by using a nozzle after production in gas. In both cases, the atoms have thermal Maxwell-Boltzmann-type probability distribution

$$P(\upsilon) = \sqrt{\frac{2}{\pi}\frac{\upsilon^2}{a^3}} e^{-\frac{\upsilon^2}{2a^2}} \tag{4.22}$$

$$a = \sqrt{\frac{k_B T}{m}} \tag{4.23}$$

of their velocity υ where T is the temperature of the ensemble of atoms with mass m. The thermal Doppler broadening and the deficiency of any means of velocity control of atoms makes collinear spectroscopy unfeasible for such beams.

Instead, atom and laser beam are overlapped perpendicular to record the resonance spectra, as shown in Fig. 4.9. The non-relativistic part of the Doppler formula

$$\nu_{\mathrm{L}} = \nu_0 \frac{1}{1-\beta\cos\alpha} \tag{4.24}$$

describes which frequency ν_0 is observed by the atoms in their rest frame depending on their velocity υ in the laboratory frame and the intersection angle α. Since the velocities for thermal beams are small, a Taylor expansion to first order in velocity

$$\nu_{\mathrm{L}} = \nu_0 (1 + \beta\cos\alpha) \tag{4.25}$$

is sufficient, which directly yields a relation for the Doppler-induced frequency shift for any intersection angle

$$\Delta\nu_{\mathrm{D(oppler)}} = \nu_0 \beta \cos\alpha\ . \tag{4.26}$$

The beam alignment, following Fig. 4.9 is at least close to being perpendicular with $\alpha = \pi/2 + \varphi$. Using

$$\cos(\pi/2 + \varphi) = \sin\varphi \approx \varphi\ , \tag{4.27}$$

this can be reduced to

$$\Delta\nu_{\mathrm{D}} = \nu_0 \beta \varphi\ . \tag{4.28}$$

Since the angle φ represents a small deviation from "perfect" perpendicular alignment, the small-angle approximation (or first-order Taylor expansion in α at $\pi/2$) can be used. Such a small deviation needs to be considered since it is practically impossible to overlap the atom and laser beam perfectly. Using these basic relations, the next sections will introduce some of the concepts in perpendicular laser spectroscopy on a collimated atomic beam, which have been used in the ^{10,11}B measurements described in chapter 7.

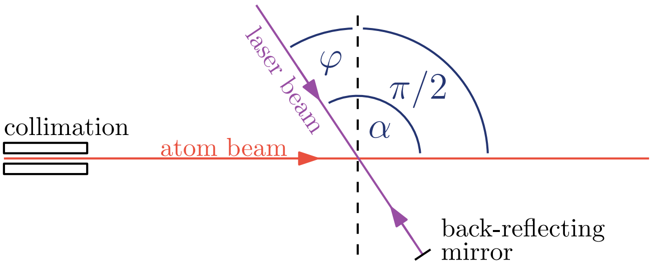

Figure 4.9.: The atomic beam is emitted from the tube on the left-hand side and intersected with the laser beam coming from the top and is back-reflected in the double-pass scheme. The drawing depicts the basic angular relations used in this section.

4.4.1 Resonance position and width

To resonantly excite the atoms in the beam, the laser frequency ν_{L} needs to be set to the atomic transition frequency ν_0. The angle φ slightly shifts the position of the resonance following Eq. 4.28. The most probable atom velocity

$$\hat{\upsilon} = \sqrt{\frac{2k_B T}{m}} \tag{4.29}$$

can be derived from the Maxwell-Boltzmann distribution. The Doppler-linewidth corresponds to the width of the Maxwell-Boltzmann velocity distribution

$$\sigma_{\mathrm{MB}} = \sqrt{\frac{(3\pi - 8)}{\pi}} \sqrt{\frac{k_B T}{m}} \,, \tag{4.30}$$

which would fully contribute if the laser is directed along the beam direction. Contrary, performing spectroscopy on a perfectly collimated beam with $\alpha = \pi/2, \varphi = 0$ would result in a vanishing Doppler width. For small angles φ, the longitudinal width will increasingly contribute to the observed width according to

$$\sigma_{\mathrm{MB},\varphi} = \nu_0 \frac{\sigma_{\mathrm{MB}}}{c} \varphi \,. \tag{4.31}$$

Since there is never a perfectly collimated beam, even for $\varphi = 0$ a residual Doppler width, related to the collimation angle, will remain. One can therefore expect to observe a constant width contribution $\sigma_{\mathrm{MB},0}$ and an additional width contribution $\sigma_{\mathrm{MB},\varphi}$, which increases linearly with the angle. The quotient q_{MB} between the Maxwell-Boltzmann shift $\Delta\nu$ related to the angle-dependent Doppler width $\sigma_{\mathrm{MB},\varphi}$ is then

$$q_{\mathrm{MB}} = \frac{\hat{v}}{\sigma_{\mathrm{MB}}} = \frac{\Delta\nu_{\mathrm{D}}}{\sigma_{\mathrm{MB},\varphi}} \approx 2.10 \tag{4.32}$$

and does not depend on any parameters of the particles or their distribution. It is thus a good indicator to test if the velocity distribution of the particles is purely thermal. Of course, this requires to separate $\sigma_{\mathrm{MB},0}$ and $\sigma_{\mathrm{MB},\varphi}$ and to distinguish these width contributions from other broadening mechanisms that affect the observed linewidth.

4.4.2 Double-pass scheme

It is practically impossible to have a perfect perpendicular overlap $\varphi = 0$, and the Doppler shift depends strongly on the angle since the incline of the cosine is steep at $\alpha = \pi/2$. Thus, atomic spectra that are recorded in this scheme are Doppler-shifted following Eq. 4.28, which also introduces a dependency of the atom velocity v, which is difficult to measure.

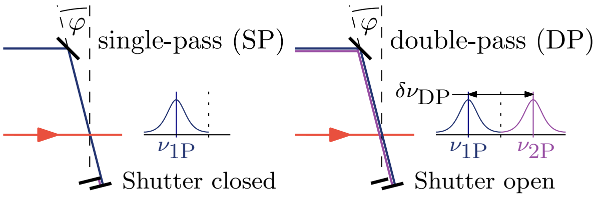

Figure 4.10.: In the double-pass scheme, the spectrum is recorded twice from the co- and counter-propagating laser beam, which is back-reflected and superimposed with itself. The resonances are shifted outwards due to the angular deviation φ from $\pi/2$.

To overcome these limitations, a scheme is applied where the laser beam is back-reflected after crossing the particle beam once and superimposed with itself. Such a scheme can be accomplished with considerably higher precision than assuring perpendicularity. A shutter system is used to turn the back-reflection on and off and thus record spectra with and without back-reflection in parallel.

Figure 4.10 shows the relative position and the nomenclature used for the double-pass scheme. The single-pass (SP) spectra, recorded with closed shutter, show the atomic transition recorded once, with the centroid shifted according to Eq. 4.28 to ν_{SP}. With the shutter open, and thus the back-reflection on, a second spectrum builds up from the second pass (2P) of the laser beam. Since the SP laser crosses the interaction region simultaneously, a composite double-pass (DP) spectrum builds up. The DP spectrum is composed of two superposed spectra, with their centroids shifted by the same absolute value in opposite directions. The first pass (1P) spectrum centroid ν_{1P} in the DP spectrum corresponds to the SP spectrum recorded in parallel, while the second pass (2P) originating from the back-reflected beam appears with the centroid at ν_{2P}. The distance between the two centroids in the DP spectrum is

$$\delta\nu_{\mathrm{DP}} = \nu_{\mathrm{2P}} - \nu_{\mathrm{1P}} \,. \tag{4.33}$$

An elaborate fitting procedure described in chapter 7 can disentangle the 1P and the 2P spectra from the DP spectrum, using fit information from the SP spectrum. The arithmetic mean

$$\nu_0 = \frac{\nu_{1\mathrm{P}} + \nu_{2\mathrm{P}}}{2} \tag{4.34}$$

of the two centroids provides the absolute transition frequency ν_0.

4.4.3 Resonance ionization

Instead of fluorescence detection of the photons, which are emitted spontaneously after resonant excitation, in many atomic systems, a two-step resonance ionization scheme can be employed. The atoms are resonantly excited from the ground state to a first excited state i with a frequency-controlled high-precision laser system A. A second laser beam B is overlapped whose photon energy is sufficiently high to excite atoms in the state i to above their ionization potential. Only when A is in resonance with the atomic transition, ions can be generated by laser B. These generated ions can be handled with electrostatic potentials and detected with almost 100 % efficiency. To reduce background from contaminants, a QMS can be used to select ions of the mass that are produced in the resonant excitation. Recording the ions transmitted through the QMS as a function of the laser frequency allows a sensitive and selective, almost background-free detection of the atomic resonance.

4.4.4 Consistent measurements

In an isotope shift measurement, like the one performed on ^{10,11}B, which is described in chapter 7, the transition frequency of two isotopes A and A' is compared. The isotope shift

$$\delta\nu_{\mathrm{IS}}^{AA'} = \nu_0^A - \nu_0^{A'} \tag{4.35}$$

is the difference between the two absolute transition frequencies. Using Eq. 4.34 and the definition from Eq. 4.33, the absolute frequencies can be calculated from

$$\nu_0 = \nu_{1\mathrm{P}} + \frac{\delta\nu_{\mathrm{DP}}}{2} \,. \tag{4.36}$$

If the overlap angle φ is not changed between the measurement of isotope A and A', the size of the Doppler shift is similar except for the difference in velocity of the two isotopes. This velocity ratio

$$r_v^{A'} = \left(r_v^A\right)^{-1} = \frac{v^{A'}}{v^A} \tag{4.37}$$

is close to 1 if both isotopes have the same thermal source where they acquire the same average kinetic energy. Such a dataset can be called consistent and allows to extract the isotope shift with higher precision, and to refine the extracted absolute transition frequencies.

Isotope shift

Combining Eq. 4.35 and Eq. 4.36 yields

$$\delta\nu_{\mathrm{IS}} = \nu_{1\mathrm{P}}^A + \frac{\delta\nu_{\mathrm{DP}}^A}{2} - \left(\nu_{1\mathrm{P}}^{A'} + \frac{\delta\nu_{\mathrm{DP}}^{A'}}{2}\right) . \tag{4.38}$$

In a consistent dataset,

$$\delta\nu_{\mathrm{DP}}^{A'} = \delta\nu_{\mathrm{DP}}^A \cdot r_v^{A'} \,, \tag{4.39}$$

which finally allows to rewrite Eq. 4.38 to

$$\delta\nu_{\mathrm{IS}} = \nu_{1\mathrm{P}}^A - \nu_{1\mathrm{P}}^{A'} + \frac{\delta\nu_{\mathrm{DP}}^A}{2} \cdot \left(1 - r_v^{A'}\right) , \tag{4.40}$$

which only depends on 1P spectra centroids (which are equivalent to the SP), and a correction from a DP spectrum from one of the isotopes, which is small for the isotopic velocity differences from a thermal source. This alternative approach is thus useful if one isotope is much less abundant or the extraction of the 2P centroid has a comparably large uncertainty, both of which is the case for the ^{10,11}B isotope shift measurement.

Absolute transition frequency

Starting from Eq. 4.36, the absolute transition frequency of one isotope A' can be calculated using the distance between the 1P and the 2P centroid from the other isotope A, corrected with r_υ. The resulting absolute transition frequency

$$\nu_0^{A'} = \nu_{1P}^{A'} + \frac{\delta\nu_{DP}^{A} \cdot r_\upsilon^{A'}}{2} \,. \tag{4.41}$$

only uses the SP centroid from isotope A' and allows to obtain a value for $\nu_0^{A'}$ without using the 2P spectrum of A'. This can be used to extract an absolute transition frequency when no 2P spectrum was recorded, or to cross-check and refine a value by using additional information from the second isotope.

5 Towards collinear Laser Spectroscopy of ^{8}B

Collinear laser spectroscopy allows determining the isotope shift in the ground-state transition frequency between the stable boron isotopes ^{10,11}B and the short-lived ^{8}B. The proton-halo character of this exotic light nucleus magnifies the field shift contribution to the isotope shift which can be extracted from the experiment using high precision atomic theory. The collinear/anticollinear laser spectroscopy scheme combines the sensitivity to work with small production rates of ^{8}B and the necessary precision to extract the isotope shift. The experimental campaign takes place at Argonne National Laboratory in Chicago, IL, USA, where a production and cooling scheme of the exotic ^{8}B is established. Many steps were taken towards measuring the isotope shift in ^{8}B, which are summarized in this chapter.

5.1 Overview

The experimental setup to measure the isotope shift of ^{8,10,11}B at Argonne National Laboratory is shown as an overview in Fig. 5.1. The experiment can be separated into three main divisions, which were worked on in parallel.

The ATLAS accelerator at ANL provides a ^{6}Li beam, which is impinged on a ^{3}He target. The reaction products, which include ^{8}B, are fed into a subsequent cooling system, which is installed in Area II at ANL. This system is operational and served as a ^{8}B source for electron-neutrino (β-ν) angular correlation measurements in the beta-decay Paul trap (BPT) in the past [105, 106]. Several improvements were implemented to increase the production rate and stability, but the subsequent gas catcher system, which cools the ions, is not able to deliver ionic boron, but only ionic molecular compounds.

The next part of the experimental setup is the molecular breakup station, which converts the molecular ^{8}B ions delivered by the production system into an ionic beam of ^{8}B. The system is based on breaking up the molecules in nanometer-thin carbon membranes and reionizing them in helium gas. At this time, in 2019, this system is in the commissioning phase, and the first successful tests were performed.

The laser spectroscopic beamline is set up in an offline laboratory at ANL. First laser spectroscopic measurements were performed on a Ca$^+$ beam. The heart of the laser spectroscopic device, the fluorescence detection region, was revised and investigated within the scope of this thesis and is introduced in chapter 6. The laser system is another distinct part of the laser spectroscopy experiment, but it is not yet set up at ANL. Similar systems have proven their capabilities in laser spectroscopic measurements at TU Darmstadt [102].

Finally, a summary of the efficiencies and the ^{8}B production rates achieved so far will be presented. Apart from the commissioning work that still needs to be done, laser spectroscopy on ^{8}B is within reach with the rates and the equipment presented in the following sections.

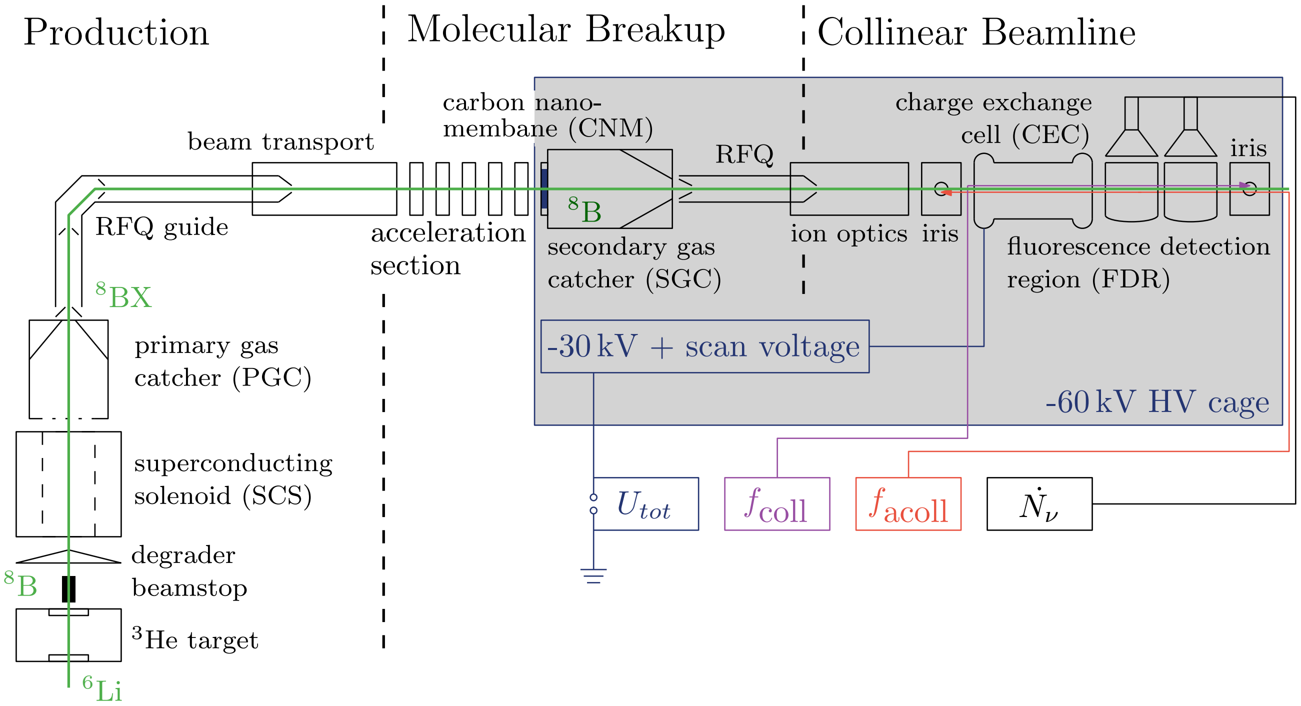

Figure 5.1.: The setup for measuring the isotope shift in ^{8}B at Argonne National Laboratory is divided into three sections. The production is based on a 41 MeV ^{6}Li beam delivered from the ATLAS[1] accelerator. The second part is dedicated to the breakup of molecules which are formed in the gas catcher cooling system behind the production target. Finally, ionic boron is extracted and fed into a collinear beamline, where it is neutralized and probed with an optical-frequency-comb-based laser system. The photon count rate $\dot{N}_\nu$ is recorded with respect to the total acceleration voltage U_{tot} and the laser frequency f_{coll} or f_{acoll} in the experiment.

5.2 ^{8}B production

Collinear laser spectroscopy is a technique that relies on a slow and cooled beam of the isotope of interest. This is in contradiction to the production mechanisms for most exotic isotopes, which rely on nuclear reactions that typically take place at MeV energy scales, and seldom allow a directional, mono-energetic output beam. Thus, an intermediate stage is implemented that catches the products from the reaction and dissipates their energy ("cooling"), before ejecting them into an electrostatic beamline.

In-flight production at ATLAS

At ATLAS, the in-flight reaction ^{3}He(^{6}Li,^{8}B)n is used in inverse kinematics to produce ^{8}B. A primary beam of ^{6}Li is accelerated to approximately 41 MeV by the ATLAS accelerator. This beam then hits a liquid-nitrogen (LN2) cooled target filled with ^{3}He, which was revised and refurbished for the upcoming laser spectroscopic experiments to maintain high production rates. At primary beam intensities of up to 450 particle-nanoampere (pnA), production rates of several thousand ions per second in a stopped and cooled configuration are observed.

Since the ^{8}B still carries a significant portion of the accelerated primary beam energy, a sophisticated catching, stopping and cooling setup is implemented to prepare it for electrostatic transport. A large-bore superconducting solenoid focuses the beam into a helium-filled gas cell. The collisions with the helium gas dissipate the energy, but impurities in the gas also lead to molecule formation.

The boron molecules are transported efficiently, but they can not be used for atomic-state-dependent laser spectroscopy. A molecular breakup system is being commissioned, which breaks the molecular bonds and bunches the boron ions towards the laser spectroscopic beamline. Section 5.3 is dedicated to this secondary molecular break-up system.

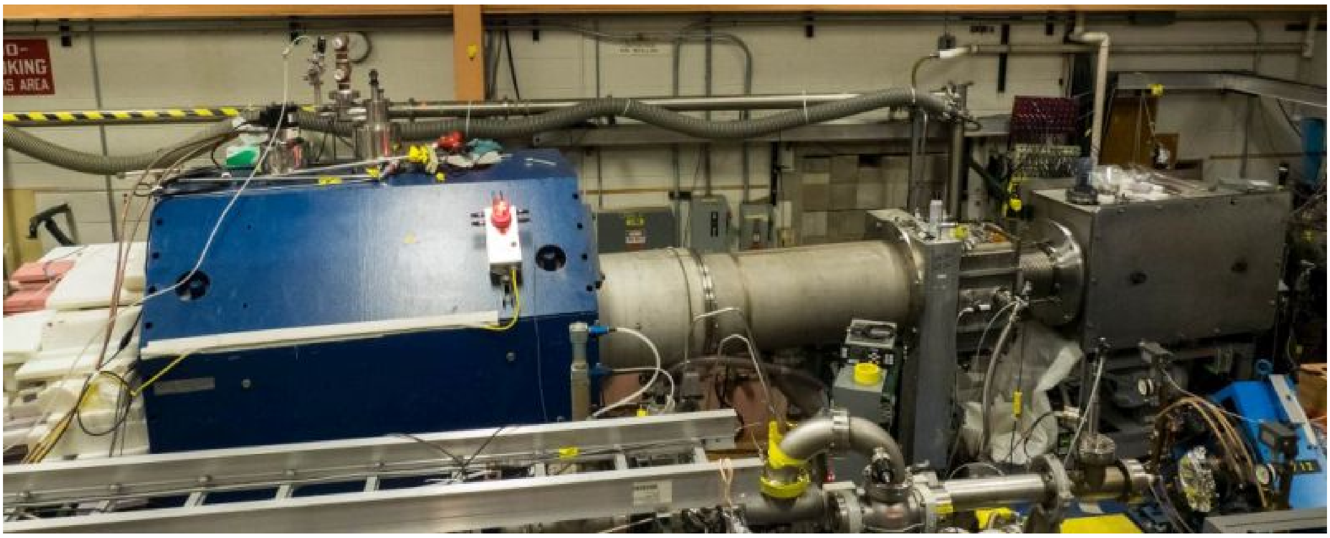

Figure 5.2.: Photograph of the production section in Area II at ANL. The target is covered in plastic to shield the users from neutron radiation. The blue superconducting solenoid (SCS) focuses the reaction product into the primary gas catcher (PGC), which feeds the stopped ions into the attached RF guiding system.

5.2.1 Production target

For the production reaction, ^{6}Li particles impinge on a ^{3}He target with energies of ~ 41 MeV. The lithium beam accelerated by the ATLAS accelerator is therefore guided into a ^{3}He-containing gas target, which is separated from the chamber vacuum by thin entrance and exit windows. This target setup was established at ATLAS around 2000 [107] and expanded around 2012 to produce ^{8}B and ^{8}Li. The production cross-section for ^{8}B was only scarcely investigated so far [108] but is estimated to be $\sim$4 mb, which is about half of that of the ^{7}Li(d,p)^{8}Li reaction, which produces the mirror nucleus ^{8}Li in the same setup. Total production of 1-2 ^{8}B/s per particle-picoampere (ppA) was estimated from the preliminary studies and is achieved in the ATLAS setup. These rates were limited by the allowed amount of neutron radiation in the experimental area, not by the stability of the target, the accelerator, or the lithium source. Due to the inevitable increase in safety measures when running at high beam intensities, which make experimental work difficult, most of the test experiments were conducted at low rates $<$50 pnA. For data-taking experiments to come, saturation and stability of the production at high rates need to be investigated more extensively beforehand.

The target is a cylindrical volume, which is elongated 4.5 cm along the beam axis. A picture of the target can be found in Fig. 5.3, together with a scheme in Fig. 5.4. The two end caps of the cylinder are stainless steel discs, which have a hole that is covered by a leak-tight $\approx 1.5\,\mu$m thin titanium foil (1.7 mg cm^{-2}), which is glued and sealed with vacuum and temperature resistant epoxy resin. The disc seals to the target volume with indium, and thus forms a reservoir for ^{3}He inside the vacuum chamber of the accelerator. The volume is tapped from the outside with two lines, so it can be pumped on and cleaned before being cooled and filled with ^{3}He. The ^{3}He requires clean handling since impurities can freeze out on the windows, reducing the production efficiency or destroying the window in the worst case.

The ^{3}He is fed-in through one of the inlets until a pressure of approximately 730 mbar is reached. A pumping system uses bellows to form a reservoir, keeping the pressure constant. Liquid nitrogen at 77 K is circulated inside the volume to cool the structure and its content. The LN2 line is also separated from the chamber vacuum and the target volume. The cool-down procedure puts stress on the thin target windows especially and also reduces the pressure of the ^{3}He gas inside. As a safety measure, the reservoir can, to a certain degree, cushion a rise in pressure.

The accelerated lithium beam impinges on the titanium target window, which has a mass thickness of 1.7 mg cm^{-2}. The filled and cooled ^{3}He inside the $s =$

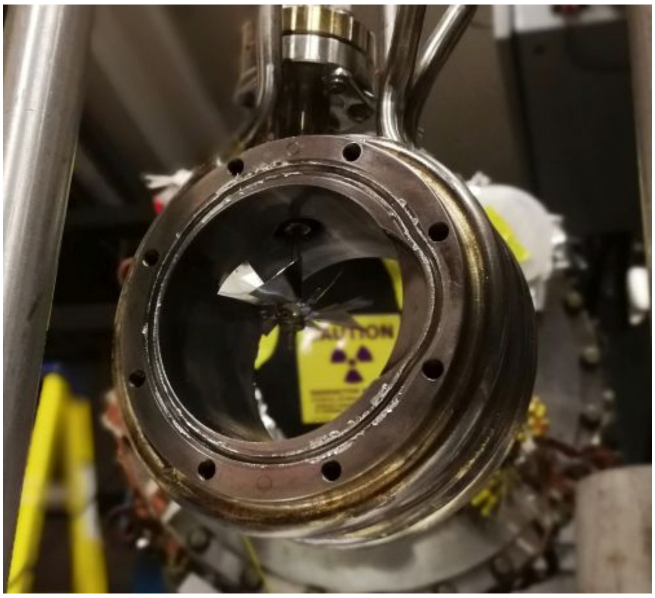

Figure 5.3.: The target without the titanium windows, which seal the volume from the vacuum chamber. The volume is filled with 730 mbar ^{3}He and cooled with liquid nitrogen to ∼80 K. The stirrer is offset from the beam axis and circulates the gas to cool the windows and to maintain constant pressure throughout the volume despite heating from the intense and high-energetic primary beam.

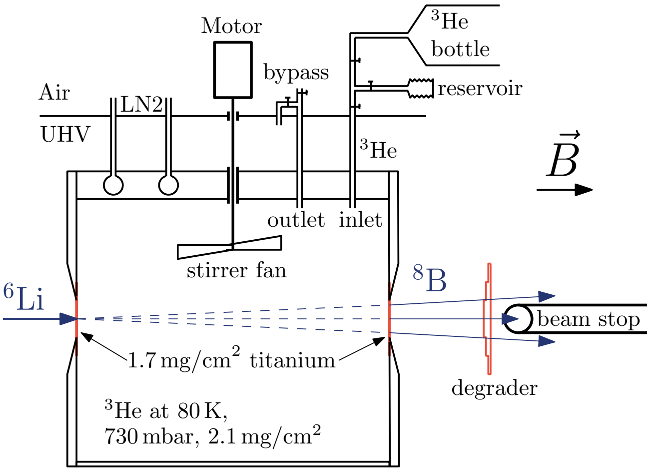

Figure 5.4.: Scheme of the target, which is filled with LN2-cooled ^{3}He. The target volume is separated with a bypass from the chamber vacuum and the liquid nitrogen line. Temperature and pressure sensors monitor the target status, and a reservoir can compensate for pressure changes. Thin titanium windows allow the primary ^{6}Li beam to enter and exit and to react with the ^{3}He. The target sits inside the magnetic field of the superconducting solenoid, which guides the reaction products into the gas catcher.

4.5 cm target has a density of $\rho_{^3\mathrm{He}} = 0.46\,\mathrm{kg\,m^{-3}}$, which corresponds to a mass thickness of

$$d = s \cdot \rho_{^3\mathrm{He}} = 2.1\,\mathrm{mg\,cm^{-2}}\ , \tag{5.1}$$

and the exit window is a second 1.7 mg/cm^2 titanium foil. Apart from the production reactions, the 41 MeV lithium beam experiences straggling inside the solid and gaseous matter, but it is not stopped inside the target or the entrance or exit window. The range of a particle beam in matter strongly depends on the nuclear charge Z of the projectile. An oxygen beam ($Z = 8$) with the same energy and target parameters would not pierce through the target. The lithium ($Z = 3$), however, only loses $\sim$ 10 MeV and experiences only a small angular straggling of up to $\sim 11°$.

This exit angle is relevant since the gas catcher, which follows downstream (see Sec. 5.2.3), only accepts a certain amount of charged particles before it saturates. Thus, the primary beam of ^{6}Li that has not reacted with the ^{3}He must be separated from the reaction products. Since the ^{8}B emerges under larger angles, a beam stop is situated on axis directly behind the target. It can be moved on this axis, which corresponds to a cutoff between 3.5° to 7° and only high-energetic particles emitted above this angular threshold are transmitted.

Power deposition and stirrer

The 10 MeV energy loss is transmitted to the target in collisions. At primary beam intensities of 450 pnA, this corresponds to a power of 4.5 W deposited to the target, distributed between the windows and the ^{3}He gas inside only from the elastic collisions with the contained particles. This substantial amount of power is focused on a small beam spot area of $1-4\,\mathrm{mm}^2$ on the entrance window. Mechanically, the windows showed to be surprisingly resistant to this stress, as long as they are not exposed to humid air between two irradiation periods.

The deposited power, however, warms the window locally, working against the LN2 cooling power. Therefore, the ^{3}He gas in the vicinity of the beam spot will be warmer than its surroundings and loose density. Naturally, there will be some circulation from the buoyancy of the heated gas, but it is suspected that this process is insufficient to keep the thermal distribution balanced inside the target. Similar effects have been seen and in-

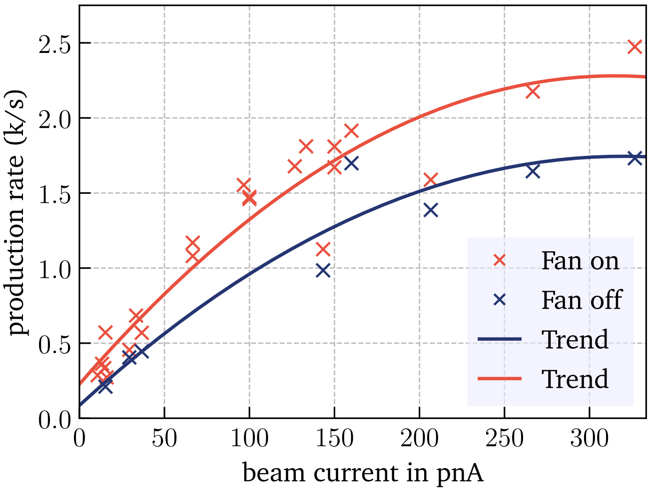

Figure 5.5.: ^{8}B production rates without (blue) and with (red) the stirrer running. Stirring the ^{3}He inside the target volume allows reaching significantly higher production rates. However, there is still a saturation effect visible, which can be attributed to the gas catcher. The continuous lines are trends to guide the eye.

vestigated by Yamaguchi et al. [109] who installed a gas circulation system to cool a target at CRIB[2] operating at similar conditions.

To overcome saturation effects at the ATLAS target for high primary beam intensities, a stirrer fan was installed inside the target volume. The fan is driven by an electric motor, which sits outside the vacuum chamber. The rotational movement is translated into the volume with a rotary feedthrough. The effect of the fan is visible in the production rates, as shown in Fig. 5.5, but not as pronounced as in the case of the CRIB target. Furthermore, high-intensity tests at up to 450 pnA have not been performed yet, and from the data, it can be extrapolated that the fan can play a significant role at these intensities.

5.2.2 Solenoid

The superconducting solenoid (SCS) is a helium-cooled large-bore superconducting magnet, which is installed behind the production target. The magnetic field of the order of 0.5 T reaches into the target itself and gradually increases in the direction of the bore. The direction of the magnetic axis is collinear with the primary beam axis. Due to the Lorentz force, the produced charged particles emerging from the target in an angle with respect to this axis are forced onto a tight circular orbit that confines them inside the strong magnetic field region. When leaving the field, the particles are refocused to the magnet axis before they diverge. This arrangement is known as a magnetic lens with a reciprocal focal length of

$$\frac{1}{f} = \frac{q^2}{4p_z^2} \int B_z^2 dz \tag{5.2}$$

with q being the particle charge, p_z the momentum, and B_z the magnetic field in the direction of the field axis [110]. By this means, the solenoid also acts as a p^2/q^2 filter and is thus particle-selective. Since the bore has a large diameter of 0.6 m, the solenoid accepts particles despite their large angular spread after the target.

This emission angle from the target is larger for ^{8}B particles that have lost more energy. To compensate, a degrader foil is situated before the solenoid entrance. It has a variable thickness, which increases towards the center, homogenizing the beam energy and increasing the transport efficiency for ^{8}B in the momentum-selective focusing of the solenoid.

In the decreasing field of the SCS on the exit side, the particles are focused into the gas catcher, which stops the beam and dissipates its energy. The field structure of the SCS is optimized for focusing the light and highly charged particles onto the thin entrance window. In an experiment, the field strength needs careful tuning to optimize yield in and behind the gas catcher. The tune is, in particular, sensitive to the incoming beam energy, but also to the spatial position of the primary beam on the target, which can change slightly from run to run.

5.2.3 Primary gas catcher

The primary gas catcher (PGC), depicted in Fig. 5.6, is placed in the decreasing magnetic fringe field behind the superconducting solenoid. It is a large-volume, helium-filled stopping cell for the reaction products from the target. The gas-filled volume is separated from the vacuum inside the magnet bore with a 1.9 mg/cm^{2} HAVAR® foil, which is reinforced by a 90 % transmission wire grid mounted on a stainless steel frame. This allows the

---

[2] Center for Nuclear Study (CNS) Radio Isotope Beam Separator in Tokio, Japan

Table 5.1.: The ionization potential (IP) of H, He, B, Na taken from [111]. It is energetically not favorable for boron ions to exchange charge with helium atoms in the gas catcher and RFQ systems. Conversely, it is favorable to neutralize boron before the laser interaction in the charge exchange cell, which facilitates a sodium atmosphere (see Sec. 5.4.2).

Element	1st IP (eV)	2nd IP (eV)
hydrogen (H)	13.60	
helium (He)	25.59	54.42
boron (B)	8.30	25.15
sodium (Na)	5.14	47.29

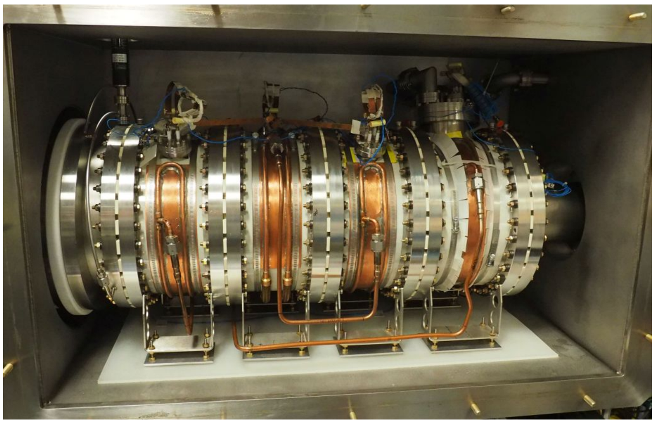

Figure 5.6.: The primary gas catcher sits inside a vacuum chamber to prevent condensation of water when it is cooled. The system is 1.5 m long with an outer diameter of 0.8 m.

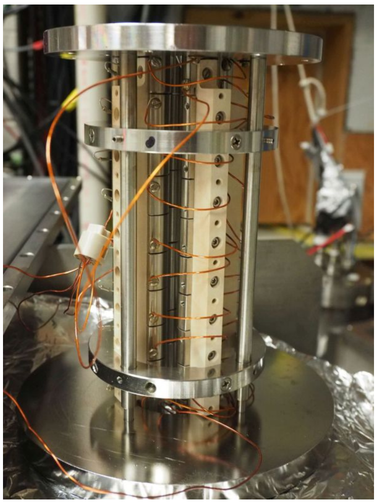

Figure 5.7.: One segment of the radiofrequency quadrupole guide that is installed behind the primary gas catcher. It consists of four segmented rods. RF is applied in a certain pattern between the segments, and an electrical potential slope transports the ions.

highly energetic ^{8}B, which is focused onto the window by the SCS, to be transmitted into the gas volume.

The PGC is filled with $\sim$ 55 mbar of helium gas, which offers the highest high first ionization potential of all noble gases with 24.6 eV, as listed in Tab. 5.1. This allows delivering the boron in a 1+ ionic state. The gas can be purified in cold traps, which freeze out contaminants that lead to neutralization and loss or formation of molecular bonds. The purification system consists of activated charcoal cold traps cooled with LN2 and a commercial Mono Torr® [3] purifier to remove any contamination. The gas, with a purity of initially 99.995 % as indicated by the manufacturer is cleaned to sub-ppb purity. Additionally, the gas catcher can be cooled during operation, or baked out under UHV conditions before filling it with clean helium.

Despite these efforts, the PGC does not provide $^{8}B^{+}$ beams but mostly molecular ions. Still, the molecules are generated in an ionic form, which suggests Van-der-Waals type bonds between a positive $^{8}B^{+}$ ion and water molecules. These molecular ions can are transported in the gas catcher. The transmission times of the PGC are in the order of 10 ms and thus negligible compared to the ^{8}B half-life. The total stopping efficiency is low for light ions (0.1 % to 1 %).

RF Extraction

The ions that are stopped inside the gas catcher are ejected from a gas nozzle, which also separates the 55 mbar helium gas pressure from the attached beamline. Here, a radio-frequency quadrupole guide is installed, which is described in chapter 4 as a special case of a linear Paul trap. The RFQ works under the vacuum conditions of approximately 10^{-3} to 10^{-5} mbar, which is differentially pumped from the gas catcher nozzle. The ions are transported via a shallow DC slope through three sections, which are separated by nozzles. The RF frequencies and amplitudes can be adjusted to optimize transport efficiency for a certain mass range. Finally, behind the last nozzle, the buffer-gas-cooled ions are ac-

---

[3] SAES Pure Gas Inc, San Luis Obispo, USA

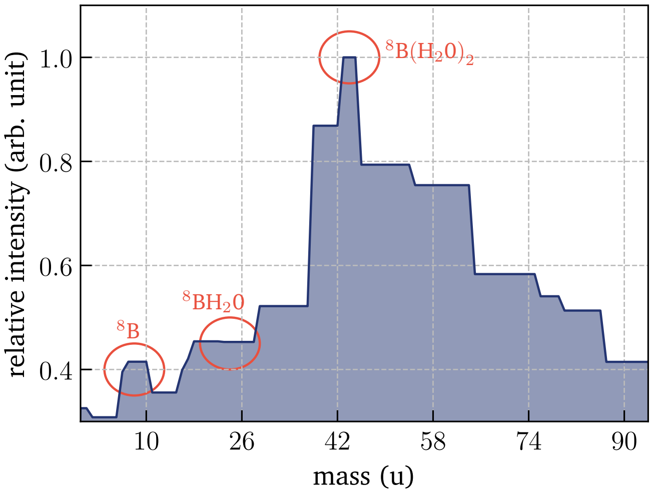

Figure 5.8.: A time-of-flight spectrum of the ejecta of the gas catcher. Ion bunches, which are emitted from the RFQ, are chopped in time segments to distinguish their mass. The small peak to the left can be attributed to ionic ^{8}B, while the dominant high-mass components fit well to boron-water molecular compounds originating from the gas catcher.

celerated into the electrostatic part of the beamline with a bias potential of −1.5 kV.

The last section of the RFQ can be used to form a longitudinal trapping potential, where the DC bias on the last electrode quadruple can be pulsed between two voltages to achieve bunching. This operation mode can be used to extract ions in a bunched mode into the beamline, which is useful to perform time-of-flight analysis of the molecule masses.

5.2.4 Molecule formation

In the deceleration process in the He gas of the PGC, the radioactive boron ions form molecular bonds with residual impurities in the stopping gas. Using the RFQ in a bunched mode for extraction of the particles, it is possible to record a time-of-flight spectrum. Shortly before a silicon detector, which detects the α-particles from the ^{8}B radioactive decay, an electrostatic steerer is pulsed between two voltages that either guide the ions on the detector (on) or away from it (off). This allows to cut certain time-of-flight regimes that correspond to a mass span from the bunch, and the corresponding rate on the silicon detector is measured.

Figure 5.8 shows the result of this measurement, which is already adapted to the flight path length to convert from TOF to mass. The resolution of this method is limited, but it indicates that most activity is observed at flight times that correspond to masses much higher than 8 u. Only a small amount is visible in the low-mass region of the spectrum that can be interpreted as ionic ^{8}B reaching the detector. The most probable molecular composition is ^{8}B(H$_2$O)$_2$, boron attached with two water molecules.

In several online experiments, the PGC and the subsequent RF transport was optimized to outlet an ionic ^{8}B beam, but no satisfactory rate of ionic boron was ever observed. The gas purity of the PGC plays the dominant role in the formation of molecules, but even the elaborate process of gas cleaning and heating out the gas catcher volume does not significantly increase the amount of “low-mass” ^{8}B in the beam. Furthermore, the RFQ is more efficient in transporting higher mass particles. The highest, most stable and least saturation-affected production rate was achieved in runs where the helium gas in the PGC was not purified at all, and the RFQ was deliberately set to transport high masses.

Finally, it was concluded that the most promising path is not to try to minimize molecule production inside the PGC, but instead, find an efficient and universal method to break up those molecules after ejection from the RFQ. The next section describes a system that was implemented to perform this task.

5.3 Molecular break-up

The molecular break-up system (MBS) is installed in one arm of a switchyard in the electrostatic beamline behind the PGC. The other arm leads to the beta-decay Paul trap. The molecular boron is accelerated to energies of up to 60 kV and shot on a nanometer-thin carbon membrane (CNM). At these relatively low energies, boron is transmitted while its electrons are stripped, in analogy to a similar process in much thicker stripper foils in high-energy accelerators. Since the molecules are bound to the atomic structure, these bonds will be broken as well. The transmitted boron beam experiences considerable angular and longitudinal straggling, which makes it unusable for electrostatic beam transport. To compensate, a second gas catcher (SGC) filled with helium catches the transmitted boron. The membranes also separate the gas catcher helium pressure from the UHV in the electrostatic section. From the SGC, the boron is extracted into an RFQ, which ejects the $^{8}B^{+}$ into the collinear beamline.

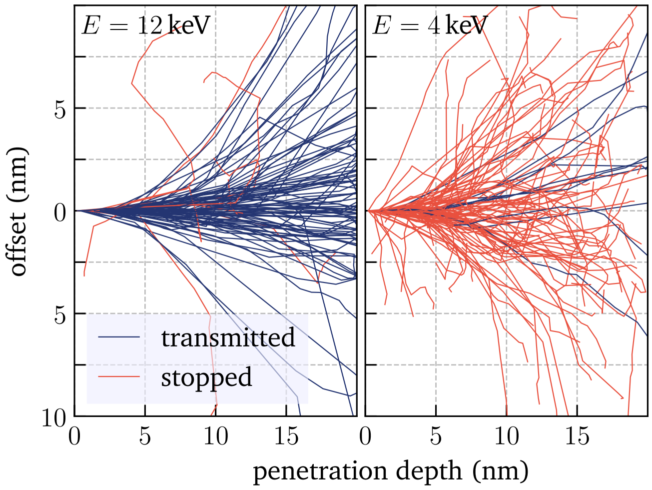

Figure 5.9.: SRIM simulation of transmission of ^{8}B through a 20 nm carbon membrane at 4 keV (left) and 12 keV (right). The trajectories of particles that are transmitted are plotted in blue, those of which are stopped inside the membrane are in red. These simulations qualitatively show that transmission is possible in this energy regime, but the exact parameters of the beam and the membranes need to be investigated carefully.

5.3.1 Transmission and break-up

The molecular breakup system, which is commissioned at the ATLAS facility, is based on several assumptions:

- ^{8}B can traverse the thin carbon foils, which is a question of the necessary energy and the actual CNM thickness.
- The molecular bond between ^{8}B and its attachments are broken up effectively while traversing the solid carbon matter of the CNM.
- The charge state of the transmitted ^{8}B is 1+, or it can be reached after transmission.

These constraints set by physics are highlighted here, followed by a technical discussion about the CNMs and the implementation of the molecular breakup station at ANL.

The range of particles in matter

The transmission of ions through matter is a well-researched topic with applications in many different fields. It is used at high-energy ion accelerator facilities to “strip” accelerated particles off their electronic shell and providing highly charged ions to experiments [112]. Another application, which became famous in recent years, is a form of cancer treatment [113] based on the stopping of ions in tissue.

The range of energetic ions in matter is limited and depends on factors such as the energy E, the velocity v and the nuclear charge Z of the projectile. The Bethe formula for non-relativistic projectiles

$$-\frac{dE}{dx} = \frac{4\pi n}{m_e v^2} \cdot \left(\frac{Ze^2}{4\pi\varepsilon_0}\right)^2 \cdot \ln\frac{2m_e v^2}{I} \tag{5.3}$$

describes this process, with m_e being the electron mass and n their density in the target [114]. I is a target parameter related to the ionization potential. Based on the Bethe formula (Eq. 5.3) and other refined models, SRIM[4] [115] is a software package that simulates the transmission of particles in solid matter and gases for a wide range of projectile energies and target materials.

Since the $^{8}BX^{+}$ molecules (X being a molecular attachment with mass M_X) are accelerated towards the membrane, only a portion $8/(8+M_X)$ is carried by the ^{8}B particle. Figure 5.8 shows a measurement that indicates

---

[4] Stopping and Range of Ions in Matter

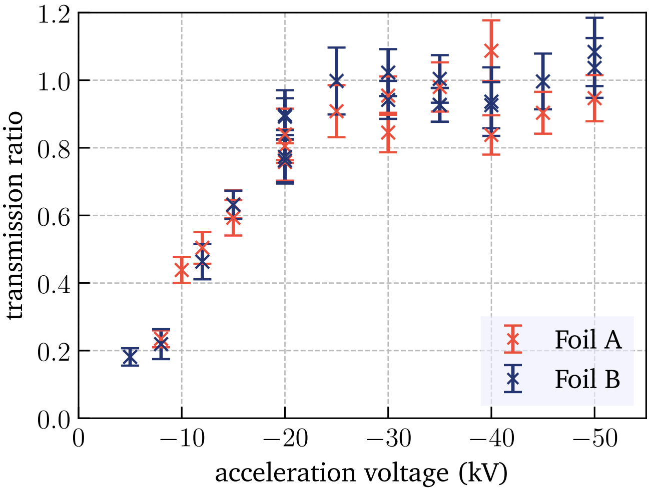

Figure 5.10.: The ratio between transmitted and stopped ^{8}B through two carbon nano-membranes (blue and red) increases with higher energies as expected. From approximately -25 kV on, a high percentage is transmitted. These measurements show the feasibility of the MBS approach and confirm the simulations.

that most of the boron molecules have a mass of 44 u, which results in 11 keV carried by the ^{8}B at −60 kV acceleration potential. Figure 5.9 shows the result of an SRIM simulation with a ^{8}B beam at 4 and 12 keV in a carbon membrane with a thickness of 20 nm. Only the higher energetic beam passes the membrane, showing that transmission of the beam at energies of tens of keV through such nanometer-thin membranes is possible, but a comprehensive analysis of their thickness is necessary.

In an experiment using the online molecular ^{8}BX beam, the transmission of ^{8}B through the used CNMs was confirmed [116]. Figure 5.10 shows the energy dependence of the transmission rate, which saturates at almost 100 % starting at −25 kV. This indicates that the CNMs are sufficiently thin and that the assumptions derived from the Bethe formula and SRIM also hold. The outgoing charge state of the transmitted particles was not tested in this experiment.

Molecular breakup

The paragraph above implicitly assumed that the projectiles molecule bond breaks up immediately on the entrance surface of the target. Only then the transmission of ^{8}B using its fractional energy carried in the compound can be explained. Since experimental results confirmed the transmission, this assumption seems to holds. Still, the actual deceleration process, which defines the range of ions in matter, can be investigated.

It is mainly sustained from nucleonic elastic collisions, like in Rutherford scattering. The Rutherford formula

$$\Delta E = \frac{4E_0\mu}{M_1+M_2}\sin^2\frac{\Theta}{2}\,[1] \qquad (5.4)$$

gives a relation between the energy loss ΔE and the scattering angle Θ, with M_1 and M_2 being the mass of the involved particles and E_0 the kinetic energy of the projectile. A collision with one target nucleus will lead to a break-up of the molecule since the energy transfer to one of the nuclei of the molecule is much larger than the total binding energy. This nucleonic part describes well those particles that experience large scattering angles and also have the biggest energy loss.

A second fraction is the electronic stopping power, which is a result of the interaction of the nuclear charge with the quasi-free electron plasma inside the carbon membrane. It can be shown that even for the thinnest layers of matter, the outgoing charge state is independent of the projectile charge state, which strongly suggests that the atomic structure is “reset” while transmitted through the membranes [117]. In a more figurative explanation, the components of the projectile are slowed at different speeds due to their nuclear mass and nuclear charge, which define their electronic interaction with the target. This immediately leads to spatial separation and splitting of the molecules, supported by the high kinetic energy of several keV compared to typical binding energies in the eV range.

Charge state after transmission

As stated before, the charge state of ions is reset when transmitted through a CNM, independent from its thickness. The electronic stopping power, which is based on the electronic interaction of target and projectile, is responsible for this process. For energies of a few keV per nucleon and following the results from Kallenbach et al. [118] shown in Fig. 5.11, about 1/3 of the transmitted boron is expected to be in the 1+ charge state, while the rest exits the membrane as neutrals. This portion increases with higher energies up to a certain point

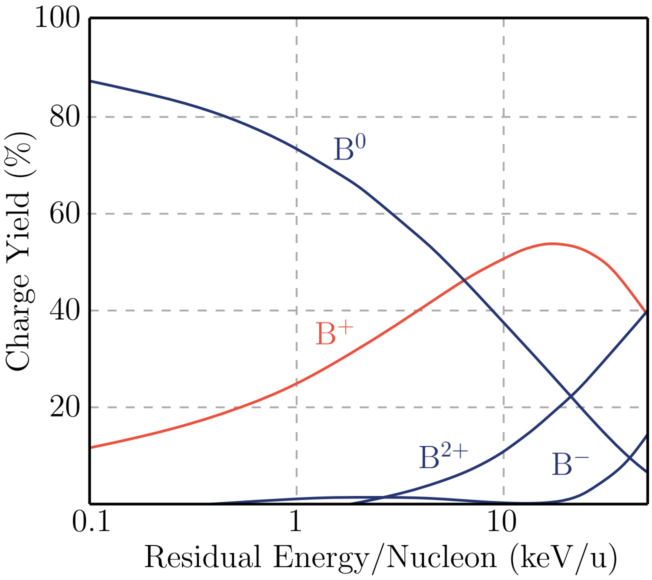

Figure 5.11.: The charge state of boron after transmission through a thin carbon membrane. For the residual energies of 1-10 keV/u, a fraction of 1/3 can be expected to be extracted in 1+ state. Note that the projectile residual energy per nucleon is plotted on the x-axis contrary to the total incident energy, which is used throughout the text, rendering the plotted curve independent from the foil thickness. This plot was taken and reworked from [118].

that will not be reached in the electrostatic acceleration of the MBS.

Neutral ^{8}B that leaves the CNM can still be ionized in the helium gas of the SGC. Since the ionization potential of helium is higher than the ionization potential of boron, the equilibrium state for boron in the helium-filled SGC is 1+, which should be reached by inelastic collisions in gas. The cross-section also increases with higher energies, which indicates that the highest possible energy should be chosen for transmission to obtain the highest fraction of 1+ ions in the gas catcher.

5.3.2 Nanometer membranes

The carbon nano-membranes (CNM) employed in the MBS are supported by a nickel mesh, which is applied on a metal ring similar to a washer. The rings have a thickness of 3mm, 19 mm outer diameter and 11 mm inner diameter, which is covered by the membrane. They are used to separate the vacuum of the electrostatic beamline from the gas catcher, and to break up the impinging molecules and transmitting the ^{8}B.

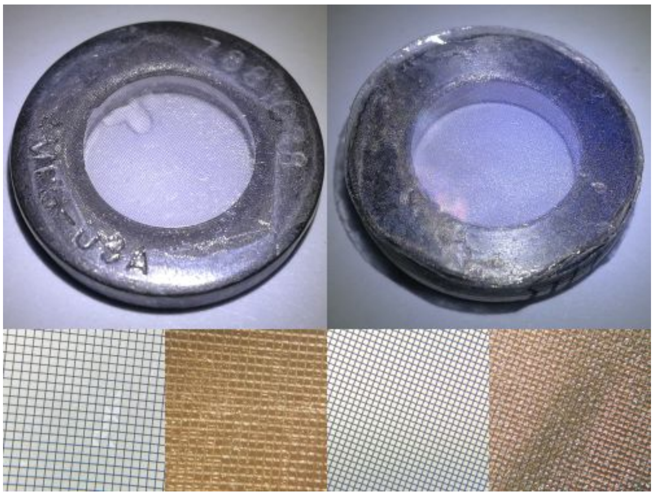

Figure 5.12.: Two types of carbon nano-membranes were used in the molecular breakup system. The outer diameter is 19 mm. Left: Type A showed tearing of several connected windows, which could, to some extent, be repaired by using vacuum glue as seen in the top left. Right: Type B membranes have a smaller mesh size with no or very few broken windows, but a rough surface structure. The lower pictures are photographed through a microscope at the same magnification.

The following constraints on the membranes can be deduced:

- The CNMs need to be thin enough to be able to transmit $Z = 5$ boron molecules. Simulations with SRIM show that the thickness should not exceed 20 nm to make transmission at up to 60 kV acceleration possible.
- The CNMs separate the gas-filled SGC from the electrostatic beamline. They have to withstand pressures of up to 50 mbar without tearing.
- The leak rate of the membranes should be marginal so that the pressure in the electrostatic beamline can be kept at a low level.
- They have to withstand continuous irradiation with the radioactive beam at high intensities without tearing or significantly changing their thickness.
- In the best case, they are easy to handle and even withstand several vacuum/air cycles without changing their physical properties.

The design thickness of the CNMs is 0.5 to 2.0 $\mu g\,cm^{-2}$, which translates into 2.2 to 8.8 nm for a density of $\rho = 2.3\,\mathrm{cm\,g^{-3}}$. This is suitable for the application, but “dead layers” of contaminant molecules are reported [119]. Since the composition and the thickness of these dead layers are not specified, the actual thickness of the carbon membranes was determined in an α-energy loss measurement [120]. This measurement yielded a thickness of approximately 15 nm, which is within the acceptable range for transmitting ^{8}B at the given energies.

The membranes sit on a 200 lines per inch (lpi) nickel mesh, where each square cell has an edge length of $\sim 125\,\mu\mathrm{m}$ and web thickness of $\sim 20\,\mu\mathrm{m}$ resulting in an open surface area of around 80 %. The mesh is necessary to stabilize the membrane over the inner surface area of the ring. Since the nickel has a considerable thickness, it is not open for transmission of boron. Thus, 20 % of the incoming beam will be lost. Since the beam spot is much bigger than the $\sim 1 \cdot 10^{-2}\,\mathrm{mm^{-2}}$ windows in the mesh, the beam will be distributed across many carbon membrane windows.

Some of the windows in the membranes were torn. The best membranes with the fewest torn windows were used for tests with the gas catcher. Also, the membranes could be repaired with vacuum-compatible epoxy resin when the defects were on the outer edges. The achieved pressures in front of the SGC suited well with the total area and the expected airflow. This was tested with high pressures of up to 50 mbar, which were held by the membranes without lasting damage. The membranes can hold several days of continuous irradiation with high beam currents, without altering the leak rate, as indicated by stable vacuum conditions.

5.3.3 Acceleration

In the electrostatic beamline behind the RFQ, the boron molecules are transported on a −1.5 kV bias. To traverse the CNM, energies of several ten kiloelectronvolt are needed. The SGC and the membrane, which separates the gas volume from the vacuum in the electrostatic beamline, sits on a high voltage platform biased with up to -60 kV, together with the entire molecule breakup station and the attached collinear beamline.

The transition between the section biased with −1.5 kV and the SGC at up to −60 kV needs to be designed carefully, not least because the space in the experimental hall is limited. Apart from this constraint, the following requirements need to be fulfilled:

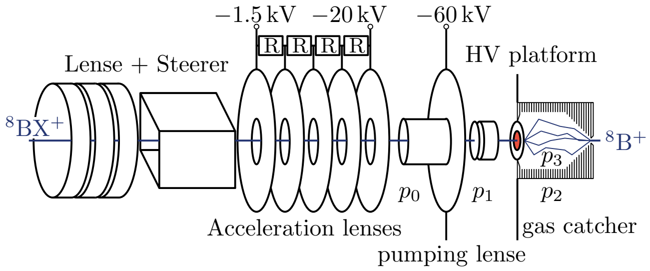

Figure 5.13.: Scheme of the acceleration stage, starting from the electrostatic beamline, which lies at -1.5 kV. After passing a lens, the beam is accelerated towards the HV platform with a set of concentric cylindrical lenses, which are connected via a high-voltage-resistor chain, supplying a gradual potential increase. The section is differentially pumped through the pumping lense providing $p_0 < p_1$

- The ^{8}B beam needs to be accelerated to a small spot, independently of the total potential difference, which can range from −30 to −60 kV.
- The membranes have a considerable leak rate, which requires a pump system strong enough to generate UHV in the acceleration section to avoid collisional ion losses.
- A movable silicon detector needs to be placed in front of the membrane to allow diagnosis.
- The membrane should be exchangeable and also be removable from the SGC opening to have more experimental flexibility and allow pumping.

The solution is depicted in Fig. 5.13, which shows the scheme of the acceleration stage. The acceleration is done via a set of concentric cylindrical electrodes, which are connected via a chain of high-voltage ceramic resistors. The highest voltage on the last electrode is set to −20 kV independently from the platform voltage. It allows focusing the beam onto the membrane at every possible platform voltage.

Two pumps are installed: One is on a cross just before the acceleration lenses, and another pump is directly in front of the membrane. The volumes are separated by the acceleration lenses and the pumping lense, which have small apertures to allow differential pumping. The pumping lense is also the last electrode for the acceleration and is set to −60 kV. For typical leak rates of

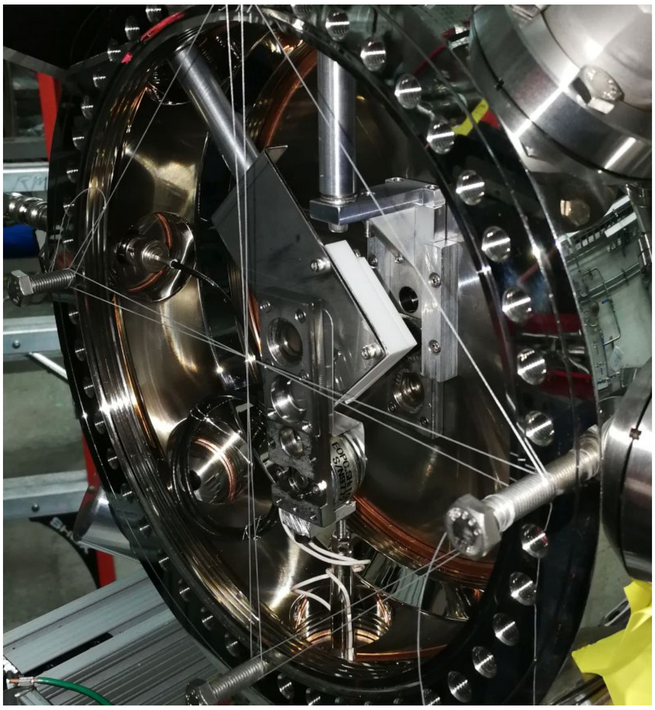

Figure 5.14.: Photograph of the entrance side of the SGC. In the octagonal extension piece, three linear feedtroughs hold the membrane ladder, a silicon detector and a test station for membrane transmission measurements. The other ports are allocated to vacuum gauges and a turbopump.

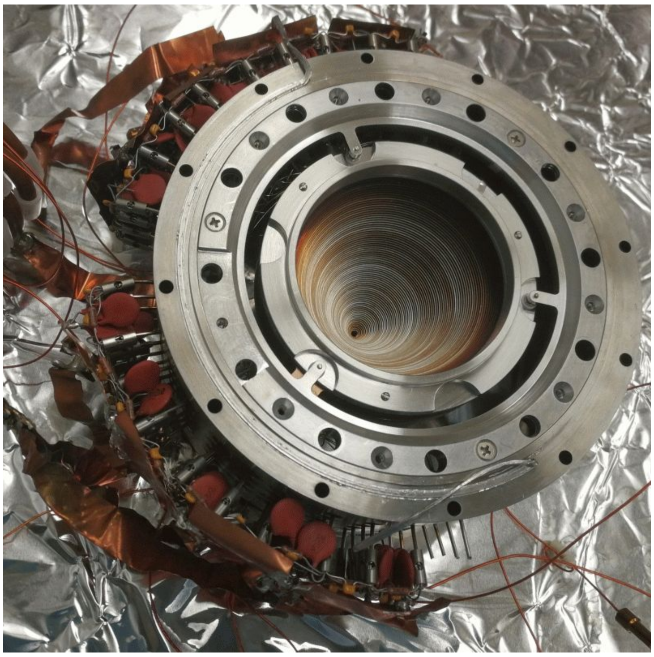

Figure 5.15.: The cone of the secondary gas catcher sits on top of the body and guides the ^{8}B ions to the nozzle. The RF carpet electrode structure, which prevents space charge pile-up in the nozzle region, is visible. On the outside of the structure, the RF and DC are coupled to provide the necessary combination of DC and RF field.

the membranes and pressures of 5 mbar inside the gas catcher, 10^{-4} mbar can be reached just in front of the membrane, which is sufficient to transport ions across the small distance.

The vacuum equipment is installed on an octagonal CF (Conflat®)-200 extension piece, which has eight CF-40 ports, as shown in Fig. 5.14. One port is equipped with a motorized linear feedthrough, which moves a target ladder in front of the SGC front opening. Two positions in this ladder are equipped with membranes, and one is left “open”. The ladder seals against the flat surface of the SGC with rubber gaskets. Another motorized linear feedthrough moves a silicon detector in and out the beam path to allow diagnosis. On another port, a membrane test station is installed, which allowed the first direct ^{8}B transmission tests.

5.3.4 Second gas catcher and RFQ

The second gas catcher follows the design principle of the PGC with the difference that it needs to stop and forward ions that enter with a much lower energy of several kilo- instead of megaelectronvolts. Its volume is significantly smaller, with ~ 15 cm length and 7.5 cm diameter. The body part is equipped with RF carpet electrodes, which allow running at higher frequencies than the PGC since the capacitance of the smaller electrodes is smaller as well, which helps to transport lighter ions. The extraction region of the gas catcher, shown in Fig. 5.15, is a nozzle with a conical RF field applied, which prevents the ions from collisions with the walls. Over the entire gas catcher and the nozzle, a DC gradient of ~ 200 V is applied in addition to the RF to establish a fast extraction from the gas catcher.

To provide enough stopping power over a few centimeters, the SGC is filled with up to 5 mbar helium gas from a clean and purified gas line. The SGC has two openings. The entrance is sealed by a CNM in normal operation, while the exit is a small nozzle. The CF-200 cross that contains the SGC is pumped with a high-flow rate pump from Osaka Vacuum[5]. This establishes differentially pumped vacuum regions inside and outside the SGC. Stopped ^{8}B ions that leave the SGC are fed into

---

[5] Osaka Vacuum LTD, Osaka, Japan

an RFQ ion guide, which will be installed behind the SGC nozzle. The RFQ will be separated into two parts by one nozzle, providing differential pumping in the two regions. The second region with better vacuum conditions will be split in shorter electrodes that can form a trapping potential. From this trap, the ^{8}B will be ejected in bunched operation mode towards the electrostatic laser spectroscopic beamline.

5.3.5 Alternative approaches

The MBS system between the production and the laser spectroscopy beamline required a considerable amount of development and investment. There are other solutions to break up radioactive molecules in an RF-guided or electrostatic beam, but none of them are established for light isotopes. The constraints are the required high efficiency, universality and the possibility of a bunched and cooled release of the stripped, singly-charged particles.

RFQ breakup

The SHIPTRAP experiment [121] uses a voltage step in an RF guide to rid the isotopes from molecular bonds. A $\sim 140\,\mathrm{V/cm}$ electric field gradient is applied behind a nozzle, leading into a region with 10^{-2} mbar. The particles are stopped immediately again by collisions with the gas and thereby lose the molecular attachments, which usually have much less binding energy than the few 100 eV generated by the acceleration.

The most significant difference to the “SHIPTRAP method” is the relatively high mass of the particles. SHIPTRAP investigates superheavy elements, which are in the 250 u mass region. Naturally, in molecular bonds with water, the water constituents are much lighter and are stripped in the dissolving inelastic collisions with the gas, while the inert high-mass particle stays on its trajectory less affected.

In the case of ^{8}B with one or several water molecules, the boron isotope is much lighter than H_2O (18 u) and is therefore much more prone to being stripped and lost due to a “bad” trajectory in the RF. In fact, in several online beam times, this technique was tested in different sections of the RF guide system. The beam rate, measured by ^{8}B 2α decays, always decreased by introducing even much smaller voltage steps, but no noteworthy change in mass distribution was observed. To prevent this, it might be possible to redesign the RFQ system in a way that is more efficient in catching the products from the break-up.

One approach is to set up a gas catcher inside the RFQ system, behind the first nozzle. The pressure conditions are similar to that of the SHIP setup. Instead of the RFQ guide, the ^{8}BX molecules are accelerated into an open catcher section with a much higher acceptance volume, which is designed to transport low masses. The transport inside this gas catcher is again established by airflow and DC gradients assisted by an RF carpet. Behind this new, small gas catcher, the ^{8}B is ejected into the last stage of the existing RFQ.

ECR or EBIS

Another possibility is the injection of the molecular beam into an electron-cyclotron resonance (ECR) source or an electron-beam ion trap (EBIS), where an inert gas or electron plasma interacts with the injected particles. In both cases, this would immediately break up the molecules. It is uncertain if the light ^{8}B stayed confined after the break-up. In general, heavier isotopes supplant light ones in such charge breeding devices. Also, the energy width of the ejecta is high, and high-precision collinear laser spectroscopy has not been performed on ions directly from an EBIT or ECR. Lastly, since the charge breeding process is continuous, it could be challenging to extract the highest fraction in the desired 1+ charge state.

MCPs instead of carbon membranes

In case the carbon membranes turn out to not transmit the boron efficiently in the 1+ charge state, and reionization in helium gas behind the CNM does not work, an alternative to such membranes is to use of special multi-channel plates. In the small but elongated holes of these MCP’s, no laminar flow can establish and thus, they can separate the gas catcher helium pressure from the ion optic beamline.

The boron molecules shot into these tiny holes in forward direction collide with the helium gas atoms directly. Effective molecular break-up into a singly charged state in collisions with helium has been shown for a LiOH^+ beam in a gas-filled penning trap at sufficiently high energies of several 100 eV [122]. This is evidence that the breakup in molecular ion-gas collisions also works for light ions, given that they stay confined after the breakup. The MCP approach allows high beam energies and can more easily be implemented into the existing MBS system. The open area of these MCPs is in the order of 50-60 % and thus within the acceptable range for the experiment, given an efficient transport through the gas catcher.

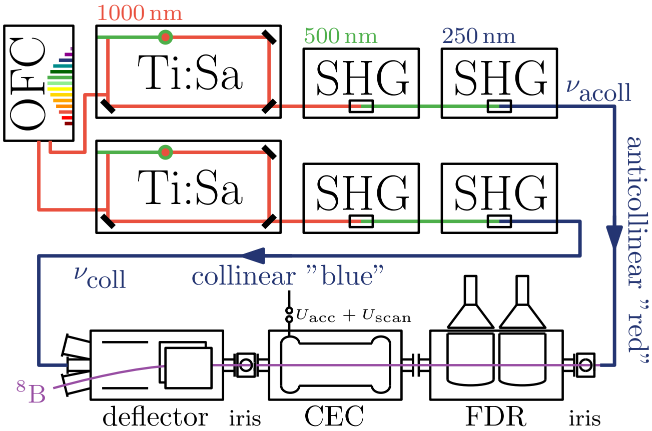

Figure 5.16.: A scheme of the lasers and the collinear beamline. The beamline consists of an ion optical deflector, a charge exchange cell and the fluorescence detection region bordered by two irises. The laser light for collinear and anti-collinear direction is generated in two independent, optical-frequency-comb-stabilized, frequency-quadrupled titanium-sapphire laser systems.

5.4 Collinear setup

The collinear beamline and the laser system is shown schematically in Fig. 5.16. The main components are an ion-optic 10° deflector, a charge-exchange cell (CEC) and a fluorescence detection region (FDR). The latter two are bordered by two iris systems, which allow a precise overlap of ion and laser beam. It is commissioned at ANL in an offline laboratory separately from the ATLAS ^{8}B source, with a beam from an offline ion source.

5.4.1 The TRIGA beamline

The beamline at ANL was initially situated at the TRIGA reactor at the Johannes-Gutenberg Universität Mainz. It was set up 2008-2011 as a prototype for the LASPEC[6] beamline at FAIR[7] [123, 124] and also served as a general test stand and development platform for collinear laser spectroscopy experiments. In this role, many advances were made, such as the implementation of a mirror-based detection system [125], a charge exchange cell [123] and the novel, versatile data-acquisition system TILDA[8] [126], which is specially designed for

---

[6] Laser Spectroscopy at FAIR

[7] Facility for Antiproton and Ion Research in Europe, Darmstadt, Germany

[8] TRIGA Laser Data Acquisition

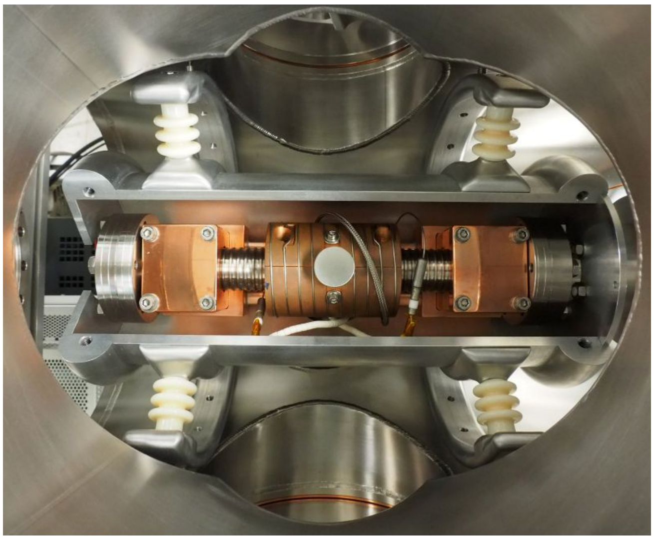

Figure 5.17.: View into the charge exchange cell from the top. An alkali metal is inserted into the chamber in the center and is heated to its vapor temperature, generating an alkali atmosphere that neutralizes the passing beam ions.

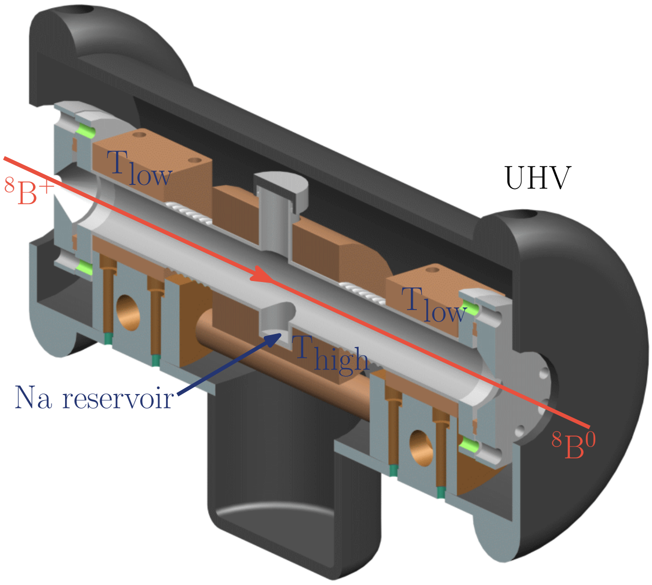

Figure 5.18.: Working scheme of the charge-exchange cell. Sodium is vaporized in the hot center of the region. It condenses on the cold surfaces and flows back into the reservoir. Ions that pass the sodium vapor are neutralized with high efficiency.

collinear laser spectroscopy. Many of these important developments were gradually adopted by online facilities such as BECOLA[9] at NSCL[10], COLLAPS[11] and also the KOALA[12] beamline in Darmstadt. Nevertheless, in 2016 the beamline in Mainz was disassembled and shipped to Argonne National Laboratory for the laser spectroscopic measurements of the boron and palladium isotopic chain. Many of the components were revised or replaced, but the structure, many components, hardware and laboratory equipment remains the same.

5.4.2 Charge-exchange cell

The charge-exchange cell, pictured in Fig 5.17, converts the ionic beam into a neutral atom beam. The potential that the ions experience in the cell while being neutralized determines the resulting atom velocity during the laser interaction. Thus, the cell is scanned in the laser spectroscopy scheme to Doppler-tune across the atomic resonance.

In the cell, an alkali metal (here, sodium), is inserted into a reservoir and heated up to a temperature of ∼ 550 K. This locally generates an alkali vapor atmosphere with a pressure of several in the beamline. Next to the hot alkali region, two cooling blocks are held on a temperature that allows the sodium to condensate. A stainless steel wire mesh distributes the liquid alkali metal across the region and allows it to flow back into the reservoir. Figure 5.18 shows the principle of this operation. The ion beam passes through this region. In principle, the same chemical considerations that prevent the boron ions in the gas catcher systems to neutralize in the helium gas apply here in the opposite way. As listed in Tab. 5.1, the ionization potential of sodium is lower than that of boron, which makes the reaction

$$B^+ + Na^0 \rightarrow B^0 + Na^+ \tag{5.5}$$

energetically favored by ∼ 3.16 eV.

This technique to neutralize a beam is widely used and confirmed, in particular in many experiments at COLLAPS and CRIS[13] [127], BECOLA [128] and at TRIUMF[14]. The reported efficiencies are high and reach up to 50 % even for light isotopes such as fluorine, without introducing significant angular deviation of the beam even for low-mass isotopes [129].

---

[9] Beam Cooler and Laser spectroscopy

[10] National Superconducting Laboratory, East Lansing, USA

[11] Collinear Laser Spectroscopy at ISOLDE-CERN

[12] Kollineare Apparatur für Laserspektroskopie und angewandte Wissenschaften

[13] Collinear Resonance Ionization Spectroscopy at CERN-ISOLDE

[14] Tri University Meson Facility in Vancouver, Canada

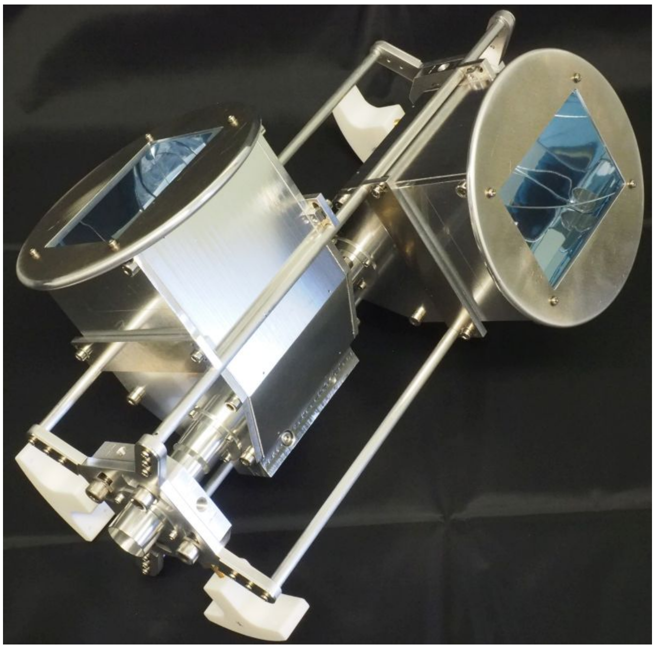

Figure 5.19.: The fluorescence detection region deployed in the collinear beamline, mounted outside the vacuum chamber. It allows background light suppression with non-linear optics. Details can be found in the text and in chapter 6, which describes the design and evaluates the performance of this setup.

In the non-resonant process, the electron configuration will be established in a "random" fashion, meaning that both the boron ground state $^2P_{1/2}$ and the $^2P_{3/2}$ level will be populated in the process. Transitions between these two levels are forbidden, and the decay from the excited $^2S_{1/2}$ to the $^2P_{3/2}$ level has a factor two higher transition rate. Thus, it might turn out that the population of the two states is inverted. The level population has to be investigated in-situ with a boron beam in the charge exchange cell. Since this determines the number of boron atoms that are available in the right atomic state, the results of this assessment have a significant effect on the total efficiency estimates.

5.4.3 Fluorescence detection region

The fluorescence detection region (FDR) is the second key component of the collinear setup, which is installed after the charge-exchange. In the 30 cm-long FDR, a sophisticated mirror system is installed that forwards photons emerging from the beam to photomultiplier tubes (PMTs), which are located behind vacuum viewports outside the vacuum chamber. The detection efficiency, which in the simplest terms is the number of resonant photons that are detected per passing atom, is the critical parameter of this system. With the help of non-imaging optical components, it is possible to discriminate those photons that do not emerge from the beam axis. This is a helpful tool to reduce the amount of laser stray light that arrives in the PMTs.

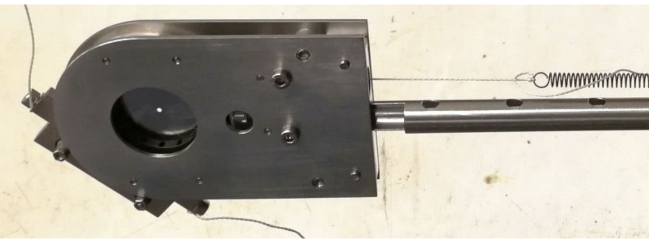

Figure 5.20.: Two irises are installed in the beamline to provide overlap between the atom and the laser beam. The iris can be actuated steplessly from outside the vacuum chamber. The spring provides the necessary reset force and allows almost hysteresis-free movement. The setup is mounted on an adjustable bellow, which can be adjusted to the beam axis with high precision and without breaking the vacuum.

Figure 5.19 shows a photograph of the FDR unmounted from the vacuum tube. Much work has been dedicated optimizing the performance parameters of the region to be efficient and well-working for the 250 nm radioactive ^8B beam at low rates. Different versions of the FDR, optimized for other beams and wavelengths, were installed at the collinear beamline KOALA in Darmstadt and the BECOLA setup. The function and performance are presented with much more detail within this work in chapter 6.

5.4.4 Iris aperture

One of the key challenges of laser spectroscopy is to have a perfect spatial overlap of particle and laser beam. The smaller and more precisely the beam diameters can be matched, the higher is the laser-field energy density and thus the efficiency of the detection. This can be understood since more particles of interest can be excited to the probe state with a lower laser power, which causes less background on the detector. An angular offset of these two beams results in a shift in observed frequency due to the Doppler effect. Thus, it is inevitable to align both laser and particle beam along the same beam axis that is defined by the ion-optical components inside the vacuum chamber. To assist this alignment, the use of irises has become customary. In the Argonne beamline, two irises, one of them depicted in Fig. 5.20, are installed between the ion optic deflector and the charge exchange cell and after the detection region close to the exit viewport, covering a distance of 1.2 m. The irises can be aligned with an adjustable bellow from outside vacuum to the beam axis defined by the elements in between.

A sophisticated wire rope system, bedded on vacuum-compatible ball bearings, allows actuating the iris steplessly from outside the vacuum chamber with a linear motion feedthrough. A spring provides a reset force that pulls back the lever and is strong enough to prevent hysteresis. The inner diameter of the iris is adjustable from 1 to 19 mm, which allows adjusting typical beams with diameters of 2-4 mm. The stepless actuation helps to cut off stray light in the actual experiment, after alignment.

5.4.5 Offline ion source

For a laser spectroscopic isotope shift measurement, it is essential to measure ν_0 of at least two isotopes under the same experimental conditions to extract a meaningful result. This is especially important for light elements such as boron, since the field shift to mass shift ratio is small, making them vulnerable for systematic errors. Since boron is a light element, even small forces acting on the particles will result in significant velocity changes.

At ATLAS, only ^{8}B is produced in an in-flight scheme, and no reference isotope emerges from the production section. An offline boron source needs to be installed in front of the SGC to feed ^{10}B and ^{11}B into the gas catcher and the subsequent cooler/buncher. Since the stable boron is emitted from the source in ionic form without molecular bonds, it will traverse the CNMs just like the ^{8}B beam. The SGC resets the beam properties, and the cooler/buncher will emit all three isotopes ^{8,10,11}B from the same potential with the same kinetic properties.

The offline source can also be used to commission the collinear beamline and the laser system independently from the SGC and the cooler/buncher. Therefore, it is attached to one of the two ports of the 10° deflector. The stable beam can then be fed into and probed directly in the beamline. To perform spectroscopy both in offline and in online configuration, the source must fulfill several constraints:

- The rates of the source have to be considerably high to allow relatively quick reference measurements in the online experiment to waste as little ^{8}B production beam time as possible.
- The source should reliably run over days or have a short and unproblematic re-activation cycle.
- It should be possible to create ions of different species: at least calcium for commissioning and then palladium and boron for spectroscopy.
- Emittance is not a big concern in the “online”-setup, as long as high rates compensate losses in the short transport route to the SGC. However, for offline spectroscopy, especially the longitudinal emittance should be small to be able to resolve the optical HFS spectrum.
- Alternatively, a bunched emitting mode allows to time-correct for different velocities within one bunch.
- Since the space in all experimental sections is limited, the source should, in the ideal case, not require a separate high-voltage platform or any more elaborate gas-handling system.

In the course of the experimental preparations, two different approaches were followed. The first approach was based on a heated carbon oven filled with boron powder. The emitted atoms were ionized with an electron filament. This turned out to be unstable, and the rates were insufficient. For this reason, a laser ion source was implemented, which became the optimal solution for offline commissioning and as an online reference source.

Laser ablation ion source

A laser ablation ion source, similar to the design proposed in [130], was installed and tested at the KOALA setup in Darmstadt. With a simple design shown in Fig. 5.21, it was possible to extract ions of several different species into the collinear beamline in bunched mode. To do so, a 5 mJ pulse of a 1064-nm laser is focused through a viewport onto a target, consisting of a small solid piece of the element to be ionized, situated

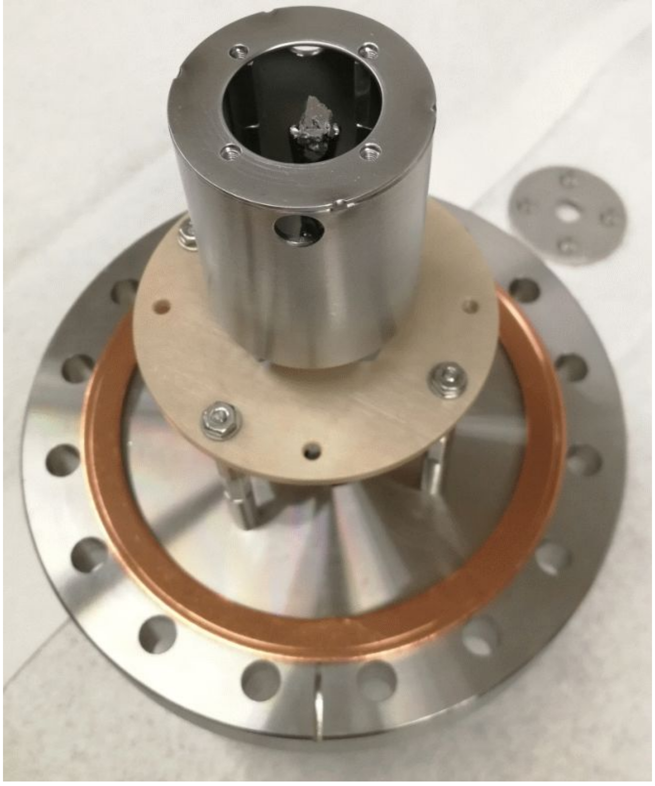

Figure 5.21.: The disassembled laser ablation source. The laser is focused through the hole in the side of the cylinder onto the target (Here: calcium). The unmounted front plate can be seen in the background. The diameter of the extraction hole influences the performance of the source.

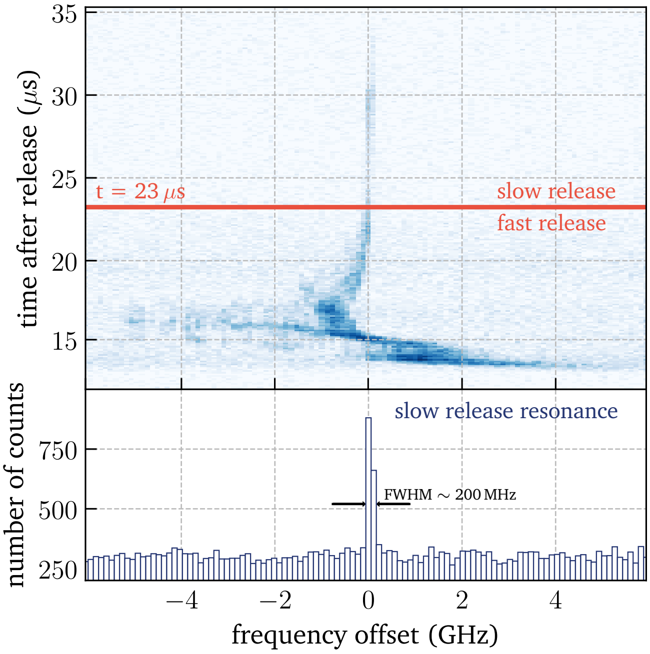

Figure 5.22.: The time and frequency spectrum of the beam generated with the laser ablation source. It can be separated into two time intervals before and after $t = 23\,\mu s$. The latter part can be used directly for collinear laser spectroscopy, the earlier part only when cooled in a buncher beforehand.

inside a short tube that sits on the acceleration potential. At the front of the tube, an endcap with an aperture is installed. A high negative potential is applied to an extraction electrode in front of this tube. This extraction field penetrates the laser ablation region and pulls ions out that are generated in the laser field.

At TU Darmstadt, this source was tested with an adjacent time-of-flight measurement to identify the generated ions by their mass-dependent flight time to a Faraday cup. Ions of boron, calcium, palladium, and many more were successfully injected into the beamline. The source was then rebuilt at ANL and commissioned at the collinear beamline with calcium ions.

Figure 5.22 shows a typical time-resolved laser spectroscopic resonance profile of ionic calcium. The laser frequency was Doppler-tuned across the D1 line by scanning the voltage of the fluorescence detection region. The intensity profile corresponds to the number of photons detected in the frequency/time bin relative to the trigger of the pulse laser. The time spectrum can be separated into two parts: In the first 10 µs after the first fluorescing ions arrive (13-23 µs), their velocity distribution is broad, and the center energy shifts by several 100 V within short intervals of microseconds. It should be noted that not every laser pulse produces the same fluorescence pattern, which implies that the ion-energy distribution changes from laser pulse to pulse.

This “fast release” region can be explained with calcium ions that leave the target surface and directly find the exit of the source region without thermalizing in the volume. Since the pulse laser generates hot plasmas with a considerable amount of internal energy, the ions do not have a homogeneous velocity distribution. This part of the spectra cannot be used directly for the precise collinear laser spectroscopy since the remaining peak widths correspond to several gigahertz, and the center is shifting from shot-to-shot. However, in online experiments, the stable beam is fed into a cooler/buncher system to obtain the same properties as the radioactive isotopes from the online source. It should be possible to trap and also use this portion of the beam by cooling and bunching it before extraction, given that it can be transported to the bunching system.

In direct collinear laser spectroscopy, e.g., for offline commissioning beamline elements such as the fluorescence detection region, the charge exchange cell or detector systems, the second time interval of the beam, starting at $\sim 23\,\mu s$ can be used. Here, ions leave the source region with a uniform velocity that corresponds to the source potential. These are ions that are extracted slowly from the source a long time after the ignition of the pulse laser plasma. The resonance generated from this "slow release" is shown in the lower part of Fig. 5.22. It exhibits a relatively small width and thus confirms a homogeneous starting potential.

Although the number of ions produced in "slow release" is much lower than in the fast process, the total number is sufficient to acquire a spectrum within a few scans. The number of ions and photons detected on resonance varies from shot-to-shot, but the position of the signal does not change. For commissioning, a measurement of the charge content of each shot needs to be implemented to normalize the photon count rate. To avoid saturation of the charge exchange cell, gating out the ions that are generated in the "fast release" with an ion optical beam switch is advisable.

The size of the extraction hole (see Fig. 5.21) plays a significant role in the ratio of ions extracted in the fast and the slow expulsion. Reducing the diameter from 7 mm to 3 mm provided a significant increase in slowly released ions. Even smaller diameters could improve this even more. Similar results were found at KOALA in Darmstadt.

Overall, the laser ablation source has a high rate, is simple to start up on occasion, and provides sufficient beam properties for offline setup as well. The bunched mode eases laser spectroscopy, and it versatilely allows different elements to be used. Finally, the source setup is small and fits within a CF-100 four-way cross. The pulse laser can be guided onto the target from outside the high voltage platform over several meters, which allows fitting the source even in tightly spaced areas.

5.4.6 Laser system

The 250 nm $2p \rightarrow 3s$ ground state transition of boron is tested in the isotope shift measurement. Since the atomic beam is probed both in collinear and anti-collinear alignment, two different frequencies need to be generated that are offset by several THz due to the large and opposite Doppler shifts for the two alignments. Doppler tuning allows the laser systems to run at fixed frequencies throughout one measurement, which in general is a much more stable operation mode than scanning. Also, monitoring and referencing the frequency is much easier for stable-frequency lasers.

To generate the laser beams with the right wavelength for the collinear and the anti-collinear measurement, two Sirah Matisse® Ti:Sa laser systems will be set up in parallel. Both of them will then be fixed independently on a mode of an optical frequency comb by using two beat-detection units and the second harmonic pattern of the comb output. A rough scheme of the laser setup is provided in Fig. 5.16.

At this time, the laser system is not yet installed and tested at ANL, where most of the commissioning is done with calcium beams, which are easier to generate, and the ground state transition lies at 393 nm. Still, the fourth-harmonic generation from 1000 nm to 250 nm was successfully demonstrated at TU Darmstadt for the offline experiment, which will be presented in chapter 7. The frequency comb stabilization of two Ti:Sa laser systems were successfully implemented while generating two laser beams at 230 nm at TU Darmstadt for the spectroscopy of In^+ ions [102].

On a more practical note, it is not yet clear if the complete laser system fits in the limited space of the experimental hall. The most straightforward solution to bypass this problem is to use fiber optics between the Ti:Sa and the first SHG cavity, or in between the two SHG cavities to separate the fundamental laser system from the much smaller coupling stages in front of and behind the beamline. This solution would also bring the advantage that the laser system could be placed in a dedicated laser operation area with temperature and humidity stabilization. On the downside, the power loss usually accompanied by fiber transport is significant. Generating a sufficient amount of stable 250-nm light while using a potentially long fiber in the system is close to the specification margins.

5.4.7 Static potentials

It is favorable to accelerate the ions to several tens of keV to reduce the Doppler-broadening of the line width caused by the thermal atom distribution. Furthermore, it is preferable to keep the laser at a fixed frequency. For scanning the resonance, the potential applied to the charge-exchange cell is varied, which effectively translates into scanning the observed frequency in the rest-frame of the atoms due to the Doppler effect.

The electrical potentials applied in the beamline, therefore, have to facilitate a variable, scannable acceleration voltage for the ions. The molecular ions leave the RFQ behind the PGC on zero potential and are transported inside a negative −1.5 kV beamline. Then, they are accelerated to up to $U_{\mathrm{MBS}} = -60\,\mathrm{kV}$ into the SGC, which breaks up the molecules, and, at the same time, resets the beam properties. Thus, the ions that are ejected from the SGC via the second RFQ cooler/buncher system have zero velocity but are situated on the U_{MBS} potential.

From here, they need to be accelerated again to energies of 30 keV inside the CEC. To facilitate this, the beamline adjacent to the second cooler/buncher is set on the same U_{MBS} platform as the MBS, with a small transport potential offset of several kilovolts. The charge-exchange-cell is then biased with up to $U_{\mathrm{acc}} = -30\,\mathrm{kV}$ relative to U_{MBS}, adding up to −90 kV. Since it is difficult to apply such high potentials internally and the setup is situated on a high-voltage platform already, the entire second half of the beamline is set on to U_{acc}. The scanning is then performed by adding another small voltage U_{scan}, which can be scanned from −500 V to +500 V.

The downside of this approach is that the beamline is entirely on high voltage of up to $U_{\mathrm{tot}} = U_{\mathrm{acc}} + U_{\mathrm{scan}} = -90\,\mathrm{kV}$, making it mechanically inaccessible during the scans and demanding a sophisticated high voltage (HV) cage design. However, the setup needs remote controls anyhow due to the high neutron radiation levels in the experimental hall. The electronics and devices to remote-control everything on the platform are all readily available. Setting up a 90 kV HV platform is technically difficult but has been done in several other experiments before.

5.5 Efficiencies

The parameters of the setup, which is being commissioned, allow estimating the ^{8}B beam rate that can be expected in front of the photon detectors. On the other hand, the parameters of ^{8}B itself and comparison with similar laser spectroscopic experiments allow estimating the rate necessary or reach similar results. This examination of the efficiencies in the apparatus from target to recording a resonance is thus split into three parts.

- The ^{8}B production efficiency in the target, including stopping in the PGC.
- The transport of the particles to the photon detectors, including preparation in the atomic state.
- The spectroscopic efficiency, which determines how many particles are needed to obtain a dataset with the required statistical uncertainty.

5.5.1 Production

The maximum ^{8}B rate that was ever observed in the system was ∼15 kcts/s on October 23rd, 2017, measured by its decay on a silicon detector. The beam current was 1000 nA Li^{3+} primary beam current, which corresponds to $\sim 2.1 \cdot 10^{12}$ particles per second. It is possible to increase the beam current even higher; the current maximum is set to 1450 nA limited by the allowed radiation levels in the adjacent experimental areas.

This rate can be cross-checked with the production estimates and results during the first commissioning phase of the target section, which did not introduce a gas catching system. The first calculations for the efficiency in the $^{3}\mathrm{He}\left({}^{6}\mathrm{Li},{}^{8}\mathrm{B}\right)\mathrm{n}$ reaction predicted a cross-section of 4 mbarn at the available beam energy, with 1 mbarn integrated over the acceptance angle and energy of the setup. This corresponds to 3 ^{8}B per particle-picoampere that could be forwarded into the PGC, which was not built at that time. In the experiments following after, rates of 2 ^{8}B/ppA were found. With the target mass thickness 2.1 mg/cm^{2} for the LN2-cooled ^{3}He target, derived in Eq. 5.1, this calculates to an approximate reaction cross-section of

$$\sigma = \frac{2\,{}^{8}\mathrm{B}}{1\,\mathrm{ppA}}\,\frac{m_{^{3}\mathrm{He}}}{d} = 0.77\,\mathrm{mbarn}\,, \qquad (5.6)$$

which is well in agreement with the prediction from [108].

The cross-section corresponds to a rate of ∼700 kcts/s at 1000 nA primary beam current without the gas catcher system. This leaves a factor of 15/700 = 2 %, which can be attributed to the PGC stopping, cooling and transport efficiency. This is well in line with expectations of 0.1 % to 1 % for such systems used for stopping diverge high-energy beams, as stated before [131]. Many improvements and changes were implemented to the target system, not least the stirrer for ^{3}He circulation. The absolute values and efficiencies are thus to be regarded with caution. Nevertheless, they show that the system works as expected, and no significant improvements should be expected from the target alone, without fundamental changes in its parameters.

The most significant finding regarding the production efficiency was that the exact primary beam energy stands out as the most sensitive parameter. The ATLAS operators perform an exact time-of-flight energy measurement and correction before delivering the requested beam on the target. Still, the parameters of the production/target/PGC system are folded with each other. A particular SCS magnetic field might work better or worse in combination with different beam energies or PGC gas pressures.

In the following analysis, the production rate of 15 kcts/s in front of the RFQ transport is used, since this value was observed and can be reproduced for a measurement. Since the primary beam rate can still be increased even within the momentarily allowed limits, there might be some potential for improvements.

5.5.2 Particle transport

The particle transport efficiencies are summarized in Tab. 5.2. After the production and PGC, they can be disentangled since there are silicon detector diagnostic stations along the way, which allow measuring the incident ^{8}B rate. The highest measured rate on the detector station after the PGC nozzle was 15 kHz and is set to 1 for a relative comparison.

The transport through the RFQ was optimized in several beam times. The maximum rates on its exit side relative to the PGC nozzle were about 2/3. The loss is due to some remaining mass selectivity in the RF systems, which favor one of the two molecule configurations of ^{8}B. This 2/3 was only reached when the frequencies and amplitude of the RF guide were adapted to favor the transport of high masses, which led to the implication that breaking up the molecules in a separate setup is easier than preventing their production.

Table 5.2.: Overview of the transport efficiency along the beamline. Each column gives a value for the different segments, and a value cumulated starting at the first nozzle. More details are given in the text.

location	efficiency	cumulative eff.
PGC nozzle	1.00	1.00
RFQ end	0.66	0.67
to CNM	1.00	0.67
SGC	0.5(1)	0.33
SRFQ	0.7(1)	0.23
to CEC	1.00	0.23
CEC	0.5(2)	0.12(5)
Rate	15 k/s	1.8(8) k/s

The electrostatic transport to the MBS entrance membrane was shown to be nearly 100 % efficient since it is electrostatic beam transport under good vacuum conditions with a low-emittance beam. The MBS is not commissioned yet. It is more guesswork to estimate its efficiency, but the grids with ∼ 80 % open surface, which support the nano-membranes, set a limit to the maximum efficiency. It would be naive to estimate a 100 % efficient breakup and transport for all transmitted particles. If 1/2 to 3/4 of the transmitted particles are forwarded to the nozzle, total efficiency of 0.5 (1) was reached. This value is used to calculate the cumulative value.

The subsequent RFQ is not built yet. It only has to transport one mass and thus will not face the same difficulties as the first RFQ if well-designed for ^{8}B^{+} ions. Still, the integrated cooler-buncher has potential loss factors since firstly, the ions have to reside in the gas for an elongated time, which requires ultra-high gas purities. Secondly, the cycling of the buncher introduces intrinsic losses. This is included as a possible efficiency of 0.6 to 0.8, using 0.7 (1) as an average for the cumulation. The full MBS, from the entrance into the CNM to exit-

Table 5.3.: A comparison of the spectroscopic efficiency of laser spectroscopy on ^{8}B with two other experiments [132, 104]. The number $x > 1$ indicates that the measurement on boron requires x times more particles to achieve the same overall resolution.

	^{36}Ca	^{12}Be
Transition strength	6.8	2.6
c/ac	2	1
HFS	4	4
g.s. population	3	3
det. efficiency	1	1
PMT sens.	1.4	1
total	228.5	31.2

ing the second RFQ, is therefore valued with 0.35 (9). The electrostatic beam transport after the MBS should not introduce any loss.

The charge-exchange cell process has demonstrated high efficiencies of up to 0.6, as shown in many online experiments, for example at COLLAPS/ISOLDE. Since boron isotopes are much lighter than many of the isotopes that were neutralized and the charge-exchange process depends on the specific atomic structure, 0.3 to 0.7 is estimated, and 0.5 (2) used for accumulation. This value also agrees with the value reported from a measurement at TRIUMF for light fluorine [129].

The result is a total efficiency from PGC exit to the fluorescence detection region of 12 ± 5 %. Using the 15 kcts/s, this can be converted to 1.8 ± 0.8 k atoms per second in front of the photon detectors. The transport time from the PGC to the fluorescence detection region is in the order of milliseconds, and radioactive decay on the flight path of the ions is thus negligible.

5.5.3 Spectroscopy

From the spectroscopic parameters of ^{8}B it is possible to derive how many particles are needed in the fluorescence detection region to acquire a reasonable resonance signal. To answer this question, it is expedient to look at similar experiments that recorded optical spectra of rare isotopes in similar setups.

Two experiments are well suited since they use a comparable spectroscopy scheme: The measurement of ^{36}Ca at BECOLA [132] and the experiment that yielded the ^{12}Be charge radius at COLLAPS [104]. Table 5.3 gives the spectroscopic and experimental parameters of the two experiments compared with the ^{8}B measurement. In each row, the number indicates the relative compensation factor needed in the planned ^{8}B measurement to achieve the same statistical significance as in the cited experiments. A higher number thus indicates that more ^{8}B particles are needed to compensate.

The transition strength is given by the rate of spontaneous absorption of resonant photons, which is $\propto A_{21} \cdot \lambda^3$. Both calcium and beryllium have a higher relative strength in the respective transition. ^{12}Be was measured in collinear and anticollinear alignment as well, but ^{36}Ca was only measured in one direction, which introduces a factor of two. The sensitivity of the photomultiplier is slightly higher for 400 nm photons than for 250 nm of boron but similar for the one used with beryllium at 313 nm.

In ^{8}B, four components of the hyperfine structure need to be measured if they can be resolved in the narrow spectrum. Also, the ground state of boron is split into the $^{2}P_{1/2}$ and the $^{2}P_{3/2}$ state, which will be populated since they are separated by less than thermal energies of 1.9 meV. The best assumption is that they will be populated in the ratio of their decay rate (A-factors) from the higher-lying $^{3}S_{1/2}$ state, which means that 2/3 of the particles will be in the upper state and not available in the transition that is to be tested. Testing the upper $^{2}P_{3/2}$ level does not increase the efficiency since here, six hyperfine structure transitions would have to be probed.

The detection efficiency is set to 1 for both experiments relative to the planned ^{8}B measurement. It incorporates different detection systems and their total efficiency. The same detection system is used in the boron and the calcium experiment. It was developed within this work and is introduced at length in chapter 6. Work is ongoing to optimize it to show the same performance at 393 nm and at 250 nm, which is challenging due to the disposability of large-scale bent UV mirrors. The beryllium measurement used an older detection system based on lenses, but the photon-ion coincidence detection used in this experiment compensates for the bunched beam

Table 5.4.: From the efficiency in Tab. 5.3, one can extract the equivalent rate needed for the ^{8}B experiment to reach the same statistical level. Also, it allows an estimation of the expected scanning time at the current rate of 1.8 (8) k cts/s.

	time h	rate (s^{-1})	eff. factor *(see Tab. 5.3)*	corr. ^{8}B rate ($10^3 \times s^{-1}$)	rate for 24 h ($10^3 \times s^{-1}$)	expected time h
^{36}Ca	33	25	228.5	5.7	7.9	105(47)
^{12}Be	8	2000	31.2	62.4	20.8	277(123)

background-reduction, in which the new system is excelling in.

The duration and the rates for both experiments at BECOLA and COLLAPS are shown in Tab. 5.4. They used 33 h and 8 h to record a resonance spectrum. Using the efficiency factors from above, this corresponds to ^{8}B rates of 7.9 kcts/s and 20.8 kcts/s when normed to a 24 h measurement. The achieved rate of 1.8 (8) k cts/s is thus at least a factor 4 to low to facilitate a measurement with the same statistical uncertainty as ^{36}Ca in the same amount of time. While the measurement time derived from ^{36}Ca (~4 days) is possible, the ~10 days derived from ^{12}Be is not practicable.

However, there is still reason to believe that this duration can be reduced even with the rates achieved so far. The transition strength is not an inevitable factor since the laser power can be increased. In a laser spectroscopy experiment, the power is usually set to a level that prevents multiple laser-particle interactions within the length of the fluorescence detection region. Thus, it can be scaled up to reach a resonant photon flux per ^{8}B beam atoms comparable to that of calcium. The possible line broadening and shifts that are introduced in this way have to be investigated extensively with the offline beam.

For ^{8}B, the mass shift is precisely known, and the field shift is only a small portion of the total isotope shift. Thus, the position of the resonance is well known and is only shifted by several 10 MHz due to the unknown field shift, which is much smaller than the natural linewidth. Thus, no “searching” of the resonance position will be required, relaxing the experimental procedure.

5.5.4 Conclusions

This examination of efficiencies shows that laser spectroscopy of ^{8}B is within reach with the production rates and efficiencies that are known or can be estimated from the setup so far. Still, some open questions and possibilities for improvement remain, which can determine if the experiment is feasible or not:

- The MBS, consisting of SGC and the adjacent RFQ cooler/buncher, is not yet commissioned and is valued with a total efficiency of 0.3. Whatever system will be used to break up and bunch the ^{8}B, this is the benchmark to provide a sufficient number of ions for laser spectroscopy.
- The CEC needs to be commissioned to get certainty about its performance, in the best case with an experimental analysis about the ground state population.
- The fluorescence detection region needs to be tested and optimized for 250 nm detection. An ongoing experiment at the KOALA beamline at TU Darmstadt aims to test the atomic boron transition in collinear alignment, which allows a definitive test of its efficiency and a facility to improve it.

With these steps ahead, the first laser spectroscopic, model-independent measurement of the proton-halo character of ^{8}B can be achieved in the near future.

6 Fluorescence detection in collinear Laser Spectroscopy

In this chapter, the fluorescence detection region (FDR) that is used in the collinear laser spectroscopy setup at ANL to measure the isotope shift in ^{8,10,11}B is presented. It is detached from the preceding chapter 5 since the FDR was developed for a broader range of applications. It is depicted in Fig. 6.1 and consists of two parts: Inside the vacuum chamber, an elliptic mirror surrounds a longitudinal 80 mm part of the beam and covers most of the solid angle that can be seen by the emitted photons in this segment. Under resonance conditions, the particles in the beam get excited by the laser field and emit photons spontaneously into random directions. Those photons are guided through a viewport to the outside of the vacuum vessel.

Here, a light guide system is installed that forwards the photons onto photomultiplier tubes (PMTs), which have a small active surface for single-photon detection. The light guide system is equipped with parabolic mirrors, which transport only those photons to the PMT that are transmitted through the viewport under a certain angle allowing to suppress background light.

The optical setup, based on non-planar mirror geometries, was introduced by Michael Hammen in 2010 [125]. Within this work, three revised versions of his prototype were built. The significant improvements made here lie in the versatile, compact mechanical design and the adaptability to different particle species and transition wavelengths. The principle of the light collection inside and outside vacuum is unaltered and was tested again with the new versions presented here. Thus, Michael Hammen's original report on the FDR, which led to the implementation of the elaborate light collection optics, is recommended for any reader who is interested in the more theoretical fundamentals of the system, as they will not be repeated here in detail.

Three versions of the setup presented here are currently in use at the BECOLA beamline at MSU, the KOALA beamline at TU Darmstadt and the future ^{8}B setup at ANL. Here, the design and the physical considerations that led to the revised version of the FDR shall be highlighted, together with the first results that were achieved.

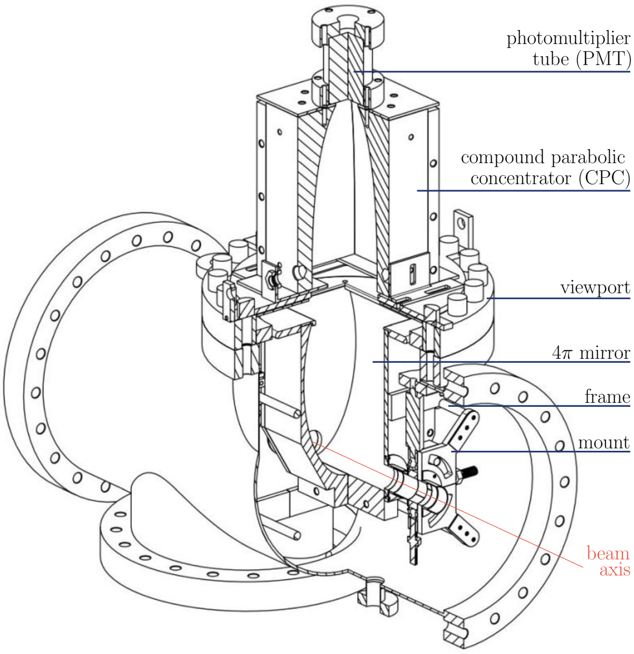

Figure 6.1.: A technical drawing from a cut fluorescence detection region, along with named components and their abbreviations used in the text. A second system is installed in the viewport that is facing downward.

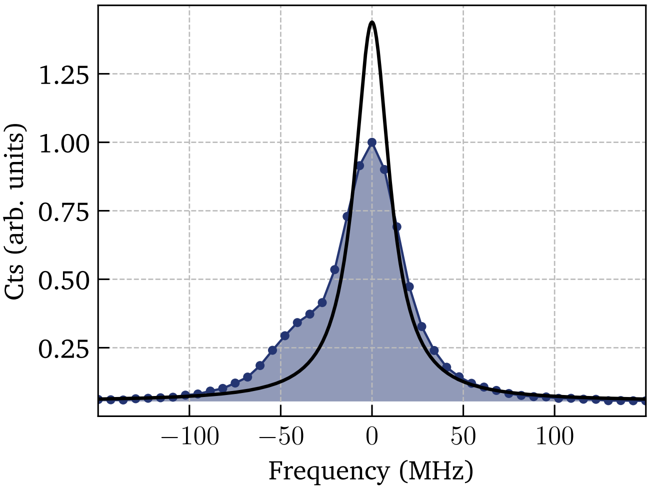

Figure 6.2.: The blue data points show a measurement of a calcium resonance, with the summed signal strength S_{Summed} indicated by the blue shaded area. The peak is asymmetric due to an inhomogeneous potential in the source region. The black curve indicates the Lorentz-profile with the same integrated area and the natural linewidth of the transition. Such a profile was observed if all particles were exactly collinear and mono-energetic, and no other broadening occurred. Its height determines S_{L}.

6.1 Signal and background

In collinear laser spectroscopy, fluorescence photons are counted while scanning the frequency of the laser that interacts with the particles in their moving frame of reference. When the laser is in resonance with an atomic or ionic level, the particles emit photons with a rate $\dot{R}$. Under resonance conditions, this rate depends on the power density of the laser field and the particle beam current. In experiments with rare, radioactive beams, the current is usually low and limited by the production and transport to the experiment. The laser power can be scaled, but high powers lead to saturation and broadening effects in the resonance, which interferes with the high precision that is usually targeted.

To start with, a brief explanation of the key concepts of signal and background in optical spectroscopy is given. This part is independent of the actual design and concept of the FDR that will be introduced in the next section using the concepts defined here.

6.1.1 Signal

Optical resonances between bound states in the absence of inhomogeneous broadening are of Lorentzian shape[1], with

$$\dot{R}_{\text{Lorentz}} = \frac{A_{\text{L}}}{\pi} \frac{\frac{1}{2}\Gamma}{(\nu - \nu_0)^2 + \left(\frac{1}{2}\Gamma\right)^2} \,. \tag{6.1}$$

Their width Γ (for $\Gamma^2/\nu_0^2 \ll 1$) is, in the case of the natural linewidth

$$\Gamma_{\text{nat}} = \frac{1}{2\pi\tau} \tag{6.2}$$

with the lifetime τ of the upper state and denoting the full width at half maximum (FWHM) of the distribution. In real experiments, Lorentzian shape is only observed in the exceptional case of ultra-high-resolution measurements on very cold ensembles ($T \to 0$). Usually, one or several broadening mechanisms contribute to the linewidth. Most prominently, the velocity distribution of the particles from the source contributes as Doppler broadening. Sometimes, such broadening mechanisms can be explicitly expressed mathematically and convoluted with the Lorentzian shape. This is particularly true for the Doppler broadening and the associated Gaussian distribution of velocities. It is regularly taken into account by applying the Voigt profile, which is a convolution of the Gaussian

$$\dot{R}_{\text{Gaussian}} = \frac{A_{\text{G}}}{\sigma\sqrt{2\pi}} e^{-\frac{(x-\mu)^2}{(2\sigma^2)}} \,, \tag{6.3}$$

and the Lorentzian distribution, according to

$$\dot{R}_{\text{Voigt}} = \int \dot{R}_{\text{Gaussian}}(t)\dot{R}_{\text{Lorentz}}(x-t)\mathrm{d}t \,. \tag{6.4}$$

Signal strength

To compare the efficiencies of different photon detection regions, it is necessary to normalize the observed

---

[1] Transitions with very small separation to other transitions, e.g., hyperfine transitions can be affected from quantum interference effects (cross damping) that lead to deviations from the Lorentzian profile.

signal rates, since the height (the maximum) of all distributions scale with their width. An efficient method is to integrate the full measured signal strength

$$S_{\mathrm{Summed}} = \int_{-\infty}^{+\infty} \dot{R}\,\mathrm{d}\nu\,, \tag{6.5}$$

which is equivalent to adding the number of photons in each recorded bin minus the fitted background. To give this value a physical meaning, it can be scaled with the Lorentzian width to

$$S_{\mathrm{L(orentz)}} = \frac{2}{\pi}\frac{S_{\mathrm{Summed}}}{\Gamma} \tag{6.6}$$

and using the natural linewidth Γ_{nat} of the investigated transition. The obtained value S_{L} is the height of the Lorentz distribution in the idealized case of a mono-energetic, parallel beam without any additional broadening mechanisms. In the desirable scenario that every particle interacts with the laser beam not more than once, this allows comparing transitions that have different shapes and widths.

Figure 6.2 shows a generic spectrum measured at the KOALA setup of the calcium D1 line, which nominally has a natural linewidth of $\Gamma_{\mathrm{nat}} = 23.4\,\mathrm{MHz}$. Due to the spectroscopic environment, the line shape is a Voigt profile since a Gaussian component contributes to the width. Also, a side peak is visible, which is due to different ion starting potentials in the thermal source. This already demonstrates the necessity of a normalization procedure. In black, the Lorentz profile is plotted that would appear if only the natural linewidth were observed. The area under the Lorentz profile is equivalent to the blue shaded area below the measured data. The corresponding height S_{L}, which is the maximum value of the black curve, is used to compare the efficiency of photon detection in the following.

Transition strength

The height of the Lorentzian line depends on the line strength of the transition, which is connected to the atomic properties of the investigated particles. The observed amount of photons is proportional to the strength of the induced absorption B_{12} under the assumption that all excited particles decay and emit a photon spontaneously within the flight time through the active detection region. This is valid, since the lifetime of the excited states is usually $\sim 10\,\mathrm{ns}$ (see e.g. Tab. 6.1), while the velocity for ^{40}Ca at 30 keV is $0.4\,\mathrm{mm\,ns^{-1}}$ in the 80 mm detection chamber. B_{12} is the Einstein absorption coefficient, which relates with

Table 6.1.: The necessary parameters to calculate the transition strength (last row) of the ground state spectroscopy transition in ionic calcium and atomic boron [111, 133]. Details on the calculation are given in the text. One design goal of the fluorescence detection region is to allow efficient detection for both wavelengths, which is challenging especially for the boron deep-UV transitions.

	transition	λ (nm)	A_{21} (s^{-1})	τ (ns)	P
Ca^{+}	$\mathrm{S}_{1/2} \rightarrow \mathrm{P}_{1/2}$	396.8	1.54×10^{8}	7.1	6.8
B^{0}	$\mathrm{P}_{1/2} \rightarrow \mathrm{S}_{1/2}$	249.7	8.4×10^{7}	4.0	1
B^{0}	$\mathrm{P}_{3/2} \rightarrow \mathrm{S}_{1/2}$	249.8	1.68×10^{8}	4.0	2

$$B_{21} = A_{21} \cdot \frac{\lambda^3}{8\pi h} \tag{6.7}$$

with the Einstein spontaneous emission coefficient A_{21} for a given transition with wavelength λ. Table 6.1 lists the A_{21}-factors of boron [133] and the calcium D1 line [111] that can be found in literature. From the relation

$$P = \frac{B_{21,\mathrm{B}}}{B_{21,\mathrm{Ca}}} = \frac{A_{21,\mathrm{B}} \cdot (250\,\mathrm{nm})^3}{A_{21,\mathrm{Ca}} \cdot (396\,\mathrm{nm})^3} = 6.8 \tag{6.8}$$

it can be derived that the transition strength of boron in the ground-state $P_{1/2} \rightarrow S_{1/2}$ transition is almost a factor 7 weaker than the calcium D1 line, given the same laser power and particle flux. This calculation can be used to compare photon detection efficiencies among different species, but also to extrapolate efficiency from one species to another. This was used in chapter 5 to estimate the necessary amount of ^{8}B in front of the photon counters from a measurement on calcium, which will be presented later in this chapter with more focus on the detection efficiency.

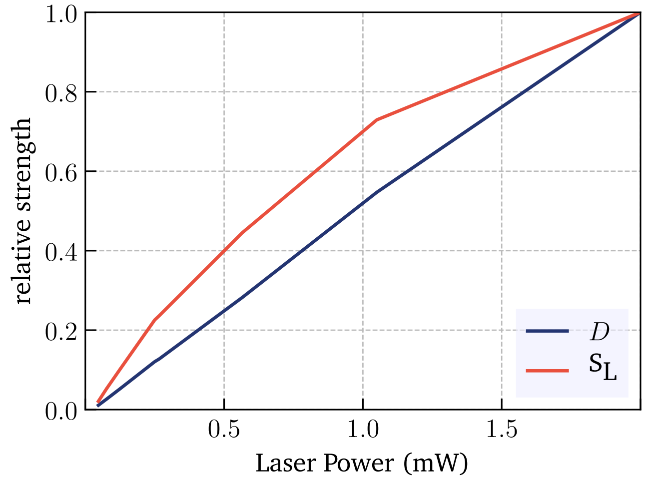

Figure 6.3.: In a measurement, the background D (blue) scales proportionally with the used laser power. The signal (red) shows saturation effects when using higher laser powers, which also cause line shifts and broadenings that should be minimized. The data for this plot was recorded in a series of measurements in the calcium D1 line, varying the laser power.

Scaling

The signal strength depends on the integrated laser power density that the particles experience on their way through the active detection region. In a single particle picture, the power density is proportional to the excitation probability. For a bunch or a beam of particles, saturation sets in at higher powers if particles can be excited more than once. This also leads to unwanted broadening effects, and possibly to a frequency shift due to photon recoil.

Figure 6.3 shows how the signal strength S_L depends on the laser power, as measured at KOALA. In the low power regime below 1 mW, S_L scales linearly until saturation effects become visible. To compare the efficiency of different photon detection regions, the measurements need to take place in this low power region and can then be scaled linearly to one laser power.

More noticable, S_L will depend on the total number of ions or atoms that are prepared in the right state. In a cw ion beam, this can be extracted as an ion current by measuring the charge drain on a Faraday cup. For exotic isotopes, where only small amounts are produced, estimating the beam current is often more difficult and less exact. In principle, S_L scales proportionally with the beam current under the condition that the beam properties do not change.

This leads to another scaling factor that is different in different setups, which is the overlap between particle and laser beam. In the best case, all ions or particles experience the laser field. A non-diverging, low-emittance beam allows bringing all particles into resonance conditions with the laser beam.

6.1.2 Background

Inadvertently, non-resonant photons and stray light will also reach the photomultiplier tubes during a measurement, independent of the laser frequency. Two principal types of background can be distinguished. Static background $D_{\text{static}}(P)$, or stray light, is dominated by scattered or reflected laser light that finds its way to the detectors. It is approximately proportional to the laser power P that is fed through the beamline, as can be seen in Fig. 6.3. A small portion is also attributed to the detector dark count rate and ambient light entering the vacuum chamber, but this is negligible in most applications.

In contrast, beam-induced background $D_{\text{beam}}(I)$ is approximately proportional to the particle beam current I. It is especially of concern when using a charge-exchange cell. In the cell, an alkali metal (or an alkaline earth metal) such as sodium is vaporized and neutralizes the passing beam in-flight. In this semi-resonant process, cascades of photons are emitted when the atoms decay to their ground state. The non-ideal vacuum conditions in the vicinity of the heated cell also contribute to the background rate. Also, residual gas and the alkali vapor is excited in inelastic collisions with the beam and emits collateral photons while and after the beam passes.

The total background rate

$$D_{\text{total}}(P,I) = D_{\text{static}}(P) + D_{\text{beam}}(I) \tag{6.9}$$

is constant in an experiment where P and I are constant while the ratio between $D_{\text{beam}}(I)$ and $D_{\text{static}}(P)$ may vary from experiment to experiment.

6.1.3 Signal-to-noise

At typical count numbers of several hundred or thousand photon count events per frequency step, Poisson statistics can be applied, which yields for the noise

$$N = \sqrt{D_{\text{total}}(P, I)} \tag{6.10}$$

given by the uncertainty of the background rate D_{total}. A signal is distinguishable from background if a certain Signal-to-Noise ratio

$$\text{SNR} = \frac{S}{N} = \frac{S_{\text{L}}}{\sqrt{D_{\text{total}}(P, I)}} \tag{6.11}$$

is achieved. Obviously, spending more time on the measurement is a valid approach to increase the SNR, since the noise only grows with the square root of the signal, which will eventually outgrow the background. In this sense it is important to choose the highest laser power possible that does not introduce uncontrolled systematic effects.

Likewise, efforts to decrease the background D increase the achievable SNR in a given time. An efficient way to suppress $D_{\text{static}}(P)$ is to accumulate the ion beam and extract it in bunches towards the detection region. The photon detectors are then gated on the passing particle bunch and only record the static background in a short time interval. This does not help to reduce $D_{\text{beam}}(I)$ since the ion beam I is growing proportionally to the accumulation time. For illustration, a simulated scheme of this method can be found in Fig. 6.4.

6.1.4 Total efficiencies

The SNR is primarily a scale basis for evaluating the quality of a recorded transition data set. It does not measure the quality of the detection system per se but allows comparing the datasets acquired under different experimental conditions. To characterize different photon-collection systems, the question is how long it does take to acquire a dataset with a certain SNR under the same experimental conditions.

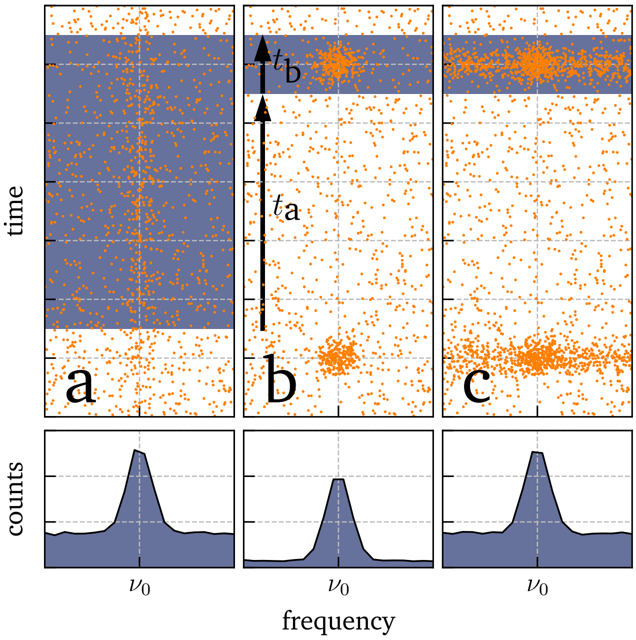

Figure 6.4.: Simulated data for a) continuous, b) bunched and c) bunched beam with beam-induced background. Each orange dot represents a detected photon in the time/frequency plane of the simulated measurement. The beam is accumulated for t_{a} and then ejected in a bunch with length t_{b}. This increases the signal-to-noise ratio by a factor of $\sqrt{(t_{\text{a}} + t_{\text{b}})/t_{\text{b}}}$. In real experiments, the compression ratio and thus the gain can be orders of magnitude higher. Typical values of 10^4 are reached. However, bunching does not provide a gain in sensitivity for beam-induced background.

The total efficiency

$$\eta_{\text{tot}} = \frac{N_{\text{beam}}}{S_{\text{L}}} \tag{6.12}$$

is defined as the number of particles N_{part} that pass the detector until one resonant photon is observed, when the laser frequency is on resonance. The normalization on S_{L} allows to compare signals with widths that differ from the natural linewidth. η_{tot} does not incorporate the background that is accumulated in the same time.

An increase in signal S_{L} by a factor of two is equivalent to a reduction of the background by a factor of four in terms of the achieved SNR. For a detection system, this means that cutting the background $D_{\text{static}}(P)$, for example by spatial filters, is only beneficial if the signal is cut correspondingly less.

Also, unlike $D_{\text{static}}(P)$, the beam-related background $D_{\text{beam}}(I)$ has the same spatial origin as fluorescence photons and can not be suppressed by optical spatial filters such as those described in the next sections. Thus, any reduction in D_{beam} proportionally reduces the amount of signal. To record signal despite strong D_{beam}, a higher total detection efficiency for photons that originate from the beam axis is favorable. Then, more events per channel are accumulated in the same period, and the signal S will outgrow the noise N faster.

To summarize, for continuous, stable ionic beams with high production rates, spatial suppression of static background $D_{\mathrm{static}}(P)$ will help to record signals with good SNR faster. Meanwhile, for bunched, low-production beams, which are charge-exchanged and thus have a large beam-induced background D_{beam}, the total efficiency η_{tot} is of utmost importance, meaning that as many beam photons as possible should be guided to the detectors.

In the following, a detection system is presented that joins these two demands and can versatilely be adapted to the experiment. A 4π detector collects and forwards photons emitted in all directions from the beam to outside vacuum. Here, a compound parabolic concentrator (CPC) is used as a light guide to forward light efficiently to the photomultiplier tubes or to suppress ambient and static background.

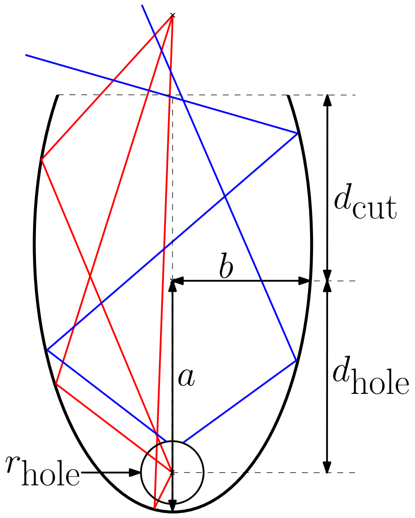

Figure 6.5.: In a (cut) ellipsis, the light that is emitted from one focal point is reflected once towards the second focal point. Stray light, which can, for example, emerge from the boundary of the entrance hole is not emitted in such a defined manner. The parameters of the ellipsis used here are $a = 77$ mm, $b = 39.7$ mm, $d_{\mathrm{hole}} = 66$ mm, $d_{\mathrm{cut}} = 44$ mm and $r_{\mathrm{hole}} = 8.5$ mm.

6.2 The 4π-Mirror

The origin of the signal photons in collinear laser spectroscopy is not a point-like source, but a cylinder that extends along the beam axis, which is defined by the overlap cross-section of the particle and the laser beam and the length of the chamber. Both beams have, in the ideal case, a Gaussian shape and the same size of typically 1-2 mm radius. Shaping and controlling both beams and their overlap angle is key to precision and has to be taken extensive care of preceding an experiment.

From this cylindrical beam axis, photons are spontaneously emitted in random spatial directions. To obtain the maximum total efficiency η_{tot}, the fluorescence detection region has to cover the most substantial part of the solid angle and forward as many emitted photons as possible towards the photon counters. These photomultiplier tubes are situated outside the vacuum region behind vacuum viewports.

6.2.1 Elliptical design

Non-planar mirrors are employed to facilitate the 4π photon collection. A mirror with an elliptical cross-

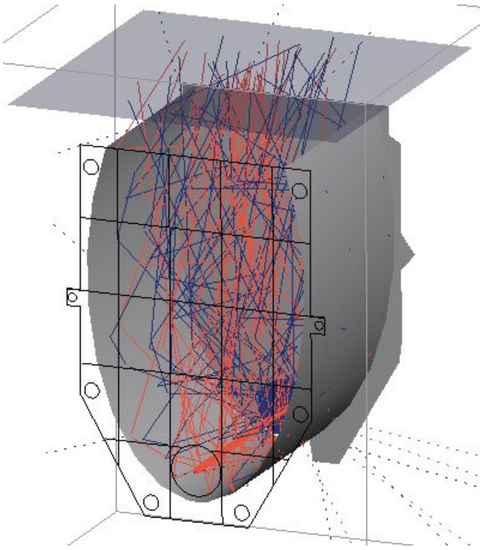

Figure 6.6.: A ray trace of the 4π mirror performed with FRED® . The light emitted from the beam axis is depicted in red, stray light in blue. The opaque area in the top simulates the exit viewport window, where, in the experiment, further optical elements are installed outside the vacuum chamber.

section is elongated 80 mm along the beam axis. The other parameters of this ellipsis can be found in Fig. 6.5. One focal axis of the ellipse is coincident with the beam axis. Photons originating on this axis are reflected once to the second focal axis, which is outside the viewport, as an example shown as red rays. Contrary, blue rays are shown, which origin from the edge of the entry hole. They are not reflected towards the focal spot.

The upper part directed towards outside vacuum is cut parallel to the viewport to allow photons to exit the elliptical mirror towards the receiver. Flat surface mirrors terminate the oval mirrors to either side (See also Fig. 6.1). Photons that are emitted under a shallow angle with respect to the beam axis are reflected on these flat end pieces but maintain their path towards the outside vacuum focal axis. The flat mirrors also have holes were the beams enter and exit the region. The diameter of these holes is 18 mm to allow adjustment of the beams through the setup and prevent diffraction on the edges.

6.2.2 Efficiency simulation

Simulations with the Monte-Carlo ray tracing software FRED® [2] were performed to evaluate the performance of the elliptical mirror. The photon source was modeled as a cylinder with 2 mm radius that spans from entrance to exit aperture of the elliptical mirror. Photons are sent out in random spatial directions from random points within the cylinder. For the simulation, the reflectivity of the mirror surfaces was set to 100 %. The viewport itself is not included into the simulation. Figure 6.6 shows a ray trace of beam photons in red and background photons in blue in the elliptical mirror. The opaque surface facing the open end of the elliptical mirror is the analysis plane, which resembles the outside of the vacuum viewport.

Table 6.2.: From the simulation, the relative amount of photons arriving at the viewport surface with i reflections can be extracted. This sums up to $\varepsilon_{4\pi}$ for (perfect) $R = 1$ mirrors. For lower R, each class of photons with i reflections has to be taken into account individually with R^i (see Tab. 6.3)

i reflections	rel. amount
0	0.03
1	0.29
2	0.33
3	0.11
4	0.04
5	0.02
$\varepsilon_{4\pi,R=1}$	0.82

About 82 % of all photons reach this analysis plane outside the viewport. The rest is either lost in the beam entry and exit aperture, or in the gap that resembles the viewport. This clearly shows the good overall efficiency of the system, based on its large solid angle acceptance. In the next step, the number of surface reflections for the photons is investigated. Only 3 % of the incoming photons are directly emitted towards the exit window. Most photons are reflected once (29 %) or twice (33 %) inside the elliptical mirror. The numbers are presented in Tab. 6.2. The forwarding efficiency of the 4π-Mirror

$$\varepsilon_{4\pi} = \left(\sum_i R^i \cdot N_i \right) / N \tag{6.13}$$

depends on the specular reflectivity R of the mirrors, where N_i the number of photons with i reflections, di-

---

[2] Photon Engineering LLC, Tucson, USA

Table 6.3.: The reflectivity of different mirrors that could be used in the elliptical mirror. The single reflectivity R of the mirror is given together with the resulting photon forwarding efficiency of the 4π mirror. This table lists specific values that can be calculated from Tab. 6.2.

mirror type	reflectivity R		forw. eff. $\varepsilon_{4\pi}$	
	250 nm	396 nm	250 nm	396 nm
"perfect"	1.00	1.00	0.82	0.82
bare Al	0.92	0.91	0.71	0.69
MIRO®	0.72	0.88	0.47	0.65
dielectric	0.99	0.99	0.81	0.81

vided by the total number of emitted photons N. Thus, $\varepsilon_{4\pi}(R)$ gives the quote of all photons sent out in the active inside region of the 4π mirror that are guided to outside the viewport.

6.2.3 Elliptical mirror surfaces

Since most photons interact with the mirror surfaces, their quality is decisive for the performance of the system. The choice of mirror is important, since broad-band mirrors usually have different specular reflectivity for different wavelengths, with a cutoff in the UV and IR. The total efficiency $\varepsilon_{4\pi}$ does not scale linearly with the given reflectivity due to multiple reflections. The number of reflections that the photons experience is listed in Tab. 6.2. For the use of the system with different particle species in different wavelength regimes, optimized elliptical mirrors can significantly improve the performance.

Exemplarily, different mirror systems, which are or could be used in the FDR, are referenced in Tab. 6.3, demonstrating the necessity of high-reflectivity mirrors. Section 6.4.4 of this chapter will highlight the constraints and requirements for such mirrors and explain how they are implemented into the system mechanically.

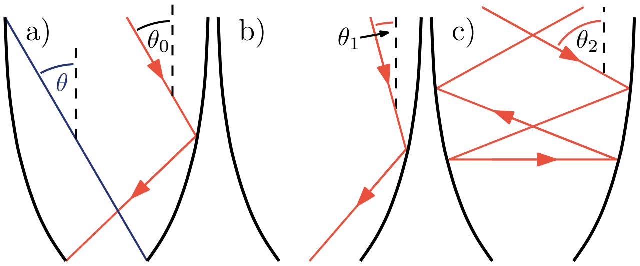

Figure 6.7.: Three possible light paths through a 2D compound parabolic concentrator: a) Photons that enter under the design angle θ are transmitted to the edge of the exit aperture. b) Photons that have an angle $\theta_1 < \theta$ are transmitted, while for c) $\theta_2 > \theta$ the CPCs rejects the photons. Reproduced from [134]

6.3 Compound parabolic concentrator

The photons are emitted through the viewport from the 4π elliptical mirror inside the vacuum chamber in random directions and from a large area. A second optical system outside the vacuum chamber is needed to forward these photons onto the detectors. These Sens-Tech[3] P25-P UV sensitive photomultipliers have a circular active surface of only 20 mm diameter.

A useful solution to forward the photons onto this small area is a non-imaging optical element, a so-called compound parabolic concentrator (CPC). They guide the light, which emerges from a large area of the viewport, to the PMT. As shown in Fig. 6.7, such 2D parabolic arrangements have an angular cutoff θ, which is the maximum angle under which photons are forwarded from the incident to the exit surface. Two of such mirror sets can be folded into a 3D parabolic concentrator. These CPCs discriminate photons exiting the viewport depending on their angle. Since photons that are the result of static background D_{static} have a less defined optical path in the elliptical mirror, their exit angles and positions will be scattered more than beam photons. Using the CPCs, this can be made use of to prevent static background photons from reaching the detectors.

The cutoff angle θ and the size of the active surface of the receiver determines the length and the entrance opening size of the CPC. Systems with a more restric-

---

[3] Sens-Tech Ltd, Surrey, UK

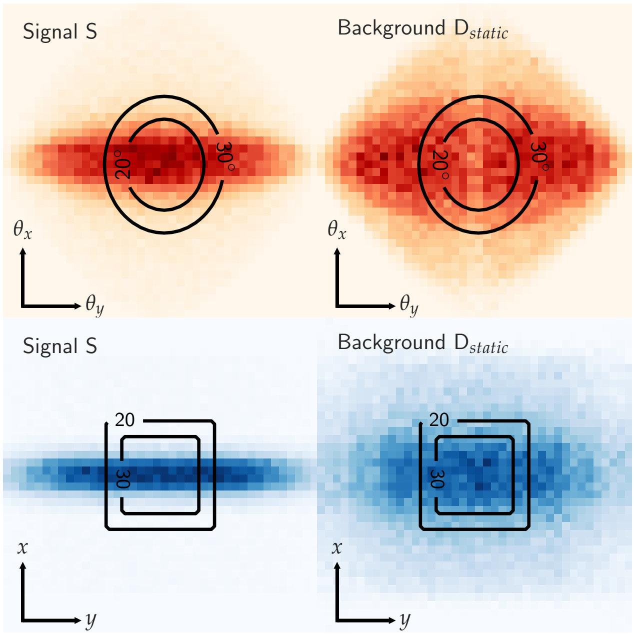

Figure 6.8.: Top/Red: The angular distribution of photons exiting the view-port window. Signal (left) and background (right) form a different pattern. Evidently, detecting photons in the center area will result in a higher SNR. In black, the theoretical acceptance angle of the CPC20 and CPC30 system is plotted. Bottom/Blue: In the spatial distribution of photons exiting the viewport window, the pattern differs as well, but the suppression of background in the spatial acceptance region of the compound parabolic concentrators is not as pronounced as in the angular case.

tive, smaller cutoff angle have a larger opening in which photons can enter.

In this section, simulations show how CPCs are employed to separate beam and background light using their difference in surface and angular distribution. Measurements on stable ionic calcium beam with and without using the CPCs confirm their performance and allow to extrapolate to experimental conditions where a beam-induced background is present.

6.3.1 Simulation of background

A simulation was done to investigate the stray light suppression potential that could be tapped with CPCs, which only forward photons that are incident with an angle smaller than a cutoff angle θ given by design. Also, their input area is limited, which introduces a spatial cutoff of rectangular shape. Thus, the elliptical 4π mirror is simulated, and the spatial and angular distribution of background and signal light on the viewport surface is investigated.

Stray light was realized as discs placed in the entry and exit aperture perpendicular to the beam axis, and having the full aperture radius. This accounts for photons that are diffracted inside the beamline. The signal light is again modeled as point-like sources inside a cylindrical volume with 1.5 mm radius, which emits photons in random angles.

A quantitative analysis of the signal/background rate is obviously not possible. Instead, the angles and positions of photons emitted from both arrays were recorded on the viewport surface just outside the vacuum chamber. Evidently, stray light has a broader angular distribution on the axis parallel to the beam, as plotted in Fig. 6.8. Also, the surface area in which the photons exit the viewport is more condensed for the signal light.

The elliptical geometry is thus more efficient for such photons that are emitted exactly from the designated axis. Photons emitted off-axis experience an imperfect reflection pattern in the ellipsis. In general, static background light will not be emitted from the beam axis and thus can be suppressed by CPCs, which provide an angular and a spatial cut-off. Also, in Fig. 6.8, the acceptance angle and rectangular area for two of such CPCs with 20° and 30° cutoff are plotted for illustration. They provide an efficient background suppression while forwarding most of the incoming signal light to the PMTs.

A second implication can be derived from these simulation results. A smaller overlapped beam diameter will increase the SNR per time in two different ways: Less total laser power is needed to generate a light field with the same power density seen by the particles. Secondly, the CPCs can distinguish better between beam and background light, and the signal light reaches the viewport window in a more condensed area.

6.3.2 CPC performance

Based on this observation, two different types of CPCs were built, having a design acceptance angle of $\theta = 20°$ (CPC20) and $\theta = 30°$ (CPC30), respectively. As a third variation, the PMT can be mounted directly to the viewport without further optical guiding elements (NoCPC). These three variations of “lightguides” will be investigated in this section.

Table 6.4.: The design parameters of the different compound parabolic concentrators (CPCs). The CPC with the smaller, more restrictive cutoff angle has a larger acceptance area. The values are determined by the geometric design, which is constrained by the chosen θ_{cutoff}. The quota of photons, which enter this acceptance area at any angle, is given by $\varepsilon_{4\pi-\text{CPC}}$.

	θ_{cutoff} (mm^2)	Area (mm)	Length	$\varepsilon_{4\pi-\text{CPC}}$	ε_{rel}
CPC20	20°	1024	132.5	0.60	0.73
CPC30	30°	484	58	0.42	0.51
NoCPC	70°	380	0	0.19	0.23
“full”	-	5200	-	0.82	1.00

Table 6.5.: The different compound parabolic concentrator (CPC) designs were mounted on the KOALA beamline under constant experimental conditions. The CPC20 achieves the highest SNR in the given experiment but accepts the least signal photons.

	S_{L}	D_{static}	SNR	rel. SNR	ε_{CPC}
CPC20	3328	13618	28.5	1.40	0.28
CPC30	3760	21820	25.5	1.25	0.45
NoCPC	3746	33671	20.4	1.00	1.00

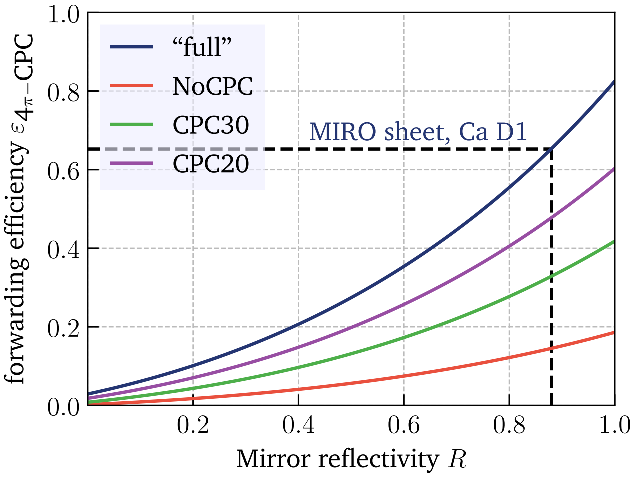

Figure 6.9.: From the number of reflections, a photon forwarding efficiency of the elliptical mirror can be estimated by folding in the mirror reflectivity. The black dashed lines mark the design reflectivity for 396 nm (calcium D1) used with the MIRO® mirrors, which are installed. Different lightguide setups accept only a portion of all emitted photons and thus limit the total combined forwarding efficiency.

Acceptance area and angle

The acceptance angle defines the length and the entrance area of the two CPCs. For the NoCPC setup, where the PMT is mounted directly to the viewport window, the “length” is zero, and the active surface of the PMT gives the area. Table 6.4 lists the physical properties of the three setups in comparison with a theoretical “full” geometric acceptance, which can detect any photon that reaches the viewport.

In Sec. 6.2.2, a simulation of the photon paths inside the 4π mirror was presented. The $\varepsilon_{4\pi} = 82\,\%$ of all photons that are forwarded to the viewport window emerge in different locations and angles. Using the acceptance area of the different lightguides allows defining the combined forwarding efficiency $\varepsilon_{4\pi-\text{CPC}}$. This takes the simulated realistic spatial distribution of photons in the plane of the viewport into account, which is also shown in Figure 6.8. For the calculation of $\varepsilon_{4\pi-\text{CPC}}$ in Tab. 6.4, a “perfect” reflectivity of the 4π mirror was assumed. For example, in the CPC30 setup, only 42 % of the light that is emitted by the beam enters the CPC, which is 51 % of the light that exits the viewport. This does not include the angular discrimination introduced by the CPCs or their limited mirror reflectivity. In Fig. 6.9, the corresponding acceptance rate of the different lightguides for $R < 1$ is shown.

The CPC efficiency

The performance of the three lightguides was compared in an offline experiment with ^{40}Ca ions at the KOALA beamline in Darmstadt. Under constant experimental conditions, they were mounted on the viewport one after another. The D1 line was scanned multiple times, and the summed signal S was normalized to the beam current monitored in a separate detection region, which was kept unchanged. With the conversion given in Sec. 6.1.1, the integrated signal strength is transformed into the Lorentz signal S_{L}. The background is only static since an continuous ionic beam was investigated.

The results from the experiment can be found in Tab. 6.5. Under the given conditions, the CPC20 shows the best performance, measured by the SNR. CPC30 and NoCPC both collect more signal photons but also more background light, which makes them worse than the CPC20 in terms of SNR.

Since the relative number of photons originating from the beam that is processed in the CPCs (regarding their spatial distribution) $\varepsilon_{4\pi-\text{CPC}}$ is known from simulations and listed in Tab. 6.4, the quota ε_{CPC} of photons cut off due to a too shallow angle can be extracted. The NoCPC accepts photons of all angles; the CPC20 transmits only 28 %, and the CPC30 45 % of all signal photons that enter.

With the reflectivity R_{CPC} of the CPCs, the total quantum efficiency of the system from the beam to the PMT is

$$\varepsilon_{\text{system}} = \varepsilon_{4\pi} \cdot \varepsilon_{4\pi-\text{CPC, relative}} \cdot \varepsilon_{\text{CPC}} \cdot R^{i}_{\text{CPC}} \tag{6.14}$$

where $\varepsilon_{4\pi}$ is the photon forwarding efficiency of the elliptical mirror for a given reflectivity $R_{4\pi}$ and $\varepsilon_{4\pi-\text{CPC, relative}}$ is the quota of photons that leave the 4π mirror in the acceptance area of the respective CPC. The CPC only forwards ε_{CPC} of all photons due to their angle, the value can be found in Tab. 6.4. Lastly, R_{CPC} is the reflectivity of the mirror in the light guide, and i is the number of reflections inside the light guide system, which is 1 for CPCs according to Fig. 6.7.

In the case of the NoCPC setup, the number of reflections is $i = 0$. Due to their larger area, the CPCs collect many more photons than the PMT mounted directly, but they will also falsely discriminate signal photons since $\varepsilon < 1$.

As a practical example, the total quantum efficiency $\varepsilon_{\text{system}}$ can be calculated for a calcium beam detected with MIRO® sheet mirrors. Following Tab. 6.3, the quantum efficiency of the 4π mirror is $\varepsilon_{4\pi} = 0.65$, the acceptance area of the CPC20 allows a relative quota of $\varepsilon_{4\pi-\text{CPC, relative}} = 0.73$. The reflectivity of the mirrors is $R = 0.88$ for calcium, and $\varepsilon_{\text{CPC20}} = 0.28$ of the incoming signal photons are transmitted with $i = 1$ reflections. This results in a $\varepsilon_{\text{System}} = 0.12$ using Eq. 6.14.

The advantage given by the larger active area of the CPC is diminished by the false suppression of signal photons, expressed by the small $\varepsilon_{\text{CPC20}} = 0.28$. The increased SNR of the CPC20 is a result of the even better background suppression only. This effect is less pronounced with the CPC30, which collects more background and less signal light, but also a larger ε_{CPC}.

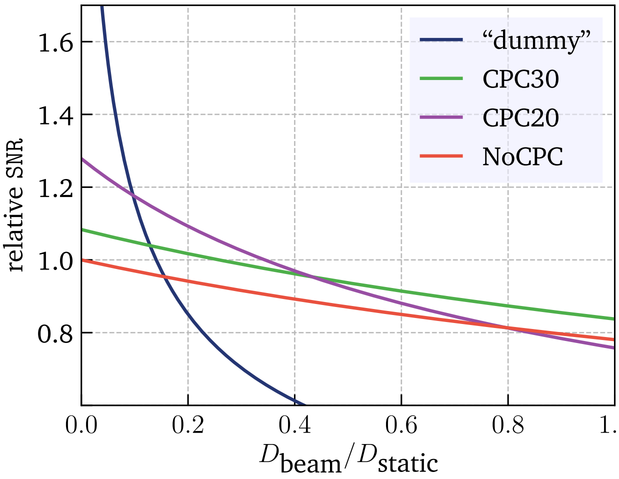

Figure 6.10.: A comparison of the SNR of different CPCs attached to the viewport window. The x-axis denotes the portion of the beam-induced background in relation to the static background. The ordinate intercept gives the efficiency when no beam-induced background is present. The SNR is scaled to 1 for the setup without CPC for better orientation. At higher beam backgrounds, the advantage of CPCs fades. A "dummy" detection system with high background suppression but accompanied by lower overall efficiency can be better for low beam backgrounds but will lose its scope at high background rates.

Concluding, under conditions where no $D_{\text{beam}}(I)$ is present, the CPC with the more restrictive cutoff angle allows generating signals with a higher SNR in shorter times. This agrees with the simulations and design expectations. This is true also for low-yield beams, but not necessarily when a beam-induced background is present, which is investigated in the following.

6.3.3 Beam-induced background

To include the effect of beam-induced background to the experimental results where no such background was present, the absolute signal strength can be used to extrapolate its effect. The magnitude of beam-induced background grows in the same way as the signal does since the photons are spatially indistinguishable, and thus the detection efficiency is equivalent. As previously stated, $D_{\text{beam}}(I)$ is proportional to the ion current, and so is the signal strength S, which means that also the beam-induced background $D_{\text{beam}}(I)$ is proportional to S.

Thus, by adding multiples of the signal count rate to the background for each setup, it is possible to compare the influence of beam-related background on the different setups.

In Fig. 6.10, the SNR is plotted for the three different setups against the relative amount of beam-related background. As expected, the CPC30 setup excels when the beam-induced background is high ($D_{\mathrm{Beam}}(I) > D_{\mathrm{Laser}}(P)$), since in this case, the higher absolute detection efficiency is superior to stray light suppression as stated above. At even higher beam-related backgrounds, the NoCPC setup overtakes in performance.

For illustration purposes, another "dummy" dataset was simulated for a fictional detection setup, which has a 1000× suppression of $D_{\mathrm{Laser}}(P)$ at the cost of a 10× less total beam-axis light collection efficiency compared to the 4π elliptical detector. Evidently, this system performs much better when no beam-induced background is present, but as soon as a beam-related background is present, the advantage is lost.

This conclusion can also be inverted. The signal strength observed with the NoCPC setup is limited by the active area of the detector, which excludes more than 3/4 of the light that exits the viewport. Employing a detector with a larger surface area or a photon guide with a larger active area would significantly increase the performance of the system in cases where the beam-induced background is significantly high. Also, the angular suppression factor $\varepsilon_{\mathrm{CPC}}$, which determines what percentage of the signal light is forwarded to the PMTs, could be increased for a system that has to cope with a significant amount of beam-induced background. Based on the results presented here, designs using large aspheric lens systems to focus the light from the 4π-mirror to the PMTs are investigated that would increase the total efficiency.

Still, these results show that the new fluorescence detection region presented here is a versatile tool to detect weak resonance signals even at high beam-related backgrounds, which can limit the performance of detection systems with less absolute efficiencies. Furthermore, it is adaptable to different environments and experimental conditions without altering the in-vacuum parts.

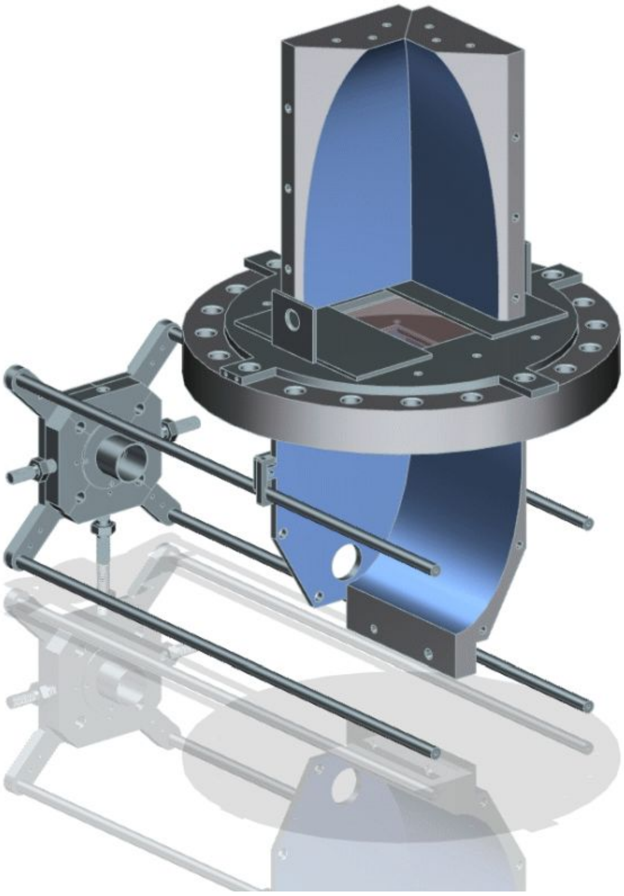

Figure 6.11.: A cross-section of one chamber of the full fluorescence detection region on its frame, which is fixed inside a vacuum tube. Two mounts hold four rods into place, which allow to place and fix the elliptical mirrors in-between, facing the viewports. More details are given in the text.

6.4 Mechanical implementation

As described above, the system is segmented into two parts: The in-vacuum 4π-mirror and the outside vacuum photon guide, which is equipped with the CPCs. Both systems rely on large-surface-area curved mirrors. In this section, the technical implementation of the two systems is described separately, and two different solutions to implement large area mirrors are discussed.

One FDR consists of two separate detection chambers. Each guides light into a distinct viewport and the PMT, which is mounted on top. Both chambers are optically detached but are set on the same acceleration potential. The chambers are separated by $\sim 25\,\mathrm{mm}$ along the beam axis and are aligned separately to the beam axis. This allows an investigation of systematic uncertainties that are introduced by changes in the particle and laser beam within this distance. Although the chambers can have different absolute efficiencies, the center frequency of the recorded resonance should not differ in a simultaneous measurement with high-precision. In the following, mostly one chamber of the FDR is described, as technically two exact copies are mounted behind each other facing different directions.

Two versions of the full detection region were built. The prototype first version (v1) is implemented in the KOALA beamline in Darmstadt. The second version (v2) was produced twice, with one version used at BECOLA, and the other, identical model set up at ANL. Although the concept and especially the optical design was kept between v1 and v2, several mechanical improvements were implemented in the revised second version and a different approach to realize the mirror systems was chosen.

6.4.1 In-vacuum frame

The interior mirror system is mounted inside a stainless steel tube with 160 mm inner diameter and 382 mm length. The tube has two staggered and opposite CF-160 ports on short extensions, where suitable silica windows with high transmission for UV photons are mounted. Additionally, in opposition to each viewport, a CF-16 nipple is placed to feed trough the potential to the system or place vacuum gauges.

The FDR is designed modularly, as shown in Fig. 6.11. The elliptical mirrors sit on a frame, which is fixed inside the tube. They can be brought in and taken out of the system through the side ports were the windows are installed. The frame is built up of four rods with 6 mm diameter, which are held in quadratic alignment with edge length $d = 91\,\mathrm{mm}$. The 4π mirrors fit between two of these rods and can be clamped to them with set screws to fix the assembly. The clamping system allows aligning the 4π mirrors to the beam axis.

The four rods are held by a mount, which presses electrical insulating PEEK® feet against the chamber wall with adaptable screws. One mount is placed at the entrance, a second one at the chamber exit. In this way, the mounts and the four rods can be aligned with the vacuum tube. This decouples the alignment of the frame to the vacuum chamber from the alignment between 4π mirrors to the frame. Practically, this means that the setup and alignment procedure can be performed in independent steps:

- Assembly of the frame and the 4π mirrors independently outside the vacuum chamber.
- Alignment of the 4π mirrors to the frame outside the chamber, but without fixing them in place.
- Mounting the frame (without mirrors) inside the vacuum tube and alignment of the frame to the tube.
- Mounting the tube in the collinear beamline, fine adjustment of the frame to other ion optical elements.
- Now, the 4π mirrors can be brought in from the side. The alignment to the frame entails the alignment to the chamber and the other ion optical elements.

The setup can be adapted to different experimental conditions since the 4π mirrors can be equipped with a new set of mirrors without disturbing the alignment. Also, the alignment of the four rods is independent of the location of the insulating feet.

6.4.2 In-vacuum mirror system

The 4π mirrors have elliptical cross-sections, with the parameters of the ellipsis listed in Fig. 6.5. They are cut 110 mm above the beam axis, which results in a rectangular opening with $80 \cdot 65\,\mathrm{mm}^2$ size. This rectangle is coplanar with the viewport window surface.

The non-conductive window surface does not have a defined potential, and thus the electric field can be distorted in the vicinity of the window. This is critical in high-accuracy measurements with ionic beams. Thus, a metallic conductive mesh with high optical transmission ($\sim$ 80 %)is placed on the rectangular opening to prevent reach-through of the electrical field and, at the same time, provide a high transmission rate for photons from inside the region.

The mesh is pressed into place by corona rings. Since the opening of the mirror chambers is close to the window, point discharges were observed from the cut edges

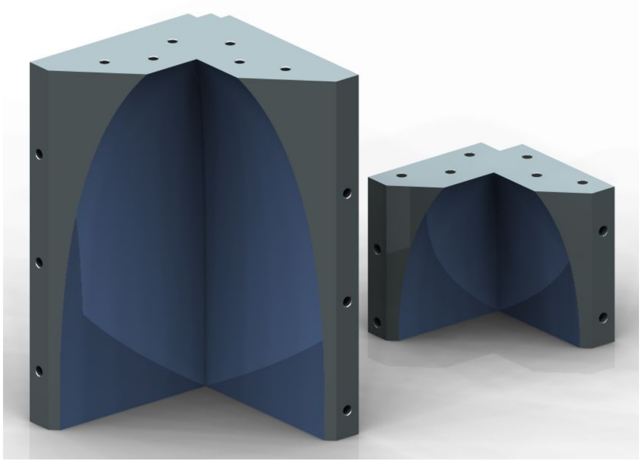

Figure 6.12.: Rendered models of the compound parabolic concentrators that are used in the fluorescence detection region. The mirror surfaces, depicted in blue, have a parabolic cross-section. The large mirror is the CPC20, the smaller one the CPC30.

of the rectangular opening. No observable current drain was measured, but the sensitive photomultiplier measured a purely voltage-dependent background, which could be attributed to the photons emerging from the discharge. The corona ring is a polished disc with round edges that fits smoothly into the viewport opening and covers all sharp edges of the mesh and the mirrors and hence reduces the local electric field strength.

6.4.3 Photon guide

The light guides are placed outside the vacuum chamber. In both versions, v1 and v2, two kinds of CPCs were implemented to guide photons that emerge from the viewport surface to the active area of the PMT. The design parameters of the CPCs are posted in Fig. 6.5. The cutoff angle defines the maximum photon angle with respect to the perpendicular axis of the viewport, for which photons are still transmitted to the PMTs. The CPCs are composite of four quarters, where the two opposite ones form the cross-section of a 2D CPC. Fig. 6.12 shows a 3D model of the design. Simulations showed that the optical performance is close to identical to a 3D concentrator. The benefit is that each quarter is only bent in one axis, making the implementation of surface mirrors by polishing or coating much easier.

6.4.4 Large area mirrors

The realization of the large, bent mirror surfaces is particularly demanding since many constraints have to be fulfilled, especially for the in-vacuum surfaces.

- As indicated in Chapter 6.2.3, the reflectivity of the mirrors for a wide range of wavelengths and down into the deep UV is of utmost importance.
- If specialized solutions are chosen to provide high reflectivity for a specific wavelength, the mirrors need to be exchangeable to allow versatility of the system.
- The surfaces exposed to the particle beam need to be electrically conductive to provide a homogeneous electrical field inside the region and prevent charge pile-up. This is especially important for ionic beams.
- The mirror surfaces are bent to relatively small radii to form the ellipsis.
- The surface areas of several hundred cm^2 are relatively high.

Two different realizations have been probed for v1 and v2. In v2, special attention was given to adapt the system to the ionic calcium D1 line at 396 nm.

Polished surfaces

In the approach used in v1, the curved mirrors were milled from plain aluminum pieces and subsequently hand-polished to optical quality. Bare aluminum has the highest possible reflectivity of all metallic mirrors down into the UV below 250 nm, which is the wavelength in the $p \rightarrow s$ transition of neutral boron. While microscopic mirror quality can be reached with reasonable effort, macroscopic errors (dents) from the milling and polishing process remain on the surface, as can be seen in Fig. 6.13. However, this technique allows a perfect conductivity and vacuum compatibility, and the error in shape is minimal since only microscopic amounts of material are removed from the surface.

More critical, bare aluminum corrodes when exposed to an oxygen-containing atmosphere. While this is not a big concern for the inside mirrors, which should be

Figure 6.13.: Two different techniques were applied to create the mirror surfaces: Sheet mirrors (top) have excellent optical properties, but they lack electrical conductivity when they are prepared for ultraviolet light. However, they allow to easily adapt the system to the wavelength used in the experiment. Hand-polished mirrors (bottom) have a better deep-UV reflection at the cost of macroscopic optical defects.

kept under vacuum or inert gas atmospheres, the CPCs need to be coated with quartz, which prevents corrosion while allowing UV reflection. For the CPCs, conductivity or vacuum compatibility is not necessary, making this approach feasible.

Sheet mirrors

The second approach for v2 used thin (0.05 mm) aluminum reflector profiles for industrial applications as mirrors. Suitable MIRO® mirror sheets from ALANOD[4] were purchased, which guarantee 90 % transmission at 396 nm. They proved to have an electrical conductivity and vacuum compatibility that is adequate for ion beam applications. Cut into the right 2D shape, they can be fitted and pressed (inside vacuum) or glued (outside vacuum) into the desired shape.

Figure 6.14.: High reflectivity mirror sheets are inserted into the elliptic mirror and pressed into form with the corona ring, which is not yet installed in this picture.

Figure 6.14 shows a picture of an elliptical mirror that is equipped with such aluminum reflectors but not yet pressed into the elliptical cylinder, which happens when the corona ring is added. The reflector profiles have excellent microscopic and macroscopic mirror quality, but they are limited to wavelengths in the near UV regime and do not reach out into the deep-UV at 250 nm.

Since the inside vacuum mirror surfaces are simply pressed into place, they can be swapped easily to mirrors with reflectivity in the desired region. For example, spectroscopy in the infrared could be optimized by using bare copper mirrors. On the UV side of the spectra, efforts are made to enhance conductive coatings towards smaller wavelengths < 250 nm. When spectroscopy is done on an atomic beam, non-conductive reflector profiles that excel in reflectivity at low wavelength, could also be used since a varying potential at the FDR will not influence the velocity of the transmitted beam.

---

[4] ALANOD GmbH & Co. KG, Ennepetal, Germany

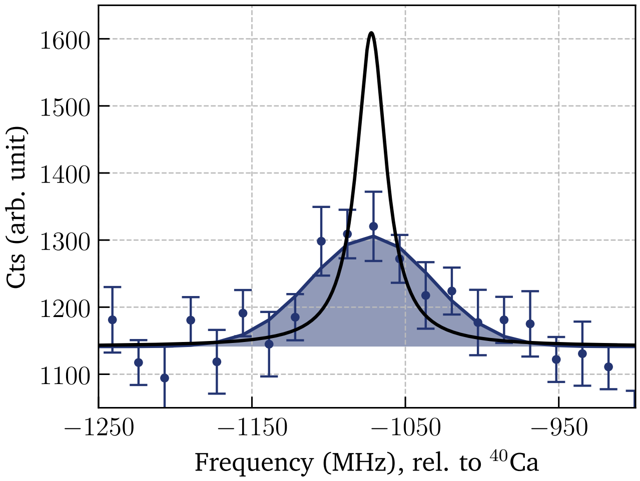

Figure 6.15.: The resonance of ^{36}Ca recorded at the BECOLA beamline. Since the resonance is relatively broad, the Lorentz-normalized signal strength S_L is much higher than the observed signal height. The frequency axis is relative to the center frequency of ^{40}Ca, measured in the same experiment [132].

Table 6.6.: Parameters extracted from the ^{36}Ca resonance, which is shown in Fig. 6.15. The "observed" column gives the values for the not-normalized spectrum as shown, while in the second column, the same parameters for a Lorentz distribution with $\Gamma_\mathrm{nat} = 23.4$ MHz and equal S_summed is calculated.

	S_Summed	S_L	SNR	η_tot
observed	1007.8	179.2	27.5	665.5
Lorentzian		467.8	71.9	254.9

6.5 Results

The fluorescence detection region described in this chapter was used in an online experiment at BECOLA, where the isotope shift in neutron-deficient calcium isotopes was measured to extract their nuclear charge radii [132]. ^{36}Ca was produced at NSCL in a projectile-fragmentation reaction of ^{40}Ca at 140 MeV/A on a thin beryllium transmission target. The produced calcium isotopes are separated from the beam and injected into a gas catcher, where they are thermalized, cooled and ejected in bunched mode towards the collinear laser spectroscopy setup BECOLA.

In the successful experiment, the D1 line in calcium at 396 nm was measured for the low-yield isotope ^{36}Ca with production rates as low as 50 ions per second. With the cooler/buncher running in 180 ms intervals for the $t_{1/2} = 102$ ms isotope, approximately 25 ions per second were observed in front of the PMTs. The cooler/buncher interval was optimized to maximize the SNR, as shorter intervals would lead to more ions in total but also an increase in the total beam gate and thus the background. The laser power was set to 0.3 mW.

Figure 6.15 shows the recorded resonance of ^{36}Ca in one of the detection chambers. Each bin is the sum of 2650 scans, in which ten bunches of 25 ions/s $\cdot$ 180 ms ions passed the detection region, summing to 119250 ions that were observed for each bin. The area of the resonance is 1007.8 counts, which corresponds to $S_\mathrm{L} = 467.8$ and $\eta_\mathrm{tot} = 254.9$ ions per photon. The measured SNR is 27.5, but it would be 71.9 if the natural linewidth of $\Gamma_\mathrm{nat} = 23.4$ MHz was observed. The parameters and calculations are summarized in Tab. 6.6.

In the beamline, a CPC20 was employed. With Eq. 6.14, the total efficiency of the full system $\varepsilon_\mathrm{System} = 0.12$ for the use with MIRO® sheets with $R = 0.88$ and calcium at 396 nm was derived. Additionally, the PMT has a quantum efficiency of 25 % at $\lambda = 393$ nm. Thus, to sum up the $\eta_\mathrm{tot} = 254.9$ ions per photon, a photon is sent out inside the active area of the detection region from every $254.9 \cdot 0.12 \cdot 0.25 = 8$ ion in the beam. From these emitted photons, again every eighth reaches the PMT, and one quarter of those are counted.

This η_tot is an extremely good value for any detection system. This speaks not only for the system itself but also for the quality of the beam overlap and the cooling/bunching system, which provided a low-emittance beam. It also shows that fluorescence laser spectroscopy is feasible even with low-yield beams by employing dedicated detection devices that are highly sensitive to the emitted photons. The only laser spectroscopy experiment with comparably low production rates using fluorescence detection was performed at COLLAPS on ^{52}Ca, with a beam of only a few hundred ions per second [135].

6.6 Outlook

The fluorescence detection region presented here will be used in the ^{8}B experiment at Argonne National Laboratory. The measurement on ^{36}Ca allows to calculate a meaningful efficiency estimate for this experiment, which is performed in chapter 5. To reach the same sensitivity and total efficiency η_{tot}, it is indispensable to employ mirrors that have the same surface reflectivity for the boron 250-nm transition wavelength. Also, since a charge exchange cell will be employed, which introduces a beam-related background, an outside-vacuum detection system that is less discriminating should be used.

The functionality and optical properties of the fluorescence detection region were simulated and verified at the KOALA setup in Darmstadt. The experiments and simulations show further potential for improvement of the system, primarily to adapt it to the ^{8}B measurement at ANL, where the boron atomic transition at 250 nm will be used after charge-exchange of an ionic beam in front of the detection region. This will introduce a large amount of beam-induced background, which can not be tackled with bunched extraction. Table 6.3 shows that the inside vacuum mirror provides an 82 % solid angle detection efficiency at perfect mirror quality. Such a high absolute efficiency η_{tot} is necessary to detect weak signals above beam-induced background. This implies two challenges for the FDR when employed for the boron measurement: The mirror quality at 250 nm and photon collection outside the vacuum chamber. This outlook will focus on how the outstanding performance at the 396 nm calcium D1 transition can be transferred to the challenging boron 250-nm deep-UV atomic transition.

6.6.1 UV mirrors

As described in Sec. 6.4.4, the mirrors have to fulfill many requirements to be suitable for the in-vacuum application and partly contradict the demand for high reflectivity. For the atomic boron beam, however, electrical conductivity is not essential, since the electrical potential does not influence the neutral beam. This opens several options to achieve higher reflectivity.

Figure 6.16.: A rendered drawing of the 4π mirror in the "lamella" design that allows using flat mirrors to form the shape of the ellipsis.

Polished aluminum sheets

In v1 of the system, polished aluminum was used inside and outside the vacuum chamber. The curved parts were polished by hand, leaving microscopic dents on the surface. Also, the surfaces exposed to the air were sealed with a fused silica coating to prevent oxidation, while the inside parts were kept uncoated, making them vulnerable to exposition to air. Although immediate reflectivity tests showed good results also for the reflectivity at 250 nm, diffuse reflection on the imperfect surface was observed.

To overcome the limitations of the manual polishing procedure and the coating, one idea is to combine the mirror sheet approach with a professional polishing process. Professional polishing was not possible for the concave geometries, but it is for flat surfaces. In principle, it should be possible to polish a thin aluminum sheet and bend it into the elliptical and the parabolic shape.

For the CPCs or lightguide, this still implies the problems with oxidation in air. Currently, investigations are ongoing to coat such surfaces with thin graphene coating. Initial inquiries suggest that such a coating is not only electrical conductive but also prevents corrosion and is stable enough to be bent after application.

Dielectric mirrors

A second approach is to segment the curved mirrors into flat mirrors, forming a “lamella” design. A first exploration simulation was performed to compare the full ellipsis with a model that is segmented into 22 flat parts. Each of these flat parts has a standard mirror size that can be produced by commercial manufacturers.

The simulations showed a significant decrease in separation between photons originating from the beam and background photons. This indicates that the background suppression would be much weaker in the “lamella” model, and the employment of CPCs, which separate based on the incident angle, might be needless.

The benefit of such a model was that the segmented mirrors could be specialized for 250 nm or any other wavelength based on the application. Dielectric mirrors provide superb reflectivity of $R > 99\,\%$ for their design wavelength. This would increase the total photon efficiency by almost a factor of 2 compared to the MIRO® sheets for 250 nm and by 25 % compared to their reflectivity at 396 nm, ultimately leading to better efficiency for boron than for calcium.

The downside of this approach is the relatively high cost of the large surface dielectric mirrors combined with their single-wavelength applicability. Using these mirrors for an experiment needs a reasonable justification for implementation that certainly is present for the ^{8}B experiment. Anyhow, more elaborate simulations need to be performed to conclude that such a device would significantly increase the overall performance.

6.6.2 Light guides

To make use of the possible increase in detection efficiency for the 4π mirror, the light guides need to be optimized. Right now, the active surface area of the CPCs limit the maximum acceptance to 73 %, 51 % and 23 % for all photons for the CPC20, CPC30 and NoCPC, respectively (see Tab. 6.3).

Additionally, the cutoff angle suppresses stray light that does not emerge from the beam axis, but it also cuts a large amount of the resonantly emitted signal photons. If the amount of beam background light is high, the stray light suppression becomes unnecessary, and it is crucial to collect as many photons emerging from the beam as possible. This could be accomplished by using dielectric mirrors similar to the “lamella” design and using four flat surfaces in a truncated-pyramid shape. Although the active area can be increased, the performance of such a “simple” design needs to be evaluated.

Lens System

Alternatively, a lens system can be employed outside the chamber to focus light from the inside mirror into the PMT. Lenses with high numerical aperture can principally be mounted onto the viewport window so that the PMT is placed in its focus. Naturally, such a system can be scaled to a large active area, but at the same time, the acceptance for beams that are not perpendicular to the viewport axis is limited. In this sense, such a lens would act as a CPC with a large active area. They can be manufactured from a material that is highly transmissive for deep-UV wavelengths, such as quartz glass.

Currently, a system is investigated that is based on two lenses, one of them inside the vacuum chamber and the other one outside as described. The design is intended to be used in an environment providing a continuous stable beam. During these planned tests, also the combination of 4π mirror and lens will be investigated.

Larger detectors

The PMTs that are used in the setup are round head-on tubes with 20 mm diameter, which have a cylindrical body extending several centimeters behind the active surface. In principle, a simple way to extend the active area on the viewport window is to use semiconductor pixel PMTs. They can be stacked to cover a substantial part of the area where beam photons will impinge.

This would significantly increase the total efficiency of the setup since no reflection or optical transmission is necessary to detect a photon. Also, this is a solution which is, to a reasonable extent, independent of the incident angle. On the other hand, the spatial resolution defined by the pixels could allow an elaborate background-beamlight analysis and distinction. Unfortunately, such pixel PMTs are not only expensive but also have poor quantum efficiencies in the UV. Currently, manufacturers state efficiencies around 5 %, which is 4-5 times lower than the cylindrical PMTs used, diminishing the advantage of the larger area that is covered.

Such semiconductors, given the necessary efficiency, might also be vacuum-compatible and could allow integrating the full detection system into the vacuum chamber. Combining the possibilities of high-reflective, potentially segmented mirrors with in-vacuum position-sensitive PMTs could lead to a new generation of fluorescence detection systems that are the next step in improving the total efficiency of laser spectroscopic experiments. This would allow accessing even rarer low-yield isotopes, with challenging transitions in a purely optical detection approach.

7 Resonance Ionization Mass Spectrometry on stable Boron

In the experiment described in this chapter, the isotope shift in the ground state transition of ^{10,11}B was determined using a two-step ionization scheme

$$2s^2\,2p\,^2\mathrm{P}_{1/2} \xrightarrow[249.75\,\mathrm{nm}]{\lambda_1} 2s^2\,3s\,^2\mathrm{S}_{1/2} \xrightarrow[<371\,\mathrm{nm}]{\lambda_2} \mathrm{B}^+ + \mathrm{e}^-$$

of neutral boron (see Fig. 3.2). The accuracy is sufficient to differentiate the field shift ($\sim 10\,\mathrm{MHz}$) from the mass shift ($\sim 5\,\mathrm{GHz}$). Combined with the atomic physics calculations for the five-electron system outlined in chapter 3, this allows to extract the difference in mean-square nuclear charge radius between the two isotopes. The result obtained is compared with novel ab-initio no-core shell model (NCSM) and Green's function Monte Carlo (GFMC) calculations, which were introduced in chapter 2. The experiment also provided the most accurate values for the frequency of the $p \to s$ ground-state transition and the corresponding spectroscopic factors of the two levels.

7.1 Experimental Setup

The experimental setup is essentially separated into two parts, vacuum beamline and laser system. In the vacuum assembly, which is schematically shown in Fig. 7.1, an offline source produces a boron atom beam, which is resonantly ionized in an ionization region (IR) (also shown in Fig. 7.2) and subsequently mass-separated by a quadrupole mass spectrometer (QMS) and detected by a single-ion sensitive channeltron detector. The laser system (Fig. 7.3) consists of a frequency-quadrupled Ti:Sa laser, which provides 250 nm light to scan and excite the probed transition with high precision, and an ionization laser, which is a Nd:YAG frequency-quadrupled to 266 nm with the sole purpose to efficiently ionize atoms from the first excited to the ionic state.

7.1.1 Offline source

To perform spectroscopy on boron atoms, a beam of such particles must be prepared first. Perpendicular laser spectroscopy, as described in chapter 4, can only be performed on slow atoms since interaction time broadening will occur if the atoms pass the IR faster than their decay lifetime of a few nanoseconds. A laser beam with a diameter of $d = 10\,\mu\mathrm{m}$ is traversed in 10 ns at a velocity of $10^3\,\mathrm{m\,s^{-1}}$. This limits the application of perpendicular laser spectroscopy to thermal atomic beams. Furthermore, a large beam current of boron atoms is required to compensate for the low relative efficiency compared to collinear laser spectroscopy.

To generate a boron atom beam, amorphous boron powder is heated in a graphite tube with currents of up to 140 A. Using an infrared pyrometer, the temperature of the white-glowing tube was estimated to be $\sim 2500\,\mathrm{K}$. Atomic boron, together with many other contaminants, is ejected in forward direction from the tube. Ionic components emitted from the source can be suppressed by applying a low ($\sim -5\,\mathrm{V}$) negative potential to the heated

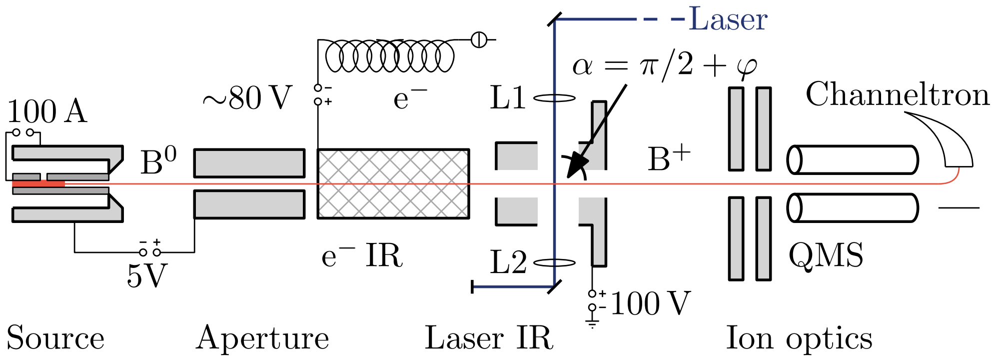

Figure 7.1.: Experimental setup without details of the laser system, which can be found in Fig. 7.3. An atomic beam is generated in an oven on the left-hand side. Pertures limit its spread. The beam can be ionized by electron bombardment (e^- IR) or by laser ionization (Laser-IR) inside the respective interaction region. The generated boron ions are transported with the help of electrostatic deflectors into a subsequent quadrupole mass filter and detected with a channeltron detector which counts single ion events after the mass separation. The lenses L1 and L2 focus the laser beam into the Laser-IR.

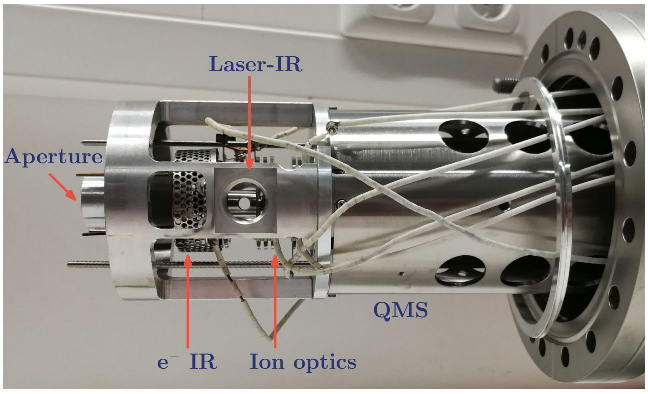

Figure 7.2.: A photograph of the installation on top of the quadrupole mass spectrometer (QMS). The atomic beam enters from the left and passes the electron ionization cage before entering the laser-interaction region. The apertures for the atom beam were removed for this picture. On the right-hand side, the casing of the QMS can be seen protruding from a CF-100 cross piece.

tube relative to the grounded elements following afterward. A tube-shaped aperture was placed in front of the oven to limit the maximum possible angular spread of the beam. The emission properties of the source play a significant role in the data analysis since it influences the observed line widths. Also, temporal changes in the emission must be considered, which are one contribution to the uncertainty caused by the reduced consistency (see Sec. 4.4.4) of a dataset, since the two isotopes were not recorded truly simultaneously. The effect of this will be investigated in Sec. 7.3.8.

7.1.2 Ionization region

Following the aperture, the atom beam enters the ionization region, which is mounted in front of the QMS. This region has two stages and was designed within this work. In the first segment, a thoriated tungsten filament is clamped around a small cage formed with a grid that screens the atomic beam, as shown in Fig. 7.1. A potential difference is applied between the filament and this cage. By heating the filament, electrons are emitted and accelerated towards the cage. They traverse the grid and ionize the atoms by impact ionization. Ions generated in this process are guided through the QMS towards the channeltron, where they are detected.

The impact ionization can be turned on and off by switching the filament current. It is useful to monitor the production rates of the atomic oven in-between measurements. The ionization process works universally for any species of atoms that are bombarded, as long as the electron energy is above the ionization potential. A mass spectrum can then be recorded by scanning the mass-selective QMS, which helps to identify the amount of boron and contaminants produced in the atomic oven.

For the laser spectroscopic measurements, the electron filament is turned off. Atoms traverse the impact ionization region undisturbed and enter the laser ionization region. This is a cylindrical piece with a particle beam entrance and exit hole on top and bottom, and through-holes on the shell that are used for the laser beams. These holes allow a small angular tilt with respect to the atom beam since their diameter is much larger than the laser beam diameters.

The laser beams, of which more details are given in Sec. 7.1.4, are overlapped and focused outside the vacuum chamber and then guided into the laser ionization region. Ion optic elements in front of the QMS generate an electrical field that penetrates the laser ionization region and is optimized to extract all ions generated from the laser beams under resonance conditions. Figure 7.2 shows a photograph of the ionization chamber, centered on the through-hole for the laser beams in the laser-ionization region.

7.1.3 Quadrupole mass spectrometer

The operation principle of the quadrupole mass spectrometer is explained in Sec. 4.1.1. It is based on a combination of a DC potential with an electrical quadrupole RF field that is applied between four cylindrical electrodes elongated along the beam axis. By changing the amplitude of the applied voltages, the transmitted mass can be tuned. The commercial model from EXTREL[1] that is used allows mass scans up to mass 64 u. For this experiment, the resonator was tuned to accept boron ions with mass 10 u or 11 u generated from the electron bombardment. Then, laser ionization was turned on instead, with the laser frequency locked to a peak of the resonance, and the system was tuned again for maximal transmission of boron ions generated by the resonant ionization.

The channeltron, located at the exit of the mass filter, is a fast single particle detector that generates a cascade of electrons that finally hit the collector surface. The electron current is amplified and discriminated, producing a TTL signal, which can be fed into the data acquisition system. The number of ion impact events is recorded with respect to the resonant laser frequency.

7.1.4 Laser system

The laser system is composed of two parts, the resonant and the ionization laser to excite and subsequently ionize boron atoms in the spectroscopic scheme

$$2s^2\,2p\;{}^2\mathrm{P}_{1/2} \xrightarrow[249.75\,\mathrm{nm}]{\lambda_1} 2s^2\,3s\;{}^2\mathrm{S}_{1/2} \xrightarrow[<371\,\mathrm{nm}]{\lambda_2} \mathrm{B}^+ + \mathrm{e}^- \,.$$

Two different continuous-wave (cw) laser systems were employed in the final setup of the measurement, which is shown in Fig. 7.3. The resonant step requires a relatively low power of only several milliwatts at a precise frequency that can be scanned. Higher laser power would lead to saturation and broadening effects. Here, a frequency-quadrupled titanium-sapphire (Ti:Sa) laser is used. The second step does not have constraints on the wavelength other than being below 371 nm, but the power output has to be stable and in the several-100 mW range. Power stability is essential here, since the ionization efficiency and thus the detected rate scales with the intensity of the ionization laser. Long term drifts can be corrected for by monitoring the output, but short-term fluctuations on the same time scale as required for recording consistent pairs of spectra for both isotopes have to be avoided to ensure an unperturbed line profile.

Resonant step laser system

The laser used for the resonance transition is a Sirah Matisse® 2 titanium-sapphire laser that is pumped with a Millenia eV® 20 W pump laser. The laser was tuned to a frequency of ∼ 300 089 800 MHz, which is close to one-fourth of the resonance frequency in the boron transition. The corresponding wavelength of 1000 nm is near the specified operation limit, and absorption lines in the ambient-air filled Ti:Sa ring cavity caused instabilities and made locking the laser on the reference cavity difficult. This was especially critical since the reference cavity is being scanned in this experiment, which is a delicate procedure even when the laser is locked in a comparatively stable position. By reducing the pump power to 18 W, higher stability was reached at the cost of lower output power. Still, with 2.6 W generated in the infrared, the laser performed slightly above specifications.

---

[1] Extrel CMS, LLC., Pittsburgh, USA

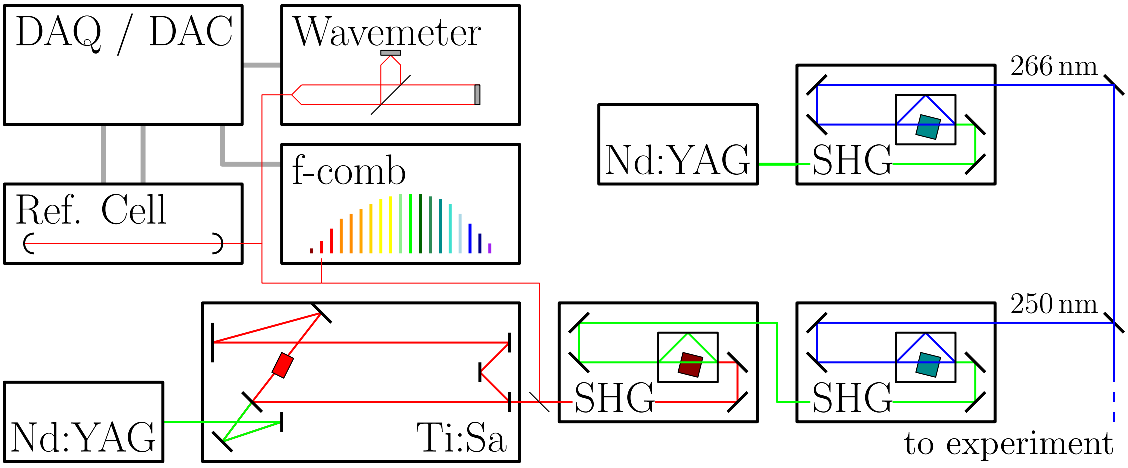

Figure 7.3.: Setup of the laser system. The second harmonic of a Nd:YAG laser pumps a Ti:Sa laser operating at 1000 nm. This light is frequency quadrupled to 250 nm. The beam is then superimposed with a 266 nm beam, which is generated as the fourth harmonic of another Nd:YAG pump laser. A reference and stabilization scheme includes a wavemeter for fast readout and stabilization and a frequency comb for absolute frequency measurements. More details can be found in the text.

The Ti:Sa beam was then directly guided into a Spectra Physics[2] Wavetrain® 2, which uses a lithium triborate (LBO) non-linear crystal placed inside a ring cavity for second-harmonic generation (SHG). The output at 500 nm was approximately 400 mW, which is close to the specified optimum for SHG power conversion under optimal conditions. This output was then fed into another Wavetrain ring cavity equipped with a barium borate (BBO) crystal, which converts the beam to 250 nm. This process was less efficient, only with considerable effort outputs above 20 mW were achieved. In principle, 20 mW is more than needed for spectroscopy, where powers of ≤ 1 mW are used. However, higher power allows easier alignment since the resonant laser is then sufficient to ionize the atomic beam in a resonantly enhanced two-photon ionization. This allows optimizing the QMS and other components under resonant conditions without maintaining the ionization laser.

Ionization Laser

The ionization step in the spectroscopy scheme can in principle be induced by any photon with $E_\gamma > 3.3$ eV, which corresponds to a wavelength of $\lambda < 371$ nm. Since the resonant step is at 250 nm, these photons can also ionize atoms from the excited 3*s* state. However, since the power required for efficient non-resonant ionization causes strong power and saturation broadening in the resonant step, it is preferred to use a second laser with a wavelength considerably different from the resonance transition.

In a first attempt, the light of a high-power 1 W UV light-emitting diode (LED) running at 370 nm was focused into the ionization region, but no sign of ionization caused by the LED light was observed. Since the LED wavelength was specified only slightly below the necessary ionization threshold, it is reasonable to presume that it actually emitted light with a wavelength that was too large. Moreover, the incoherent light emitted with a substantial divergence from a several mm area limits the possible focusing that would be required to achieve high intensities.

Finally, a Coherent[3] Verdi® V8 was employed that delivers light at 532 nm. It was frequency-doubled in a Wavetrain ring cavity equipped with an LBO crystal to provide 266 nm. At an input power of 5 W, approximately 300 mW ultraviolet light was generated. Although at higher input power, an increased output power of up to 800 mW was achieved, the output of the SHG deteriorated with a time constant that became shorter for higher powers. Thus, at around 300 mW, the SHG could be driven with long-term stability expedient for the measurements. Furthermore, the short-time stability for the measurement was better at these powers

---

[2] Newport Spectra-Physics GmbH, Darmstadt, Germany

[3] Coherent Inc., Santa Clara, USA

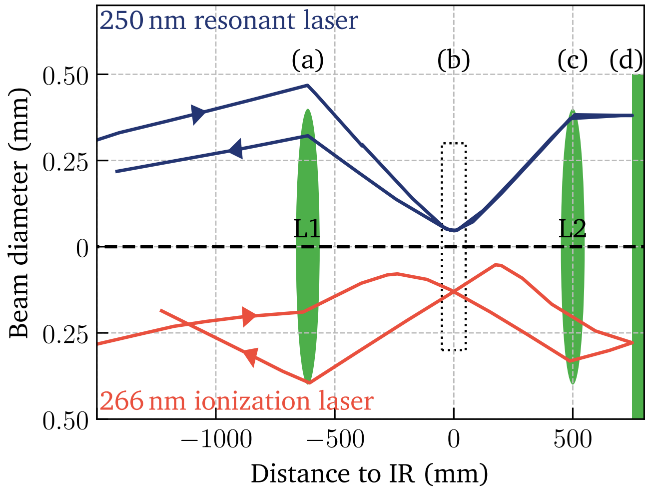

Figure 7.4.: Simulated beam diameters of the two laser beams. After being overlapped, lense (a) with $f = 500\,\mathrm{mm}$ focuses the resonant beam (blue, top) and the ionization laser beam (red, bottom) into the interaction region (b). A second lense (c) with $f = 500\,\mathrm{mm}$ is positioned in front of the back-reflecting mirror (d) and is thus passed twice. The arrangement is optimized to focus the resonant beam into the ionization region twice with similar properties. The ionization laser beam is thus not aligned optimally, but this is not harmful to the resonance ionization scheme.

as well, and the laser was less vulnerable to mechanical disturbances.

7.1.5 Laser alignment

The alignment procedure consists of two steps: Combining both laser beams and guiding them into the ionization region inside the vacuum beamline and back-reflecting them after the first pass through the ionization region.

The primary overlap is done by using a dichroitic beam splitter plate. The plate is reflective for the resonant beam and has a high transmission for the ionizing laser and, thus, both beams can be superimposed. Reflections from this plate were used to monitor the power of both laser beams. After conjoining the two beams, they are guided onto a mirror that directs them into the vacuum chamber through a UV viewport. The mirror is mounted on a translation stage that can be moved with a micrometer screw. This allows changing the traversing angle α through the ionization region without the need of a second mirror. On the translation stage in front of the mirror, a lens (L1) is mounted with a focal length of 500 mm, corresponding to the distance from the ionization region.

After crossing the ionization region, the beam is leaving the vacuum chamber on the opposite side through another UV viewport. Here, a shutter is installed that is controlled remotely and blocks the beam if needed. To realize the back-reflection, the beam is guided through another lens (L2) with the same focal length of 500 mm, forming a 1:1 telescope with L1 before being reflected by a plane mirror. The beam then follows the same path back through L2 and the ionization region.

To ensure the quality of the overlap, several iris apertures are placed within the beam path that the beam has to pass from both directions. After the alignment through these irises, the back-reflected beam disturbed the second harmonic generation ring cavities placed more than ∼ 2 m upstream, which indicated an almost perfect alignment. For the measurements, the back-reflected laser beam was then slightly misaligned in the vertical direction, which does not affect α, to avoid such disturbances. The remaining uncertainty in the quality of the overlap of the two ionization spots of the resonant beam is evaluated based on the datasets in Sec. 7.3.7.

To increase the power of the laser field and to limit ionization to a spot inside the IR, the resonant beam was focused to observe an ionization signal. The lenses L1 and L2 were well suited for this procedure. After passing the ionization region once, the distances between the exit window, L2 and mirror were optimized to establish a telescope optic that back-reflected the resonant beam with similar focal properties as the input beam.

A scheme of this optical path was calculated based on the properties of the two beams and the optical elements in the right distances, displayed in Fig. 7.4. Since the ionization laser beam has different optical properties, it does not follow the optical path designed for the resonant laser beam exactly. Thus, the focus of the ionization laser lies outside of the IR for both first and second pass. This is insofar convenient since a strong but rather homogeneous laser field is formed in the IR. In that way, the ionization laser is less likely to induce separate zones were ionization is differently efficient.

7.1.6 Data acquisition

To record a resonance, the ionization rate indicated by the number of ions per second detected by the channeltron is measured versus the laser frequency. The Ti:Sa laser is scanned using the scheme introduced in Sec. 4.2.1.

A small amount of the Ti:Sa light is fed into a HighFinesse[4] WSU30 wavemeter. The data acquisition software (DAQ) written in Python 3.5 uses this frequency as a reference for scans and stabilization. The computer running the DAQ is equipped with a 16 bit multi-channel digital-to-analog converter (DAC), which is connected to feed an analog voltage signal to the controller of the Ti:Sa reference-cell piezo controller. A simple proportional software stabilization scheme is implemented to stabilize the set frequency on each measurement step, while the count rate on the channeltron is recorded. Additionally, the resonant- and ionization-laser power fed by two power meters placed into reflections of the two beams is continuously read.

The four hyperfine structure peaks span approximately 1 GHz with line widths of $\Gamma_{\text{tot}} \sim 200\,\text{MHz}$. The isotope shift separates the spectra of ^{11}B and ^{10}B by $\sim 5\,\text{GHz}$. Hence, the resonant laser has to bridge that distance. Due to the frequency quadrupling, the Ti:Sa laser has to accommodate only one forth of these frequency changes, which does not pose a problem. The subsequent SHG cavities tolerate such scans and follow the frequency change without notable power or stability losses.

Absolute frequency measurement

To correct for uncertainties in the wavelength determination by the wavemeter, an optical frequency comb (OFC) was employed, which allows realizing highly accurate absolute frequency measurements. An OFC-based frequency measurement can only be performed in certain intervals that correspond to the repetition rate f_{rep} of the comb. Section 4.2.3 outlines how an OFC can nevertheless be used in a measurement where the frequency is scanned.

The Menlo Systems[5] OFC used in the ^{10,11}B experiment allowed a frequency measurement every $f_{\text{rep}}/2 = 100\,\text{MHz}$. During the integration time $t_{\text{comb}} = 40\,\text{s}$ of the OFC, the P-stabilization of the Ti:Sa laser frequency on the wavemeter and the data recording continued. Since the Ti:Sa light is frequency-quadrupled, every $4 \cdot f_{\text{rep}}/2 = 400\,\text{MHz}$ a data point with extraordinarily good frequency uncertainty and high statistics was recorded. Such data points allow the extraction of absolute transition frequencies with high accuracy from the recorded spectra and also help to analyze and eliminate uncertainties introduced by the wavemeter.

---

[4] HighFinesse Laser and Electronic Systems GmbH, Tübingen, Germany

[5] Menlo Systems GmbH, Planegg, Germany

7.2 Analysis and fitting

The acquired data needs to be fitted to extract values for the rest frame transition frequency centroids ν_0, the A-factors and the isotope shift $\delta\nu_{\mathrm{IS}}$. In this section, an overview of the recorded data sets is given. Before fitting the hyperfine spectra, the uncertainties used in the fit need to be assessed, and special attention is drawn to the uncertainties in the wavelength measurement. Finally, the fitting procedure is described, including a comprehensive description of how parameters obtained from the single-pass spectra were used to constrain and converge the more complicated fits for the double-pass spectra.

7.2.1 Data overview

To extract the isotope shift from the centroid frequencies, it is helpful to have consistent spectra of ^{10}B and ^{11}B that are recorded under identical angular setups. To accomplish this, spectra of both isotopes were recorded without changing the laser beam alignment or the atomic oven. This is a consistent set of corresponding spectra.

In total, there are five consistent spectra of ^{10}B from which two have an SP and a DP spectrum, and three only were measured in SP arrangement, but have a full corresponding ^{11}B spectrum. For ^{11}B, nine spectra were recorded in SP and DP alignment, and likewise, two of them can also be referred to the full ^{10}B spectra. An overview of the datasets can be found in Tab. 7.1. The corresponding letters B-K are used throughout this work to indicate the underlying data sets in the analysis. Each letter corresponds to an angular setting and the timely order of the recording procedure. The same letter in a spectrum of ^{10}B and ^{11}B indicates consistency. Other than that, the letters have no physical meaning in the analysis.

7.2.2 Wavelength uncertainties

The primary goal of the experiment is to extract the frequency shift between the hyperfine structure centroids of ^{10,11}B with an accuracy in the order of a few megahertz. Naturally, it is important to experimentally determine the frequency of the resonant laser in each step with a corresponding accuracy.

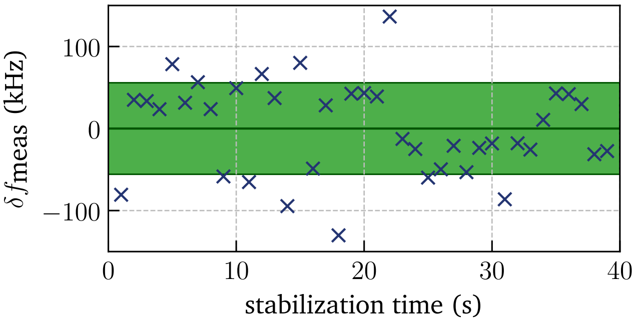

Figure 7.5.: A typical frequency data point measurement. The resonant laser is software-stabilized on the wavemeter. During the stabilization, the optical frequency comb (OFC) reads the laser frequency in 1 s intervals. The standard deviation of 56 kHz indicates the quality of the stabilization scheme since OFC and wavemeter act completely independently.

For each measurement step, the Ti:Sa laser first is driven to the set frequency, and then a simple digital P-stabilization is employed to maintain the frequency during the step duration of several seconds. As described in Sec. 7.1.4, this was performed based on the digital readout of the wavemeter. Intrinsically, the wavemeter gave a ~ 200 kHz standard deviation for the stabilization scheme on each data point. Every 100 MHz in the fundamental 1000 nm laser, corresponding to 400 MHz in the 250 nm ultraviolet forth-harmonic, a measurement with an optical frequency comb (OFC) was interspersed. The OFC measured the frequency for $t_{\mathrm{comb}} = 40$ s, each measurement integrating for 1 s. In this time, the Ti:Sa laser was still locked at the set frequency via the reference cell.

In Fig. 7.5, a forty-second measurement of this locking scheme recorded with the frequency comb is shown. The y-axis gives the absolute frequency minus a constant offset as measured by the OFC in one-second intervals. Thus, the standard deviation of the OFC frequency measurement showed the average frequency scatter introduced by the locking scheme. A typical value for the standard deviation is ~ 50 kHz, which translates to 200 kHz in the frequency-quadrupled ultraviolet light.

Wavemeter scatter

More than that, the offset of the wavemeter, as well as the variable scatter, could be allocated from measuring some data points simultaneously with the OFC. Figure 7.6 shows how the data points gathered by the OFC and the wavemeter were combined. For one exam-

Table 7.1.: The datasets that were recorded in the experiment: The letters correspond to different alignments with different overlap angles φ. Five spectra were recorded consistently in the same alignment for both isotopes, which allows a precise extraction of the isotope shift. Some spectra of ^{10}B were only recorded in single pass (SP) mode, while most of the spectra where recorded in SP and double-pass (DP) arrangement.

Isotope	B	C	D	E	F	G	H	J	K
^{10}B		SP	SP		DP			DP	SP
^{11}B	DP	DP	DP	DP	DP	DP	DP	DP	DP

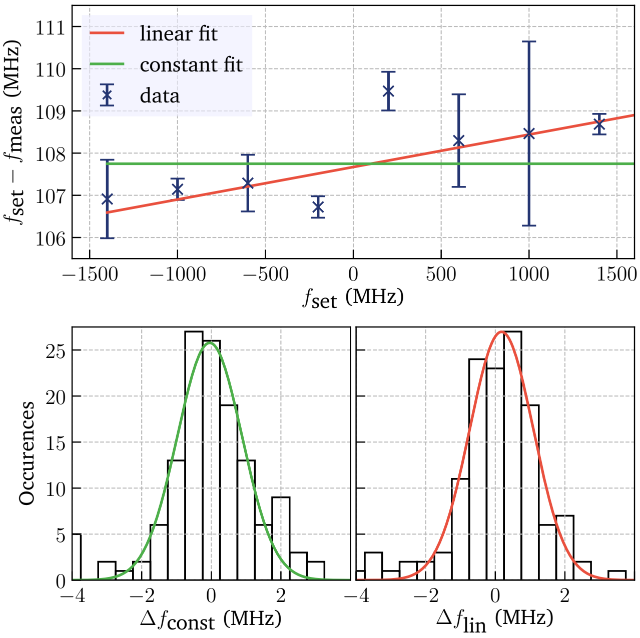

Figure 7.6.: On some data points, the laser frequency was measured by a frequency comb and a wavemeter simultaneously. Top: The difference between the two measurement methods for an example dataset. A linear (red) and a constant (green) fit is shown. Bottom left: The difference between all data points and the constant fit. Bottom right: The difference between all data points and the linear fit. Both interpolations yield a standard deviation of 0.9 MHz, which is used as uncertainty in the data sets.

ple dataset, the frequency offset measured by the OFC is plotted versus the set frequency of the laser, stabilized on the wavemeter. In the fourth harmonic, an offset of around 100 MHz and a scatter of a few MHz is observed. This agrees with the specified accuracy from the WSU30 wavemeter of 30 MHz in the fundamental Ti:Sa output that was measured. A constant and a linear regression line is fitted to the data, giving a simple relation between the frequency that the wavemeter calculates and the OFC measurement.

The difference between the fitted line and every single data point in each scan measured with both comb and wavemeter is plotted in the histograms below. Fitting a Gaussian distribution reveals that the scatter around the regression line has a width of 0.9 MHz in both cases. The $\sigma_{x,\text{WM}} = 0.9\,\text{MHz}$ uncertainty is thus incorporated via Gaussian error propagation into the frequency uncertainty of all data points that were measured with the wavemeter only. This contribution dominates the x-error bars for wavemeter-only data points, since the locking performance only introduces $\sigma_{x,\text{lock}} = 0.2\,\text{MHz}$ uncertainty. For the data points where the comb measured the frequency directly, this correction does not need to be included. Thus, the uncertainty of those data points is only determined by the quality of the digital lock $\sigma_{x,\text{lock}}$.

Furthermore, these data points have a higher number of counts, since here, the OFC integrated longer than the average step duration, also resulting in smaller statistical error bars. Consequently, the spectra are hinged on those “OFC data points”, which thus define the absolute position of the spectra much more than the “wavemeter data points” that have more significant frequency uncertainties.

7.2.3 Fitting routine

Fitting is done by χ^2-minimization

$$\chi^2 = \sum_{i=1}^{N} \left(\frac{N_i - f(x_i)}{\sigma_i} \right)^2 \tag{7.1}$$

of the recorded spectra applying the HFS model that can be derived from the atomic and nuclear properties of each isotope. The single data points with number of counts N have error bars that correspond to their statis-

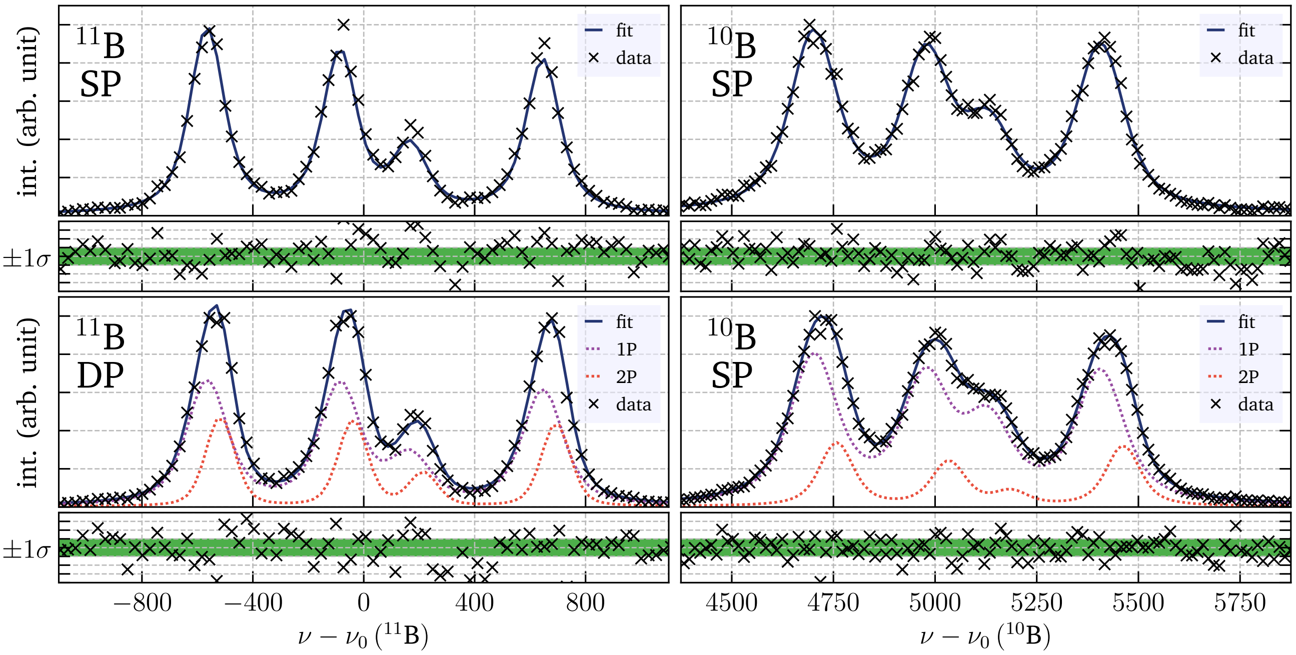

Figure 7.7.: A consistent dataset ('J') with the SP spectrum of ^{11}B (top left) and ^{10}B (top right) as well as the DP spectrum of ^{11}B (bottom left) and ^{10}B (bottom right). The residuals are plotted below the spectra with the green box indicating 1 σ deviation. From the parameters of the fit, the first pass (1P) and the second pass (2P) spectra can be disentangled from the superimposed DP dataset. Details on the fitting procedure can be found in the text. The plots from all other datasets are shown in appendix A.

tical uncertainty $\sigma_i = \sqrt{N_i}$, assuming Poisson statistics. Data points with $N_i = 0$ at the edges of the recorded spectra were assigned an uncertainty of 1. The peak count rates were sufficiently high to legitimate not using maximum-likelihood fitting routines, which can interpret low count rate spectra better. Since the frequency is not known precisely, its uncertainty needs to be incorporated into the fit. This is done by introducing the effective variance

$$\sigma_i^2 = \sigma_{N_i}^2 + \left(\frac{df(x_i)}{dx_i} \sigma_{x_i} \right)^2 \tag{7.2}$$

by locally linearizing the HFS model function, which is a good approximation assuming that the correlation between count rate and frequency is considerably low. This is valid since within the Lorentzian width $\Gamma_{\text{nat}} = 40.1\,\text{MHz}$ of the transition the expected count rate does not significantly change within the uncertainty intervals of $\sigma_{x_i} \leq 0.9\,\text{MHz}$.

Fitting a full dataset consists of two steps: The SP spectrum is fitted first. Then, variables and parameters from this fit are fixed, and the DP spectrum is fitted. Since the two spectra are overlapped closely, fit convergence of the DP spectra was difficult to reach without putting some constraints on the minimization. For the SP spectra, the following side conditions were implemented:

- the Gaussian and Lorentzian width, as well as the upper 3*s* *A*-Factor, was bound to be ≥ 0.
- the Racah intensities were not fixed for the relative amplitudes since the peaks do not follow the expected height distribution.
- all Peaks in the HFS share the same width.
- the *A*-value of the lower 2*p* state is fixed in the χ^2-minimization using the literature value [136] of 122.5851(9) MHz and 366.0765(15) MHz for ^{10}B and ^{11}B, respectively.

With the results of the SP spectra, the DP spectra were fitted. For clarification, SP still refers to the settings from the single-pass without back-reflection. 1P ("first pass") now describes the properties of the first pass in the DP spectrum, while 2P stands for the properties of the second pass HFS. Thus, 1P + 2P = DP. The following fit settings were used:

- all Peaks in the 1P and 2P HFS share the same width.

- the SP centroid is transferred to 1P.
- Racah intensities are still not used, but the relative peak amplitudes from 1P and 2P are fixed to be the same.
- the lower (2*p*) and upper (3*s*) *A*-factor fitted from SP is adopted to 1P and 2P as well.
- the background rates of 1P and 2P fit are equal, which effectively bind them to be positive.

With this comprehensive set of rules, all spectra converged. It is important to choose the start parameters in a way that convergence is reached quickly or at all in some spectra, but other than that, no critical changes were required to converge single spectra individually. In Fig. 7.7, the procedure is summarized for an example spectrum of ^{11}B, with all fit results plotted. For an overview, the corresponding ^{10}B spectrum taken at the same angle φ is shown as well. Together, the spectra shown is a complete, consistent dataset. In appendix A, the other eight spectra are shown, and the bare fit results of all of them are listed in Tab. A.1.

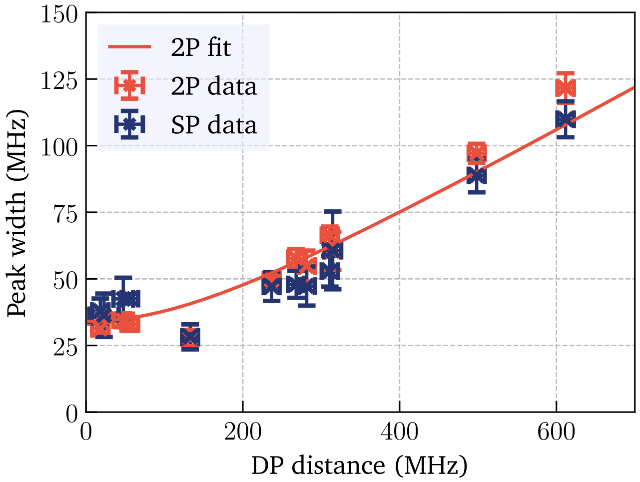

Figure 7.8.: The Gaussian width, extracted from the fits, is plotted versus the distance between SP and 2P centroid. For a thermal source, a linear dependency is expected. There is a residual Gaussian width that does not depend on the overlap angle and induces the offset at zero, as presented in Eq. 7.5 and is caused by the angular spread of the atom beam and the laser beams.

7.3 Line widths and systematic uncertainties

The basic angular relations and the Doppler shift for probing the atomic beam with a laser beam in perpendicular alignment can be found in Sec. 4.4. Most prominently, v is the velocity of the atoms and φ is the deviation from a "perfect" perpendicular overlap with $\alpha = \pi/2$. In good approximation, the transition frequency ν_0 is observed with a shift of

$$\Delta\nu_\mathrm{D} = \nu_0 \frac{v}{c} \varphi \tag{7.3}$$

in the experiment. This section is dedicated to disentangling the different sources of line broadening and uncertainty in v and φ that are mainly a result of the thermal velocity distribution of the atoms emitted from the oven, and the intersection geometry of the atomic beam and the laser beam.

7.3.1 Line width contributions

The shape of the peaks is composed of several contributions. The natural linewidth $\Gamma_\mathrm{nat} = 40.1\,\mathrm{MHz}$ is related to a Lorentzian shape and is determined by the properties of the participating atomic levels.

Since the atoms in the beam are produced in a thermal source, their velocity v is distributed following a Maxwell-Boltzmann profile. Due to the Doppler effect, which is linear in v according to 7.3, this leads to a thermal line broadening approximated by a Gaussian line shape. This broadening is not observed for a perfectly collimated particle beam with a perfectly collimated laser beam under exactly $\alpha = \pi/2$, since then $\varphi = 0$ for all atoms. However, in the experiment, neither of these is fulfilled. A Voigt-profile, which is a convolution of a Lorentzian and a Gaussian distribution, is usually used in the analysis of spectral lines . In the fit, the two contributions can be resolved with corresponding Lorentzian width Γ and Gaussian width σ_G. In principle, also the Maxwell-Boltzmann distribution could be folded into the line shape to accommodate the knowledge about the atom velocity distribution. However, the spectroscopic resolution is not sufficient to differentiate three different convoluted line shapes from the data sets. Especially for fitting the DP spectra, the parameters needed constraints to reach convergence, which contradicts introducing more complex models. The χ^2 values of the fits proved a reasonably good model agreement. Furthermore, in the residuals of the fits, no apparent signs of model disagreement can be found.

The influence of the thermal velocity distribution on the Gaussian width can be tested with the quotient

$$q_{\mathrm{MB}} = \frac{\hat{v}}{\sigma_{\mathrm{MB}}} = \frac{\Delta\nu_{\mathrm{D}}}{\sigma_{\mathrm{MB},\varphi}} \approx 2.10 \tag{7.4}$$

between the Doppler shift $\Delta\nu_{\mathrm{D}}$ and the Doppler width $\sigma_{\mathrm{MB},\nu}$, which is constant for all angles φ as derived in Sec. 4.4.1. The total width

$$\sigma_{\mathrm{tot}} = \sqrt{\sigma_0^2 + \sigma_{\mathrm{MB},\varphi}} = \sqrt{\sigma_0^2 + \left(\frac{\Delta\nu_{\mathrm{D}}}{q_{\mathrm{MB}}}\right)^2} \tag{7.5}$$

is composed of an angle-independent residual Gaussian width σ_0 and the thermal broadening $\sigma_{\mathrm{MB},\nu}$ that depends on φ. This formula can be fitted to the extracted Gaussian width as a function of Doppler shift for all datasets, as displayed in Fig. 7.8. The disagreement between the extracted proportionality constant $q_{\mathrm{MB,\,exp}} = 3.0(3)$ from the theoretical value shows that a part of the total width is shifted to the Lorentzian contribution in the fit. On the other hand, the linear fit shows good agreement in general, which justifies the procedures to extract transition frequencies from the shifted spectra.

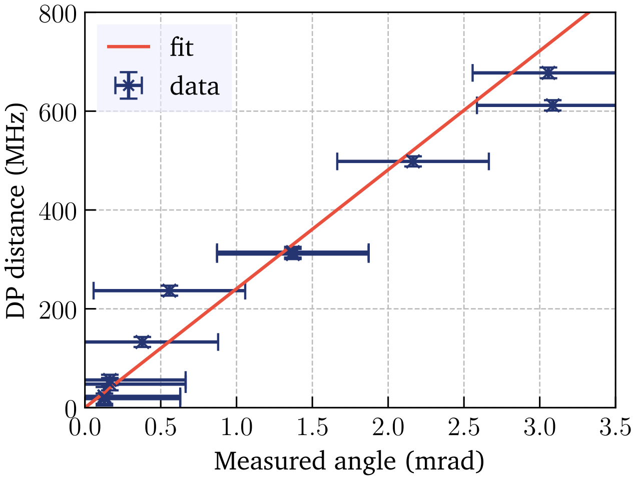

Figure 7.9.: The distances between the two centroids in the SP and the 2P fit are plotted versus the overlap angle φ that was read out manually. Since their distance depends on the velocity of the atoms, which depends on the temperature and the angle, the temperature of the source can be extracted from the slope to be 2600 (400) K.

The residual Gaussian width is

$$\sigma_0 = 34.3(15)\,\mathrm{MHz} \tag{7.6}$$

and can be explained with the geometrical size of source and overlap region, as will be discussed below.

7.3.2 Oven temperature

The temperature of the oven corresponds to the velocity of the emitted atoms and their thermal width. From the data alone, the temperature cannot be fitted since the shift ν_{D} and the width $\sigma_{\mathrm{MB},\varphi}$ both are proportional to $\sqrt{T}$ and φ. However, the overlap angle φ was measured mechanically for each data set by determining the angle in which the laser beam crossed the interaction region. This measurement is considerably coarse, and a precision of 5 mrad was conservatively estimated from the geometric setup. Still, with the data available, it is possible to extract values for the mean velocity and temperature, which have large error bars but are suitable for qualitative analysis. The peak distance between SP and 2P spectra $\nu_{\text{SP-2P}}$ depends on the overlap angle

$$|\nu_{\text{1P-2P}}(\varphi)| = 2\,\nu_0 \frac{\hat{\upsilon}}{c}\,|\varphi| \tag{7.7}$$

with a factor 2, since the SP and the 2P spectra are both Doppler-shifted outwards due to the overlap angle φ. This proportionality relation with inclination $m = 2\nu_0\hat{\upsilon}/c$ can be plotted from the available data and χ^2-fitted, as shown in Fig. 7.9. In principle, the two different isotopes with different masses and different rest-frame transition frequencies ν_0 have different velocities, but the limited precision in manually determining the overlap angle clouds the isotopic difference. Instead, a medium mass of $\overline{m}$=10.5 u and rest-frame frequency of $\nu_0 = 1\,200\,362\,000\,\text{MHz}$ was chosen, and all values for both isotopes are evaluated together for this qualitative argument. The resulting velocity is

$$\hat{\upsilon} = 2100(160)\,\text{m}\,\text{s}^{-1}\,. \tag{7.8}$$

Since the mean velocity and temperature are connected by the underlying Maxwell-Boltzmann distribution with

$$\hat{\upsilon} = 1.04\sqrt{\frac{2k_BT}{\overline{m}}}\,, \tag{7.9}$$

it is possible to assign a temperature of

$$T_{\text{oven}} = 2600(400)\,\text{K} \tag{7.10}$$

to the atomic beam. The temperature agrees well with the value acquired with a pyrometer ($\sim 2500\,\text{K}$). This fitted value of T_{oven} and its corresponding uncertainty will be used throughout the further analysis.

7.3.3 Atom beam characteristics

In this section, the ejection of boron atoms from the source and its influence on the line width is investigated. This is one of the contributions that explain the angle-independent width σ_0 that was extracted above. The atomic beam is emitted from a tube with $d_{\text{oven}} = 2.0(1)\,\text{mm}$ inner diameter, which is filled with boron powder. The center of the ionization region is $s = 0.29(4)\,\text{m}$ away from the middle of the tube. The uncertainty in this distance already reflects the lack of knowledge where, inside the tube, the boron atoms are emitted. A sketch of the geometric setup is shown in Fig. 7.10.

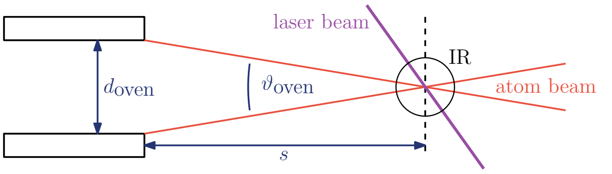

Figure 7.10.: The atomic beam is emitted from the tube on the left-hand side. For the assumption of a point-like ionization spot, the angular distribution of incoming atoms depends on the diameter of the tube d_{oven} and its distance s.

The angle under which atoms can reach the ionization spot is then

$$\vartheta_{\text{oven}} = \frac{d_{\text{oven}}}{s} = 6.9(10)\,\text{mrad} \tag{7.11}$$

assuming that it is point-like. The influence of the extent of the laser interaction zone will be discussed below. This angular spread can be converted to a contribution to the Gaussian line width of

$$\sigma_{\text{oven}} = \nu_0 \frac{\upsilon}{c}\vartheta_{\text{oven}} = 58.0(96)\,\text{MHz}\,. \tag{7.12}$$

This is already much larger than the total line width extracted from the spectra. However, no collimation of the atomic beam was considered, but a homogeneous emission into the whole open solid angle. This assumption is unrealistic since the graphite oven tube already provides some collimation. Under the assumption that the mean free path of the atoms emitted from the surface of the boron powder is long enough to exit the tube unhindered, the extraction angle is given by the emission characteristics from the graphite surface of the inside of the tube. From the dimensions of the oven, some collimation can be assumed [137], which makes atoms with small deviations from the forward angle more probable. A factor of 2 can easily be explained with this behavior, which brings the width σ_{oven} introduced by the source

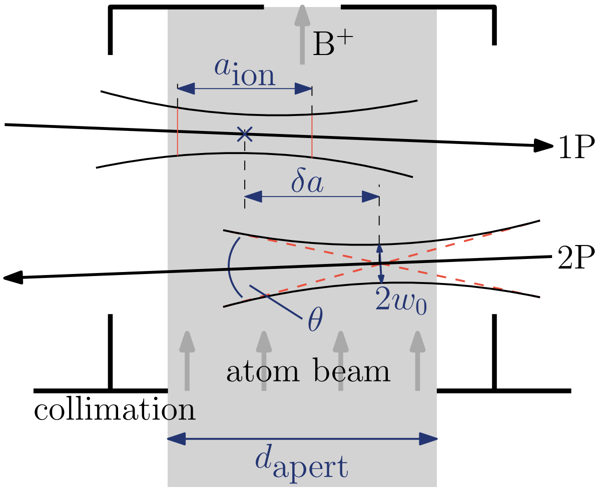

Figure 7.11.: The foci of the resonant laser beams are not point-like but have a waist with diameter $2w_0$, which can be different for the 1P and the 2P beam. To generate boron ions, they both have to lie in the atom beam (depicted in gray, upwards), which is collimated to $d_\mathrm{apert} = 2\,\mathrm{mm}$. The region in which the power density for ionization is sufficiently high has a length a_ion. These regions can be offset by Δa between the two beams. For clarity, the vertical offset is exaggerated in this scheme.

into a range that matches well with the observed width $\sigma_0 = 34.3(15)\,\mathrm{MHz}$.

7.3.4 Laser spot properties

Not only the atom beam but also the laser beam has angular spread since it is not perfectly collimated. Instead, a shallow focus was set into the ionization region to increase the power density there. The focus is not a spot, but rather a longitudinally extended cylindrical volume around the focus in which the power density is sufficiently high to induce ionization. The extent of this region also contributes to the width, since atoms with different angles cross this volume. Both contributions from the angular spread and longitudinal extension are considered in the following, taking the different beam properties from the first and second pass laser beam into account.

Laser beam focus

From the laser path depicted in Fig. 7.4, it is possible to calculate the divergence angle θ of the focus, which is defined in Fig. 7.11. The beam photons have angles relative to the laser axis that deviate by up to $\theta/2$, which is 1.5 mrad for the 1P (=SP) and 1.3 mrad for the 2P beam. This angular shift leads to a Doppler-induced focal broadening

$$\sigma_\mathrm{focal} = \nu_0 \frac{v}{c} \theta \tag{7.13}$$

of the lines, assuming that the angular distribution is normally distributed. This is the case for a beam with a 2D spatial Gaussian intensity distribution. Even for a perfectly collimated atomic beam with $\varphi = 0$, this broadening would occur.

The corresponding width for the SP beam is $\sigma_\mathrm{focal} = 12.6(19)\,\mathrm{MHz}$, and can be used as upper estimate also for the DP beam. The uncertainty of this calculation is difficult to assess since the beam spot properties are extrapolated from measurements of the upstream beam diameter and the optical elements used in the beam. Here, the difference $\Delta\theta/2 = 0.2\,\mathrm{mrad}$ between 1P and 2P beam is chosen.

Longitudinal beam spot

The longitudinal size a_ion of the laser beam spot is the length in which the laser beam power density is sufficiently high to excite and subsequently ionize the boron atoms resonantly. It is defined by the overlap volume of the resonant and non-resonant laser beam, which are focused into the ionization region. Since the laser axis is perpendicular to the atomic beam axis, the laser beam spot extent a_ion induces a spectral width

$$\sigma_\mathrm{longitudinal} = \nu_0 \frac{c}{\hat{v}} \frac{a_\mathrm{ion}}{s} \tag{7.14}$$

since atoms are emitted from the source, which is considered point-like in this case, in the distance s onto the length a_ion. Since the foci are shallow, the length in which the available laser power is sufficient is relatively large. A stronger focus would result in a smaller a_ion but introduce a stronger laser beam spread, which increases the size of σ_focal.

A first estimate for a_ion is the Rayleigh length of the resonant laser beam

$$z_\mathrm{R} = \frac{\pi \omega_0^2}{\lambda} = 7\,\mathrm{mm}\,, \tag{7.15}$$

which is the distance in which the beam diameter cross-section increases by a factor of $\sqrt{2}$, and thus, the beam intensity drops by a factor of 2. This is much larger than the diameter of the atom beam, which is limited by the apertures with diameter $d_{\text{apert}} = 2\,\text{mm}$ and the last one placed shortly before the laser-interaction zone. Thus, the atom beam limits the ionization zone, giving an upper estimate of the longitudinal extent, which results in a width of

$$\sigma_{\text{longitudinal}} = 58.0(110)\,\text{MHz}\,, \tag{7.16}$$

which is almost a factor of two larger than expected from the observed total linewidth $\sigma_0 = 34.3(15)\,\text{MHz}$. This can be explained by assuming that the diameter of the collimated atom beam is only $\sim 0.7\,\text{mm}$, which is smaller than expected from the apertures with 2 mm diameter just in front of the interaction region. An alternative explanation arises from the interplay between the resonant and the ionization laser beam, which both have to form a maximum at the spot where the ionization occurs. Also, the acceptance volume from where generated ions traverse the QMS might limit the spread of the effective laser-atom beam interaction zone. In any case, a combination of these explanations allows the statement that the residual Gaussian width can be attributed to the geometric properties of the overlap of the three beams. The extracted estimates for a_{ion} help to range the quality of the overlap of 1P and 2P beam introducing systematic uncertainties, which are discussed later.

7.3.5 Lorentz width

The spectra were fitted with a Voigt profile, which is a convolution of a Gaussian and a Lorentzian line shape. Most geometric properties of the setup contribute to the Gaussian width, which is also approximated to describe the thermal distribution of the atoms. Most prominently, the natural linewidth appears in a Lorentzian shape, which has the size $\Gamma_{\text{nat}} = 40.1\,\text{MHz}$ for the measured transition in boron. Power broadening can also contribute to the Lorentzian width since the natural linewidth is only observed as long as induced emission is negligible. If the resonant laser power is too high, induced emission occurs, and the lifetime of the 3*s* state is shortened accordingly.

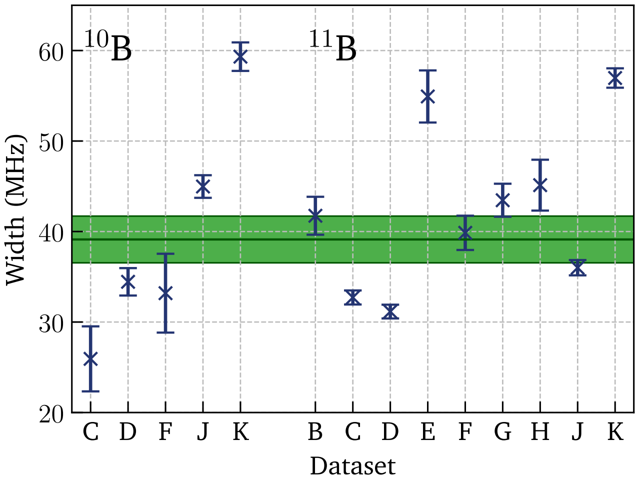

Figure 7.12.: The Lorentz widths extracted from the spectra fitted with a Voigt profile. The mean value agrees with the natural linewidth $\Gamma_{\text{nat}} = 40.1\,\text{MHz}$. The large scatter can be explained since the Voigt profile does not accurately describe the underlying Maxwell-Boltzmann distribution.

The observed Lorentzian widths for the different scans are shown in Fig. 7.12. The weighted average 39.1(26) MHz is in agreement with the natural linewidth, but the scatter is high. This is most likely due to uncertainties in the separation between Gaussian and Lorentzian width contribution in the fitting routine.

7.3.6 Total line width

Table 7.2 provides an overview on the line width contributions discussed so far. To summarize, the contributions can be differentiated into three parts according to their shape and origin.

The Doppler width $\sigma_{\text{MB},\varphi}$ is introduced by the Maxwell-Boltzmann velocity distribution of the atoms and depends on the overlap angle φ, which is different for every measurement set. Its size varies between 0 and 120 MHz, and the relation between φ and σ_{Doppler} shows that Doppler width and shift agree with that of a thermal source.

Neither the atom beam nor the laser beam is perfectly collimated. This introduces a width that is caused by the distribution of angles in which the laser beam and atoms can interact. The total width of this geometric width can be summarized to

$$\sigma_{\text{geom}} = \sqrt{\sigma^2_{\text{oven}} + \sigma^2_{\text{focal}} + \sigma^2_{\text{longitudinal}}}\,. \tag{7.17}$$

Table 7.2.: Survey of the line width contributions that are observed in the experiment. The Doppler width is variable and depends on the overlap angle; it is zero for $\varphi = 0$. The Gaussian widths result from the properties of the atom source and the laser interaction region, and the total Gaussian width is the squared sum of the single contributions. The fitted Gaussian width σ_0 is about half of the expected size, indicating that the collimation of the atom beam was underestimated. The natural linewidth can be extracted from the Voigt fits and agrees with the literature value.

	Symbol	Shape	Value (MHz)	Source
Doppler width	σ_{MB}	M.-B.	0-120	Overlap angle φ
Atom beam	σ_{oven}	Gaussian	58(10)	Oven diameter d_{oven} in distance s
Laser Spread	σ_{focal}	Gaussian	13(2)	Laser focal angle θ
Longitudinal	$\sigma_{\mathrm{longitudinal}}$	Gaussian	58(11)	Laser spot extent a_{ion}
Total Gaussian width	σ_{geom}	Gaussian	83(15)	Gaussian sum of widths
Total Gaussian width	σ_0	Gaussian	34.2(15)	Extracted from Fit
Natural Linewidth	Γ_{nat}	Lorentzian	39.1(26)	Extracted from Fit

The properties of the laser beam are well understood since the Gaussian distribution of the intensity profile and the respective angular spread along the beam axis can be measured and calculated. The width introduced by the size of the oven and the interaction region, however, is overestimated using the geometric parameters. This hints that the atomic beam is well collimated, which can be expected from the size and length of the carbon atomic oven. The discrepancy between the calculated width σ_{geom} and the observed width σ_{tot} can thus be explained by the angular expulsion characteristics of the oven.

Finally, the natural linewidth Γ_{nat}, which has Lorentzian shape can be extracted as a parameter from the Voigt fits. The value 39.1 (26) MHz agrees with the literature value of 40.1 MHz.

7.3.7 Angular overlap

The uncertainty from the angular overlap between the 1P and the 2P laser beams is one of the most dominant, but also an assessable source of uncertainty. The laser beams cross the laser ionization region once and are back-reflected from a back-reflecting mirror behind the vacuum chamber. From here, they cross the ionization region again but in the opposite direction. As depicted in Fig. 7.4, the focus of the laser beam is altered with different optical elements in the beam path, which ultimately lead to a similarly focused resonant beam within the laser ionization region for both directions. The ionization laser beam has slightly different optical beam properties, and its extended focus is shifted outwards and lies not directly inside the ionization region. Two possible sources of uncertainty can be identified: The precision of the angular overlap between the 1P and the 2P laser beam is limited and can be offset, and the two foci can ionize atoms at different spots inside the ionization region.

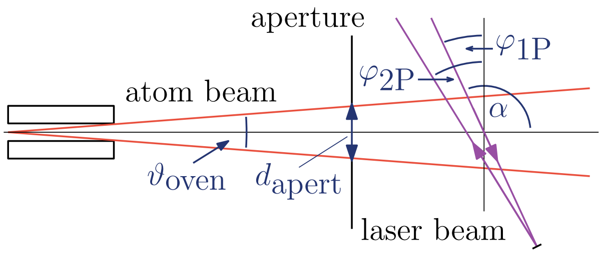

Figure 7.13.: The atomic beam, coming from the left, is emitted into an angular range $\vartheta_{\mathrm{oven}}$, which is limited by the last aperture in front of the ionization region with $d_{\mathrm{apert}} = 2$ mm. The imperfect perpendicular overlap is done at angle $\alpha = \pi/2 + \varphi$ and can be different for the 1P and 2P laser beam, depending on the quality of the overlap. In the ideal case, $\delta_{\mathrm{BR}}\varphi = \varphi_{1\mathrm{P}} - \varphi_{2\mathrm{P}} = 0$

In the experiment, laser ionization was optimized while looking at the SP spectrum with the resonant laser at the maximum power available. When the RFQ settings and the position of the focal point were optimized for maximum production and detection, the shutter was opened, and the back-reflection was overlapped with the incoming beam. Then, the resonant laser power was reduced, so that no ionization occurred without the ionization laser. This effectively minimized the effect of power broadening, as investigated in Sec. 7.3.5. Since the laser beam passes a vacuum viewport twice after the first pass, the laser power available in the second pass is lower than in the first pass.

For that reason, the 2P spectrum was generally smaller in amplitude compared to the 1P spectrum. Also, it was impossible to generate a 2P spectra with a deliberately misaligned back-reflection. Apparently, too little overall power was available for the two-step ionization using just the back-reflected beam. Only when 1P and 2P beam were overlapped sufficiently well, the laser field is strong enough to stimulate the ionization step. Since for all spectra good 2P spectra were observed, this puts constraints on the quality of the back-reflection overlap, since the volumes in which ionization takes place must be intersected. These interaction volumes can be estimated to be cylindrical, with parameters determined from the laser focal properties and the previous investigation of the widths.

The incoming and the back-reflected beam can be offset by $\delta_{\mathrm{BR}}\varphi = \varphi_{1\mathrm{P}} - \varphi_{2\mathrm{P}}$ according to Fig. 7.13, which is constrained by the beam radii. Optimal alignment implies $\delta_{\mathrm{BR}}\varphi = 0$, but the uncertainty $\Delta_{\mathrm{BR}}\varphi$ in this variable, according to

$$\varphi_{1\mathrm{P}} - \varphi_{2\mathrm{P}} = \delta_{\mathrm{BR}}\varphi \pm \Delta_{\mathrm{BR}}\varphi \tag{7.18}$$

needs to be considered. In the same way, the longitudinal offset $\delta a = 0$ is defined in Fig. 7.11, causing an angular uncertainty $\Delta_{\mathrm{longitudinal}}$.

Angular offset

The 1P and the 2P laser beam have different focal properties, which are calculated and illustrated in Fig. 7.4. The beam superposition was performed along the beam path between the exit of the second SHG cavity and the beam splitter plate approximately $s = 2\,\mathrm{m}$ away from the back-reflecting mirror. Here, primary and reflected beam have a measured beam spot radius of $w_{0,1\mathrm{P}} \sim 0.7\,\mathrm{mm}$ and $w_{0,2\mathrm{P}} \sim 0.5\,\mathrm{mm}$ respectively. The uncertainty of the angular overlap can thus be estimated to be

$$\Delta_{\mathrm{BR}}\varphi = \frac{w_{0,1\mathrm{P}}}{s} = 0.4\,\mathrm{mrad}\,, \tag{7.19}$$

conservatively using the larger beam spot radius as an upper estimate. To verify this value, also the size of the ionization spot inside the ionization region can be used as an indicator for the quality of the overlap. The reflective mirror is approximately 0.75 m away from the center of the ionization region. The maximal offset of 0.4 mrad uncertainty would introduce an offset of 0.2 mm between the two beam spots from primary and reflected laser beam inside the IR. The laser beam diameter for the 266 nm ionization laser can be calculated to be $\sim 0.15\,\mathrm{mm}$ in the focal point; the resonant laser is focused to $\sim 0.05\,\mathrm{mm}$. This agrees well with the observed precision in the overlap.

Longitudinal offset

Additionally, the position of the focus of the back-reflected beam can be shifted along the laser beam axis. This could potentially lead to two separate ionization spots. Under the assumption of a point-like, uncollimated source, this uncertainty is equivalent to a misalignment between 1P and 2P beam, since the atomic beam is observed under a different angle $\sim \varphi$. In Sec. 7.3.4, the beam spot length was deduced, showing that it is confined by the atom beam diameter of 2 mm rather than the intensity of the laser beams. Using the observed linewidth, it can be concluded that the width is even smaller and rather corresponds to a longitudinal beam spot extent of $a_{\mathrm{ion}} =\sim 1\,\mathrm{mm}$. This incorporates that the atom beam is actually collimated, and thus the atoms have a slimmer angle distribution than estimated from a point-like source.

Even if this amount separates the two beam spots, it is hardly explainable why the ionization zone of the two spots should be isolated and not overlap each other longitudinally without much loss in “ionization potential”, since their intensity decreases to 50 % within the much larger Rayleigh length of $z_{\mathrm{R}} = 7\,\mathrm{mm}$ (see Eq. 7.15). Additionally, if both beam spots are shifted outwards in the opposite direction and thus induce the largest laser ionization zone separation possible, the difference in overlap angle φ partially cancels. This is why $\delta a = 0.25\,\mathrm{mm}$ is estimated.

Since the source is $s = 0.29\,(4)\,\mathrm{m}$ away from the laser spot, this corresponds to a shift of

$$\Delta_{\mathrm{l(ongitudinal)}}\varphi = 0.9(1)\,\mathrm{mrad} \tag{7.20}$$

in which the source is effectively observed. This can be treated as uncertainty in the otherwise perfect overlap of the two interaction regions with $\delta_{\mathrm{l(ongitudinal)}} = 0$. The longitudinal misalignment of the two beams does not immediately affect the angle φ, but it contributes in the same way as a misaligned back-reflected laser beam since the laser/atom-beam intersection angle is different for the primary and reflected beam.

The possible longitudinal offset is much larger than the angular offset, has the same effect in φ but is not correlated. Thus, the uncertainty of the mean angular overlap

$$\left|\delta_{\mathrm{a(ngle)}}\varphi\right| = |\delta_{\mathrm{BR}}\varphi| + |\delta_{\mathrm{l}}\varphi| = 0 \tag{7.21}$$

is

$$\Delta_{\mathrm{a(ngle)}}\varphi = \sqrt{(\Delta_{\mathrm{BR}}\varphi)^2 + (\Delta_{\mathrm{l}}\varphi)^2} = 1.0\,\mathrm{mrad}\ , \tag{7.22}$$

which will be used as angular overlap uncertainty in the analysis and discussion.

7.3.8 Angular drifts

In the previous discussion, the properties of the source and the laser were supposed to be stationary, i.e., not changing in time. However, some spectra that are evaluated in this analysis are taken in a period of several hours. In these intervals, parameters like temperature or angular expulsion might have changed. The half-life of the boron powder in the atom source was several hours, which means that macroscopic amounts of material were “burned”, and the oven had to be refilled several times. This already shows that, for example, the angular spread of the atomic beam might change within hours, since the layer from which the boron is emitted changes when a significant amount of material is removed.

Table 7.3.: Summary of the angular uncertainties present in the experiment. The largest contribution is the possible misalignment of the laser focal spots, which can be offset longitudinally. The angular and longitudinal back-reflection offset can be square-summed since they are uncorrelated. Drifts in time might occur since the oven burns a significant amount of boron within the measurement time.

Misalignment	**Symbol**	**Size** (mrad)
Angular Back-Reflection	$\Delta_{\mathrm{BR}}\varphi$	0.4
Longitudinal Offset	$\Delta_{\mathrm{l}}\varphi$	0.9
Total Overlap	$\Delta_{\mathrm{a}}\varphi$	1.0
Drift in time	$\Delta_t\varphi$	0.8

It is difficult to estimate the maximum amount of change in the several hour-interval that was characteristic of the change between the two boron isotopes. If the central emittance spot in the line of sight to the ionization area changes its position by 0.5 mm, which is a quarter of the inner tube diameter, this corresponds to a change of 0.8 mrad in observed transition frequency. This can be used as a conservative estimate for the angular stability, including the source characteristics within several hours. To keep the consistent notation introduced for the angular overlap, the angular drift in time is $\delta_t\varphi = 0$ with uncertainty $\Delta_t\varphi = 0.8\,\mathrm{mrad}$.

7.3.9 Total angular uncertainty

The total angular uncertainty that has to be included in the evaluation is listed in Tab. 7.3. The sum of the overlap uncertainty $\Delta_{\mathrm{a}}\varphi = 1.0\,\mathrm{mrad}$ plays a significant role for the determination of absolute transition frequencies. The drift in time $\Delta_t\varphi = 0.8\,\mathrm{mrad}$ is also relevant especially when two spectra are combined that are recorded after each other in time. This is the case for consistent ^{10}B and ^{11}B spectra, which are recorded under the same angle φ and are thus used to extract the isotope shift.

7.4 Results

Three significant physical results can be extracted from the measurement series. Firstly, the hyperfine *A*-factors of the participating atomic levels. The *A*-factor of the excited 3*s* state is determined experimentally for the first time. Secondly, the absolute transition frequency of the $2p \rightarrow 3s$ transition in both isotopes is measured. The third result, with the most significant and immediate physical relevance, is the measurement of the isotope shift, which has been measured for the first time with accuracy sufficient to extract the difference in mean-square nuclear charge radius between the two isotopes. The extraction of the three results will be discussed in the following sections giving special attention to the investigation of uncertainties based on the previous discussion.

7.4.1 Extraction of observables

The three observables A, ν_0 and $\delta\nu_{\mathrm{IS}}$ (in general: Ξ) were each measured several times independently, which allows using the mean value and the corresponding uncertainty extracted from all datasets. Here, this scheme is outlined as a reference for the data and uncertainty analysis that follows.

Each Ξ is measured i times in i different datasets, each providing one value ξ_i either directly as a fit parameter (A) or by combining several parameters using the corresponding formulas (ν_0 and $\delta\nu_{\mathrm{IS}}$). The statistical uncertainty is obtained from the fit σ_{fit}. The uncertainty in ξ_i can be calculated from σ_{fit} in combination with the systematic errors that were derived in the last section, providing σ_{ξ_i}.

From the set of single data points $\xi_i \pm \sigma_{\xi_i}$, it is possible to extract a weighted mean value

$$\Xi = \frac{\sum_i \xi_i \sigma_{\xi_i}^{-2}}{\sum_i \sigma_{\xi_i}^{-2}} \tag{7.23}$$

of each of the observables Ξ with the "inner error"

$$\sigma_{\mathrm{inner}} = \left(\sum_i \sigma_{\xi_i}^{-2} \right)^{-\frac{1}{2}} . \tag{7.24}$$

For $i \rightarrow \infty$, $\sigma_{\mathrm{inner}} \rightarrow 0$, which converts the systematic uncertainty from each individual measurement into a statistical uncertainty in Ξ. This is possible since each dataset was taken under completely different conditions: By changing the angle φ between each dataset, the focal properties in the IR changed, and the back-reflection had to be re-established. No identified systematic error contributes similarly for each ξ_i and would thus introduce a systematic shift in Ξ. The laser frequency is measured periodically with an optical frequency comb (see. Sec. 4.2.3), and the data points measured with a wavemeter only have a "realistic" uncertainty derived from the comparison with the OFC. This frequency uncertainty is integrated into the statistical uncertainty of the fit. Other systematic uncertainties are eliminated in the double-pass scheme introduced in Sec. 4.4.4.

Since the "fit model" for the values Ξ is a constant, there should be no model disagreement expressed by the "reduced Chi-squared" value

$$\chi^2_{\mathrm{red}} = \frac{\chi^2}{\nu} , \tag{7.25}$$

which is the sum of the squared deviations according to Eq. 7.1, per degree of freedom ν. If all systematic uncertainties were captured correctly and the number of individual measurements i is large enough to compensate statistical variations, this is expressed by $\chi^2_{\mathrm{red}} = 1$. However, only a few measurements were performed for each observable, and the assessment of systematic errors is not necessarily quantitatively correct, which causes the inner error not to reflect the variance of the individual data points ξ_i completely. This can be compensated by including the model agreement χ^2_{red} into the uncertainty using

$$\sigma_{\mathrm{tot}} = \sigma_{\mathrm{inner}} \cdot \sqrt{\chi^2_{\mathrm{red}}} . \tag{7.26}$$

In the results, the uncertainty discussion following the extraction of each observable is focused on the size of the individual error bars given by σ_{ξ_i}, while the final value and its uncertainty is defined according to Eq. 7.23 and Eq. 7.26 respectively.

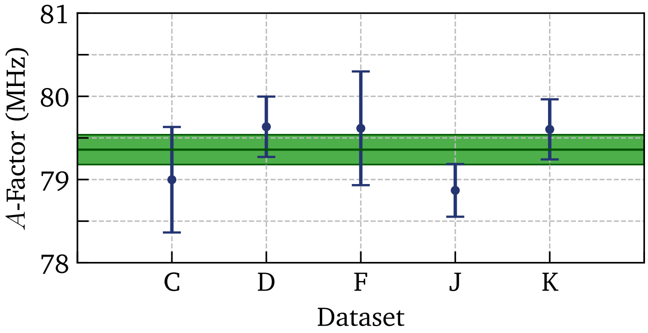

Figure 7.14.: The magnetic hyperfine factor A for the excited $3s$ state in ^{10}B is obtained from the weighted mean value of 5 measurements as 79.3 (2) MHz.

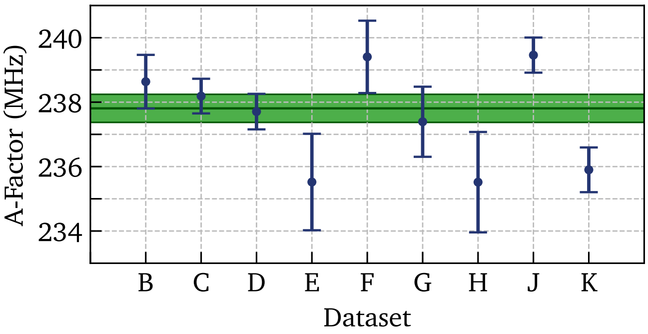

Figure 7.15.: The magnetic hyperfine factor A for the excited $3s$ state in ^{11}B is obtained from the weighted mean value of 9 measurements as 238.0 (4) MHz.

7.4.2 Magnetic hyperfine factors A

The spectral lines of boron are split due to the nuclear spin I and its interaction with the electron angular momentum J. The magnitude of the splitting is associated with the magnetic dipole moment. Since a $J_i = 1/2 \rightarrow J_f = 1/2$ transition is probed, no influence from higher order contributions than the magnetic dipole moment can occur. According to Eq. 3.25, the transition frequency of one hyperfine peak is given by

$$\nu_i = \nu_0 + \frac{C_\mathrm{u}}{2} A_u - \frac{C_\mathrm{l}}{2} A_l \qquad (7.27)$$

with ν_i being the observed frequency, shifted from the center-of-gravity (fine-structure) frequency ν_0. Since C_u and C_l are factors determined by the quantum numbers of the upper and lower level, the corresponding upper and lower A-factors $A_u = A_{3s}$ and $A_l = A_{2p}$ can be extracted from the set of four peaks visible in the recorded spectra of boron.

Table 7.4.: The A-factors extracted from the spectra in this work in comparison to values from other publications. The $2p\ ^2\mathrm{P}_{1/2}$ was fixed to the value from [136] in this work. The value provided by [91] is the result of a purely theoretical calculation, which only uses the nuclear magnetic moments as input. The corresponding plots are shown in Fig. 7.14 and 7.15. For both isotopes, this is the first time that the $3s\ ^2\mathrm{S}_{1/2}$ A-factor is reported.

	Level	A (MHz)	Ref.
^{10}B	$2p\ ^2\mathrm{P}_{1/2}$	122.5851(9)	[136]
		122.4624(6)	[91]
	$3s\ ^2\mathrm{S}_{1/2}$	79.3(2)	this work
^{11}B	$2p\ ^2\mathrm{P}_{1/2}$	366.0765(15)	[136]
		365.7101(18)	[91]
	$3s\ ^2\mathrm{S}_{1/2}$	238.0(4)	this work

The A-factor of the ground state is well known from RF transitions, which can be measured higher accuracy than achievable from the hyperfine spectra. The literature values for both isotopes ^{10,11}B [136] that were used in the χ^2 minimization routine are listed in Tab. 7.4, together with the result from a recent, purely theoretical calculation that only uses the nuclear magnetic moments as input [91]. The A-factor of the upper $3s$ state is not known experimentally so far since the magnetic moment of the short-lived excited state has not been accessed by RF measurements.

To determine A_{3s}, only the fits of the SP spectra are considered. The value extracted from the SP fit is later used as a constraint in the 2P fit to reach convergence, so no additional information is obtained by the 2P spectrum. The final value is obtained from the weighted mean of all measurements that were taken in SP mode, in the scheme explained in Sec. 7.4.1. The slight angular shift φ does not alter the level splitting and thus has no significant influence on the A-values. The results are listed in Tab. 7.4 and plots of the individual values and the mean are presented Fig. 7.14 and 7.15. The single values can be found in appendix A in Tab. A.1.

Table 7.5.: Transition frequencies extracted in this work in comparison to values from other publications. The corresponding plots are shown in Figs. 7.16 and 7.17. The uncertainties are reduced by a factor of ∼ 60.

Isotope	Transition Freq ν_0 (MHz)	Ref
^{10}B	1 200 363 905(120)	[138]
	1 200 364 066.2(17)	this work
^{11}B	1 200 358 689(90)	[138]
	1 200 354 700(7400)	[91] (theory)
	1 200 359 033.9(14)	this work

Hyperfine structure anomaly

The comparison of A-factors

$$A = g_I \mu_N \frac{B_0 h}{J} \tag{7.28}$$

in the two isotopes allows investigating the hyperfine anomaly, which is introduced in Sec. 3.1.3. From the values extracted here,

$$r_{\mathrm{A}}\left(^{11}\mathrm{B}\right) = \frac{A_{2p}\left(^{11}\mathrm{B}\right)}{A_{3s}\left(^{11}\mathrm{B}\right)} = 1.538(3) \tag{7.29}$$

for ^{11}B and

$$r_{\mathrm{A}}\left(^{10}\mathrm{B}\right) = \frac{A_{2p}\left(^{10}\mathrm{B}\right)}{A_{3s}\left(^{10}\mathrm{B}\right)} = 1.546(3) \tag{7.30}$$

for ^{10}B. A significant hyperfine structure anomaly can be excluded at the level of experimental accuracy since

$$R_{\mathrm{HSA}} = \frac{r_{\mathrm{A}}\left(^{11}\mathrm{B}\right)}{r_{\mathrm{A}}\left(^{10}\mathrm{B}\right)} = 1.005(3)\,. \tag{7.31}$$

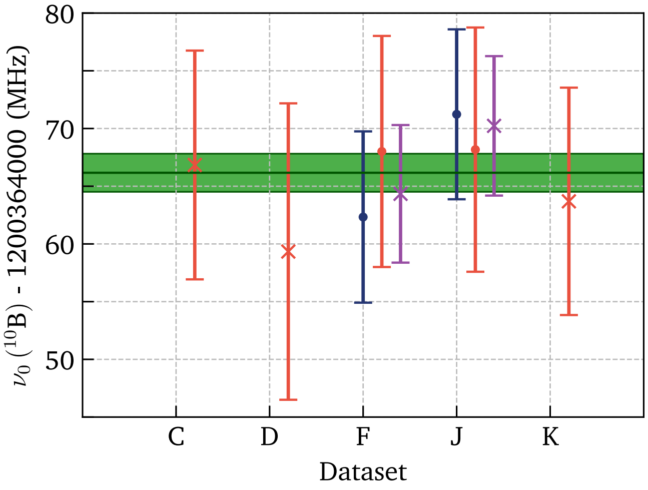

Figure 7.16.: Rest frame transition frequency of ^{10}B. The values of each individual measurement can be extracted in two different ways, depicted in blue and red. In case both methods are possible, the weighted average can be formed (purple). The values used for the weighted mean, displayed as a green line with uncertainty bar, use cross symbols. More details can be found in the text.

7.4.3 Absolute transition frequencies

From an individual dataset, the rest-frame transition frequency can be extracted using Eq. 4.34 where the centroid of the 1P spectrum is identical to the centroid of the SP spectrum due to the fitting constraint, giving

$$\nu_{0,\mathrm{simple}} = \frac{\nu_{\mathrm{SP}} + \nu_{2\mathrm{P}}}{2}\,. \tag{7.32}$$

The values for $\nu_{0,\mathrm{simple}}$ derived in this simple scheme are plotted in blue in Figs. 7.16 and 7.17.

The velocities of the ^{10}B and ^{11}B atoms in the beam are related since they acquire the same average kinetic energy in the thermal source. The velocity ratio, defined in Eq. 4.37,

$$r_v = r_v^{10} = \frac{v^{10}}{v^{11}} = \sqrt{\frac{m_{11}}{m_{10}}} = 1.0486 \tag{7.33}$$

is thus simply the square-root of the ratio of isotopic masses. To avoid confusion, r_v is used exclusively in the following equations and is synonymous to r_v^{10}. This allows to use Eq. 4.41,

$$\nu_{0,\mathrm{alt}}^{A'} = \nu_{\mathrm{SP}}^{A'} + \frac{\delta\nu_{\mathrm{DP}}^{A} \cdot r_v^{A'}}{2}\,, \tag{7.34}$$

which embeds the information of the DP spectrum of one isotope A to extract ν_0 of the other isotope A' by scaling

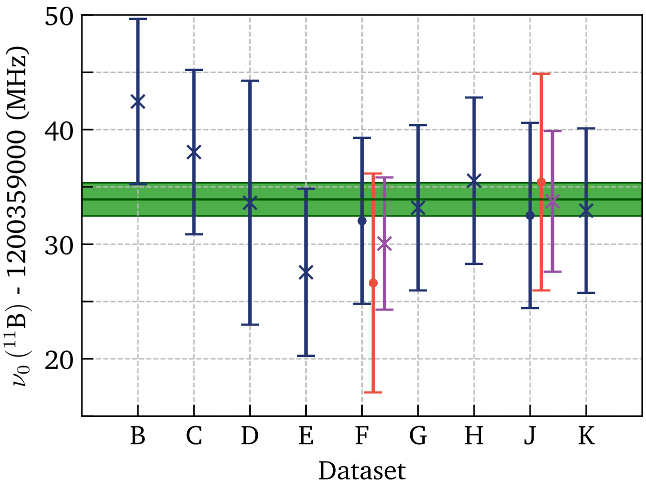

Figure 7.17.: Rest frame transition frequency of ^{11}B. The values of each individual measurement can be extracted in two different ways, depicted in blue and red. In case both methods are possible, the weighted average can be formed (purple). The values used for the weighted mean, displayed as a green line with uncertainty bar, use cross symbols. More details can be found in the text.

it with the derived velocity ratio. This is especially interesting for the spectra C, D and K in ^{10}B were no DP spectrum was recorded. However, it allows to extract a second value with additional information for many other spectra as well, plotted in green.

For the final value for ν_0, which is the weighted average of the individual measurements, the value

$$\nu_{0,\mathrm{combined}} = \frac{\nu_{0,\mathrm{simple}} + \nu_{0,\mathrm{alt}}}{2} \tag{7.35}$$

is used when a DP spectrum was recorded, and a consistent measurement of the other isotope exists as well. The combined values are plotted in purple. Those values that are used for the weighted average are marked as a cross. The uncertainty discussion of the individual data points follows below. The plotted values and the corresponding uncertainty for each dataset can be found in appendix A.

From the five ^{10}B spectra,

$$\nu_0\left(^{10}\mathrm{B}\right) = 1\,200\,364\,066.2(17)\,\mathrm{MHz} \tag{7.36}$$

can be extracted. The nine ^{11}B spectra yield

$$\nu_0\left(^{11}\mathrm{B}\right) = 1\,200\,359\,033.9(14)\,\mathrm{MHz}\,. \tag{7.37}$$

The values emerging from this measurement improve the accuracy of the previously obtained values by Johannson [138] by more than one order of magnitude and agrees with them within 1.3σ and 1.5σ, respectively. A summary of all past and this experimental value can be found in Tab. 7.5.

Uncertainty estimation

In the estimation of uncertainties in the rest-frame transition frequency, the two cases $\nu_{0,\mathrm{simple}}$ and $\nu_{0,\mathrm{alt}}$ have to be distinguished. The combination of the two values, $\nu_{0,\mathrm{combined}}$ is the weighted mean with the according uncertainty.

To estimate the uncertainty in Eq. 7.32, it is important to include the possible mismatch $\delta_\mathrm{a}\varphi$ between the incoming and the back-reflected laser beam, according to Sec. 7.3.7. This results in a modified equation

$$\nu_{0,\mathrm{simple}} = \left(\nu_\mathrm{SP} + \nu_\mathrm{2P} + \delta_\mathrm{a}\varphi\,\beta\,\nu_0\right)/2 \tag{7.38}$$

where $\delta_\mathrm{a}\varphi = 0$, but the corresponding uncertainty $\Delta_\mathrm{a}\varphi = 1.0\,\mathrm{mrad}$ needs to be considered. The velocity is given as $\beta = \upsilon/c$. Using Gaussian error propagation, the total uncertainty is given by

$$\begin{aligned} \sigma^2_{\text{tot, simple}} &= && (\Delta\,\nu_\mathrm{SP})^2 \\ &+ && (\Delta\,\nu_\mathrm{2P})^2 \\ &+ \left(\frac{\hat{\upsilon}\,\nu_0}{2c}\right) &\cdot\; & (\Delta_\mathrm{a}\varphi)^2 \end{aligned} \tag{7.39}$$

where the first two terms include the statistical uncertainty that result from the fits. The third term includes the quality of the back-reflection, and is summarized in Tab. 7.3. Due to the scale of the uncertainty, choosing the exact value for ν_0 does not have a significant effect.

The uncertainty in $\nu_{0,\mathrm{alt}}$ requires to additionally introduce the possibility of an angular drift in time $\delta_t\varphi$, which is 0 in the ideal case but carries the uncertainty $\Delta_t\varphi = 0.8\,\mathrm{mrad}$. The generalized formula for the absolute transition frequency $\nu^{A'}_{0,\mathrm{alt}}$ of isotope A' using the DP spectrum from isotope A is

$$\begin{aligned}\nu^{A'}_{0,\mathrm{alt}} &= \nu^{A'}_{\mathrm{SP}} + \delta_t \varphi \beta \nu_0 \\ &+ \left(\nu^{A}_{\mathrm{2P}} - \nu^{A}_{\mathrm{SP}} + \delta_{\mathrm{a}} \varphi \beta \nu_0\right) \cdot \frac{r^{A'}_{v}}{2} \,. \qquad (7.40)\end{aligned}$$

For this alternative approach evaluated using Eq. 7.34, the uncertainty analysis is slightly more extensive. The total uncertainty is

$$\begin{aligned}\left(\sigma^{A'}_{\text{tot, alt}}\right)^2 &= \left(\tfrac{1}{2}\right)^2 \cdot \left(\Delta \nu^{A'}_{\mathrm{SP}}\right)^2 \\ &+ \left(\frac{r^{A'}_{v}}{2}\right)^2 \cdot \left(\Delta \nu^{A}_{\mathrm{2P}}\right)^2 \\ &+ \left(\frac{r^{A'}_{v}}{2}\right)^2 \cdot \left(\Delta \nu^{A}_{\mathrm{SP}}\right)^2 \qquad (7.41) \\ &+ \left(\frac{\hat{v}\,\nu_0}{2c} r^{A'}_{v}\right)^2 \cdot \left(\Delta_{\mathrm{a}}\varphi\right)^2 \\ &+ \left(\frac{\hat{v}\,\nu_0}{2c}\right)^2 \cdot \left(\Delta_t\varphi\right)^2 \,.\end{aligned}$$

The first term includes the total statistical uncertainty from the fit. Alike, the second and the third term include the statistical uncertainty from the fit of the other isotope. The fourth term includes the misalignment between the first and second pass laser beam, which is conservatively estimated to be $\delta_{\mathrm{a}}\varphi = 1.0\,\mathrm{mrad}$ like in Eq. 7.39. Lastly, the temporal changes in the expulsion characteristics are included, as discussed in Sec. 7.3.8.

The single data points have systematic uncertainties of ~7 MHz, and they are averaged, resulting in a statistical error of 1.4 MHz for ^{11}B and 1.7 MHz for ^{10}B. The uncertainties seem to be slightly overestimated, which allows scaling by χ^2 to reduce the total uncertainty. The result is reasonably insensitive to different sizes of the single systematic uncertainty contributions. As discussed before, averaging of these systematic uncertainties is possible since the angle φ and thus also the parameters $\delta_{\mathrm{a}}\varphi$ and $\delta_t\varphi$ were changed in a randomly from dataset to dataset. No significant systematic error was found that contributed to each data point in the same direction.

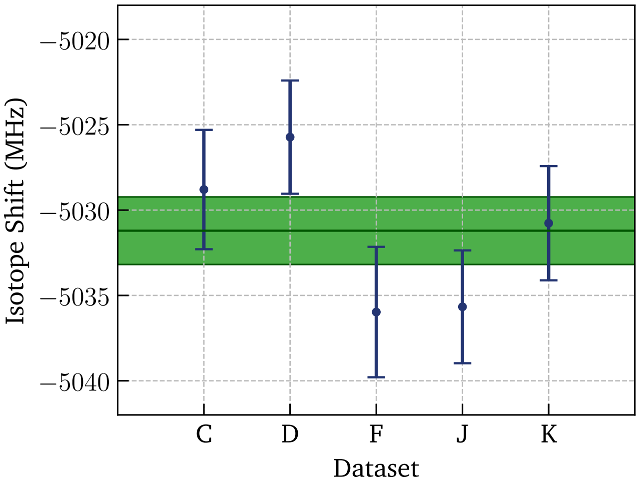

Figure 7.18.: Five spectra allowed to extract the isotope shift with the reduced uncertainty scheme presented in the text. The individual error bars are dominated by the time-dependent shift that might occur due to changing spatial expulsion behavior of the offline source.

7.4.4 Isotope shift

The isotope shift can be directly extracted from the new values for the absolute transition frequencies listed in Tab. 7.5, which yields

$$\delta\nu_{\mathrm{IS}} = \nu^{10}_{0} - \nu^{11}_{0} = -5032.3\,(22)\,\mathrm{MHz} \qquad (7.42)$$

using Gaussian error propagation for the uncertainty. From the datasets, it is possible to extract the isotope shift with an alternative scheme that actively cancels systematic uncertainties dataset by dataset before averaging. This is possible since, for each of these consistent datasets, the angle φ was left untouched while switching between the two isotopes, and the oven current and temperature did not change. Thus, the ^{10}B and ^{11}B SP spectra are both Doppler-shifted in the same direction with a functionally related, but not identical magnitude. The difference results from the velocity difference due to the different isotopic mass, since all atoms emerge from the oven with the same kinetic energy. The velocity ratio r_v (see Eq. 7.33) describes this difference and is constant as long as the experimental parameters are constant, as is the case for consistent datasets.

Table 7.6.: The isotope shift is calculated from five different consistent datasets where spectra from ^{10}B and ^{11}B were recorded subsequently with identical experimental conditions. The uncertainty contributions from the SP and 2P fits and the angular misalignment and shift are included. The numbers presented here are the square root of the uncertainty term in the Eq. 7.46.

Dataset	Isotope Shift (MHz)	σ_{IS} (MHz)	ν_{SP}^{10} (MHz)	ν_{SP}^{11} (MHz)	$\Delta\nu_{\mathrm{DP}}^{11}$ (MHz)	$\Delta_{\mathrm{a}}\varphi$ (MHz)	$\Delta_t\varphi$ (MHz)
C	−5028.8	3.5	1.4	0.6	0.0	0.3	3.1
D	−5025.7	3.3	0.7	0.6	0.4	0.3	3.1
F	−5036.0	3.8	1.7	1.3	0.0	0.3	3.1
J	−5035.6	3.3	0.7	0.7	0.2	0.3	3.1
K	−5030.8	3.3	0.8	0.8	0.0	0.3	3.1
tot.	−5031.3	2.0					

Table 7.7.: The isotope shift extracted from other publications in comparison with the value from this work. The mass shift is the mass-related part of the total isotope shift and was calculated theoretically as presented in Sec. 3.2.1. The discrepancy equates to the field shift.

$\delta\nu_{\mathrm{IS}}$ (MHz)	Ref.
−5250(360)	[139]
−4110(360)	[140]
−5220(150)	[138]
−5023.00(8)	mass shift
−5031.3(20)	this work

Following Eq. 4.40, the isotope shift is calculated from

$$\delta\nu_{\mathrm{IS}} = \nu_{\mathrm{SP}}^{11} - \nu_{\mathrm{SP}}^{10} + \frac{\delta\nu_{\mathrm{DP}}^{11}}{2}\cdot(1-r_{\upsilon}) \ , \qquad (7.43)$$

which only depends on the two SP transition frequency centroids and the 2P centroid from ^{11}B. Since the mass ratio is close to 1, and $1-r_{\mathrm{v}} = -0.049$, the 2P spectra, which were much more difficult to measure and to fit, only contribute slightly to the value of the isotope shift. Figure 7.18 shows the five values extracted with Eq. 7.43 from the datasets together with their uncertainty bars and the averaged value of

$$\delta\nu_{\mathrm{IS}} = -5031.3(20)\,\mathrm{MHz}\ . \qquad (7.44)$$

The negative sign used here consistently indicates that the absolute transition frequency of ^{11}B is lower than that of ^{10}B.

Uncertainty analysis

In order to incorporate the uncertainties in Eq. 7.43, two more terms need to be added, so that

$$\delta\nu_{\mathrm{IS}} = \nu_{\mathrm{SP}}^{11} - \nu_{\mathrm{SP}}^{10} + \delta_t\varphi\beta\nu_0 + \left(\frac{\Delta\nu_{\mathrm{DP}}^{11}}{2} + \delta_{\mathrm{a}}\varphi\beta\nu_0\right)\cdot(1-r_{\upsilon})\ . \qquad (7.45)$$

The term containing $\delta_t\varphi$ reflects the possible change the of expulsion angle of the source in between the measurement of ^{10}B and ^{11}B. Likewise, the term with $\delta_a\varphi$ includes misalignment between incoming and back-reflected beam. Since both $\delta_t\varphi$ and $\delta_a\varphi$ cannot be determined and experimental conditions have been optimized to minimize their absolute value, they are assumed to be zero and only their uncertainties $\Delta_t\varphi$ and $\Delta_a\varphi$ will be considered in the analysis.

The total squared uncertainty is

$$\begin{aligned}\sigma_{\mathrm{IS}}^2 &= \left(1+\tfrac{(1-r_v)}{2}\right)^2 &&\cdot\ (\Delta_{\mathrm{SP}}^{11})^2\\ &+ \left(\tfrac{(1-r_v)}{2}\right)^2 &&\cdot\ (\Delta_{\mathrm{2P}}^{11})^2\\ &+ &&\ (\Delta_{\mathrm{SP}}^{10})^2\\ &+ \left(\tfrac{\hat{v}\nu_0}{2c}\right)^2 &&\cdot\ (\Delta_t\varphi)^2\\ &+ (1-r_v)^2\left(\tfrac{\hat{v}\nu_0}{2c}\right)^2 &&\cdot\ (\Delta_{\mathrm{a}}\varphi)^2 \quad . \end{aligned} \tag{7.46}$$

The single-pass-spectrum SP and 2P uncertainties $\Delta_{\mathrm{SP/2P}}^{A}$ are the uncertainties associated with the respective fit, which can also be found in the appendix A. They enter into the uncertainty budget with different magnitudes in relation to r_v. The last two terms include the uncertainty expulsion angle shift in time, estimated to be $\Delta_t\varphi = 0.8\,\mathrm{mrad}$, which sums up to 3.1 MHz, being the largest direct contribution to the uncertainty budget. The quality of the overlap is estimated by $\Delta_{\mathrm{a}}\varphi = 1.0\,\mathrm{mrad}$, but the corresponding uncertainty is scaled down with $(1-r_{\mathrm{v}})^2$ and thus only contributes with approximately 0.3 MHz to the total uncertainty.

The value for the centroid of the second-pass, extracted from the double-pass spectra fit, usually exhibits a large uncertainty of several megahertz. In some cases, the double-pass spectra were not recorded for ^{10}B at all since the production rates from the oven dropped significantly, and the measurements were focused on collecting statistically valuable data for the single-pass spectrum. The difference $\delta\nu_{\mathrm{DP}}^{11}$ between the SP and the 2P for ^{11}B has a relatively large uncertainty but its contribution to the isotope shift is marginal since it also scales with $1-r_{\mathrm{v}} = -0.0486$.

A summary of the different numerical contributions to the uncertainty can be found in Tab. 7.6. The uncertainty budget is dominated by $\Delta_t\varphi$ as expected since tiny shifts in angle lead to significant deviations in the isotope shift. Figure 7.18 shows the isotope shift from the five complete datasets with their respective error bars. The relatively large scatter of the five extracted values for the isotope shift can only be well explained when $\Delta_t\varphi$ is included as systematic uncertainty that does not shift the values in a particular direction.

The value $\delta\nu_{\mathrm{IS}} = -5031.3\,(2.0)\,\mathrm{MHz}$ agrees well with the isotope shift extracted from the absolute transition frequencies, and has a slightly smaller uncertainty, which is sufficient to extract nuclear structure information from the measurement. The isotope shift has never before been explicitly measured, but measurements of the absolute transition frequencies allow to extract the isotope shift, as listed in Tab. 7.7. The latest value from [138] results in a shift of 5216 (150) MHz. This corresponds to almost two orders of magnitude improvement in the precision of this measurement.

7.5 Evaluation

The measurement of the isotope shift allows the extraction of the difference in the mean-square nuclear charge radius between ^{10}B and ^{11}B with the help of exact atomic theory calculations. In the following, this method is outlined, and the result is compared with nuclear theory calculations. The argumentation widely follows the letter [45], which was published with the results from this experiment, atomic theory and nuclear model calculations.

7.5.1 Field shift and nuclear charge radius

The isotope shift in an atomic spectrum is caused by the difference in nuclear mass and volume. A comprehensive introduction to this topic is given in Chap. 3. The mass shift in the ground-state transition of boron was calculated by K. Pachucki and M. Puchalski to be $\delta\nu_{\mathrm{MS}} = -5023.00(8)\,\mathrm{MHz}$. The difference to the measured isotope shift of $\delta\nu_{\mathrm{IS}} = -5031.3\,(2.0)\,\mathrm{MHz}$ is caused by the field shift and related to the change in mean-square nuclear charge radius by

$$\delta\nu_{\mathrm{FS}} = K_{\mathrm{FS}}\langle r_c^2\rangle \ . \tag{7.47}$$

The field shift can be calculated from the experimental result by subtracting the theoretical mass shift $\delta\nu_{\mathrm{MS}}$

$$\delta\nu_{\mathrm{FS}} = \delta\nu_{\mathrm{IS}} - \delta\nu_{\mathrm{MS}} = -8.3\,(2.0)\,\mathrm{MHz} \ . \tag{7.48}$$

Since also the electron wave function and thus the field shift factor $K_{\mathrm{FS}} = 16.91\,(9)\,\mathrm{MHz/fm^2}$ can be calculated, this allows to extract the change in nuclear charge radius between ^{10}B and ^{11}B to

$$\langle r_c^2\rangle^{11} - \langle r_c^2\rangle^{10} = -0.49\,(12)\,\mathrm{fm}^2 \ . \tag{7.49}$$

This value is obtained by the high precision measurements that are described in this chapter and by the novel atomic theory calculations for the five-electron system. The combination of these two fields of physics on a high precision level allows a test of yet another field of physics on a high precision level, namely nuclear theory.

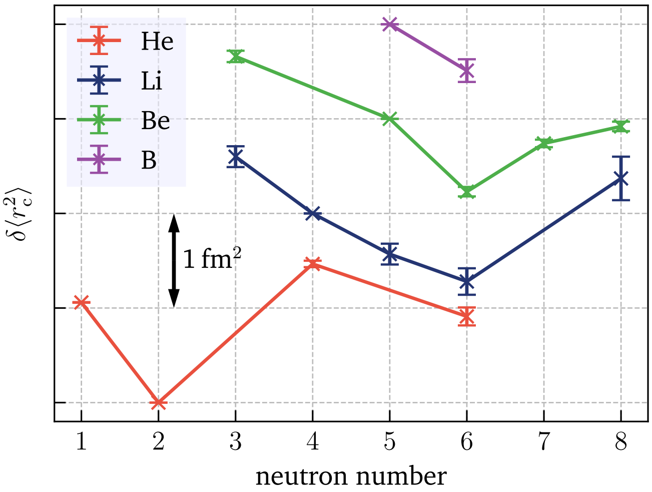

Figure 7.19.: A collection of $\delta\langle r_c^2\rangle$ from different laser spectroscopic experiments investigating different elements (He: [38, 39], Li: [98, 40], Be: [41, 104]). The newly obtained value for boron (purple) follows the trend of the other isotopic chains.

7.5.2 Comparison with nuclear structure theory

As mentioned in the introduction of this chapter, the boron system is an exciting domain for nuclear theory, since the few-body system can be accessed with ab-initio theories that model the nucleus from fundamental interactions. Also, the result obtained can be compared with other light isotopes, which sheds light on possible cluster structures and related behavior of the nucleons in the nuclear volume.

Comparison with other light systems

The negative sign of $\delta\langle r_c^2\rangle^{10,11}$ reveals that the charge radius of ^{11}B is smaller although it is the heavier nuclear system. This can be explained with a cluster structure, which also helps to phenomenologically understand the charge radii of isotopes of the neighboring elements.

A collection of charge radii along the isotopic chain of helium, lithium and beryllium together with the new results for boron is shown in Fig. 7.19. The decrease in charge radius from the heavier to the lighter isotope is well in line with the results for lithium and beryllium. The decrease in charge radius from ^{7}Li to ^{6}Li can be interpreted as the result of a triton (t) instead of a deuteron (d) bound to an alpha cluster. The same effect is visible for the boron isotopic chain, where the d binds two

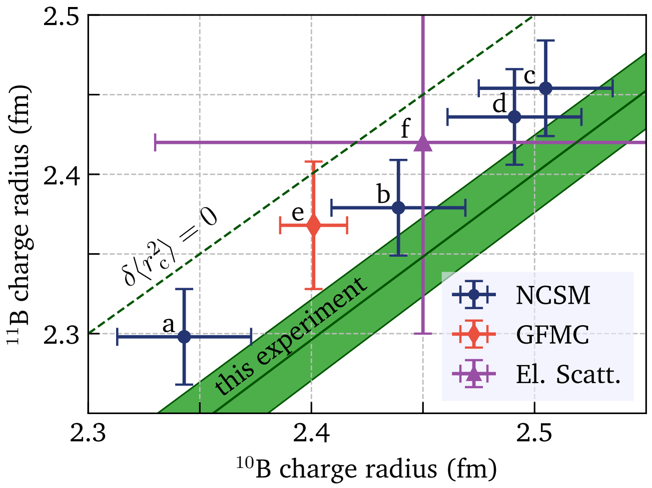

Figure 7.20.: Each point in the graph corresponds to a pair of ^{10,11}B charge radii. The isotope shift measurement presented here gives a difference in charge radius, which is depicted as a line with the respective green uncertainty band. Different theoretical results (circles and diamonds) are plotted as well as results from electron scattering (triangle).

alpha clusters less tightly in the case of ^{10}B than a t in ^{11}B.

In comparison with beryllium, the double alpha cluster structure ^{8}Be is unbound ($t_{1/2} = 6.7 \cdot 10^{-17}$ s) and so is ^{9}B ($t_{1/2} = 8.4 \cdot 10^{-19}$ s), which indicates that the additional proton does not support binding the system. On the other hand, an additional neutron does, making ^{9}Be a stable isotope of beryllium. In the same way, adding neutrons to ^{10}B and the neighboring isotopes increases the binding strength indicated by the charge radii.

These empirical arguments are obviously not sufficient in describing all that can be learned from the experimental findings, but help to explore the nature of nuclear structure on an intuitive level.

Ab-initio theories

In a more elaborate approach, two ab-initio nuclear structure theories predict values for the mean-square nuclear charge radius for both isotopes of boron, which allow deducing their difference measured in this laser spectroscopic experiment. One of them is the no-core shell model (NCSM), the other one is Green's Function Monte Carlo (GFMC), which both were introduced in the nuclear theory chapter 2.

Figure 7.20 shows the experimental result in the ^{10}B/^{11}B charge radius plane. Each point represents a set of mean-square nuclear charge radii for the two isotopes. Since only the difference in this charge radius was measured, the result obtained by the laser spectroscopic measurement presented here is resembled by a line with the corresponding uncertainty band. The originally non-linear shape of this line is not perceivable on the scale represented in the graph.

The triangle (f) marks the result from electron scattering [141]. The large error bars indicate that from these results, it is not even reliably predictable that ^{11}B is smaller in size than ^{10}B.

The results of the nuclear model calculations are also included in the graph. The points a)-d) in red show the NCSM calculations with different interactions, cut-offs and flow parameters. All calculated values lie approximately on a straight line, which is shifted towards a smaller $\delta\langle r_c^2\rangle^{10,11}$, but is also compatible with the experimental value. The same is true for the GFMC calculation e) in green, which uses a fundamentally different approach to calculate charge radii for ^{10}B and ^{11}B.

The trend to predict a smaller difference in mean-square charge radii than measured experimentally could hint to nuclear phenomena in the boron nuclei that are not well understood and thus not incorporated into the fundamental forces used for the ab-initio calculations. However, on the current level of experimental accuracy, their correctness is also not excluded since they all lie within a 2σ uncertainty band. The absolute radii vary considerably for the different theories but are still within 1σ from the electron scattering result. Thus, an improved "absolute" radius measurement would provide significant information for the test of nuclear theory.

After all, the calculations presented here show the latest results for some of the most complex nuclear systems that were ever addressed with these models. Although they already provide remarkable predictions on a high precision level, they can only be further improved when they are accompanied by high-precision, model-independent measurements on light and also exotic systems as shown and presented in this work.

8 Summary and Outlook

The focus of this work is the expansion of high-resolution laser spectroscopy of light isotopes to boron, which is the lightest element that has not been investigated up to date. The measurement of the isotope shift

$$\delta\nu_{\mathrm{IS}} = \delta\nu_{\mathrm{MS}} + K_{\mathrm{FS}}\delta\langle r_c^2\rangle \ .$$

in different isotopes of one element allows to extract the difference in mean-square nuclear charge radius $\delta\langle r_c^2\rangle$.

Just recently, the theoretical calculation of the mass shift $\delta\,\nu_{\mathrm{MS}}$ and the field shift factor K_{FS} was performed specifically for the ground state transition

$$2s^2\,2p\;^2\mathrm{P}_{1/2} \xrightarrow{249.75\,\mathrm{nm}} 2s^2\,3s\;^2\mathrm{S}_{1/2}$$

of the atomic boron five-electron system. The accuracy allows the extraction of the field shift from a correspondingly accurate measurement of the isotope shift. This optical transition is sensitive to a change in nuclear charge radius (expressed by a large field shift factor K_{FS}), the excitation wavelength can be reached with state-of-the-art highly-accurate commercial laser systems, and the preparation of boron in the neutral atomic state is possible.

In the experiments described in this thesis, the isotope shift in the stable isotopes of boron ^{10}B and ^{11}B was measured for the first time with a precision that allows extracting the differential mean-square nuclear charge radius. Also, the efforts to expand these measurements to the best-known proton halo candidate, the short-lived ^{8}B, are outlined, and significant progress has been made towards this ambitious goal.

8.1 Laser spectroscopy on ^{10,11}B

An atomic beam of the two stable isotopes of boron, ^{10}B and ^{11}B, was produced in an electrothermal graphite oven at temperatures of about 2600 K and collimated with small apertures to restrict the Doppler width in laser spectroscopy. This beam was overlapped with two superimposed laser beams in perpendicular alignment. One laser is used to excite the resonance transition while the second one provides sufficient energy to ionize the excited atoms non-resonantly. The produced ions were detected almost background-free with a quadrupole mass spectrometer. An elaborate measuring scheme employing retroreflection of the laser beams into the interaction region was used to reduce systematic shifts caused by deviations from a truly perpendicular alignment between atom and laser beam.

The most important result of this work is the isotope shift

$$\delta\nu_{\mathrm{IS}} = -5031.3(20)\,\mathrm{MHz} \tag{8.1}$$

between ^{10}B and ^{11}B in the ground state $p \rightarrow s$ transition. This value allowed us to extract the change in mean-square nuclear charge radius

$$\delta\langle r_c^2\rangle^{11} = \langle r_c^2\rangle^{11} - \langle r_c^2\rangle^{10} = -0.49\,(12)\,\mathrm{fm}^2 \ ,$$

with the negative sign indicating that ^{11}B is the smaller isotope and thus the more tightly bound nuclear system. This result can be qualitatively explained by the cluster structure of these light nuclei. It was also used to benchmark more advanced ab-initio theories, namely Green's function Monte Carlo (GFMC) and no-core shell model (NCSM) calculations. Both approaches predict a slightly smaller difference in nuclear size, but overall, the agreement between experiment and theory on this level of precision is remarkable.

8.2 The ^{8}B project

The isotope shift measurement that was performed on the stable boron isotopes will be extended to the exotic, short-lived ^{8}B, which is produced at a high-energy target at the ATLAS facility at Argonne National Laboratory (ANL). Here, collinear spectroscopy will be used in a quasi-simultaneous collinear/anticollinear measurement to reach the required accuracy. Towards this goal, the production rate of ^{8}B was increased, and a molecular breakup system was developed. The latter became necessary since the produced ^{8}B ions are stopped in a gas cell and leave the stopping cell with water molecules attached to them. The breakup system is based on the transmission of the compounds through nm-thin carbon membranes, which resets their atomic shell and thus breaks the molecular bond. The transmission through these membranes and their thickness was investigated in several experiments and showed promising results. The subsequent gas catcher, which will cool the ions before releasing them into the collinear beamline, is currently being commissioned.

Fluorescence detection region

In parallel to the efforts in production and state preparation, the collinear beamline that was formerly situated at the TRIGA reactor in Mainz was shipped to ANL and set up in an offline laboratory. A new laser ionization source was implemented, allowing offline testing of the components and preparation for “online” beam. Special attention was given to the fluorescence detection region to achieve a high detection efficiency for the fluorescence photons.

Therefore, the existing system was revised and redesigned to allow for versatile adaption to various wavelengths used in the experiments: Apart from the systems implemented at the KOALA beamline in Darmstadt and at ANL, another copy was installed at the BECOLA beamline at NSCL. There, it served well in detecting the optical resonance of ^{36}Ca with production rates of only ~ 50 particles per second. The effort to transfer this outstanding efficiency to the more challenging wavelength used for boron (250 nm) is ongoing.

8.3 Outlook

From the production estimates and the spectroscopic efficiency, an estimate of the feasibility of the ^{8}B isotope shift measurement was conducted. It showed that the measurement is within reach and compares to similar laser spectroscopic experiments at the limits of isotopic stability. However, some components still require elaborative tests and experimental demonstration of their efficiency, most notably the molecular breakup system, the sodium-vapor filled charge-exchange cell and the fluorescence detection region at the boron wavelength. This will be performed as the next step of the experiment. Meanwhile, two other experiments at TU Darmstadt follow the path to investigate the boron isotopic chain and contribute to the isotope shift measurement of ^{8}B. So far, laser spectroscopy on systems with more than one electron was only able to provide differences in mean-square nuclear charge radius between isotopes. The corresponding atomic theory has not yet reached a precision level that would allow extracting the finite size effect from the single transition energy itself. However, a program was started to calculate the transition in He-like systems with the accuracy required to extract $\langle r_c^2 \rangle$ by Krzysztof Pachucki and coworkers [57].

These developments are particularly interesting for the light elements at least up to carbon, which offer a suitable transition for laser spectroscopy from the ortho-helium like state. This state can be prepared in an electron-beam ion source, allowing to measure absolute charge radii in the stable isotopes of all light elements with $Z \leq 6$. This includes measurements on ^{10}B^{3+} and ^{11}B^{3+} that in combination with the foreseeable results from the online experiment provide an accurate absolute charge radius of ^{8}B. Furthermore, a more precise value of the ^{7}Be charge radius, which could be measured in the respective Be^{2+} state, would help to determine the supposed proton-halo character of ^{8}B, since it defines the size of the halo core. This would also be the first measurement to provide a reliable $\delta \langle r_c^2 \rangle$ value between two isotopes of neighboring elements. The combination of all-optical nuclear charge radii with the results from existing and proposed isotope shift measurements would significantly increase our knowledge not only of the boron isotopic chain but across the “light” part of the nuclear chart.

Bibliography

[1] E. Rutherford. The scattering of α and β particles by matter and the structure of the atom. Philosophical Magazine **21**, 669 (1911).

[2] M. Planck. Ueber das Gesetz der Energieverteilung im Normalspectrum. Annalen der Physik **309**, 553 (1901).

[3] N. Bohr. The Spectra of Helium and Hydrogen. Nature **92**, 231 (1913).

[4] W. Wien. Über positive Elektronen und die Existenz hoher Atomgewichte. Annalen der Physik **318**, 669 (1904).

[5] O. Masson. The constitution of atoms. Philosophical Magazine **41**, 281 (1921).

[6] E. Rutherford. Collision of α particles with light atoms. An anomalous effect in nitrogen. Philosophical Magazine **37**, 581 (1919).

[7] J. Chadwick. The existence of a neutron. Proc. R. Soc. Lond. A. **136** (1932).

[8] H. A. Bethe, R. F. Bacher. Nuclear Physics A. Stationary States of Nuclei. Rev. Mod. Phys. **8**, 82 (1936).

[9] O. Hahn, F. Strassmann. Über den Nachweis und das Verhalten der bei der Bestrahlung des Urans mittels Neutronen entstehenden Erdalkalimetalle. Naturwissenschaften **27**, 11 (1939).

[10] L. Meitner, O. Frisch. Disintegration of Uranium by Neutrons: a New Type of Nuclear Reaction. Nature **143**, 239 (1939).

[11] H. Yukawa. On the Interaction of Elementary Particles. I. Proceedings of the Physico-Mathematical Society of Japan. 3rd Series **17**, 48 (1935).

[12] O. Haxel, J. H. D. Jensen, H. E. Suess. On the ”Magic Numbers” in Nuclear Structure. Phys. Rev. **75**, 1766 (1949).

[13] M. G. Mayer. Nuclear Configurations in the Spin-Orbit Coupling Model. I. Empirical Evidence. Phys. Rev. **78**, 16 (1950).

[14] M. G. Mayer. Nuclear Configurations in the Spin-Orbit Coupling Model. II. Theoretical Considerations. Phys. Rev. **78**, 22 (1950).

[15] H. Fritzsch, M. Gell-Mann, H. Leutwyler. Advantages of the color octet gluon picture. Physics Letters B **47**, 365 (1973).

[16] W. Marciano, H. Pagels. Quantum chromodynamics. Physics Reports **36**, 137 (1978).

[17] E. Epelbaum, H.-W. Hammer, U.-G. Meißner. Modern theory of nuclear forces. Rev. Mod. Phys. **81**, 1773 (2009).

[18] R. B. Wiringa, V. G. J. Stoks, R. Schiavilla. Accurate nucleon-nucleon potential with charge-independence breaking. Phys. Rev. C **51**, 38 (1995).

[19] R. Machleidt, I. Slaus. The nucleon-nucleon interaction. Journal of Physics G: Nuclear and Particle Physics **27**, R69 (2001).

[20] V. Bernard, U.-G. Meißner. Chiral Perturbation Theory. Annual Review of Nuclear and Particle Science **57**, 33 (2007).

[21] N. Ishii, S. Aoki, T. Hatsuda. Nuclear Force from Lattice QCD. Phys. Rev. Lett. **99**, 022001 (2007).

[22] S. R. Beane, E. Chang, S. D. Cohen, W. Detmold, H. W. Lin, T. C. Luu, K. Orginos, A. Parreño, M. J. Savage, A. Walker-Loud. Light nuclei and hypernuclei from quantum chromodynamics in the limit of SU(3) flavor symmetry. Phys. Rev. D **87**, 034506 (2013).

[23] I. Tanihata, T. Kobayashi, O. Yamakawa, S. Shimoura, K. Ekuni, K. Sugimoto, N. Takahashi, T. Shimoda, H. Sato. Measurement of interaction cross sections using isotope beams of Be and B and isospin dependence of the nuclear radii. Physics Letters B **206**, 592 (1988).

[24] J. Carlson, S. Gandolfi, F. Pederiva, S. C. Pieper, R. Schiavilla, K. E. Schmidt, R. B. Wiringa. Quantum Monte Carlo methods for nuclear physics. Rev. Mod. Phys. **87**, 1067 (2015).

[25] C. Forssén, P. Navrátil, S. Quaglioni. The ab initio No-Core Shell Model and Light Nuclei. Few-Body Systems **49**, 11 (2011).

[26] I. Tanihata, H. Hamagaki, O. Hashimoto, Y. Shida, N. Yoshikawa, K. Sugimoto, O. Yamakawa, T. Kobayashi, N. Takahashi. Measurements of Interaction Cross Sections and Nuclear Radii in the Light p-Shell Region. Phys. Rev. Lett. **55**, 2676 (1985).

[27] J. N. Bahcall, W. F. Huebner, S. H. Lubow, P. D. Parker, R. K. Ulrich. Standard solar models and the uncertainties in predicted capture rates of solar neutrinos. Rev. Mod. Phys. **54**, 767 (1982).

[28] Y. Fukuda, et al. Evidence for Oscillation of Atmospheric Neutrinos. Phys. Rev. Lett. **81**, 1562 (1998).

[29] Q. R. Ahmad, et al. Measurement of the Rate of $\nu_e + d \to p + p + e^-$ Interactions Produced by ^8B Solar Neutrinos at the Sudbury Neutrino Observatory. Phys. Rev. Lett. **87**, 071301 (2001).

[30] Q. R. Ahmad, et al. Direct Evidence for Neutrino Flavor Transformation from Neutral-Current Interactions in the Sudbury Neutrino Observatory. Phys. Rev. Lett. **89**, 011301 (2002).

[31] T. Minamisono, T. Ohtsubo, I. Minami, S. Fukuda, A. Kitagawa, M. Fukuda, K. Matsuta, Y. Nojiri, S. Takeda, H. Sagawa, H. Kitagawa. Proton halo of ^{8}B disclosed by its giant quadrupole moment. Phys. Rev. Lett. **69**, 2058 (1992).

[32] T. Sumikama, T. Nagatomo, M. Ogura, T. Iwakoshi, Y. Nakashima, H. Fujiwara, K. Matsuta, T. Minamisono, M. Fukuda, M. Mihara. Electric quadrupole moment of the proton halo nucleus ^{8}B. Phys. Rev. C **74**, 024327 (2006).

[33] W. Schwab, H. Geissel, H. Lenske, K. H. Behr, A. Brünle, K. Burkard, H. Irnich, T. Kobayashi, G. Kraus, A. Magel, G. Münzenberg, F. Nickel, K. Riisager, C. Scheidenberger, B. M. Sherrill, T. Suzuki, B. Voss. Observation of a proton halo in ^{8}B. Zeitschrift für Physik A Hadrons and Nuclei **350**, 283 (1995).

[34] J. H. Kelley, S. M. Austin, A. Azhari, D. Bazin, J. A. Brown, H. Esbensen, M. Fauerbach, M. Hellström, S. E. Hirzebruch, R. A. Kryger, D. J. Morrissey, R. Pfaff, C. F. Powell, E. Ramakrishnan, B. M. Sherrill, M. Steiner, T. Suomijärvi, M. Thoennessen. Study of the Breakup Reaction $^8B \to ^7$Be $+ p$: Absorption Effects and $E2$ Strength. Phys. Rev. Lett. **77**, 5020 (1996).

[35] F. Negoita, C. Borcea, F. Carstoiu, M. Lewitowicz, M. G. Saint-Laurent, R. Anne, D. Bazin, J. M. Corre, P. Roussel-Chomaz, V. Borrel, D. Guillemaud-Mueller, H. Keller, A. C. Mueller, F. Pougheon, O. Sorlin, S. Lukyanov, Y. Penionzhkevich, A. Fomichev, N. Skobelev, O. Tarasov, Z. Dlouhy, A. Kordyasz. ^{8}B proton halo via reaction and breakup cross section measurements. Phys. Rev. C **54**, 1787 (1996).

[36] M. Smedberg, T. Baumann, T. Aumann, L. Axelsson, U. Bergmann, M. Borge, D. Cortina-Gil, L. Fraile, H. Geissel, L. Grigorenko, M. Hellström, M. Ivanov, N. Iwasa, R. Janik, B. Jonson, H. Lenske, K. Markenroth, G. Münzenberg, T. Nilsson, A. Richter, K. Riisager, C. Scheidenberger, G. Schrieder, W. Schwab, H. Simon, B. Sitar, P. Strmen, K. Sümmerer, M. Winkler, M. Zhukov. New results on the halo structure of ^{8}B. Physics Letters B **452**, 1 (1999).

[37] A. Dobrovolsky, G. Korolev, A. Inglessi, G. Alkhazov, G. Colò, I. Dillmann, P. Egelhof, A. Estradé, F. Farinon, H. Geissel, S. Ilieva, Y. Ke, A. Khanzadeev, O. Kiselev, J. Kurcewicz, X. Le, Y. Litvinov, G. Petrov, A. Prochazka, C. Scheidenberger, L. Sergeev, H. Simon, M. Takechi, S. Tang, V. Volkov, A. Vorobyov, H. Weick, V. Yatsoura. Nuclear-matter distribution in the proton-rich nuclei ^{7}Be and ^{8}B from intermediate energy proton elastic scattering in inverse kinematics. Nuclear Physics A **989**, 40 (2019).

[38] L.-B. Wang, P. Mueller, K. Bailey, G. W. F. Drake, J. P. Greene, D. Henderson, R. J. Holt, R. V. F. Janssens, C. L. Jiang, Z.-T. Lu, T. P. O'Connor, R. C. Pardo, K. E. Rehm, J. P. Schiffer, X. D. Tang. Laser Spectroscopic Determination of the ^{6}He Nuclear Charge Radius. Phys. Rev. Lett. **93**, 142501 (2004).

[39] P. Mueller, I. A. Sulai, A. C. C. Villari, J. A. Alcántara-Núñez, R. Alves-Condé, K. Bailey, G. W. F. Drake, M. Dubois, C. Eléon, G. Gaubert, R. J. Holt, R. V. F. Janssens, N. Lecesne, Z.-T. Lu, T. P. O'Connor, M.-G. Saint-Laurent, J.-C. Thomas, L.-B. Wang. Nuclear Charge Radius of ^{8}He. Phys. Rev. Lett. **99**, 252501 (2007).

[40] R. Sánchez, W. Nörtershäuser, G. Ewald, D. Albers, J. Behr, P. Bricault, B. A. Bushaw, A. Dax, J. Dilling, M. Dombsky, G. W. F. Drake, S. Götte, R. Kirchner, H.-J. Kluge, T. Kühl, J. Lassen, C. D. P. Levy, M. R. Pearson, E. J. Prime, V. Ryjkov, A. Wojtaszek, Z.-C. Yan, C. Zimmermann. Nuclear Charge Radii of ^{9,11}Li: The Influence of Halo Neutrons. Phys. Rev. Lett. **96**, 033002 (2006).

[41] W. Nörtershäuser, D. Tiedemann, M. Žáková, Z. Andjelkovic, K. Blaum, M. L. Bissell, R. Cazan, G. W. F. Drake, C. Geppert, M. Kowalska, J. Krämer, A. Krieger, R. Neugart, R. Sánchez, F. Schmidt-Kaler, Z.-C. Yan, D. T. Yordanov, C. Zimmermann. Nuclear Charge Radii of ^{7,9,10}Be and the One-Neutron Halo Nucleus ^{11}Be. Phys. Rev. Lett. **102**, 062503 (2009).

[42] T. Udem, A. Huber, B. Gross, J. Reichert, M. Prevedelli, M. Weitz, T. W. Hänsch. Phase-Coherent Measurement of the Hydrogen $1S-2S$ Transition Frequency with an Optical Frequency Interval Divider Chain. Phys. Rev. Lett. **79**, 2646 (1997).

[43] R. Pohl, et al. The size of the proton. Nature **466**, 213 (2010).

[44] C. E. Carlson. The proton radius puzzle. Progress in Particle and Nuclear Physics **82**, 59 (2015).

[45] B. Maaß, T. Hüther, K. König, J. Krämer, J. Krause, A. Lovato, P. Müller, K. Pachucki, M. Puchalski, R. Roth, R. Sánchez, F. Sommer, R. B. Wiringa, W. Nörtershäuser. Nuclear Charge Radii of ^{10,11}B. Phys. Rev. Lett. **122**, 182501 (2019).

[46] N. Stone. Nuclear Magnetic Dipole and Electric Quadrupole Moments: Their Measurement and Tabulation as Accessible Data. J. Phys. Chem. Ref. Data **44**, 031215 (2015).

[47] T. Stovall, J. Goldemberg, D. Isabelle. Coulomb form factors of ^{10}B and ^{11}B. Nuclear Physics **86**, 225 (1966).

[48] Z.-T. Lu, P. Mueller, G. W. F. Drake, W. Nörtershäuser, S. C. Pieper, Z.-C. Yan. Colloquium: Laser probing of neutron-rich nuclei in light atoms. Rev. Mod. Phys. **85**, 1383 (2013).

[49] P. J. Mohr, B. N. Taylor, D. B. Newell. CODATA recommended values of the fundamental physical constants: 2010. Rev. Mod. Phys. **84**, 1527 (2012).

[50] M. Tanabashi, et al. Review of Particle Physics. Phys. Rev. D **98**, 030001 (2018).

[51] J. L. Friar, J. Martorell, D. W. L. Sprung. Nuclear sizes and the isotope shift. Phys. Rev. A **56**, 4579 (1997).

[52] I. Tanihata, H. Savajols, R. Kanungo. Recent experimental progress in nuclear halo structure studies. Progress in Particle and Nuclear Physics **68**, 215 (2013).

[53] K. Riisager, A. Jensen. The radius of ^{8}B and solar neutrinos. Physics Letters B **301**, 6 (1993).

[54] K. Riisager, A. Jensen, P. Møller. Two-body halos. Nuclear Physics A **548**, 393 (1992).

[55] J. Jansen, R. Peerdeman, C. D. Vries. Nuclear charge radii of ^{12}C and ^{9}Be. Nuclear Physics A **188**, 337 (1972).

[56] W. D. Myers, K.-H. Schmidt. An update on droplet-model charge distributions. Nuclear Physics A **410**, 61 (1983).

[57] V. A. Yerokhin, V. Patkóš, K. Pachucki. Relativistic corrections to the Bethe logarithm for the $2\ ^3S$ and $2\ ^3P$ states of He. Phys. Rev. A **98**, 032503 (2018).

[58] A. Krieger, W. Nörtershäuser, C. Geppert, K. Blaum, M. L. Bissell, N. Frömmgen, M. Hammen, K. Kreim, M. Kowalska, J. Krämer, R. Neugart, G. Neyens, R. Sánchez, D. Tiedemann, D. T. Yordanov, M. Zakova. Frequency-comb referenced collinear laser spectroscopy of Be+ for nuclear structure investigations and many-body QED tests. Applied Physics B **123**, 15 (2016).

[59] P. Imgram, K. König, J. Krämer, T. Ratajczyk, R. A. Müller, A. Surzhykov, W. Nörtershäuser. Collinear laser spectroscopy at ion-trap accuracy: Transition frequencies and isotope shifts in the $6s\,^2S_{1/2} \rightarrow 6p\,^2P_{1/2,3/2}$ transitions in Ba$^+$. Phys. Rev. A **99**, 012511 (2019).

[60] R. B. Wiringa, R. A. Smith, T. L. Ainsworth. Nucleon-nucleon potentials with and without Δ(1232) degrees of freedom. Phys. Rev. C **29**, 1207 (1984).

[61] S. C. Pieper, R. B. Wiringa. Quantum Monte Carlo Simulations of light Nuclei. Annual Review of Nuclear and Particle Science **51**, 53 (2001).

[62] S. C. Pieper. The Illinois Extension to the Fujita-Miyazawa Three-Nucleon Force. AIP Conf. Proc. **1011**, 143 (2008).

[63] V. G. J. Stoks, R. A. M. Klomp, C. P. F. Terheggen, J. J. de Swart. Construction of high-quality NN potential models. Phys. Rev. C **49**, 2950 (1994).

[64] R. Machleidt. High-precision, charge-dependent Bonn nucleon-nucleon potential. Phys. Rev. C **63**, 024001 (2001).

[65] J. Carlson, V. Pandharipande, R. Wiringa. Three-nucleon interaction in 3-, 4- and -body systems. Nuclear Physics A **401**, 59 (1983).

[66] N. Kalantar-Nayestanaki, E. Epelbaum, J. G. Messchendorp, A. Nogga. Signatures of three-nucleon interactions in few-nucleon systems. Reports on Progress in Physics **75**, 016301 (2011).

[67] R. Machleidt, D. Entem. Chiral effective field theory and nuclear forces. Physics Reports **503**, 1 (2011).

[68] S. Weinberg. Nuclear forces from chiral lagrangians. Physics Letters B **251**, 288 (1990).

[69] S. Weinberg. Effective chiral lagrangians for nucleon-pion interactions and nuclear forces. Nuclear Physics B **363**, 3 (1991).

[70] B. Povh, K. Rith, C. Scholz, F. Zetsche, W. Rodejohann. Teilchen und Kerne, Springer Spektrum (2014), 9th edn.

[71] D. R. Entem, R. Machleidt. Accurate charge-dependent nucleon-nucleon potential at fourth order of chiral perturbation theory. Phys. Rev. C **68**, 041001 (2003).

[72] M. H. Kalos. Monte Carlo Calculations of the Ground State of Three- and Four-Body Nuclei. Phys. Rev. **128**, 1791 (1962).

[73] B. S. Pudliner, V. R. Pandharipande, J. Carlson, S. C. Pieper, R. B. Wiringa. Quantum Monte Carlo calculations of nuclei with $A <\sim 7$. Phys. Rev. C **56**, 1720 (1997).

[74] S. C. Pieper. Quantum Monte Carlo Calculations of Light Nuclei. Nuclear Physics A **751**, 516 (2005). Proceedings of the 22nd International Nuclear Physics Conference (Part 1).

[75] R. B. Wiringa, S. C. Pieper, J. Carlson, V. R. Pandharipande. Quantum Monte Carlo calculations of $A = 8$ nuclei. Phys. Rev. C **62**, 014001 (2000).

[76] S. C. Pieper, V. R. Pandharipande, R. B. Wiringa, J. Carlson. Realistic models of pion exchange three nucleon interactions. Phys. Rev. C **64**, 014001 (2001).

[77] A. Ekström, G. R. Jansen, K. A. Wendt, G. Hagen, T. Papenbrock, B. D. Carlsson, C. Forssén, M. Hjorth-Jensen, P. Navrátil, W. Nazarewicz. Accurate nuclear radii and binding energies from a chiral interaction. Phys. Rev. C **91**, 051301 (2015).

[78] R. Roth, S. Binder, K. Vobig, A. Calci, J. Langhammer, P. Navrátil. Medium-Mass Nuclei with Normal-Ordered Chiral NN+3N Interactions. Phys. Rev. Lett. **109**, 052501 (2012).

[79] H. Hergert, S. Binder, A. Calci, J. Langhammer, R. Roth. Ab Initio Calculations of Even Oxygen Isotopes with Chiral Two-Plus-Three-Nucleon Interactions. Phys. Rev. Lett. **110**, 242501 (2013).

[80] E. Gebrerufael, K. Vobig, H. Hergert, R. Roth. Ab Initio Description of Open-Shell Nuclei: Merging No-Core Shell Model and In-Medium Similarity Renormalization Group. Phys. Rev. Lett. **118**, 152503 (2017).

[81] R. Roth, A. Calci, J. Langhammer, S. Binder. Evolved chiral $NN + 3N$ Hamiltonians for ab initio nuclear structure calculations. Phys. Rev. C **90**, 024325 (2014).

[82] D. R. Entem, R. Machleidt, Y. Nosyk. High-quality two-nucleon potentials up to fifth order of the chiral expansion. Phys. Rev. C **96**, 024004 (2017).

[83] B. R. Barrett, P. Navrátil, J. P. Vary. Ab initio no core shell model. Progress in Particle and Nuclear Physics **69**, 131 (2013).

[84] S. K. Bogner, R. J. Furnstahl, R. J. Perry. Similarity renormalization group for nucleon-nucleon interactions. Phys. Rev. C **75**, 061001 (2007).

[85] P. Navrátil, J. P. Vary, B. R. Barrett. Large-basis ab initio no-core shell model and its application to ^{12}C. Phys. Rev. C **62**, 054311 (2000).

[86] P. Navrátil, J. P. Vary, B. R. Barrett. Properties of ^{12}C in the Ab Initio Nuclear Shell Model. Phys. Rev. Lett. **84**, 5728 (2000).

[87] T. Hüther, K. Vobig, R. Roth. (in preparation).

[88] M. I. Eides, H. Grotch, V. A. Shelyuto. Theory of light hydrogenlike atoms. Physics Reports **342**, 63 (2001).

[89] W. Demtröder. Experimentalphysik 3, Springer-Verlag Berlin Heidelberg (2010).

[90] W. King. Isotope Shifts in Atomic Spectra, Springer US (1984).

[91] M. Puchalski, J. Komasa, K. Pachucki. Explicitly correlated wave function for a boron atom. Phys. Rev. A **92**, 062501 (2015).

[92] V. c. v. Patkóš, V. A. Yerokhin, K. Pachucki. Higher-order recoil corrections for triplet states of the helium atom. Phys. Rev. A **94**, 052508 (2016).

[93] W. Paul, M. Raether. Das elektrische Massenfilter. Zeitschrift für Physik **140**, 262 (1955).

[94] W. Paul, H. P. Reinhard, U. von Zahn. Das elektrische Massenfilter als Massenspektrometer und Isotopentrenner. Zeitschrift für Physik **152**, 143 (1958).

[95] P. H. Dawson. Quadrupole Mass Spectrometry and Its Applications, AIP (1995).

[96] K. Blaum. Resonante Laserionisations-Massenspektrometrie an Gadolinium zur Isotopenhäufigkeitsanalyse mit geringsten Mengen. Ph.D. thesis, Johannes Gutenberg Universität Mainz (2000).

[97] K. Blaum, C. Geppert, P. Müller, W. Nörtershäuser, E. Otten, A. Schmitt, N. Trautmann, K. Wendt, B. Bushaw. Properties and performance of a quadrupole mass filter used for resonance ionization mass spectrometry. International Journal of Mass Spectrometry **181**, 67 (1998).

[98] G. Ewald, W. Nörtershäuser, A. Dax, S. Götte, R. Kirchner, H.-J. Kluge, T. Kühl, R. Sanchez, A. Wojtaszek, B. A. Bushaw, G. W. F. Drake, Z.-C. Yan, C. Zimmermann. Nuclear Charge Radii of ^{8,9}Li Determined by Laser Spectroscopy. Phys. Rev. Lett. **93**, 113002 (2004).

[99] G. Savard. Large radio-frequency gas catchers and the production of radioactive nuclear beams. Journal of Physics: Conference Series **312**, 052004 (2011).

[100] F. Paschen. Ueber die zum Funkenübergang in Luft, Wasserstoff und Kohlensäure bei verschiedenen Drucken erforderliche Potentialdifferenz. Annalen der Physik **273**, 69 (1889).

[101] T. Udem, R. Holzwarth, T. W. Hänsch. Optical frequency metrology. Nature **416**, 233 (2002).

[102] K. König. Laser-Based High-Voltage Metrology with ppm Accuracy. Ph.D. thesis, TU Darmstadt (2018).

[103] K. König, P. Imgram, J. Krämer, B. Maaß, K. Mohr, T. Ratajczyk, F. Sommer, W. Nörtershäuser. On the performance of wavelength meters. Submitted to Applied Physics B (2019).

[104] A. Krieger, K. Blaum, M. L. Bissell, N. Frömmgen, C. Geppert, M. Hammen, K. Kreim, M. Kowalska, J. Krämer, T. Neff, R. Neugart, G. Neyens, W. Nörtershäuser, C. Novotny, R. Sánchez, D. T. Yordanov. Nuclear Charge Radius of ^{12}Be. Phys. Rev. Lett. **108**, 142501 (2012).

[105] M. T. Burkey, G. Savard, A. Gallant, N. D. Scielzo, J. A. Clark, T. Y. Hirsh, D. P. Burdette, E. Heckmaier, J. Klimes, K. Kolos, S. T. Marley, G. E. Morgan, R. Orford, S. Padgett, J. Pierce, R. Segel, K. S. Sharma, L. Varriano, B. S. Wang. Precision $\beta - \nu$ correlation measurements with the Beta-decay Paul Trap. Hyperfine Interactions **240**, 36 (2019).

[106] A. P. Galván, R. E. Segel, N. D. Scielzo, A. Aprahamian, F. Buchinger, M. Burkey, S. Caldwell, J. A. Clark, J. Crawford, A. Czeszumska, D. Henderson, S. T. Marley, G. Morgan, P. Mueller, E. B. Norman, A. Nystrom, R. Orford, S. W. Padgett, N. Paul, G. Savard, K. Siegl, K. S. Sharma, M. G. Sternberg, S. Strauss, R. Yee. Status Update on the $\beta - \nu$ Correlation Measurement in the β-Decay of ^{8}B. Proceedings of the Conference on Advances in Radioactive Isotope Science (ARIS2014) (2014).

[107] B. Harss, R. C. Pardo, K. E. Rehm, F. Borasi, J. P. Greene, R. V. F. Janssens, C. L. Jiang, J. Nolen, M. Paul, J. P. Schiffer, R. E. Segel, J. Specht, T. F. Wang, P. Wilt, B. Zabransky. Production of radioactive ion beams using the in-flight technique. Review of Scientific Instruments **71**, 380 (2000).

[108] C. R. McClenahan, R. E. Segel. Cross sections for the ^{7}Li$(d,p)^{8}$Li, ^{6}Li$(^{3}$He$,n)^{8}$B, ^{6}Li$(d,\alpha)^{4}$He, ^{6}Li$(d,p)^{7}$Li, and ^{6}Li$(d,n)^{7}$Be reactions. Phys. Rev. C **11**, 370 (1975).

[109] H. Yamaguchi, Y. Wakabayashi, G. Amadio, S. Hayakawa, H. Fujikawa, S. Kubono, J. He, A. Kim, D. Binh. Development of a cryogenic gas target system for intense radioisotope beam production at CRIB. Nuclear Instruments and Methods in Physics Research Section A: Accelerators, Spectrometers, Detectors and Associated Equipment **589**, 150 (2008).

[110] V. Kumar. Understanding the focusing of charged particle beams in a solenoid magnetic field. American Journal of Physics **77**, 737 (2009).

[111] A. Kramida, Yu. Ralchenko, J. Reader, and NIST ASD Team. NIST Atomic Spectra Database (ver. 5.6.1) (2018).

[112] F. Marti. Heavy Ion Strippers. In Proceedings of LINAC2012, Tel-Aviv, Israel. 2012.

[113] H. Eickhoff, T. Haberer, G. Kraft, U. Krause, M. Richter, R. Steiner, J. Debus. The GSI cancer therapy project. Strahlentherapie und Onkologie **175**, 21 (1999).

[114] H. Bethe, J. Ashkin. Passage of radiation through matter, in Experimental Nuclear Physics Vol I, John Wiley & Sons, New York (1953).

[115] J. F. Ziegler. SRIM - The Stopping and Range of Ions in Matter (2019).

[116] M. Simon. Ionentransmission durch nanometerdicke Kohlenstoffmembranen. Bachelor-Thesis (2019).

[117] A. Bürgi, M. Gonin, M. Oetliker, P. Bochsler, J. Geiss, T. Lamy, A. Brenac, H. J. Andrä, P. Roncin, H. Laurent, M. A. Coplan. Charge exchange of low energy ions in thin carbon foils. II. Results for ions of B, C, F, Ne, Na, Si, S, Cl, Ar, K, and Fe. Journal of Applied Physics **73**, 4130 (1993).

[118] R. Kallenbach, M. Gonin, P. Bochsler, A. Bürgi. Charge exchange of B, C, O, Al, Si, S, F and Cl passing through thin carbon foils at low energies: Formation of negative ions. Nuclear Instruments and Methods in Physics Research Section B: Beam Interactions with Materials and Atoms **103**, 111 (1995).

[119] J. F. Ziegler, J. P. Biersack, U. Littmark. The Stopping and Range of Ions in Solids, Pergamon Press (1985).

[120] F. Lenz. Untersuchung ultradünner Kohlenstofffolien mit α -Strahlung und langsamen Borionen. Bachelor-Thesis (2018).

[121] M. Block, D. Ackermann, K. Blaum, C. Droese, M. Dworschak, M. Eibach, S. Eliseev, T. Fleckenstein, E. Haettner, F. Herfurth, F. P. Heßberger, S. Hofmann, J. Ketelaer, J. Ketter, H. J. Kluge, G. Marx, M. Mazzocco, Y. N. Novikov, W. R. Plaß, A. Popeko, S. Rahaman, D. Rodríguez, C. Scheidenberger, L. Schweikhard, P. G. Thirolf, G. K. Vorobyev, C. Weber. Penning trap mass measurements of transfermium elements with SHIPTRAP. Hyperfine Interactions **196**, 225 (2010).

[122] M. G. Sternberg, R. Segel, N. D. Scielzo, G. Savard, J. A. Clark, P. F. Bertone, F. Buchinger, M. Burkey, S. Caldwell, A. Chaudhuri, J. E. Crawford, C. M. Deibel, J. Greene, S. Gulick, D. Lascar, A. F. Levand, G. Li, A. Pérez Galván, K. S. Sharma, J. Van Schelt, R. M. Yee, B. J. Zabransky. Limit on Tensor Currents from ^{8}Li β Decay. Phys. Rev. Lett. **115**, 182501 (2015).

[123] J. Krämer. Construction and Commissioning of a Collinear Laser Spectroscopy Setup at TRIGA Mainz and Laser Spectroscopy of Magnesium Isotopes at ISOLDE (CERN). Ph.D. thesis, Johannes Gutenberg-Universität Mainz (2010).

[124] J. Ketelaer, J. Krämer, D. Beck, K. Blaum, M. Block, K. Eberhardt, G. Eitel, R. Ferrer, C. Geppert, S. George, F. Herfurth, J. Ketter, S. Nagy, D. Neidherr, R. Neugart, W. Nörtershäuser, J. Repp, C. Smorra, N. Trautmann, C. Weber. TRIGA-SPEC: A setup for mass spectrometry and laser spectroscopy at the research reactor TRIGA Mainz. Nuclear Instruments and Methods in Physics Research Section A: Accelerators, Spectrometers, Detectors and Associated Equipment **594**, 162 (2008).

[125] M. Hammen. Development, Construction and Test of an Efficient Fluorescence Detection Region for Collinear Laser Spectroscopy at TRIGA-Mainz. Diploma thesis, Johannes Gutenberg Universit¨ at Mainz (2010).

[126] S. Kaufmann. Laser spectroscopy of nickel isotopes with a new data acquisition system at ISOLDE. Ph.D. thesis, TU Darmstadt (2019).

[127] R. Neugart, J. Billowes, M. L. Bissell, K. Blaum, B. Cheal, K. T. Flanagan, G. Neyens, W. Nörtershäuser, D. T. Yordanov. Collinear laser spectroscopy at ISOLDE: new methods and highlights. Journal of Physics G: Nuclear and Particle Physics **44**, 064002 (2017).

[128] A. Klose, K. Minamisono, C. Geppert, N. Frömmgen, M. Hammen, J. Krämer, A. Krieger, C. Levy, P. Mantica, W. Nörtershäuser, S. Vinnikova. Tests of atomic charge-exchange cells for collinear laser spectroscopy. Nuclear Instruments and Methods in Physics Research Section A: Accelerators, Spectrometers, Detectors and Associated Equipment **678**, 114 (2012).

[129] C. Levy, T. Cocolios, J. Behr, K. Jayamanna, K. Minamisono, M. Pearson. Feasibility study of in-beam polarization of fluorine. Nuclear Instruments and Methods in Physics Research Section A: Accelerators, Spectrometers, Detectors and Associated Equipment **580**, 1571 (2007).

[130] R. F. Garcia Ruiz, A. R. Vernon, C. L. Binnersley, B. K. Sahoo, M. Bissell, J. Billowes, T. E. Cocolios, W. Gins, R. P. de Groote, K. T. Flanagan, A. Koszorus, K. M. Lynch, G. Neyens, C. M. Ricketts, K. D. A. Wendt, S. G. Wilkins, X. F. Yang. High-Precision Multiphoton Ionization of Accelerated Laser-Ablated Species. Phys. Rev. X **8**, 041005 (2018).

[131] M. G. Sternberg. Limits on tensor currents from ^{8}Li β decay. Ph.D. thesis, The University of Chicago (2013).

[132] A. J. Miller, K. Minamisono, A. Klose, D. Garand, C. Kujawa, J. D. Lantis, Y. Liu, B. Maaß, P. F. Mantica, W. Nazarewicz, W. Nörtershäuser, R. P.-G. Pineda, S. V., D. M. Rossi, F. Sommer, C. Sumithrarachchi, A. Teigelhöfer, J. Watkins. Proton superfluidity and charge radii in proton-rich calcium isotopes. Nature Physics **15**, 432 (2019).

[133] A. E. Kramida, A. N. Ryabtsev. A critical compilation of energy levels and spectral lines of neutral boron. Physica Scripta **76**, 544 (2007).

[134] J. C. Chavez. Introduction to Nonimaging Optics, CRC Press Inc (2008).

[135] R. F. Garcia Ruiz, M. L. Bissell, K. Blaum, A. Ekström, N. Frömmgen, G. Hagen, M. Hammen, K. Hebeler, J. D. Holt, G. R. Jansen, M. Kowalska, K. Kreim, W. Nazarewicz, R. Neugart, G. Neyens, W. Nörtershäuser, T. Papenbrock, J. Papuga, A. Schwenk, J. Simonis, K. . A. Wendt, D. T. Yordanov. Unexpectedly large charge radii of neutron-rich calcium isotopes. Nature Physics **12**, 594 EP (2016). Article.

[136] H. Lew, R. Title. Structure of the $2s^2 2p\ ^2\mathrm{P}_{1/2}$ state of Boron 10 and 11. Can. J. Phys. **38**, 868 (1960).

[137] N. Ramsey. Molecular beams, Clarendon Press (1956).

[138] S. Johansson, U. Litzén, J. Kasten, M. Kock. A 25 mA isotope shift in B I at 2090 A - A possible diagnostic of the cosmic B-11/B-10 ratio? The Astrophysical Journal **403**, L25 (1992).

[139] S. Mrozowski. Über den Isotopenverschiebungseffekt im Spektrum des Bors. Zeitschrift für Physik **112**, 223 (1939).

[140] E. W. Burke. Isotope Shift in the First Three Spectra of Boron. Phys. Rev. **99**, 1839 (1955).

[141] T. Stovall, J. Goldemberg, D. Isabelle. Coulomb form factors of 10B and 11B. Nuclear Physics **86**, 225 (1966).

A Spectra of ^{10,11}B

Overview

Table A.1.: The values extracted from the fits of the datasets.

	ν_{SP} (MHz)	ν_{DP} (MHz)	$\nu_{0,\mathrm{simple}}$ (MHz)	$\nu_{0,\mathrm{alt}}$ (MHz)	$\nu_{0,\mathrm{combined}}$ (MHz)	A_{3s} (MHz)	σ_G (MHz)	Γ (MHz)
				^{10}B				
		($\nu + 1\,200\,364\,000$ MHz)						
C	191.0(14)			66.8(99)		79.0(6)	58.8(38)	22.0(43)
D	47.3(7)			59.3(128)		79.6(4)	32.5(20)	30.9(18)
F	−95.0(17)	219.6(36)	62.3(74)	68.0(100)	64.3(60)	79.6(7)	60.5(45)	40.0(49)
J	43.2(7)	99.2(35)	71.2(74)	68.2(110)	70.2(60)	78.9(3)	39.0(12)	37.8(9)
K	133.4(8)			63.7(99)		79.6(4)	31.2(28)	50.4(19)
				^{11}B				
		($\nu + 1\,200\,359\,000$ MHz)						
B	291.6(10)	−206.7(18)	42.4(72)			238.6(8)	94.8(20)	34.6(21)
C	156.4(6)	−80.3(12)	38.0(72)			238.2(5)	49.3(11)	30.3(9)
D	22.2(6)	45.1(160)	33.6(110)			237.7(6)	35.7(12)	26.5(9)
E	−278.3(20)	333.4(22)	27.6(73)			235.5(15)	117.5(28)	48.0(29)
F	−123.4(12)	187.5(20)	32.0(72)	26.6(96)	30.1(58)	239.4(11)	63.5(25)	35.1(21)
G	−100.8(12)	167.2(16)	33.2(72)			237.4(11)	55.1(24)	40.0(20)
H	−105.2(17)	176.3(20)	35.5(73)			235.5(16)	52.1(34)	40.0(29)
J	8.7(6)	56.3(75)	32.5(81)	35.4(95)	33.7(61)	239.5(5)	35.2(16)	42.6(10)
K	99.4(7)	−33.5(13)	32.9(72)			235.9(7)	27.9(23)	53.4(12)

Dataset B

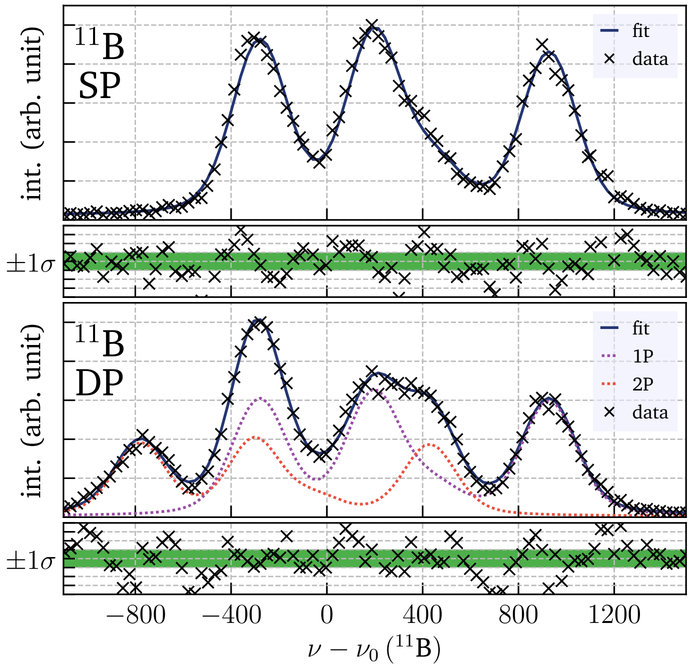

Dataset C

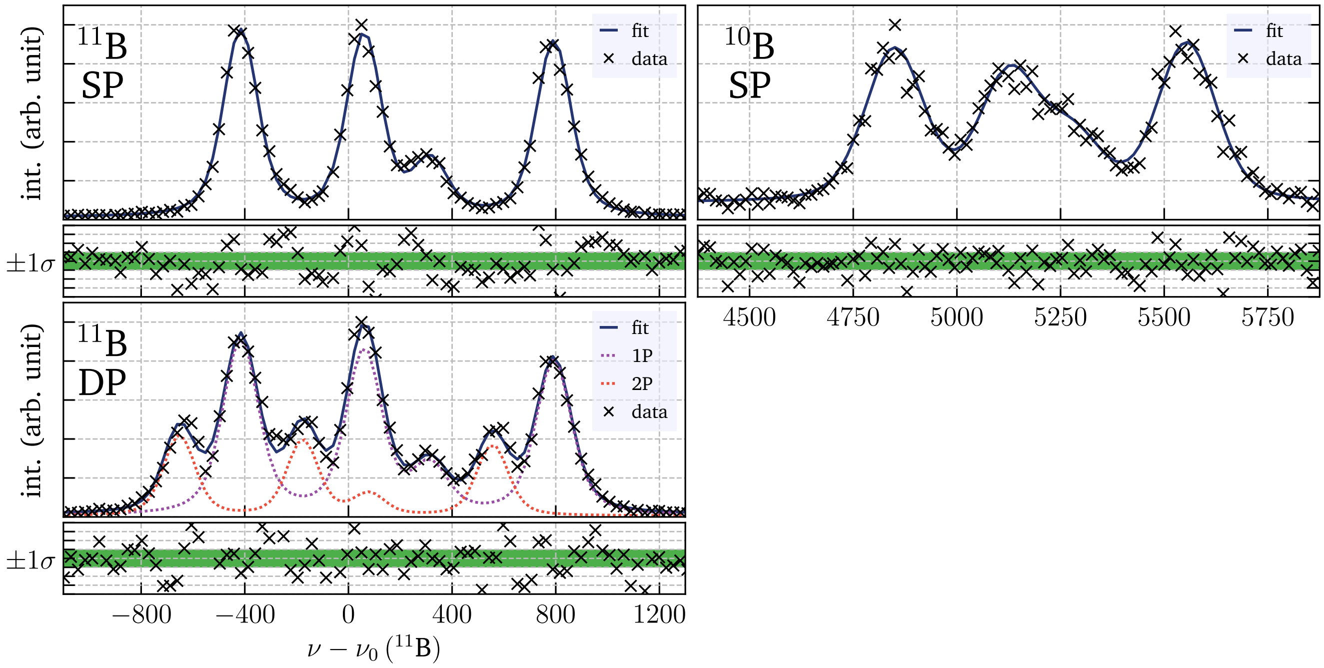

Dataset D

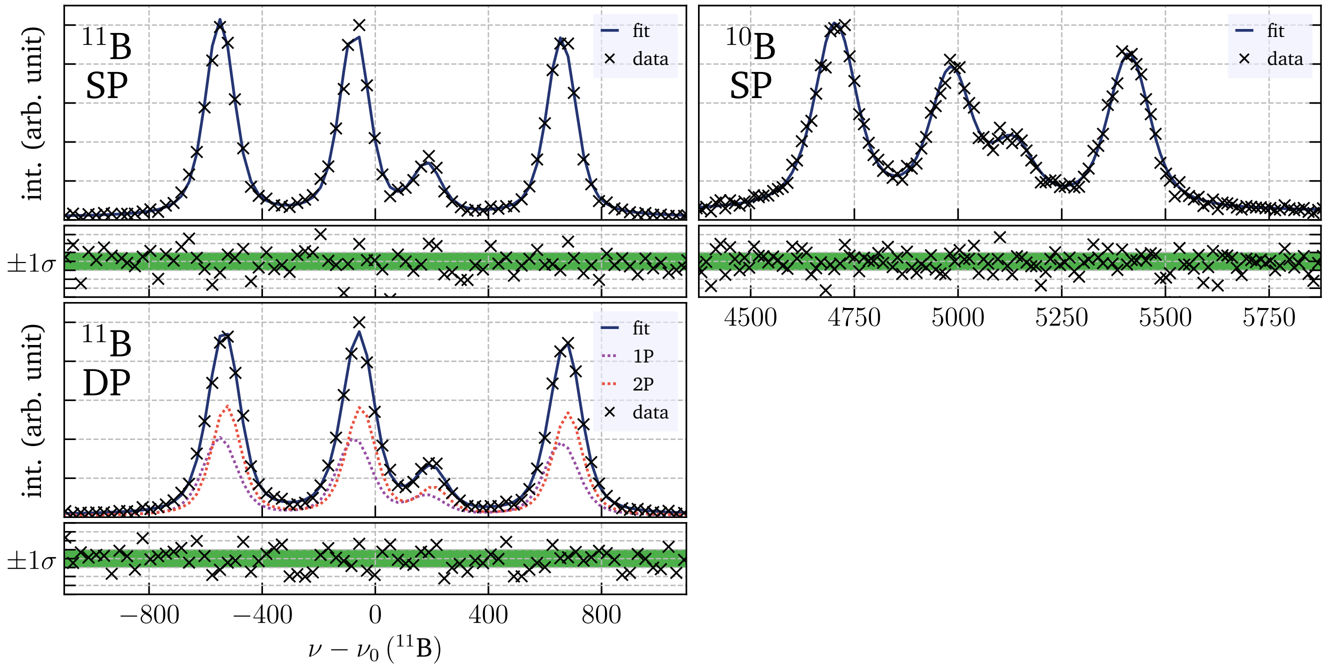

Dataset E

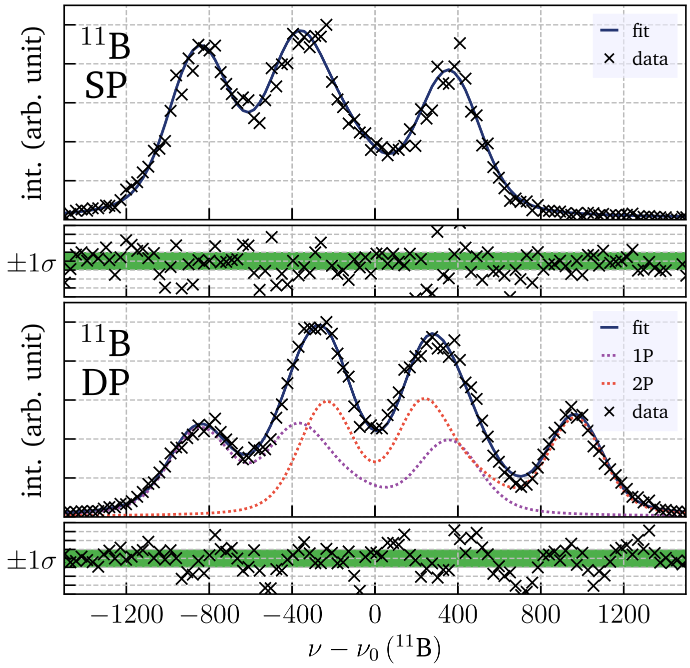

Dataset F

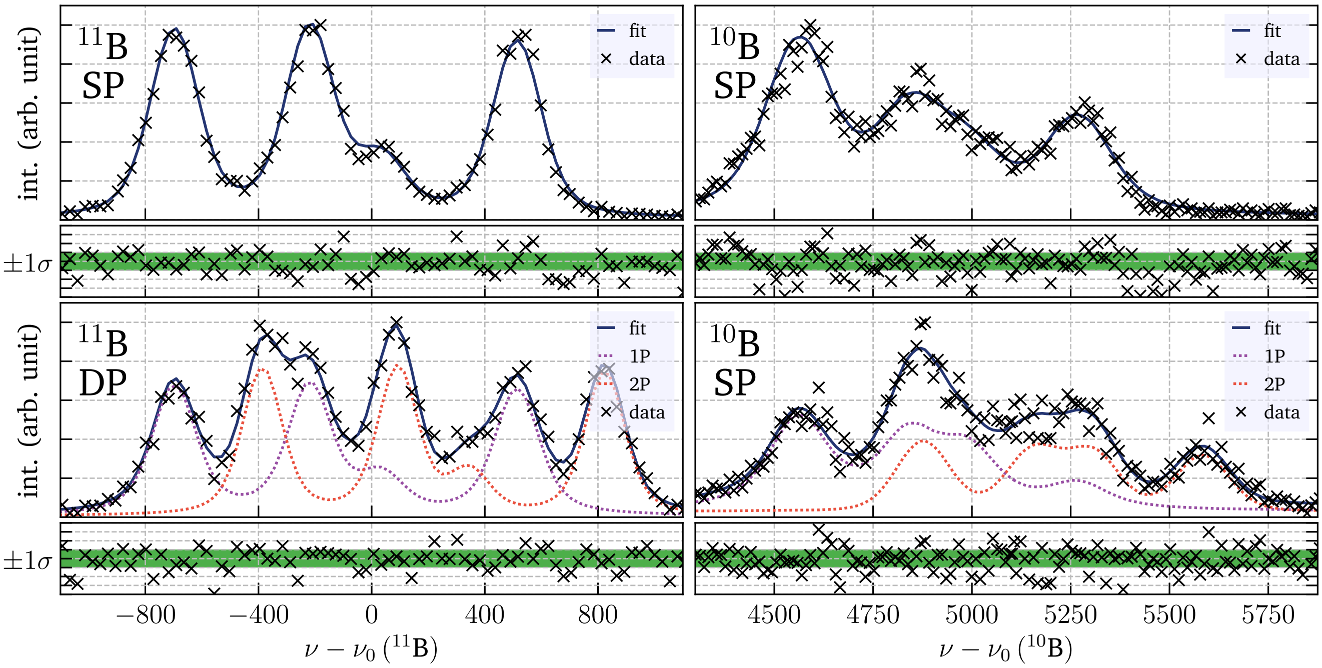

Dataset G

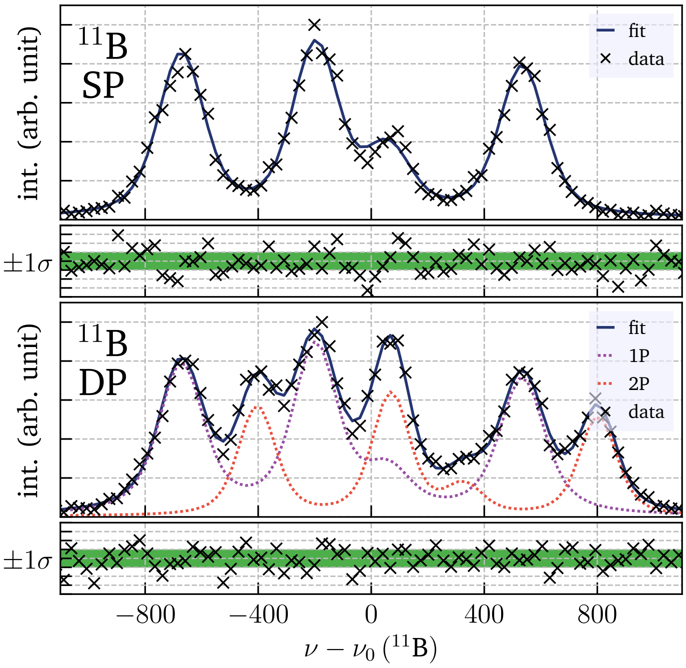

Dataset H

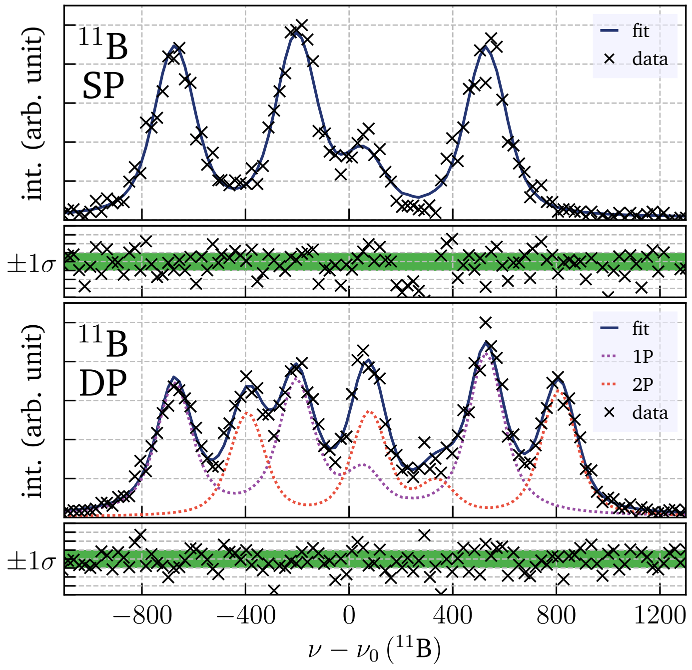

Dataset J

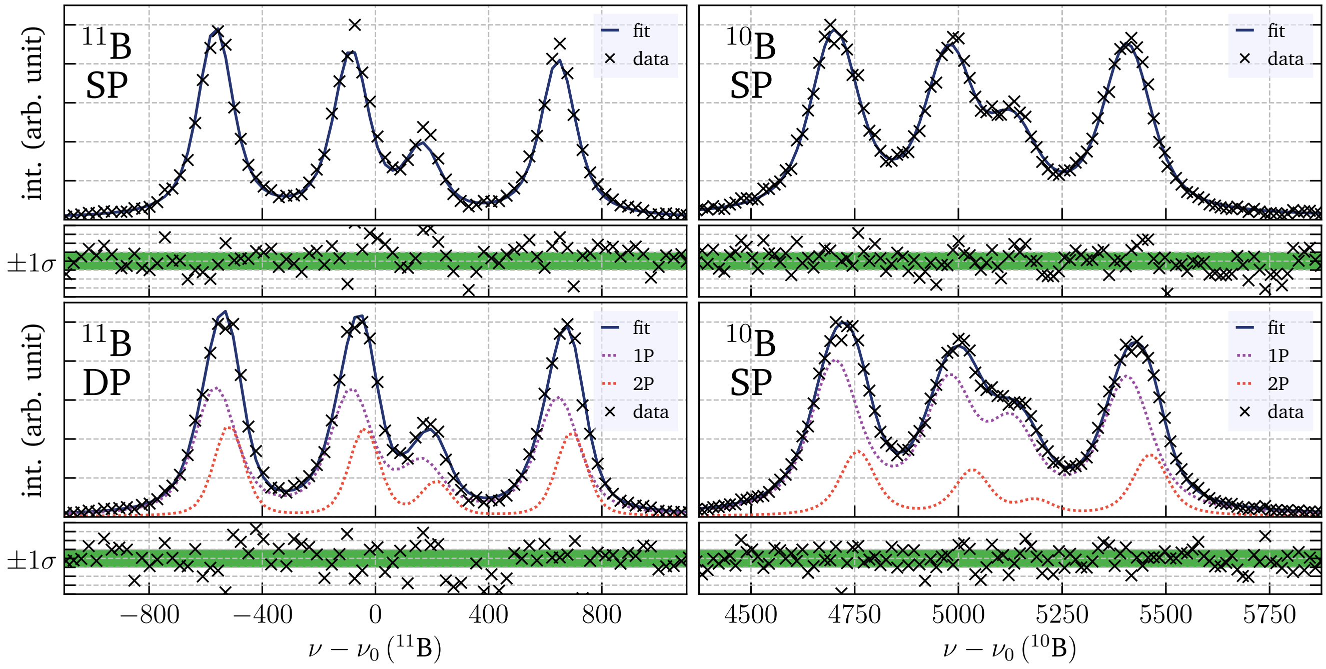

Dataset K

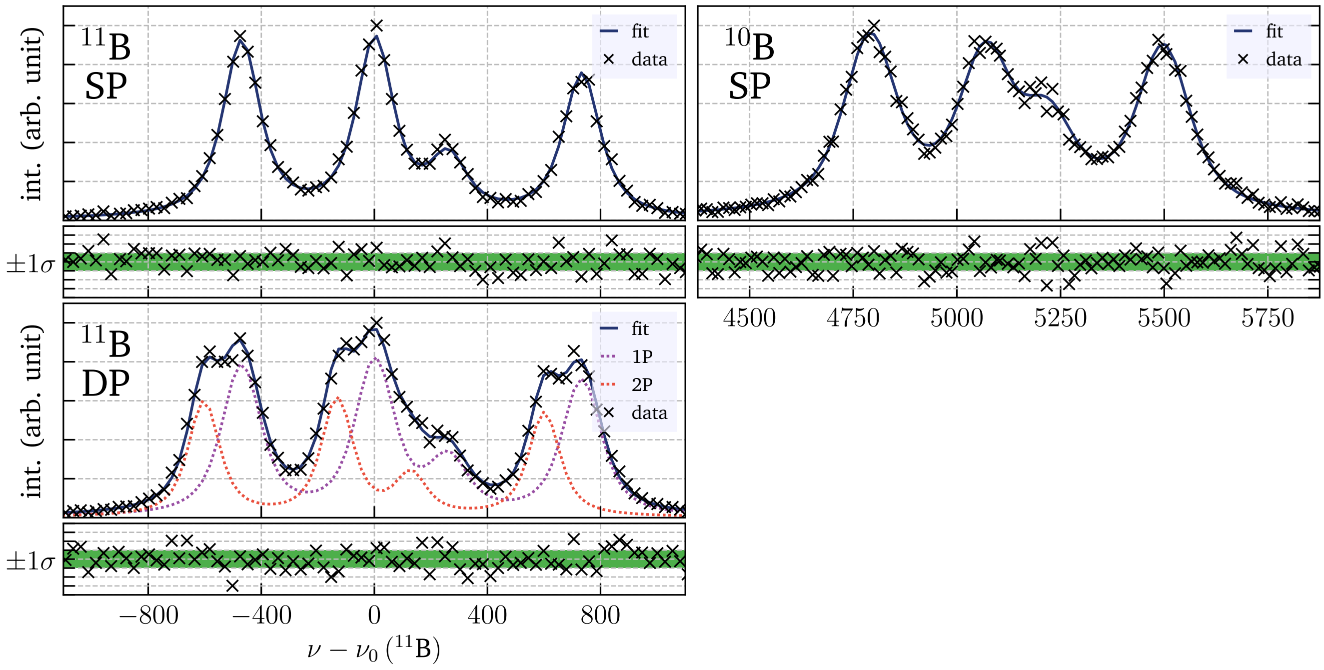

^{11}B
SP
^{10}B
SP
^{11}B
DP
fit
data
1P
2P
int. (arb. unit)
±1σ
−800
−400
0
400
800
4500
4750
5000
5250
5500
5750
$\nu - \nu_0\,(^{11}\mathrm{B})$

Acknowledgements

This section is dedicated to the people who contributed so much to the successful completion of this thesis, who enabled me during my doctoral studies and to those who I spent so many memorable hours with during the last ten years.

First of all, I want to thank my advisor Wilfried Nörtershäuser for trusting me with working on this fascinating project and for the great support he gave me in my Ph.D. from the first day on. He always had an open door for fruitful discussions, and always managed to stir my curiosity and enthusiasm.

I could find true and similar words about Peter Müller, who was my advisor at ANL. I still admire his way of never losing sight of small details, doing hands-on work, while keeping track of the big picture.

The work at ANL would not have been possible without Guy Savard and Jason Clark. Thank you very much for the many hours that you spent not only at night in the triangle room for this project but of course also for all the time besides, filled with interesting and exciting conversations.

Jake, Kevin, Tom, Matt, Michael, thank you for the friendly welcome at ANL and the many delightful lunch breaks at Chuck's, and also for lending a helping hand when- and wherever needed in the lab.

I also want to thank Frank from the workshop for his excellent work, and everyone in the ANL administration for hosting me and organizing my stay.

Of course also many thanks to the people who proof-read and corrected parts of my thesis. Especially Wilfried, who managed to squeeze in so much time for corrections and discussion, but of course also Felix, Kristian, Jörg, Ashton, Julia, Thomas Hüther and Alessandro Lovato.

I also want to acknowledge not only the financial support from the successful SFB1245, but also thank the many people who worked so hard to establish it here at the IKP. I always experienced a positive and productive work atmosphere throughout the institute.

Representing the administration, I want to thank Carina Seeger, who was always happy to help me with all the bureaucracy. Similarly, for the IKP workshop, Dirk Oppermann always took his time to discuss my drawings in a helpful way, and always delivered excellent work.

Also, I wish to thank Thomas Walter, Robert Roth and Thomas Aumann for taking part in my examination.

Nicht viel von dieser Arbeit wäre möglich gewesen ohne die Hilfe der gesamten LaserSpHERe-Arbeitsgruppe, bei der ich mich herzlich für die vielen gemeinsamen Stunden, Experimente, Diskussionen und ausgezeichnete Zusammenarbeit bedanken möchte. Natürlich Felix, aber auch Jörg, Phillip und Tim schafften es mit mir über den Ozean, und ich bedanke mich nicht nur für die Hilfe dort, sondern auch für die schönen Stunden nach dem späten „Feierabend“ die wir dort verbracht haben.

Fast auf den Tag genau vor 10 Jahren saß ich im Vorkurs zum Physikstudium neben Kristian und löste mit ihm gemeinsam Aufgaben um die Wette. Es ist kein Zufall daß ich mit ihm, Tim und Felix lange ein Büro geteilt habe –Sie sind schon lange vorher meine besten Freunde geworden, zusammen mit Christoph, Daniel, Lena, Lydia, Marc, Marian, Max und Tobias. Ich danke euch für die schöne Zeit und für alle Höhen und Tiefen die wir geteilt haben.

An dieser Stelle will ich auch Felix nochmal explizit nennen, mit dem ich so viel Zeit gemeinsam in den USA verbracht habe: Nicht nur im Labor, sondern auch auf Wandertouren durch Nationalparks, auch mit Daniel, Marc und Phillip. Diese Reisen werden mir immer in wunderbarer Erinnerung bleiben.

Julia, vielen Dank für deine Unterstützung und dein Vertrauen in mich. Ich hoffe und glaube, dass wir noch viele so schöne gemeinsame Stunden verbringen können, wie in der bislang viel zu knapp bemessenen Zeit.

Weil sie einen besonderen Platz einnehmen sollen, will ich ganz zum Schluß meiner Familie danken. Meinen Schwestern Elrike und Henriette, und meinen Eltern Wolfram und Maria für die Liebe, Geduld und die Unterstützung die ihr mir entgegen bringt. Vielen Dank dafür.

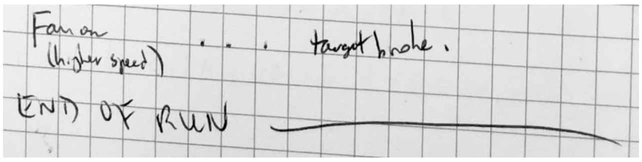

Fan on
(higher speed) . . . target broke.
END OF RUN

Curriculum Vitae

Bernhard Josef Wolfram Maaß

date of birth: 26.06.1990
place of birth: Hanau
e-mail: bmaass@ikp.tu-darmstadt.de

Graduation

07/2015 - 01/2020	Graduation in the group of Prof. Wilfried Nörtershäuser, Institut für Kernphysik, Technische Universität Darmstadt. Thesis title: *Laser Spectroscopy of the Boron Isotopic Chain*
	Regular participation at experiments at GSI Helmholtzzentrum für Schwerionenforschung Darmstadt, CERN European Organization for Nuclear Research, Geneva, NSCL National Superconducting Laboratory, East Lansing.
	Visiting researcher at Argonne National Laboratory, Lemont
	Member of the Sonderforschungsbereich SFB 1245 Member of the Helmholtz Graduate School for Hadron and Ion Research Member of the Graduiertenschule Giersch Awarded with the Giersch-Excellence-Award 2018

Academic education

10/2009 - 12/2014	Studies of physics, Technische Universität Darmstadt
10/2013 - 12/2014	Master's degree in the group of Prof. Wilfried Nörtershäuser, GSI Helmholtzzentrum für Schwerionenforschung Darmstadt and Institut für Kernphysik, Technische Universität Darmstadt. Thesis title: *Geladene Teilchen in der HITRAP-Kühlfalle*
09/2012 - 01/2013	Bachelor's degree in the group of Prof. Thomas Aumann Institut für Kernphysik, Technische Universität Darmstadt. Thesis title: *Teilchen mit Strahlrapidität nach dem* R^3B*-Reaktionstarget*

School education

06/2009	Abitur at Grimmelshausen Gymnasium Gelnhausen

List of publications

Ground-state electromagnetic moments of ^{37}Ca

A. Klose, K. Minamisono, A. J. Miller, B. A. Brown, D. Garand, J. D. Holt, J. D. Lantis, Y. Liu, B. Maaß, W. Nörtershäuser, S. V. Pineda, D. M. Rossi, A. Schwenk, F. Sommer, C. Sumithrarachchi, A. Teigelhöfer, and J. Watkins

Phys. Rev. C 99, 061301(R) (2019)

Laser Spectroscopy of Neutron-Rich Tin Isotopes: A Discontinuity in Charge Radii across the N=82 Shell Closure

C. Gorges, L. V. Rodríguez, D. L. Balabanski, M. L. Bissell, K. Blaum, B. Cheal, R. F. Garcia Ruiz, G. Georgiev, W. Gins, H. Heylen, A. Kanellakopoulos, S. Kaufmann, M. Kowalska, V. Lagaki, S. Lechner, B. Maaß, S. Malbrunot-Ettenauer, W. Nazarewicz, R. Neugart, G. Neyens, W. Nörtershäuser, P.-G. Reinhard, S. Sailer, R. Sánchez, S. Schmidt, L. Wehner, C. Wraith, L. Xie, Z. Y. Xu, X. F. Yang, and D. T. Yordanov

Phys. Rev. Lett. 122, 192502 (2019)

Nuclear Charge Radii of ^{10,11}B

B. Maaß, T. Hüther, J. Krause, J. Krämer, K. König, A. Lovato, P. Müller, M. Puchalski, K. Pachucki, R. Roth, R. Sánchez, F. Sommer, R. B. Wiringa, W. Nörtershäuser

Phys. Rev. Lett. 122, 182501 (2019)

Lifetimes and g-factors of the HFS states in H-like and Li-like bismuth

V. Hannen, J. Vollbrecht, Z. Andelkovic, C. Brandau, A. Dax, W. Geithner, C. Geppert, C. Gorges, M. Hammen, S. Kaufmann, K. König, Y. A. Litvinov, M. Lochmann, B. Maaß, J. Meisner, T. Murböck, R. Sánchez, M. Schmidt, S. Schmidt, M. Steck, T. Stöhlker, R. C. Thompson, C. Trageser, J. Ullmann, C. Weinheimer, W. Nörtershäuser

J. Phys. B: At. Mol. Opt. Phys. 52, 085003 (2019)

Proton superfluidity and charge radii in proton-rich calcium isotopes

A. J. Miller, K. Minamisono, A. Klose, D. Garand, C. Kujawa, J. D. Lantis, Y. Liu, B. Maaß, P. F. Mantica, W. Nazarewicz, W. Nörtershäuser, S. V. Pineda, P.-G. Reinhard, D. M. Rossi, F. Sommer, C. Sumithrarachchi, A. Teigelhöfer and J. Watkins

Nature Physics 15, 432 (2019)

High voltage measurements on the 5 ppm relative uncertainty level with collinear laser spectroscopy

J. Krämer, K. König, Ch. Geppert, P. Imgram, B. Maaß, J. Meisner, E. W. Otten, S. Passon, T. Ratajczyk, J. Ullmann, and W. Nörtershäuser

Metrologia 55, 268 (2018)

First determination of ground state electromagnetic moments of ^{53}Fe

A. J. Miller, K. Minamisono, D. M. Rossi, R. Beerwerth, B. A. Brown, S. Fritzsche, D. Garand, A. Klose, Y. Liu, B. Maaß, P. F. Mantica, P. Müller, W. Nörtershäuser, M. R. Pearson, and C. Sumithrarachchi

Phys. Rev. C 96, 054314 (2017)

High precision hyperfine measurements in Bismuth challenge bound-state strong-field QED

J. Ullmann, Z. Andelkovic, C. Brandau, A. Dax, W. Geithner, C. Geppert, C. Gorges, M. Hammen, V. Hannen, S. Kaufmann, K. König, Y. A. Litvinov, M. Lochmann, B. Maaß, J. Meisner, T. Murböck, R. Sánchez, M. Schmidt, S. Schmidt, M. Steck, T. Stöhlker, R. C. Thompson, C. Trageser, J. Vollbrecht, C. Weinheimer, and W. Nörtershäuser

Nat. Commun. 8, 15484 (2017)

Charge Radii of Neutron Deficient ^{52,53}Fe Produced by Projectile Fragmentation

K. Minamisono, D. M. Rossi, R. Beerwerth, S. Fritzsche, D. Garand, A. Klose, Y. Liu, B. Maaß, P. F. Mantica, A. J. Miller, P. Müller, W. Nazarewicz, W. Nörtershäuser, E. Olsen, M. R. Pearson, P.-G. Reinhard, E. E. Saperstein, C. Sumithrarachchi, and S. V. Tolokonnikov

Phys. Rev. Lett. 117, 252501 (2016)

Changes in nuclear structure along the Mn isotopic chain studied via charge radii

H. Heylen, C. Babcock, R. Beerwerth, J. Billowes, M. L. Bissell, K. Blaum, J. Bonnard, P. Campbell, B. Cheal, T. Day Goodacre, D. Fedorov, S. Fritzsche, R. F. Garcia Ruiz, W. Geithner, Ch. Geppert, W. Gins, L. K. Grob, M. Kowalska, K. Kreim, S. M. Lenzi, I. D. Moore, B. Maass, S. Malbrunot-Ettenauer, B. Marsh, R. Neugart, G. Neyens, W. Nörtershäuser, T. Otsuka, J. Papuga, R. Rossel, S. Rothe, R. Sánchez, Y. Tsunoda, C. Wraith, L. Xie, X. F. Yang, and D. T. Yordanov

Phys. Rev. C 94, 054321 (2016)

Quadrupole moments of odd-A $^{53-63}$Mn: Onset of collectivity towards N = 40

C. Babcock, H. Heylen, M. L. Bissell, K. Blaum, P. Campbell, B. Cheal, D. Fedorov, R. F. Garcia Ruiz, W. Geithner, W. Gins, T. Day Goodacre, L. K. Grob, M. Kowalska, S. M. Lenzi, B. Maass, S. Malbrunot-Ettenauer, B. Marsh, R. Neugart, G. Neyens, W. Nörtershäuser, T. Otsuka, R. Rossel, S. Rothe, R. Sánchez, Y. Tsunoda, C. Wraith, L. Xie, X. F. Yang

Phys. Lett. B 760, 387–392 (2016)

Beamline for low-energy transport of highly charged ions at HITRAP

Z. Andelkovic, F. Herfurth, N. Kotovskiy, K. König, B. Maaß, T. Murböck, D. Neidherr, S. Schmidt, J. Steinmann, M. Vogel, G. Vorobjev

Nucl. Instr. Meth. Phys. Res. A 795, 109-114 (2015)

An improved value for the hyperfine splitting of hydrogen-like ^{209}Bi^{82+}

J. Ullmann, Z. Andelkovic, A. Dax, W. Geithner, C. Geppert, C. Gorges, M. Hammen, V. Hannen, S. Kaufmann, K. König, Y. Litvinov, M. Lochmann, B. Maass, J. Meisner, T. Murböck, R. Sánchez, M. Schmidt, S. Schmidt, M. Steck, T. Stöhlker, R. C Thompson, J. Vollbrecht, C. Weinheimer and W. Nörtershäuser

J. Phys. B: At. Mol. Opt. Phys. 48, 144022 (2015)